Flows of Herschel-Bulkley fluids in confined environments : applications to the cementing of oil wells

Anne-Laure Vayssade

▶ **To cite this version:**

Anne-Laure Vayssade. Flows of Herschel-Bulkley fluids in confined environments : applications to the cementing of oil wells. Fluids mechanics [physics.class-ph]. Université Pierre et Marie Curie - Paris VI, 2015. English. NNT : 2015PA066214 . tel-01227891

HAL Id: tel-01227891

https://theses.hal.science/tel-01227891

Submitted on 12 Nov 2015

HAL is a multi-disciplinary open access archive for the deposit and dissemination of scientific research documents, whether they are published or not. The documents may come from teaching and research institutions in France or abroad, or from public or private research centers.

L'archive ouverte pluridisciplinaire **HAL**, est destinée au dépôt et à la diffusion de documents scientifiques de niveau recherche, publiés ou non, émanant des établissements d'enseignement et de recherche français ou étrangers, des laboratoires publics ou privés.

Thèse de doctorat de l'Université Pierre et Marie Curie

Spécialité

Sciences mécaniques, acoustique, électronique et robotique
(ED 391)

présentée par

Anne-Laure Vayssade

pour obtenir le grade de

Docteur de l'Université Pierre et Marie Curie

Flows of Herschel-Bulkley fluids in confined environments. Applications to the cementing of oil wells.

Soutenance prévue le 17 Septembre 2015 devant le jury composé de :

M. Axel Buguin	Président
M. Andrew Parry	Co-encadrant
M. Nicolas Flamant	Examinateur
M. Michel Cloitre	Examinateur
M. Vincent Senez	Rapporteur
M. Philippe Coussot	Rapporteur
M. Patrick Tabeling	Directeur de thèse

Laboratoire de Microfluidique, MEMS et Nanostructures
UMR Gulliver CNRS-ESPCI 7083

Etudes et Productions Schlumberger
1, rue Henri Becquerel
92140 Clamart

École Doctorale 391 : Sciences mécaniques, acoustique, électronique et robotique
Campus Curie - ChimieParisTech - LGGPTS
11, rue Piere et Marie Curie
75 231 Paris cedex 05

Abstract

Abstract

In 2010, in the Gulf of Mexico, the blowout of the Macondo well was the largest accident in the history of the petroleum industry. It appeared clearly that the cement sheath in the annular gap of the well that is supposed to hinder leakages failed. Leakages are due to the presence of mud (the mud is used during the well fabrication) in the annular gap that damage cement hardening.

We use the microfluidic tool to address the question of the mud film left in the annular gap during the cementing process. The cement and the mud will be modelled by microgel suspensions, which turn out to have similar rheological characteristics. Important dimensionless numbers can be made comparable so that useful information can be extracted from studies performed in microfluidic environments. We perform experiments in which we displace microgel suspensions by another fluid. We image the film left behind the finger and we observe its evolution over time and as a function of the front velocity. Various geometries are tested in which the walls chemistry are tuned to allow or prevent slippage. We show that slippage is a crucial parameter of the experiments.

Additionally to this approach, we have also performed a study on the flow of Herschel-Bulkley fluids in confined systems. This study revealed a novel effect associated to a characteristic length that has not been reported before. This fundamental study reveals the richness of Herschel-Bulkley flow dynamics.

Keywords

yield stress fluids, microfluidics, slippage, miscible displacements, cementing, rheology

Ecoulements de fluides de Herschel-Bulkley en systèmes confinés. Applications à la cimentation des puits de pétrole

Résumé

En 2010, la plus grande catastrophe de l'histoire de l'industrie pétrolière s'est produite dans le golfe du Mexique avec l'explosion du puit de pétrole Macondo. Les causes de l'accident sont connues : la couche de ciment dans l'espace annulaire du puit qui est supposée empêcher les fuites, a cédé. Ces fuites sont dues à la présence de boue (la boue est utilisée lors du forage du puit avant sa cimentation) dans l'annulaire dégradant la prise du ciment.

Nous utilisons la microfluidique afin d'étudier la question des films de boue qui restent sur les parois de l'annulaire. Le ciment et la boue sont modélisés par des suspensions de microgel qui ont des propriétés rhéologiques similaires. Des nombres sans dimension comparables entre la microfluidique et la situation réelle permettent d'extraire de cette étude des informations pertinentes pour l'industrie pétrolière. Nous menons des expériences de déplacements de suspensions de microgel par d'autres fluides et nous mesurons l'évolution de l'épaisseur du film laissé derrière l'interface en fonction du temps et de la vitesse de l'interface. Nous testons différentes géométries dans lesquelles les propriétés de surface sont modifiées afin d'empêcher ou de permettre le glissement des fluides dans le système. Nous montrons que le glissement est un paramètre crucial de l'expérience.

De plus, nous avons aussi étudié l'écoulement de fluides de Herschel-Bulkley en systèmes confinés. Cette étude a mis en évidence un nouvel effet associé à une longueur caractéristique qui n'avait pas encore été mentionnée dans la littérature. Cette étude fondamentale révèle la richesse de la dynamique des fluides de Herschel-Bulkley.

Mots-clefs

fluides à seuil, microfluidique, glissement, déplacements miscibles, cimentation, rhéologie

Contents

Introduction **9**

1 Industrial context and conclusions **11**
1.1 Industrial context . . . 11
1.1.1 Well fabrication and implications of cementing . . . 11
1.1.2 Well cementing fluids . . . 15
1.1.3 Problem encountered during well cementing . . . 17
1.1.4 Presentation of casing hardware . . . 18
1.1.5 Rules to help cementing stages and casing hardware . . . 21
1.1.6 Simulations: what is done nowadays in the oil industry? . . . 23
1.2 Conclusions . . . 24

2 Characterization of microgel suspensions **27**
2.1 Microgel suspensions: a "soft glassy material" . . . 27
2.1.1 Description of soft glassy materials . . . 27
2.1.2 Description of the microgel suspensions . . . 29
2.2 Microgel suspensions: a non-Newtonian fluid . . . 31
2.2.1 Thixotropy/rheopexy . . . 31
2.2.2 Non thixotropic/rheopectic fluids . . . 32
2.2.3 Visco-elasticity . . . 32
2.2.4 Summary of non-Newtonian behaviours . . . 33
2.2.5 Conclusions on the non-Newtonian behaviour of microgel suspensions 33
2.3 Rheological measurements of microgel suspensions . . . 34
2.3.1 Constitutive law and fluid movement . . . 34
2.3.2 Principles of rheological measurements . . . 36
2.3.3 Linear rheology . . . 37
2.3.4 Non-linear rheology . . . 38
2.3.5 Aging and rejuvenation . . . 41
2.3.6 Yield stress . . . 41
2.4 Conclusions on microgel rheology . . . 44

3 Material and methods **47**
3.1 Fabrication and surface treatments of microfluidic systems . . . 47
3.1.1 Fabrication of silicon masters . . . 47
3.1.2 Fabrication of PDMS systems (PolyDiMethylSiloxane) . . . 48
3.1.3 Fabrication of NOA systems . . . 49
3.1.4 Surface treatments . . . 51
3.1.5 Compatibility of surface treatments with NOA fabrication protocol . 55
3.1.6 Conclusions on system fabrication . . . 57

3.2 Micro-Particle Image Velocimetry (µPIV) 57
3.2.1 Flow configuration 59
3.2.2 Optical environment and experimental protocol 60
3.2.3 Image analysis and profile reconstruction 61
3.3 Experimental set-up used for the study of fluid displacement 62

4 Dynamical role of slip heterogeneities in confined systems 65
4.1 Introduction 65
4.1.1 Slippage in general and in the case of microgel suspensions 65
4.1.2 A brief review on experiments performed on soft glassy materials flows 67
4.2 Experimental study of Herschel-Bulkley fluids in channels with slip heterogeneities 69
4.2.1 Velocity profiles 70
4.2.2 Slip velocities 70
4.2.3 Asymmetric Herschel-Bulkley model 72
4.3 Discussion 75
4.3.1 Scaling analysis 75
4.3.2 Channel size criterion 76
4.3.3 Does cooperativity effects come into play? 77
4.3.4 Truncated plug flow profiles 77
4.4 Conclusions 80

5 Displacement of Herschel-Bulkley fluids in microchannels 89
5.1 Introduction 89
5.1.1 Newtonian immiscible fluids 89
5.1.2 Newtonian miscible fluids 92
5.1.3 Non-Newtonian fluids 93
5.1.4 Other aspects of fluid displacements 95
5.2 Strategy for the study of the displacement of Herschel-Bulkley fluids 96
5.2.1 Objectives of the chapter 96
5.2.2 Geometries of the straight channels used in the study 97
5.2.3 Channels with geometry variations in the streamwise direction . . . 98
5.3 The problem of the suppression of the slip in the channels 98
5.4 Experimental study of the displacements of HB fluids in square straight channels 100
5.4.1 Description of the phenomena in square channels 100
5.4.2 Evolution of the film thickness with the speed 103
5.4.3 Evolution of the film thickness with time 105
5.4.4 Summary of the results in straight channels 106
5.5 Experimental study of the displacements of HB fluids in channels with restrictions 106
5.5.1 Description of the phenomena in the restriction channels 106
5.5.2 Evolution of the film thickness with time 107
5.5.3 Summary of the results in channels with restrictions 108
5.6 Experimental study of the displacements of HB fluids in channels with corrugations at the wall 109
5.6.1 Description of the experiments in channels wih corrugations at the wall 109
5.6.2 Evolution of the drainage of the fluid in the corrugations with time . 109
5.7 Towards a more realistic geometry: the Hele-Shaw cell 110
5.7.1 Typical behaviour of the interface with no slip 110

5.7.2 Typical behaviour of the interface with slip . . . 112
5.8 Conclusions . . . 112

6 Simulations with Computational Fluid Dynamics 115
6.1 Introduction . . . 115
6.1.1 Mass and momentum equations . . . 116
6.1.2 Mesh . . . 116
6.1.3 Discretization method: Finite Volume Method . . . 116
6.1.4 Solver methods . . . 118
6.1.5 Multiphase flows, the Volume Of Fluid method . . . 120
6.1.6 Courant number . . . 120
6.1.7 Boundary conditions . . . 120
6.1.8 Yield stress fluids: Regularization law and augmented lagrangian method . . . 121
6.2 Objectives of the chapter . . . 121
6.3 Validation of the Fluent code . . . 122
6.3.1 Single Herschel-Bulkley fluid in two-dimensional plane channels . . . 122
6.3.2 Single Bingham fluid in two-dimensional wavy-channels . . . 123
6.3.3 Two Bingham fluids in straight channels . . . 125
6.3.4 Summary of the validation of Fluent . . . 129
6.4 Fluid rheologies . . . 129
6.5 Comparison with displacements experiments in straight channels . . . 130
6.5.1 Evolution of the film thickness with the speed . . . 130
6.5.2 Evolution of the film thickness with time . . . 131
6.5.3 Three-dimensional and two-dimensional modelling of straight channels 132
6.5.4 Summary of the displacements simulations in straight channels . . . 132
6.6 Comparison with displacements experiments in channels with restrictions . 133
6.6.1 Evolution of the film thickness with the speed . . . 133
6.6.2 Three-dimensional and two-dimensional modelling of channels with restrictions . . . 134
6.6.3 Summary of the displacements simulations in channels with restrictions 135
6.7 Comparison with displacements experiments in channels with corrugations at the wall . . . 135
6.7.1 Evolution of the drainage of the fluid in the corrugations with time . 135
6.7.2 Summary of the displacements simulations in channels with corrugations at the wall . . . 137
6.8 Conclusions . . . 137

Conclusion 139

A Fabrication of the microgel suspension 141

B The recirculation model 143
B.1 Maximale thickness of the layer: h_{max} . . . 143
B.2 Onset of the recirculation: h_{circ} . . . 143
B.3 Why does the minimum dissipation occurs at the onset of the recirculation? 145

C Flow of a Herschel-Bulkley fluid in a channel of various cross sections 147

D Estimation of the velocity of the interface **149**
D.1 Phase 1: Before breakthrough time . . . 149
D.2 Phase 2: After breakthrough time . . . 153
D.3 Phase 3: the displacing fluid is alone in the channel . . . 153

E Experiments in channels with angles **155**

Résumé de la thèse en français **157**
1 Introduction . . . 157
2 Caractérisation des suspensions de microgel . . . 159
3 Matériel et méthodes . . . 159
3.1 Fabrication et traitements de surface des systèmes microfluidiques . 159
3.2 Vélocimétrie par images de particules (µPIV) . . . 160
3.3 Système expérimental pour l'étude des déplacements de fluides . . . 160
4 Rôle des hétérogénéités de surfaces en systèmes confinés . . . 161
4.1 Profils de vitesse . . . 161
4.2 Modèle de Herschel-Bulkley asymétrique . . . 163
4.3 Discussion . . . 163
4.4 Conclusions . . . 164
5 Déplacements de fluides à seuil dans des micro-canaux . . . 164
5.1 Stratégie pour l'étude des déplacements de fluides de Herschel-Bulkley 164
5.2 Etude expérimentale du déplacement de fluides de Herschel-Bulkley dans des canaux droits à sections carrées . . . 164
5.3 Etude expérimentale du déplacement de fluides de Herschel-Bulkley dans des canaux avec des restrictions . . . 166
5.4 Etude expérimentale du déplacement de fluides de Herschel-Bulkley dans des canaux avec des cavités . . . 166
5.5 Conclusions . . . 167
6 Analyse numérique de dynamique des fluides . . . 167
6.1 Comparaison avec la littérature . . . 167
6.2 Comparaison avec les expériences . . . 167
6.3 Conclusions . . . 168
7 Conclusions . . . 168

Bibliography **171**

Introduction

The construction of an oil well starts with a drilling stage. Inside the hole drilled, long steel tubes (casings) are assembled. To consolidate and to exploit the well it is necessary to isolate the casing from the neighbouring rock side. This operation is the cementing stage. It consists in injecting cement in the annular space between the casing and the formation. The cement is injected from the surface through the casing towards the bottom of the well. The cement is then pushed back up into the annular space. The aim of this process is to fill completely the annular gap with cement.

On its way the cement has to displace drilling fluids or spacers that are present in the casing and in the annular space. Several cementing tools are placed in the annular space, there are centralizers, collars, liners or scratchers. In many cases, the drilling muds and spacers are more viscous than the cement. Therefore the interface between the fluids is unstable and viscous fingering can occur during the displacement of the fluids. However, in the conditions of operation used in the oil industry, fluid densities are adjusted so as this instability is suppressed. Still, the displaced fluid may leave a residual film across the annular gap. Such a film is a significant problem because it can induce the formation of mudcakes or get mixed with the cement. In all these cases, the presence of mud films affects the proper hardening of the cement. Therefore leaks may appear and fluid or gas migration between different geological layers can occur through the annular gap resulting in loss of production efficiency, in a loss of the well or even, such as for the Macondo well in the Gulf of Mexico in 2010, in environmental disasters.

We will use the microfluidic tool to address the question of the mud film left in the annular gap during the cementing process. The cement and the mud will be modelled by microgel suspensions, which turn out to have similar rheological characteristics. Indeed, microfluidic scales (10 µm) are much smaller than the gap sizes (several cm). Nonetheless, important dimensionless numbers can be made comparable so that useful information can be extracted from studies performed in microfluidic environments. Adopting this approach permits to work with all sorts of geometries, fluids, boundary conditions, while taking advantage of the presence of observation windows of excellent quality.

Additionally to this approach, we have also performed a study on the flow of Herschel-Bulkley fluids in confined systems. This study revealed a novel effect associated to a characteristic length that has not been reported before. This fundamental study reveals the richness of Herschel-Bulkley flow dynamics.

Following these considerations, we have organized the work in six chapters:

- ✧ **Chapter 1** introduces the petroleum problematic. We describe the fabrication of a well, the current practices and the problems encountered during cementing process.

- ✧ **Chaper 2** describes the synthesis and characterization of the model fluids used in the experiments. The model fluid is a microgel suspension above the jamming transition which consequently exhibits a yield stress.

- ✧ **Chaper 3** presents the microfabrication techniques used to build microfluidic channels that can sustain high pressure drops without deformation. Various surface treatments were applied to tune independently the surface properties of the channels. The two experimental set-up, a µPIV and the displacement set-up, are described.

- ✧ **Chapter 4** is dedicated to the flow of a single phase microgel suspension in a microfluidic channel. The fluid is characterized by imaging the flow with a µPIV set-up. The results are compared to macroscopic rheological measurements of chapter 2. Non-Newtonian fluids are prone to slip on smooth surfaces. We show that slip heterogeneities control the flow structure as the size of the system decreases.

- ✧ **Chapter 5** presents the results of displacement experiments of Herschel-Bulkley fluids. Various geometries are investigated (straight microchannels, straight microchannels with restrictions, with corrugations). Emphasis is made on the influence of slippage in these geometries, in particular on the film dynamics left behind the displaced fluid.

- ✧ **Chapter 6** presents numerical results obtained with the CFD (Computational Fluid Dynamics) software Fluent. First the code is tested against reference cases found in the literature using a different method for the modelling of the rheology of yield stress fluids. Then we compare the simulations to the experiments.

Chapter 1

Industrial context and conclusions

The production capacities and longevity of an oil well depends on the quality of its fabrication. In our study we focus on the cementing stage of the well construction. We resume the main problematic and current techniques of cementing operations, more information can be found in [133].

1.1 Industrial context

The zonal isolation of an oil well is the major condition for a productive and safe exploitation of the well over many years. The isolation depends on the success of the well cementing stage which is still a challenge to perform. Research is carried out to improve the current cementing techniques.

1.1.1 Well fabrication and implications of cementing

The construction of an oil well follows different steps. First, a hole is drilled in the ground, this is the *drilling* stage. Then a *logging* procedure collects geological information to verify if there is oil at this location. Note that only one of seven exploration wells turns into a production well. The next step is to place the *casing* and to carry out the *primary cementing*. The casing is a steel pipe which prevents the well from collapsing. A well is thousands of meters deep. To prevent collapse, the well is drilled and cased in several stages. The casing is cemented to isolate the rock from the well and to isolate the different types of formations: it provides *zonal isolation*. Regularly stabilizing the well means that the drilling, casing and cementing steps are repeated in a row to achieve piecewise the desired depth of the well. After a casing is set, the hole is smaller so that, as the well is being constructed by sections, the size of the casing inserted to stabilize the well decreases. Figure 1.1 represents the drilling, casing and cementing stages of the construction of a well repeated in a row (three times) to achieve the desirable depth.

Once the well is stabilized and cemented, a *tubing* is installed in the casing and sealed with a *packer*. The reservoir fluids are extracted by the tubing and not directly by the casing. It allows to protect the casing from corrosion. A tubing can easily be replaced, as well as its joint. Since the cemented casing isolates the well from the oil reservoir, a *perforating* step need to be accomplished in order to let the oil enter the well. This is done with a special gun lowered into the well. Finally, the production can start. Figure 1.2 represents the tubing, perforating and production stages of a well.

In the thesis we are interested in the cementing stage. The aim is to fill the *annular gap* with cement. The annular gap is the thin space between the casing and the formation.

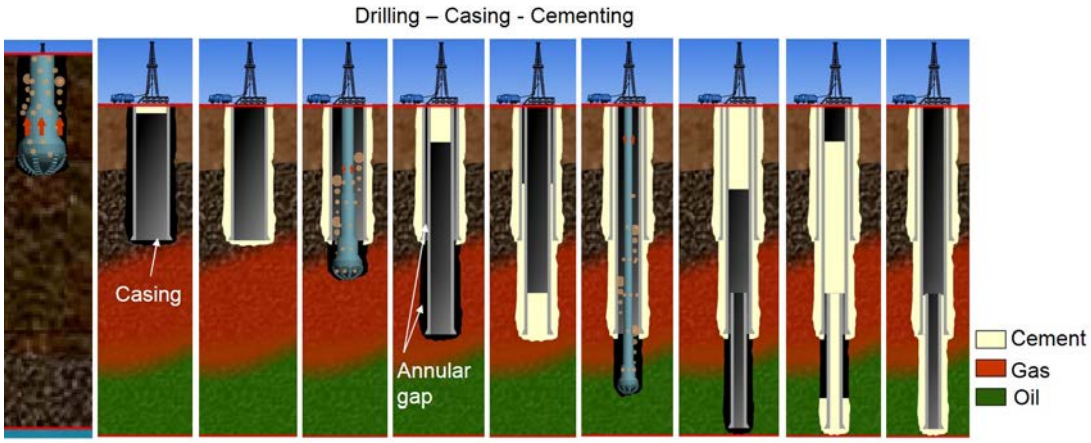

Figure 1.1 – From left to right: repetition of the drilling, casing and cementing stages for the construction of a well.

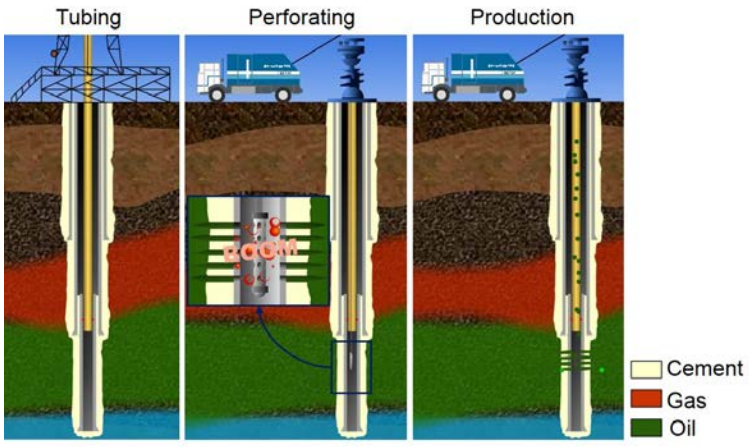

Figure 1.2 – From left to right: tubing, perforating and production of a well.

To fill this gap, the cement is pumped from the surface to the bottom of the well through the casing. At the bottom, the cement goes back up in the annular space (see figure 1.1). On its way upwards, the cement displaces the *drilling mud*. Drilling muds are introduced during the drilling phase to clean the well from the cutting parts created by the drilling. They are designed to suspend the cuttings of the rocks. After drilling, the mud occupies the casing and the annular space.

The primary cementing stage is critical for the exploitation and the viability of the well. If the mud is not well displaced and replaced completely by cement, it can affect the isolation of the well. Indeed, a bad displacement of the mud by the cement can lead to local mixing of the cement with the mud and also to the formation of residual films of mud that stay along the casing or along the formation. The mixing of the cement with the mud can hinder the cement to set. The residual film of mud in contact with the porous formation dehydrates itself and is transformed into a porous material which is called the *mudcake*. The mudcake can also be formed before the cementing stage during the drilling when the mud is circulated in the well. The cementing process should ideally be able to remove the mudcakes. If not removed, the mudcakes constitute channels in the annular gap through which the fluids of the neighbouring formation can migrate.

The primary cementing stage conditions the future performances of a well and its longevity. During its life, the well is submitted to various conditions that can affect the cement sheath. The perforating stage can shatter the cement sheath near the perforating zone. The production process induces temperature and pressure fluctuations in the well. The risks for the cement sheath are:

— Cracking: due to expansion/contraction of the cement sheath
— Debonding: the bond between the cement/formation or the cement/casing fails
— Shear failure: complete failure of the cement sheath

All of these phenomena depend also on the mechanical properties of the cement (elasticity and compressive strength). The consequence is represented on figure 1.3: flow paths (channeling or microannuli) are created in the cement sheath through which the fluids used during the production process or the fluids from the neighbouring formation (water or gas for example) can flow. If a continuous microannulus is formed, the losses are not negligible. It results in an environmental cost when fluids are injected where it should not be, or in drilling hazards and risks of blowout when additional field developments are carried out. Also the production equipment can be destroyed.

The consequences of a bad cementing are economically and environmentally catastrophic. The full production potential of the well cannot be reached and remedial cementing operations have to be carried out. The presence of microannuli in the well can lead to the contamination of subsurface zones (freshwater forexample), to the destruction of production equipments or to drilling risks. The 2010 accident on the Deepwater Horizon platform in the Gulf of Mexico is an example of environmental disaster that a bad cementing could cause.

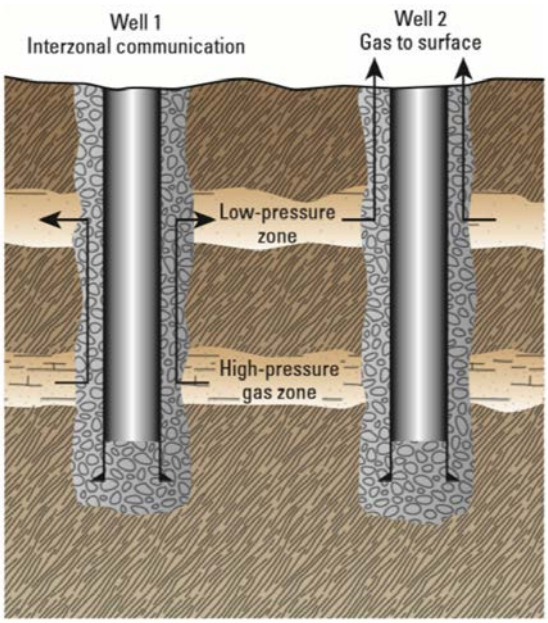

Figure 1.3 – Annular migration of gas between two formation zones (left) or up to the surface (right). Reproduction from [133].

Accident at the Macondo well

In April 2010, the largest oil spill in the petroleum industry (4.9 million barrels) started in the Gulf of Mexico at the Macondo well. The damages are human (11 deaths) and environmental (the beaches of Louisiana were flooded with oil, marine wildlife still continues to die at abnormal rates). BP paid around $20 billion dollars for the damages caused.

The investigations conducted on the Macondo accident pointed out that BP and its supplier Halliburton favoured a low-cost strategy over safety for the construction of the Macondo well. The technical cause of the blowout of the well is clear: the cement job failed in sealing off hydrocarbons in the formation [54].

The well cementing is the most important fabrication stage for the well safety and productivity. We briefly recall some of the major decisions that led to the accident. Several casing hardware were not installed properly or not in a sufficient quantity. For example, there were not enough centralizers placed around the casing to ensure its centralization in the wellbore. The mud conditioning stage is supposed to clean the wellbore before the injection of the cement. The volume of mud circulated during mud conditioning was underestimated. Overall, in what concerns the Macondo well, it has been shown that the preparation of the well was not appropriate for the realization of a successful cementing operation.

As a result, the pressure of the surrounding formation broke the cement sheath at the bottom of the well leading to a flow of hydrocarbons in conditions where the production equipement was not installed yet. In addition, the safety equipment placed at the surface was activated too late to prevent the explosion.

1.1.2 Well cementing fluids

There are different kind of fluids circulating in the well during its fabrication: drilling muds during the drilling stage, spacers, washers and cement slurries during the cementing stage. These fluids all need to be designed and used in a given order to finally ensure a good displacement of the mud and thus a good zonal isolation.

Drilling mud, compatibility with cement

Drilling muds are designed to allow cuttings transport during the drilling phase. Before the cementing phase, the mud is *conditioned*, which means that its properties are changed to facilitate the cementing stage by having a less viscous fluid to displace or by avoiding the formation of gelled mud. During conditioning it is possible to change the density and the rheology of the mud. In most of the cases it is a yield stress shear-thinning fluid well described by an Herschel-Bulkley law. The first step for conditioning is to remove the cuttings from the mud. This decreases the mud yield stress. By adding dispersants, water or oil, the plastic viscosity of the mud can also be reduced. After conditioning, the mud can still be modelled by a Herschel-Bulkley law.

Other considerations complicate the understanding of drilling fluid rheological properties because drilling fluids in the well are not homogeneous for the following reasons:

— Drilling fluids have time-dependent rheological properties (thixotropic fluids): at rest, their yield stress or gel strength increases with time because the mud gels allow the cuttings to stay suspended in the mud. Muds can develop high gel strength in large washout sections.
— Filtercakes form near permeable formation because the mud is submitted to dynamic filtration: its continuous phase fluid flows into the porous formation. Without fluid-loss control, the filtercakes can grow. Their properties are various and their cohesion and adhesion to the surfaces depend on the mud composition.
— The cuttings parts or weighting agents might settle on the low side of deviated wells forming *solid beds.*

Drilling fluids are emulsions that could be either water-based muds (WBM) or oil-based muds (OBM). The emulsion stability is obtained using surfactants. Cementing engineers talk about *fluid compatibility.* The criteria for fluid compatibility are not clear but some characteristics of incompatibility between mud and cement are:

— Some components in the water phase in OBMs have a strong gelling or accelerating effect on cement.
— The emulsifiers in the mud adsorb on the cement grains and inhibit hydration of cement.

OBMs are less compatible with cement than WBMs. Mixing between incompatible fluids leads to the formation of highly viscous bodies which become difficult to displace. Compatibility between the fluids depends on mud and cement chemistries.

The fluid properties can also be changed by contamination coming from cuttings or from the mud circuit. In most of the cases, it is necessary to avoid contact between the mud and the cement particularly when OBMs are used. To avoid mixing between incompatible fluids, one solution is to use preflushes such as washes or spacers between the fluids.

Preflushes: washes and spacers

The function of preflushes is to avoid mixing between the cement and the mud, they can also be designed to help mud displacement. The main requirements for these fluids are:

— They have to be compatible with both the mud and the cement.
— Their rheologies and densities are set to optimize mud displacement.
— Their chemical composition should allow a proper cleaning of the well surfaces. After cleaning, the surfaces have to be water-wet. Also they should not change the rock wettability or damage the formation.

Several preflushes might be necessary to meet all these requirements. Washes have viscosities and densities close to that of water or oil. Turbulent flows can be achieved, which can help remove the mudcakes and gelled mud. Spacers are more viscous than washes, they flow mostly in a laminar regime. The properties of washes and spacers are adjusted by adding surfactants, polymers, clays or weighting agents.

Cement slurries

The most widespread cements in oil wells are the Ordinary Portland Cement (OPC). Portland cement is an hydraulic cement, which means that it develops compressive strength thanks to hydration: a reaction between water and the chemical compounds of the cement takes place. To harden, the cement has to be left in place in air or underwater. The main advantages of the set of Portland cement is that it is insoluble in water and it has a very low permeability. These characteristics make Portland cement a well suited binding material for zonal isolation in oil wells.

The cement paste is produced when water is added to a *clinker*. The clinker contains the minerals that interact with water to form the cement. The principal mineralogical composition of Portland cement clinker is: CaO (60-70%), SiO_2 (18-22%), Al_2O_3 (4-6%) and Fe_2O_3 (2-4%). When these anhydrous compounds are brought in contact with water, they are decomposed to form hydrated compounds that precipitate. This reaction between the cement clinker and water leads to a continuous cement thickening and then hardening.

Cement additives allow to accommodate the cement properties to a wide range of operating conditions: severe temperatures and pressure, the presence of corrosive fluids, the formation porosity. The additives mainly act on:

— the settling time of the cement: accelerators and retarders
— the density of the cement: extenders and weighting agents
— the viscosity of the cement: dispersants decrease the viscosity
— the loss of slurry or water phase: fluid loss control agents hinder the filtration of the water-phase of the cement into the porous formation and lost-circulation agents promote bridging over fractures and cavernous zones.

The additives provide thousands of possible formulations for cement slurries.

Cement pastes are non-Newtonian fluids. Mostly they are shear-thinning and they often have a yield stress. The three main models used to describe cement paste rheology are:

— the power law model for shear-thinning fluids.
— the Bingham model for plastic fluids, i.e. fluids with a yield stress.
— the Herschel-Bulkley model which combines yield stress and shear-thinning behaviour.

As spacers, cement slurries may exhibit time-dependent behaviour, they are thixotropic fluids. This is due to physical interactions and chemical reactions that occur between the particles. More details on thixotropic behaviours is given in chapter 2. The rheology of cement depends also strongly on pressure and temperature. It is still a challenge to obtain accurate rheological characterization of cement pastes [37].

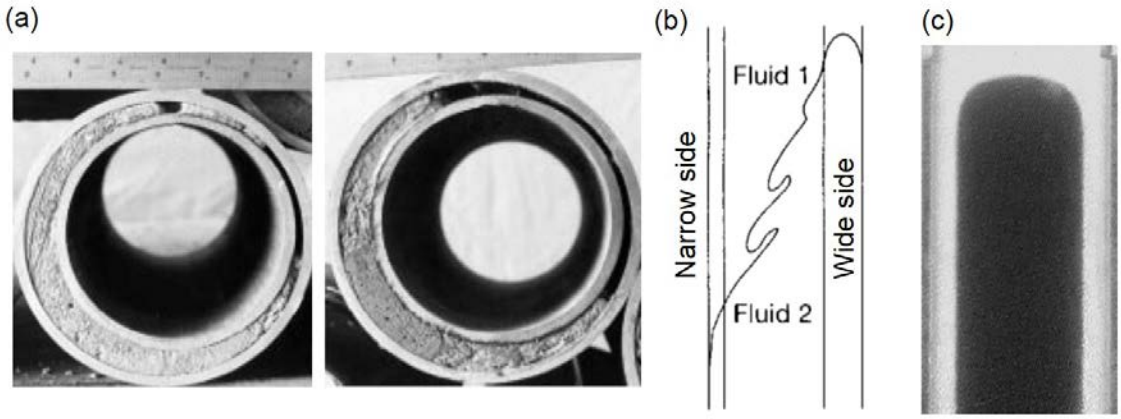

Figure 1.4 – (a) Unsuccessful mud-displacement experiment in an eccentric annulus: the narrow gap is not filled with cement, reproduction from [89]. (b) Gravitational instabilities that promote an azimuthal flow from the wide side to the narrow side of the annulus, reproduction from [177]. (c) Viscous fingering during the iso-density displacement of a Herschel-Bulkley fluid by another one with a lower yield stress, reproduction from [58].

1.1.3 Problem encountered during well cementing

The annular gap is the thin space left between the formation and the casing. Its length range from 1000 m to 6000 m and its width is around 1 to 5 cm. Ideally, the casing should be perfectly centered in the formation but it is rarely the case. Often, the casing is *eccentric*. Eccentricity induces a distortion of the velocity profile around the casing. The fluid flows faster on the wide side of the annulus and fluids with a yield stress can be completely static on the narrow side of the annulus. It results in poor mud displacements and poor cementing jobs as shown on figure 1.4 (a). The difference of velocity between the narrow and the wide side of the annulus can also destabilize the interface to form shear waves. If the displacing fluid is heavier, gravity instabilities can form in addition and it can promote flow from the wide side to the narrow side of the annulus [177] as sketched on figure 1.4 (b). If the displacing fluid is lighter, it can bypass the narrow side of the annulus.

When a fluid is displacing a more viscous fluid, a viscous instability develops. Instead of piston-like displacement, a finger of the less viscous fluid enters the more viscous fluid and reduces the efficiency of the displacement across the gap (figure 1.4 (c)).

In paragraph 1.1.2, we have seen that the contact between the formation and the drilling fluids leads to the formation of gelled mud, solid beds and filtercake in the annular. They create inhomogeneities of the drilling fluid being displaced and they induce local restriction of the annular gap.

Instabilities appear during the displacement of drilling fluids due to density or viscosity differences between the displaced and the displacing fluids. The annular geometry is often eccentric and azimuthal flows can take place, the fluids involved are non-Newtonian so their viscosities depend on the flow rate applied. Moreover gelled mud, solid beds and filtercakes can form in the annular. All these parameters complicate greatly the displacement of the drilling fluids and show that the choices of flow rate pumping, fluid rheology and fluid densities are interdependent.

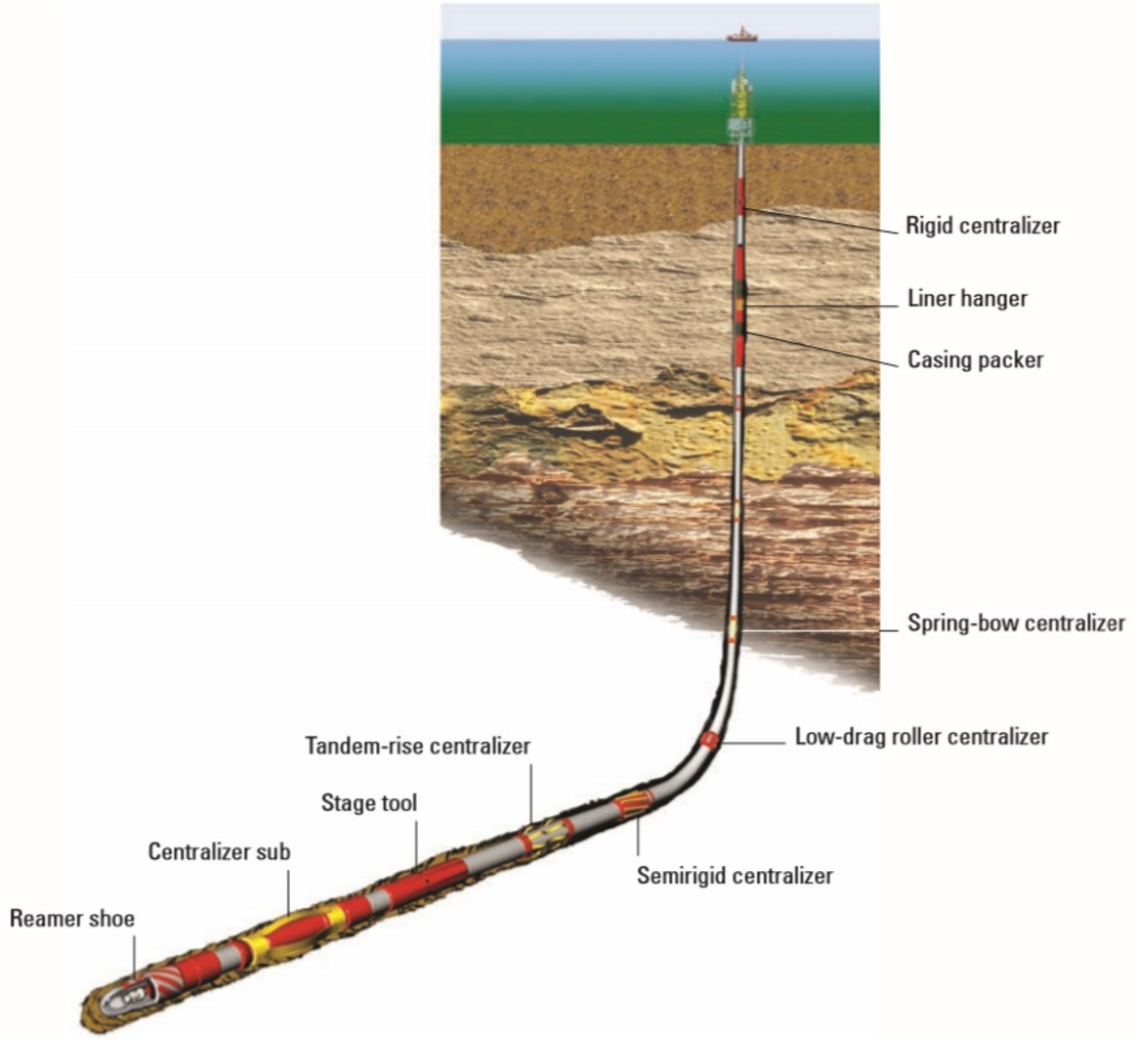

Figure 1.5 – Application of casing hardware for a primary cementing job. Reproduction from [133].

1.1.4 Presentation of casing hardware

Casing hardware is the equipment that is used on or within the casing to help casing placement and cementing operations. Figure 1.5 shows an application of the use of casing hardware.

Casing hardware are present all along the casing in the well: the guide shoe protects the casing while it is being run in the well, the centralizers insure that the casing is centered in the wellbore. The main casing hardware are detailed below, they can be split into two main categories: hardware that are placed inside and outside the casing.

Inside the casing

Figure 1.5 (a) shows cementing plugs in a casing. Cementing plugs are used to separate cement slurries from drilling fluids. Sometimes plugs are also used to separate chemical washes or spacers from the mud. They also indicate when cement placement is finished. The bottom plug precedes the cement slurry, when set at the bottom of the well it permits the flow of the slurry through it. The top plug comes after the slurry, when it lands on the

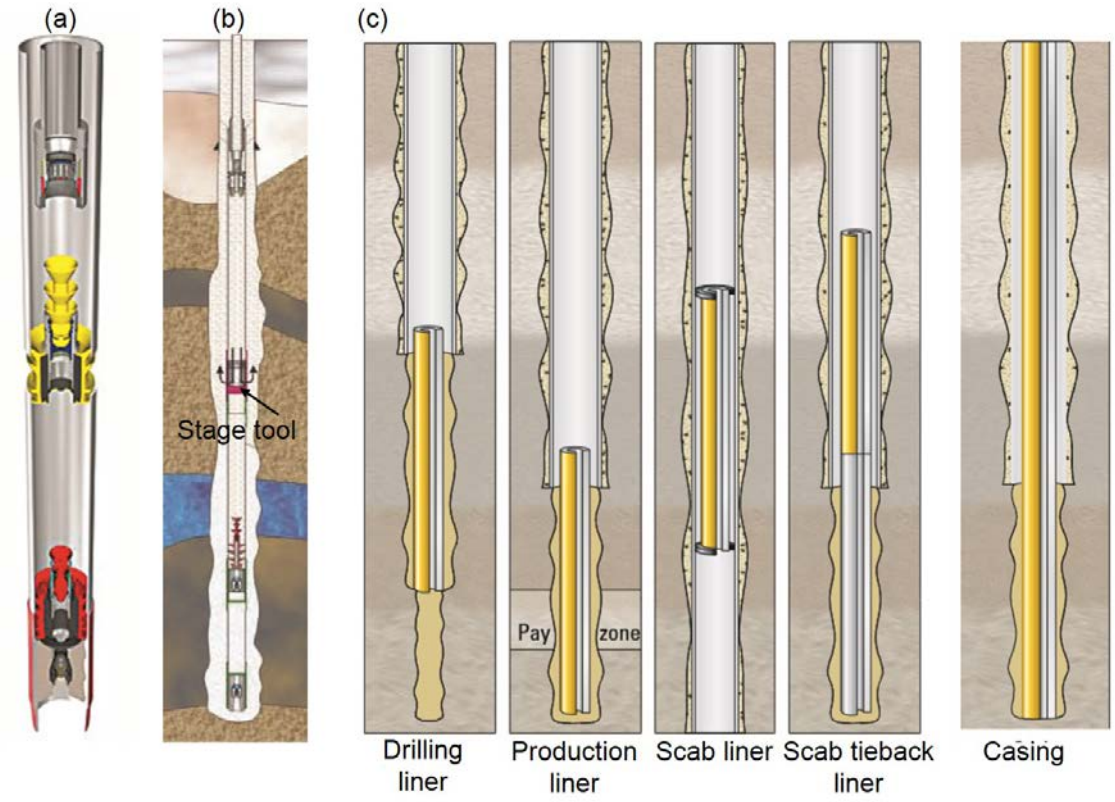

Figure 1.6 – Hardware inside the casing. (a) A bottom plug (red) has reached the float collar, the top plug (yellow) displaces the fluids between the two plugs. The yellow plug avoids mixing with the fluid above. (b) A stage tool permits intermediate access to the annular. (c) Different types of liner from left to right: drilling liner consolidate a weak formation zone for further drilling operations, a production liner, a scab liner to repair damage on the casing, a scab tieback liner extends upwards of an existing liner, unlike the liner the casing extends up to the surface. Reproduction from [133].

bottom plug, the pressure increases meaning that the cementing stage is completed.

Stage tools are placed within the casing as shown on figure 1.5 (b) to provide an intermediate passage for the fluids to the annular, it allows to cement selected intervals of the annular. It is used to protect some weaker formation zones: this zones can be cemented separately with another lighter cement.

Different kinds of liners are represented on figure 1.5 (c). Liners are shorter than casings, they are easier to manipulate and their cementing is faster. They can be used near weak formations to prevent them from caving in (drilling liners). Liners are also placed for production (production liner). Since the diameter of the casing just above the liner is larger than the diameter of the liner, it allows to run larger completion equipments down to the production location and therefore it increases well productivity. A scab liner is used to repair damages on the casing. If a scab liner extends up to an existing liner it is called a scab tieback liner.

Outside the casing

Figure 1.7 shows pictures of the external casing hardware. A guide shoe is installed at the bottom of the casing and guides the casing toward the center of the borehole when it is lowered in the well (figure 1.7 (a)). It protects the casing from hitting rock ledges and

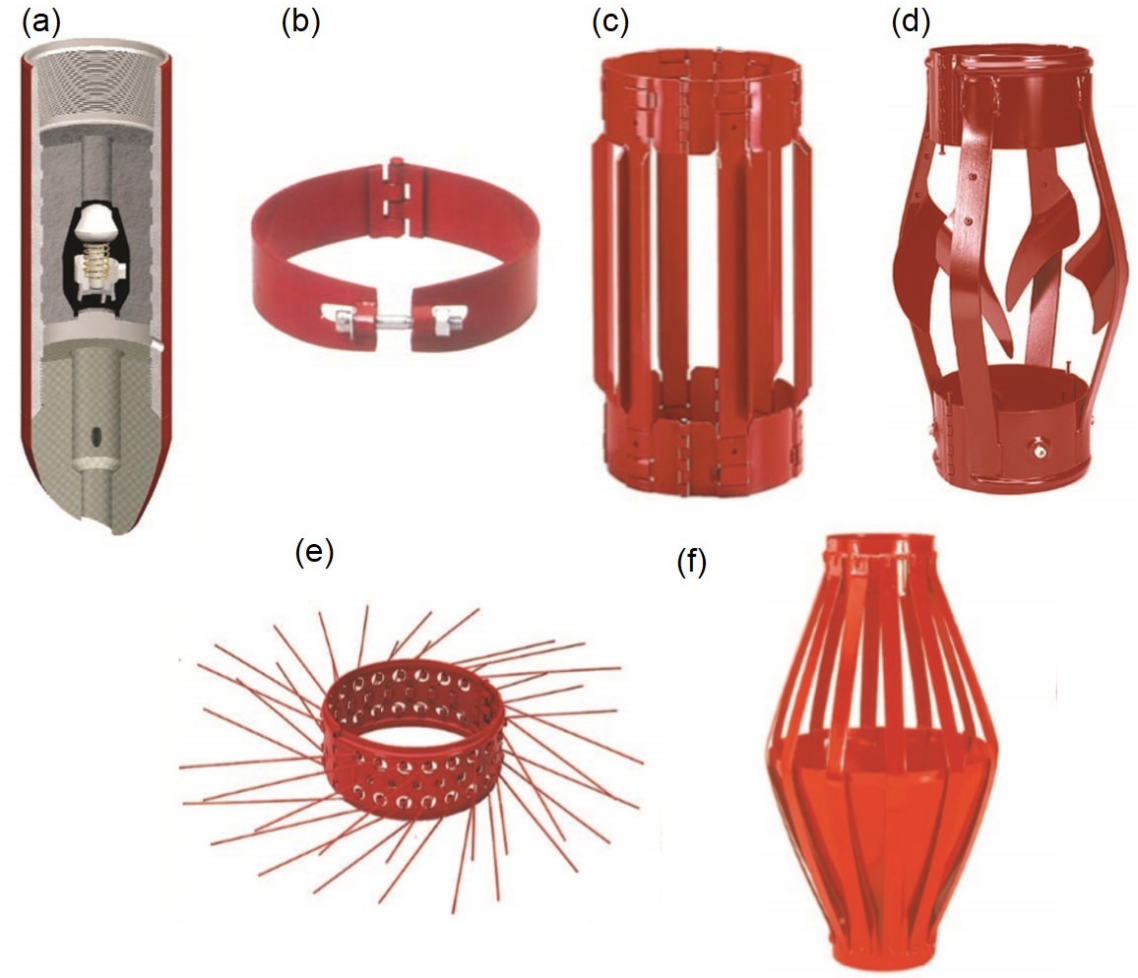

Figure 1.7 – Hardware outside the casing: (a) a guide shoe with a rounded nose, (b) a stop collar, (c) a rigid centralizer, (d) a turbolizer: a turbulence-inducing centralizer, (e) a scratcher and (f) a cement basket. Reproduction from [133].

washouts. While the next section of the well is constructed, the guide shoe is being drilled. A float shoe is a guide shoe with a check valve that prevent the fluid to flow from the annulus to the casing while the casing is run in the well. Various nose designs are available for guide and float shoes. For example a round nose deviates the casing from ledges and obstructions.

Annular pack off equipments have expanding rubber that pack off against the formation, therefore they provide sealing and centralization. They are used to protect weak formation from gas and fluid migrations and from excessive hydrostatic pressures. They are used below stage or port collars.

External attachments enhance cement displacement, the most common devices are: stop collars (figure 1.7 (b)), centralizers (figure 1.7 (c) and (d)), scratchers (figure 1.7 (e)) and baskets (figure 1.7 (f)). Stop collars limit or stop the travel of external attachments. Collars can also be equipped with check valves to prevent wellbore fluids from entering the casing during casing placement. Centralizers are placed to avoid sticking while the casing is lowered and then it keeps the casing centered in the borehole. It improves cement placement by creating a more uniform gap thickness. Their designs may also help mud removal while running the casing or limit friction with the formation when rollers are

mounted on them. Scratchers are designed to remove immobile mud and mudcakes from the wellbore wall. They work during casing rotation or reciprocation. Cementing baskets limit mixing between wellbore fluids that have different densities. They are used with stage tools: when a section is cemented, the heavy cement slurry could mix with the lighter fluid below the stage tool while hardening, cement basket prevents it.

1.1.5 Rules to help cementing stages and casing hardware

Since the 1930s, experimental and numerical research on cement placement allowed a better understanding of the mechanisms that take place in the wellbore. Some "good cementing practices" for cementing job design could be defined and new tools such as casing hardware were designed especially for improvement of cementing operations. The requirements for a good cementing job are:

1. remove the mud from the borehole.
2. keep incompatible fluids apart.
3. remove all solids from the walls.

The parameters that the job designer can tune are:
— the well preparation, mud conditioning, mud circulation.
— the fluid rheology, densities and sequence.
— the flow regime: turbulent or laminar.
— the choice of casing hardware and casing movements.

Viscous forces are linked to fluid rheology, wellbore geometry and flow conditions. Buoyancy forces are linked to fluid densities and inclination of the well. Some instabilities are triggered both by viscous and gravity forces as in the example of azimuthal flows in paragraph 1.1.3. Some of these parameters are interdependent and the main mechanisms involved in the displacement depend on the length scale: in slim deviated annulus viscous forces dominate whereas in large vertical annulus buoyancy forces dominate.

Here we give explanations about the current practices and recommendations in the oil industry for achieving good cementing jobs. These recommendations are based on academic experiments, numerical studies and on statistical field analysis.

Well preparation, mud conditioning, mud circulation

The well preparation refers to the drilling phase. Good drilling practices are important to avoid dogleg, washout zones that are difficult to clean. An ideal borehole has smooth walls with low severity doglegs, controlled pressure, is free from cuttings, stable, and its mud is mobile.

Mud conditioning is the stage that consists in circulating the mud in the wellbore while cleaning and thinning it. Cleaning occurs thanks to filtration of the mud, and thinning is achieved thanks to additives that reduce the mud gel strength, yield stress, density and plastic viscosity. The aim is to reduce the driving forces that will be necessary to displace the mud as well as to increase the mud mobility.

Once the casing is in place, the mud should be circulated. Indeed during the placement of the casing the mud stays at rest and gels or builds filtercakes. Circulation helps to erode gelled mud and filtercake, and gives opportunity to further clean the mud and reduce its yield stress and plastic viscosity. Since the mud is a thixotropic shear-thinning fluid, under shear its yield stress and plastic viscosity decrease.

The fluid rheology, densities and sequence

Spacer and washers are used to avoid mixing between incompatible drilling fluids and cement slurries. They can help to remove mud filtercakes and solid beds. If they flow through the porous filtercake or solid beds, they are able to induce fluidization and thus they weaken the bed. Chemical or physico-chemical effects can result in solid removal thanks to interfacial tension reduction, diffusion of dispersants into the static layer or dissolution of solid components: the filtercakes and solid beds are eroded. The densities and rheological properties of spacers and washers should lie between those of the mud and lead slurry.

Drilling fluid rheology is adjusted during the conditioning stage, the aim is to reduce their yield stress and plastic viscosity. But information on their rheological behaviour are difficult to interpret since they are thixotropic fluids and that the presence of solid beds, filtercakes and cuttings make the mud inhomogeneous.

Ideally, the cement slurry should be more viscous and more dense than the drilling fluid. But the cement slurry is also chosen with regards to the final mechanical properties it should reach: extreme downhole temperature or pressure changes, chemical resistance, fluid loss control among others.

Effect of the flow regime

The pumping rate sets the flow regime in cooperation with the fluid rheologies. The effect of turbulent flows on the cementing process is not clear.

Turbulent flows allows the propagation of eddies, which induce pressure fluctuations that can cause the removal or detachment of mud filtercakes by abrasion: parts of the filtercake or solid bed are broken by the impact of the flowing fluid. If the shear rates created are sufficient, some parts of the filtercakes and solid beds can also be removed by shearing.

For a centralized vertical casing, recent test rig and numerical results showed that density and rheology hierarchy is fundamental for laminar displacement. When the flow is turbulent, the interface between fluids is stabilized even if no hierarchy for rheology and density is respected [7].

For eccentric annulus, experiments showed that immobile mud starts by channeling of the displacing fluid on the wide side of the annulus whatever the flow regime is (laminar or turbulent). Under laminar conditions, increasing the density ratio and viscosity ratio or the flow rate reduces the mud channel width. In turbulent flow regimes, the mud channel may be destabilized if the contact time is long enough, but if no destabilization occurs the mud channel is larger than in the case of a laminar displacement. In turbulent displacements, it is more difficult to determine the conditions for an efficient displacement.

There are several limitations to the use of turbulence on the field. Often turbulent flows are impossible to reach because the critical pumping rate needed (which itself depends on the fluid rheology) exceeds the capabilities of field equipment. Another limitation comes from the formation that might not sustain the pressure gradient applied if it is too weak. Fractures or erosion of the formation take place. In practice, washers can be pumped in the turbulent regime, but cement slurries are often too viscous and pumping occurs mostly in the laminar regime.

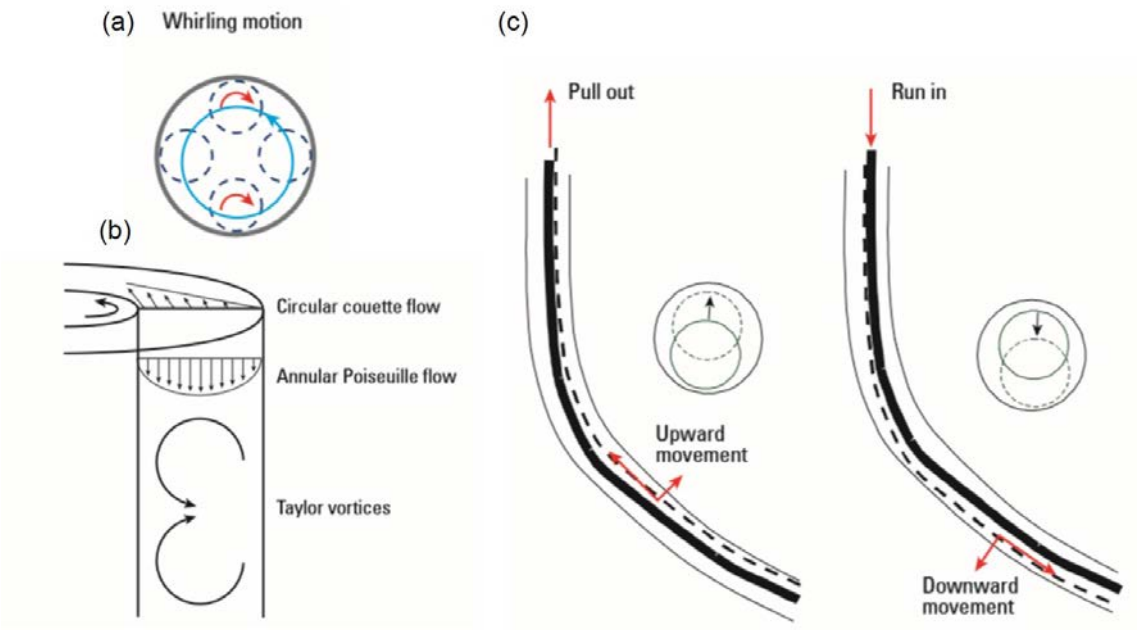

Figure 1.8 – Reproduction from [133]. (a) Whirling movement of the casing induced by its rotation at high speeds. (b) Taylor vortices in the annular gap created by the combination of axial and azimuthal flows during casing rotation. (c) Axial and lateral movements of the casing during reciprocation.

Casing movement and casing hardware

Casing hardware are objects placed in the well to help removing mudcakes and to get the best centralization possible for the casing. The main casing hardware are presented in 1.1.4. Here we focus on their functions during mud displacement and circulation and on the use of casing movement strategies.

The possibilities for casing movement are casing rotation and casing reciprocation. Figures 1.8 (a) shows that when the casing is rotated at high speeds, it can develop whirling motion in addition to rotation around its axis. The pipe rotation also induces Taylor vortices that increase the wall shear stress as sketched on figure 1.8 (b). Figure 1.8 (c) illustrates that during reciprocation the casing moves up and down but also laterally.

Since Taylor vortices increase the wall shear stress, it is a good track to try to exceed the mud yield stress and therefore enhance mud displacement or mud circulation. Mechanical abrasion of the filtercake or solid bed is achieved when casing hardware such as scratchers are used in addition to casing movement.

In eccentric annulus, casing movement and casing hardware improve mud removal on the narrow side of the annulus.

The drawbacks of casing reciprocation are pressure surge and a risk for the casing to be stuck.

1.1.6 Simulations: what is done nowadays in the oil industry?

Software tools were developed by oil field engineers to help design cementing jobs. The aim is to optimize the casing centralization (right choice and position of the casing hardware), to select the sequence of fluids, to determine volume and properties of each of the fluids, and to set the pumping rate.

Considering the dimension of the annular (very thin 2-3 cm and very long 1000-6000 m), the flow in the wellbore is approximated by neglecting the curvature of the annulus. Therefore the flow in the annular gap is equivalent to the flow between parallel plates. The model used is based on Bittleston *et al.* [15]. Under this approximation, expressions for the shear stress and velocity profiles can easily be derived. Because cement, mud and spacers are viscoplastic, in practice most of the displacements are performed in a laminar regime.

The effect of pipe eccentricity is well taken into account in laminar regime, but it is more difficult when the fluids have a yield stress. Also the models used for the rheological behaviour and density behaviour of cement pastes and mud needs to be improved (dependence in temperature and pressure, thixotropy).

The influence of casing movement is not fully captured and is the subject of academical research [26]. Modeling turbulent flow is still a challenge and the models do not consider gel mud and filtercakes.

The two-dimensional simulations allow to design fluid properties (density and rheology) in order to suppress viscous fingering instabilities that occur across the azimuthal direction. But, the phenomena and potential instabilities that may take place in the annular gap are not taken into account.

Summary of the qualitative recommendations

Mud removal is a complex problem for which experiments and numerical studies allowed to define some recommendations for the cementing operation which are summarized below:

- Change the drilling fluid properties before removing the drillpipe: lower gel strength, yield stress and plastic viscosity
- Get the best centralization possible for the casing placement in the wellbore
- Circulate the mud at the highest rate possible before circulation of the preflushes
- The casing should be equipped with scratchers, centralizers and various casing hardware and casing movement should take place
- If mud rheology can not be decreased sufficiently, it should be separated from the cement with compatibles preflushes
- The displacing and displaced fluid should be compatible
- Use chemical wash
- The density and rheology of the spacer should lie between that of mud and cement
- Use mechanical plugs to avoid mixing of fluids in the pipe
- Density or viscosity hierarchy of the fluids depends on the wellbore geometry.

If a cement job is of poor quality, there is some possible remedial cementing techniques, such as squeeze cementing that can, in some cases, repair the damages. Squeeze cementing operations consist in forcing cement in fissures or holes in the annular space. But it induces additional costs.

1.2 Conclusions

The fluids and the operating conditions used in the cementing process are chosen in function of the geometry, the fluid compatibility and the flow dynamics (for instance avoiding fingering). A number of engineering rules guiding the choice are well established to determine this choice.

However, today there is still a lack of information concerning the phenomena occurring at the gap scale (films, morphology of the interface,...) in the annular region where

cementing is achieved. A residual layer of mud may form and this film may induce leaks. This remark provides the motivation of the work undertaken in chapter 5.

Industrial context and conclusions

✧ **Well cementing process**
- A successful well cementing is the condition for a safe, productive and durable exploitation of an oil well.
- The main stages of an oil fabrication are: drilling, casing, cementing to achieve the desirable depth. The final steps are tubing and perforating.
- Different fluids circulate in the well: the drilling mud, washers, spacers and cement slurries.

✧ **Problems during well cementing**
- The cement slurries have to displace the drilling mud, and eventually washers or spacers. Gravitational and viscous instabilities may develop and lead to an incomplete displacement of the mud or of the washers and spacers.
- The geometry of the well such as eccentricity or mudcakes also lead to incomplete cementing displacements.

✧ **Current solutions and rules for cementing operations**
- Get the best centralization possible for the casing in the borehole.
- Use casing hardware and casing movements strategies to centralize the casing, to help displacing the mud and to avoid the formation of mudcakes.
- Use washers and spacers.
- Adjust the rheologies and densities of the fluids.
- The choices of the fluid rheologies, densities, the type and positions of the casing hardware are made with the help of simulation tools.

✧ **Conclusions**
- Annular gap phenomena remain to be investigated.

Chapter 2

Characterization of microgel suspensions

2.1 Microgel suspensions: a "soft glassy material"

Microgel suspensions belong to the class of soft glassy material [30]. We briefly define soft glassy materials before defining microgel suspensions.

2.1.1 Description of soft glassy materials

A glass is an amorphous solid, which means that its structure is not crystalline and that it exhibits a glass transition: by decreasing its temperature, a glass goes from a molten state to a solid and brittle state with an amorphous structure. Thus the glass is in a *metastable* state and its structure continues to evolve. This relaxation process called *aging* can go on for very long periods of time, that are not accessible experimentally. The reverse process of aging is called *rejuvenation*. It consists in erasing from the material the memory of the aging configuration. In glass, it is sufficient to increase again the temperature to melt it. Models have been developed to represent relaxation and aging phenomena in glassy systems [20, 125].

Sollich *et al.* suggested that many soft materials, such as foams, emulsions and pastes, share common properties with glassy materials: they are structurally disordered and can reach different metastable states upon flow cessation [170]. Therefore, soft material should be useful to study aging phenomena analogous to those found in glasses but at accessible experimental times. These materials are named *soft glassy materials*. This analogy between glassy systems and soft materials leads to new theoretical modelling in the dynamics of soft glassy systems [169, 72]. Still two main differences can be underlined between glassy systems and soft glassy materials:

— The mechanism that brings the material from metastability to rejuvenation of the sample: in glass, the temperature is decreased (to reach metastability) or increased (to rejuvenate the sample), while in soft glassy materials a large stress is applied (sample rejuvenation) or removed (metastability) [30]

— Thermal motion is not the dominant mechanism at play during relaxation. Larger energy barriers than thermal energy have to be crossed during relaxation. They are associated to rearrangements of the microstructure of the material: for example when a droplet or a bead moves its neighbours [170].

To understand some fundamental dynamics of these systems, such as aging, yield stress

or non linear rheology, there is a need for modeling these systems. The aim is to relate the macroscopic behaviour of the material to its microscopic structure and its objects properties. Different approaches used to represent these materials can be summarized as follows:

— Phenomenological approach: modify the constitutive equation with parameters, these models are generally easy to implement.
— Mesoscopic approach: coarse-grained approach of the medium based on the mechanisms happening at the microscale.
— Molecular dynamic simulations: model directly the particle-particle interactions to deduce bulk properties.

We give a brief overview of molecular simulations approaches. Then we describe succinctly the mesoscopic and phenomenological approaches. For more details about the theoretical framework of these methods we refer to the review of Mansard *et al.* [114] for the mesoscopic approach and to the review of Vlassopoulos *et al.* [184] for the microscopic approach.

Molecular simulations

The material is described at the particle level through particle-particle interactions. The simulations differ in the way these inter-particle interactions are modelled: Lennard Jones potential [49, 183], mode coupling theory [68], elastic repulsion combined to viscous dissipation [46, 115] or elastohydrodynamic interactions (EHD) [164].

Recently, the last two approaches have been successful in reproducing quantitative nonlinear properties of soft glassy materials in confined systems [115] and in several rheological experiments such as LAOS test [124] and aging process [123].

Mesoscopic and phenomenological approaches

In mesoscopic approaches, the medium is decomposed into elements containing several droplets (for emulsions) or beads (for microgel). There are analogies between the studies in what concerns the rearrangement mechanism: a particle under shear starts to deform elastically up to a yield point where the particles rearrange to new positions, they switch neighbours. This is called a *plastic event*.

These approaches have often influenced each other to obtain theoretical description of an important source of experiments performed on different kind of complex fluids (dense granular flows, microgel suspensions, concentrated emulsions, star polymers, micelles). They have evidenced several physical phenomena: transient and permanent shear-banding, yield stress, non-local rheology, influence of confinement, cooperative effects.

The models developed differ in the way they describe the rearrangements of the fluid particles and how they model the consequences of a rearrangement on the other fluid particles. For more details, we refer to a recent review on the subject [114].

The first contribution we wish to start with is the SGR (Soft Glassy Rheology) theory [170]. In this description, the particles are trapped in energy wells from which they have to escape to undergo a plastic event. The dynamic is set by an effective noise temperature x. The medium is characterized by a distribution of energy wells to mimic disorder.

In the mode-coupling theory [72], each element is associated to a given stress σ_i according to a stress distribution $P(\sigma, t)$ which also mimics the structural disorder of the

material. Under shear, the elements deform elastically up to a microscopic yield stress σ_y where the plastic rearrangement occurs. A plastic event induces a stress relaxation in the medium, so that the stress of each element evolves accordingly [149, 151].

A different approach is the STZ theory (Shear Transformation Zone) [49] in which plastic events occur only at given location, i.e. in the STZ. This theory was inspired by numerical results: they observed that irreversible deformation occur in the material in localized region and along preferential orientations.

Pouliquen and Forterre expressed the idea of nonlocality to spatially correlate the plastic events [152]: a shear induced somewhere in the material induces stress fluctuations, which themselves can induce a shear somewhere else.

The same idea was implemented in the SGR model by writing a diffusive equation for the effective noise temperature [51]. In the kinetic elastoplastic model (KEP) [16], which follows the mode-coupling theory, the stress relaxation diffuses in the medium. The diffusion coefficient D is related to the rate of plastic events Γ through a nonlocal relation [150], indeed D depends both on Γ and on the variations of Γ. Therefore, the models account for spatial cooperativity in the medium.

The KEP model [16] can be simplified to a phenomenological expression [65] where two relevant quantities appear: the fluidity [42], representing the rate of plastic events in the system, and a cooperative length [150] over which the nonlocal elastic relaxation occurs in the system. The fluidity has been shown to be linked to the local velocity fluctuations [84].

Further developments of the KEP model account for attractive interactions between the particles [116]: the number of physical links between the particles N, is introduced in the KEP model.

Many of these approaches could be validated by experimental results. In particular, the KEP model has recently proven to remarkably reproduce different experimental results (dense granular media [74], concentrated emulsions [65]) and simulations. Its popularity is also due to the fact that it can be simplified to a phenomenological rheological law, so that comparison with different kind of experiments is fast.

2.1.2 Description of the microgel suspensions

The microgel suspensions are colloidal particles made of a polymer network swollen by a solvent as sketched on figure 2.1 (b).

The suspensions used in this study are prepared from polyelectrolyte microgels in water. The microgels are synthesized by standard emulsion polymerization at low pH (≈ 2) from ethyl acrylate (64 wt.%), methacrylic acid (35 wt.%), and a bifunctional monomer as a crosslinker [31]. The polymer latexes obtained at the end of the synthesis are cleaned by ultrafiltration. The solid content of the stock suspension is determined by thermogravimetry. Stock suspensions at solid content of 27.2 wt.% and 24.5 wt.% were used.

Samples are prepared by dilution of the stock solution with ultrapure water (see annexe A). At low pH, the microgels are insoluble in water, and behave as hard particles. The addition of sodium hydroxide (1M) causes the ionisation of the methacrylic acid units. The osmotic pressure of the counterions then provokes the swelling of the microgels as sketched on figure 2.1 (b). In all the experiments reported in this study, the molar ratio of the added base to the available acid groups is around 1, so that the totality of the carboxylic functions are neutralized. The particles have a hydrodynamic radius of 220 nm, with a

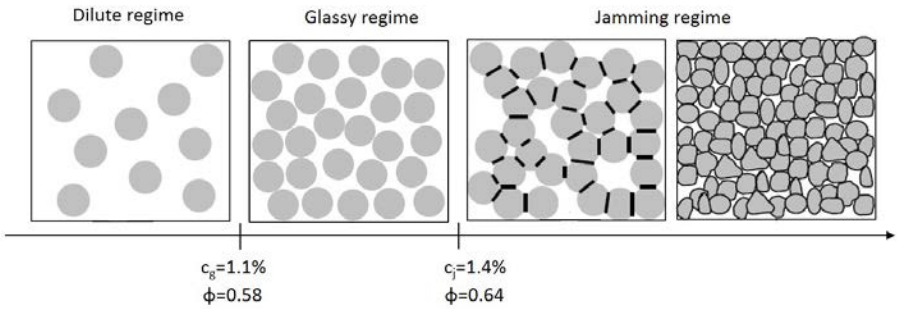

(a) Microgel regimes as a function of polymer concentration

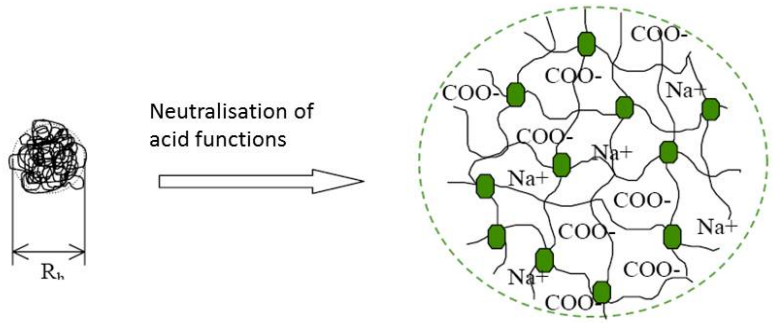

(b) Microgel swelling

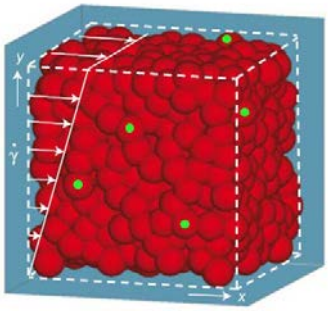

(c) Microgel suspension in the jamming state

Figure 2.1 – Microgel description. (a) As the concentration c of the microgel increases, the suspension exhibits 3 regimes: a dilute regime, a glassy regime and a jamming regime. Reproduction from [126]. (b) The microgel is insoluble in water and behaves as hard particles at low pH. The addition of sodium hydroxide causes the microgel to swell. Reproduction from [126]. (c) The microgel suspension in the jamming regime with fluorescent dye embedded in the microgel structure. Reproduction from [164].

polydispersity of 10%.

Figure 2.1 (a) illustrates the different concentration regimes of the microgel suspensions. In the dilute regime, the colloids are submitted to Brownian motion. The critical concentration c_g sets the transition to the glassy regime. In the glassy regime, the particles are trapped in a cage and the suspension has an amorphous structure. At the jamming concentration c_j, we are at the close packing volume fraction for hard spheres. In our case, since the particles are deformable, it is possible to exceed this concentration. As in the glassy regime, the cage structure is present but the particles are in closer contact with each other and the surface between two particles is a facet as shown on figure 2.1 (a).

Some of the suspensions are seeded at low concentrations with 500 nm in diameter fluorescent sulfonate-functionalized polystyrene tracers from Duke Scientific. The tracers have been chosen to have a size comparable to that of the swollen microgels. They are added before swelling to ensure that they are uniformly dispersed in the suspension as represented on figure 2.1 (c). Each tracer is in contact with many surrounding microgels so that it experiences the same sequence of dynamical events and moves at the same velocity as its neighbours [164]. After preparation the microgels are kept at rest for at least 24 hours. Experiments are performed at high volume fractions above jamming (above $C = 0.016$ $\mathrm{g \cdot g^{-1}}$ corresponding to $\phi = 0.72$) where the suspensions exhibit yielding properties. C

corresponds to the mass concentration of the polymer in the final solution. Increasing C leads to higher volume fraction of microgel beads and it modifies the rheological properties of the solution.

2.2 Microgel suspensions: a non-Newtonian fluid

The response of a Newtonian fluid to a deformation is always linear, whatever the deformation amplitude or frequency are. To characterize Newtonian fluids, it is sufficient to measure the viscosity η of the fluid since the stress applied σ to the element of fluid is proportional to its deformation rate $\dot{\gamma}$: $\sigma = \eta\dot{\gamma}$.

Non-Newtonian fluids belong to another class of fluids for which the above relation is not anymore proportional and most commonly the viscosity may depend on shear rate or shear rate history. These non-linear properties come from the presence of objects in the fluid that are larger than the atomic scale but stay smaller than the characteristic dimension of the flow. These objects rearrange themselves under deformation and give non-Newtonian properties to the fluid.

For all fluids, the speed of variation of the stress is as important as its amplitude to determine its behaviour [69]. To rationalize this idea, Markus Reiner introduced the Deborah number De, which represents the ratio of the relaxation time of the fluid structure to the characteristic time of the solicitation (The number is named after the prophet Deborah who said: "Even the mountains flowed before the Lord"). Non-Newtonian fluid behaviours are related to how the objects in the fluid interact and what rearrangements inside the fluid structure are observable at the time scale of the experiment.

Some examples of non-Newtonian fluids are found in nature (blood) or in everyday products (cosmetics, food products) [69]. As they are encountered in many industrial processes, they attract a lot of interest from the scientific community: emulsions in the cosmetic domain, polymers in extrusion processes, or cement pastes in oil and gas industry.

In the following we briefly describe the main non-Newtonian fluids properties (thixotropy, viscoelasticity,...). There is no real consensus on the way to classify non-Newtonian behaviours. We give some definition according to our comprehension of the phenomena and in the spirit of the recent review of Larson [96]. This will be useful to be precise about the description of the properties of the fluids we are using.

2.2.1 Thixotropy/rheopexy

Under a constant stress the viscosity of a thixotropic and rheopectic fluid will respectively decrease and increase with time. This is due to an evolution of the structure of the fluid and to rearrangements between the microstructures. We propose two main categories of fluids to define when thixotropic or rheopectic effects might occur:

— the objects within the fluid have attractive interactions, which will result in thixotropic or rheopectic effects.

— the objects within the fluid have repulsive interactions, neither thixotropic nor rheopectic effects are observed.

For example, in cement paste, the thixotropic properties are due to the flocculation and deflocculation of the cement particles suspended in the paste. A schematic example is shown in figure 2.2 for a cement paste without additives: the increase of the shear rate breaks the flocculated particles, a further increase of the shear rate can lead to reflocculation of the individual cement particles. The construction/deconstruction of these macrostructures depends on the shear rate history.

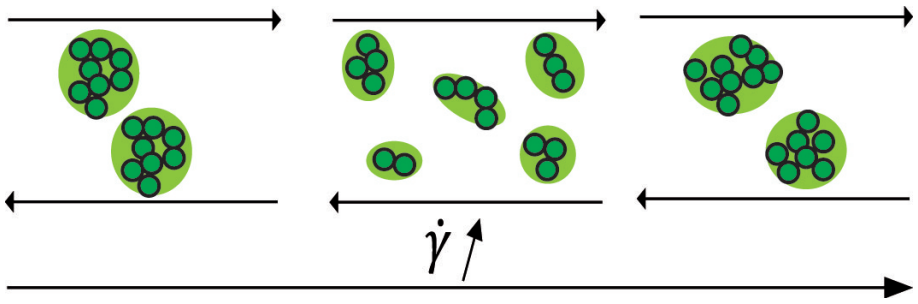

Figure 2.2 – Evolution of the structure of a cement paste without additives under various shear rates.

In practice it means that the viscosity obtained from rheological measurements depends on the duration of the experiment and on previous solicitations applied to the material. The material response shows hysteresis behaviour to measurement cycles. The hysteresis behaviour of the material depends on De. At sufficiently low speed solicitation, when the material has enough time to rearrange its internal structure, no hysteresis effect is observed.

Figure 2.2 shows that the structures inside the fluid evolve as time goes on. This evolution is due to interparticle interactions. So, in thixotropic/rheopectic fluids, the times which set the transitions between the different states of the material are related to the time of interparticle interactions.

2.2.2 Non thixotropic/rheopectic fluids

As said above, non thixotropic/rheopectic fluids are the fluids in which the objects have repulsive interactions. But in addition to repulsive interactions, the objects in the fluid may be submitted to topological constraints when the objects are in contact with each other. In this case, the objects are not entropic anymore. Indeed, elastic forces will become much more important than thermal energy. This will lead to different relaxation mechanisms and to different relaxation times.

For example, a dilute polymer solution is made of objects with repulsive interactions and no topological constraint. The relaxation time of such a material is of the order of the relaxation time of the polymer chains, which is an intrinsic time of the material. If the polymer concentration is increased up to the overlapping concentration, the polymer is submitted to topological constraints due to overlapping of the chains. Relaxation times will be longer because they will also depend on the interactions between the chains.

For microgel suspensions in the dilute regime, the beads are only submitted to Brownian motion. In the jamming regime, the particles are highly concentrated, a particle is in a cage surrounded by neighbouring particles in contact through flat facets. Thermal motion is negligible in this situation and what matters is the elasticity of the cage. The relaxation time does not depend on the beads but rather on the contacts between them. Microgel suspensions in the jamming regime do not have intrinsic relaxation times anymore. Instead, their relaxation times are extremely long and they often can not be reached at experimental time scales.

2.2.3 Visco-elasticity

An elastic solid and a pure viscous fluid represent two extreme types of material. For an elastic solid submitted to a low deformation γ, the stress response σ is proportional

to the deformation: $\sigma = G\,\gamma$ where G is the elastic modulus of the material. When the stress in unloaded, the material recovers its original configuration. For a pure viscous fluid, the stress σ is proportional to its rate of deformation $\dot{\gamma}$: $\sigma = \eta\,\dot{\gamma}$ where η is the viscosity of the fluid. Viscous materials undergo irreversible deformation. A visco-elastic material has an intermediate behaviour between a pure elastic solid and a pure viscous fluid when submitted to a deformation. The transition from elastic response to viscous response is observable over time. A famous example of visco-elastic material is the silly putty paste [117]: a silly putty bullet bounces when thrown on the floor, before forming a puddle after a few days. This time dependent behaviour shows that the microscopic structure of the material is rearranging over time. A relaxation time can be defined as:

$$\tau \approx \eta/G \tag{2.1}$$

which sets the transition between elastic and viscous behaviour of the material. The deformation rate $\dot{\gamma}$, which is a characteristic time of the flow is compared the relaxation time of the material. We find again here the Deborah number defined earlier $De = \dot{\gamma}\,\tau$. In terms of frequency, a visco-elastic material exhibits elastic properties at high frequencies and viscous properties at low frequencies.

2.2.4 Summary of non-Newtonian behaviours

The importance of the Deborah number defined earlier is confirmed by the above definition of visco-elasticity. Indeed, it is clear that the important parameters to take into account in order to "classify" a material are:

1. The time scale of the experiment
2. The time scale in the material

Depending on which time scales (elastic times, viscous times and/or thixoptropic/rheopectic times) the experiment time crosses, the material will exhibit various properties as sketched on figure 2.3. For example, a fluid can be both thixotropic/rheopectic and visco-elastic. The silly putty paste goes from a brittle state to bouncing and finally flows as a viscous liquid depending on the time or frequency of the solicitation as seen on figure 2.3 (middle and bottom line from left to right).

2.2.5 Conclusions on the non-Newtonian behaviour of microgel suspensions

In this work, we use microgel suspensions in the jamming regime. At the time scales of the experiments, the microgel suspensions properties can be summarized as follows:

1. The microgel is neither thixotropic nor rheopectic (because of the repulsive interactions between the beads)
2. The microgel is a visco-elastic-plastic fluid
   — at low deformation: elastic response of the material.
   — at high deformation: the fluid flows. In our case, the microgel suspensions flow above a yield stress. The topological constraints imposed by the cage structure imply that under a non-zero stress the bead does not manage to move its neighbours.

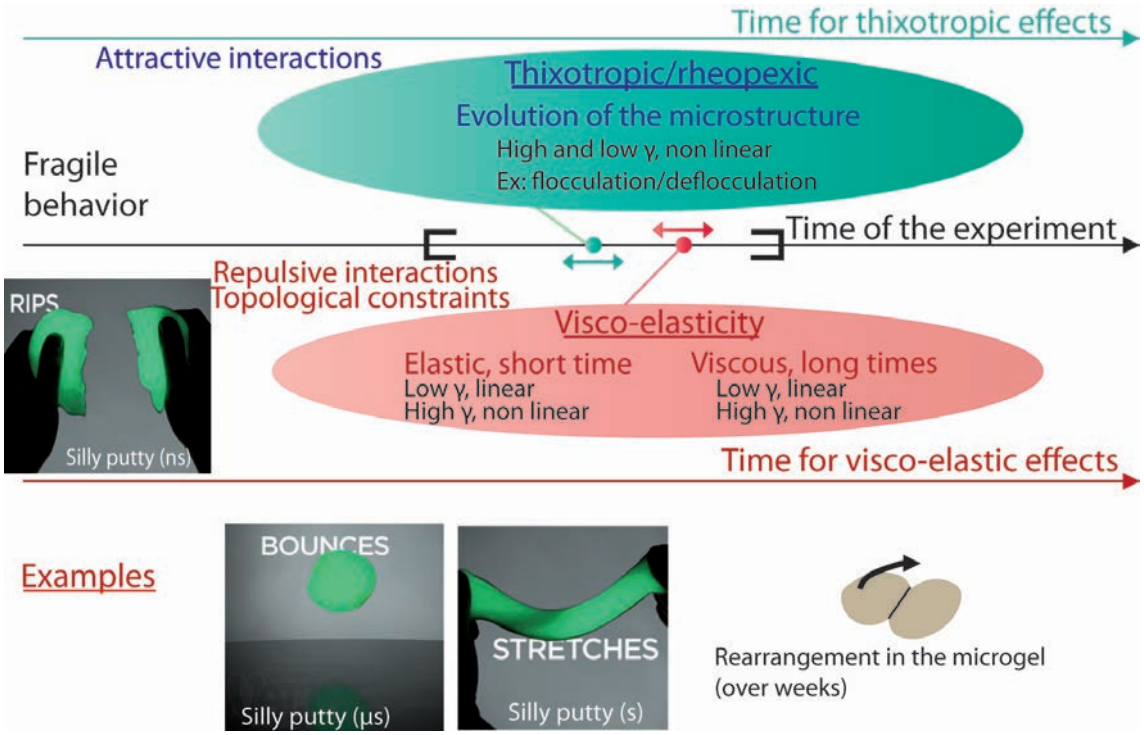

Figure 2.3 – Non-Newtonian fluid behaviours. Thixotropic fluids often show hysteresis effect during rheological measurements because the elementary structures in the fluid are constantly evolving as shown in figure 2.2.

2.3 Rheological measurements of microgel suspensions

2.3.1 Constitutive law and fluid movement

The constitutive law of a material (solid or liquid) is a mathematical relationship linking the stress applied on the material to its deformation.

Stress in a fluid

The stress tensor gathers surface forces that act on a fluid element. Its general form is:

$$\boldsymbol{T} = -p\boldsymbol{I} + \boldsymbol{\sigma} \tag{2.2}$$

where $\boldsymbol{T}$, the *total stress tensor* is decomposed as the sum of a term containing the normal stress for a fluid at rest ($\mathbf{I}$ is the identity tensor and p the hydrostatic pressure) and the *deviatoric stress tensor* $\boldsymbol{\sigma}$ containing the terms contributing to deformation. The components of the deviatoric stress tensor on a fluid element are sketched on figure 2.4 (a).

Deformation in a fluid

The study of deformation consists in looking at how two points in a material separate under stress: this depends on the current and past state of deformation of the material. In a solid, the new position of a point depends on its past position and on time. In a fluid, one has to consider the change of velocity with the position in the material. In fact, Newton wrote the first constitutive law relating the "resistance" of the fluid to the "velocity by which the parts of the fluid are being separated": $\sigma_{xy} = \eta \frac{\mathrm{d}v_x}{\mathrm{d}y}$. Therefore, the notion of

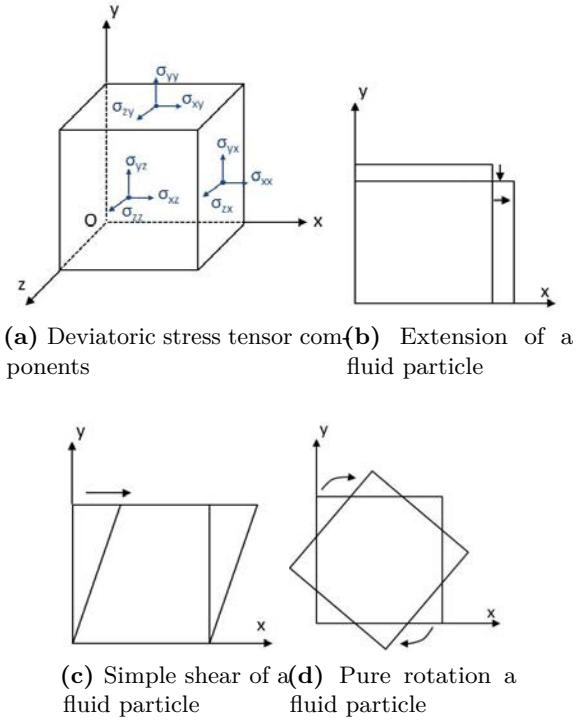

(a) Deviatoric stress tensor components

(b) Extension of a fluid particle

(c) Simple shear of a fluid particle

(d) Pure rotation a fluid particle

Figure 2.4 – Stress and deformation on a fluid particle. (a) Representation of the deviatoric stress tensor components on a fluid particle (b) Extension deformation is represented by the diagonal components of the tensor e_{ij}. (c) Shear deformation is represented by the non-diagonal components of the tensor e_{ij}. (d) A pure rotation does not deform the fluid particle, it is represented by the w_{ij} components of the tensor.

deformation in a solid is replaced by the rate of deformation in a fluid [107]: the quantities to consider are $G_{ij} = (\partial v_i/\partial x_j)$, elements of G the *tensor of rate of deformation*. It can be decomposed in a symmetric part e_{ij} and an anti-symmetric part w_{ij} by writing:

$$e_{ij} = \frac{1}{2}\left(\frac{\partial v_i}{\partial x_j} + \frac{\partial v_j}{\partial x_i}\right) \tag{2.3}$$

and

$$w_{ij} = \frac{1}{2}\left(\frac{\partial v_i}{\partial x_j} - \frac{\partial v_j}{\partial x_i}\right) \tag{2.4}$$

The e_{ij} part is associated to the fluid element deformation such as extension deformation (figure 2.4 (b) and shear deformation (figure 2.4 (c)). w_{ij} is associated to a pure rotation of the fluid element without deformation as sketched in figure 2.4 (d). For an incompressible fluid, $tr\,(e_{ij}) = 0$ and e_{ij} is often noted d_{ij} in the literature. d_{ij} are the elements of $\boldsymbol{D}$ is the *rate of deformation tensor*.

Constitutive law and fluid motion

The constitutive law is the function relating the deviatoric stress tensor $\boldsymbol{\sigma}$ to the rate of deformation tensor $\boldsymbol{D}$, both described in the previous paragraphs. A flow induces important deformations in the fluid. At a length scale sufficiently larger than a fluid particle and smaller than the characteristic length of the flow, the momentum equation describes the

Table 2.1 – Relation between the parameters of the rheometer and the physical quantities of the sample.

Rheometer parameters	Sample physical quantities
Rotational speed ω	Shear rate $\dot{\gamma}$
Deflection angle α	Deformationγ
Torque F_T	Shear stress σ
Normal force F_N	First normal stress difference N_1

movement of the fluid:

$$\rho\frac{\partial\vec{u}}{\partial t} + \rho(\vec{u}.\vec{\nabla})\vec{u} = \rho\vec{g} - \vec{\nabla}p + \vec{\nabla}.\boldsymbol{\sigma} \tag{2.5}$$

ρ is the fluid density, $\vec{u}$ the velocity vector, p the pressure, and $\boldsymbol{\sigma}$ the deviatoric stress tensor.

The constitutive law combined to the equation of the fluid motion leads to the full determination of the flow.

2.3.2 Principles of rheological measurements

Relation between rheological measurements and the constitutive law

The objective of rheological measurements is to determine how a material deforms under stress and to find its constitutive law. In our experiments, we use a rotational rheometer Anton Paar MCR 501, which can apply a simple shear to a sample. The main principles of operating the rheometer are:

— The sample is loaded between the upper and the bottom part
— The bottom part stays still and the upper part rotates
— The rheometer is able to measure/impose: the rotational speed ω, the rotational displacement α, the torque on the rotational part F_T, the normal force exerted by the sample on the upper geometry F_N.
— The rheometer's control parameters are related to the physical quantities of the sample: the stress σ, the deformation γ, the deformation rate $\dot{\gamma}$, the first normal stress difference N_1 (see table 2.1).

The device parameters allow to apply two kinds of solicitation to the material, either a continuous or an oscillatory deformation. Different geometries such as Couette, cone and plate and plate and plate are available for the measurements (figure 2.5). The functions relating the parameters of the rheometer to the physical quantities of the sample are geometry dependent.

The choice of the geometry depends mostly on the sample consistency. Couette geometry is preferred for liquid-like materials whereas plate and plate or cone and plate geometries are more suitable for pastes. Cone and plate configurations are more precise than plate and plate as the sample is sheared more homogeneously.

Linear and non-linear regimes

A Newtonian fluid always responds linearly to a deformation regardless of its deformation amplitude or frequency. With non-Newtonian fluids, the response to deformation does not stay linear. This effect is due to rearrangements and deformations of its own microstructure (soft beads, polymer chains...). But even with non-Newtonian fluid, it is possible to obtain

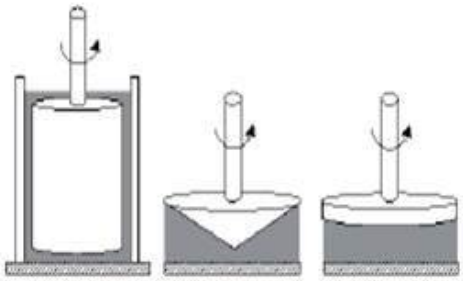

Figure 2.5 – Different geometries available for the rotational rheometer: Couette, cone and plate, plate and plate.

a linear response to deformations if the deformation applied is sufficiently small. The distinction between linear and non linear regimes can be summarized as follows:

Linear rheology is the domain in which deformation applied to a material is sufficiently small to get a linear response. The internal structure of the fluid is not disrupted.

Non linear rheology is the domain in which deformation applied to a material is important so its internal structure is disrupted and it leads to macroscopic flow. The material's response is non-linear.

There is no general way to determine the transition between the linear and non-linear regimes. But models have been developed to describe the fluids in either of these two regimes. A rheological measurement allows to determine the parameters of these models: deformation amplitude, frequency and rate can be controlled to get the full picture of a material. In a flow situation where deformations are important and continuous, we are in the domain of non-linear rheology.

The bulk flow properties of the microgel suspensions are measured using the cone and plate geometry. The shearing surfaces are sandblasted (surface roughness ≈2-4 µm) to suppress slip. We measure the rheological properties of the microgel in the linear and non-linear regime.

2.3.3 Linear rheology

In the linear regime, the sample is submitted to small deformation. Its response to deformation changes from an elasto-plastic response to a viscous response as time goes on and always stays proportional to the deformation. The stress response of the fluid over time can be written as:

$$\sigma\ (t) = \int_{-\infty}^{t} G\left(t - t'\right) \dot{\gamma}\left(t'\right) dt' \tag{2.6}$$

G is the relaxation modulus. Maxwell wrote the simplest model of a relaxation function with one relaxation time τ [117].

$$G\left(t\right) = G_0 exp^{-t/\tau} \tag{2.7}$$

The relaxation modulus for a Newtonian viscous fluid, a Hookean solid elastic and a viscoelastic fluid with one relaxation time is sketched on figure 2.6 (a). Maxwell's model represents a spring of elasticity G_0 in series with a viscous damper of viscosity η as drawn on figure 2.6 (b). It is possible to generalize Maxwell's model to get a description of more complex fluids that have many relaxation times.

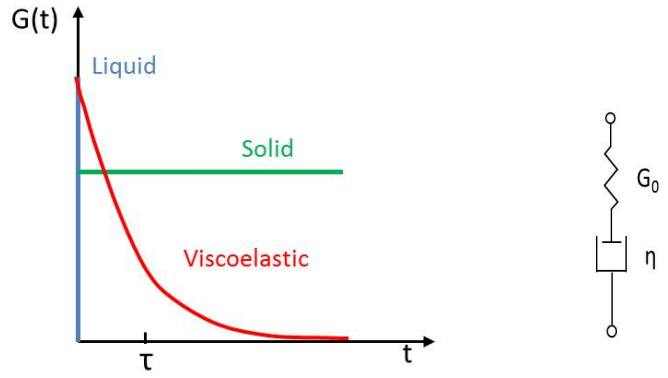

(a) Relaxation modulus for different type of fluids

(b) Mechanical model of Maxwell

Figure 2.6 – Linear viscoelasticity. (a) Relaxation modulus of a Newtonian viscous fluid (blue), a Hookean elastic solid (green) and a viscoelastic fluid (red). Reproduction from [44]. (b) A spring (elastic modulus G_0) in series with a viscous damper (viscosity η) forms Maxwell's model of a viscoelastic fluid with a single relaxation time $\tau = \eta/G_0$.

The transition between the elastic regime and the viscous regime sets the relaxation time τ of the material. To measure the function $G(t)$, sinusoidal deformations of the form $\dot{\gamma} = \dot{\gamma_0} \cos(\omega t)$ can be applied to test the material response at different frequencies ω. The stress response over time is:

$$\sigma(t) = \dot{\gamma_0} \left(G'(\omega) \sin(\omega t) + G''(\omega) \cos(\omega t) \right) \tag{2.8}$$

Where G' the *elastic modulus* is in phase with the strain amplitude and G'' the *loss modulus* is in phase with shear rate. At low frequency, G'' dominates as the material behaves as a viscous liquid. At high frequency, G' dominates and the material behaves as an elastic solid. The relaxation time is located at the cross-over between the curves of G' and G'' as a function of ω.

2.3.4 Non-linear rheology

Above a critical deformation, the structure of the fluid undergoes macroscopic rearrangements and the material flows. Non-Newtonian fluid response becomes non-linear. An important diversity of fluid responses exists and three main effects differentiate them from Newtonian fluids:

— the viscosity variation with the shear rate, determined in pure shear flow situation
— the presence of normal forces, also determined in shear flow situation
— extensional viscosity.

Non-linear viscosity, the flow curve

In a flow situation the fluid elements are sheared. The *flow curve* relates the stress response σ of the material to an applied constant rate of deformation $\dot{\gamma}$. In this situation, the stress of non-Newtonian fluids can vary with the rate of deformation. Typical rheological behaviours are plotted on figure 2.7 (a):

— Newtonian: the stress varies linearly with the rate of deformation, the viscosity is constant (blue).

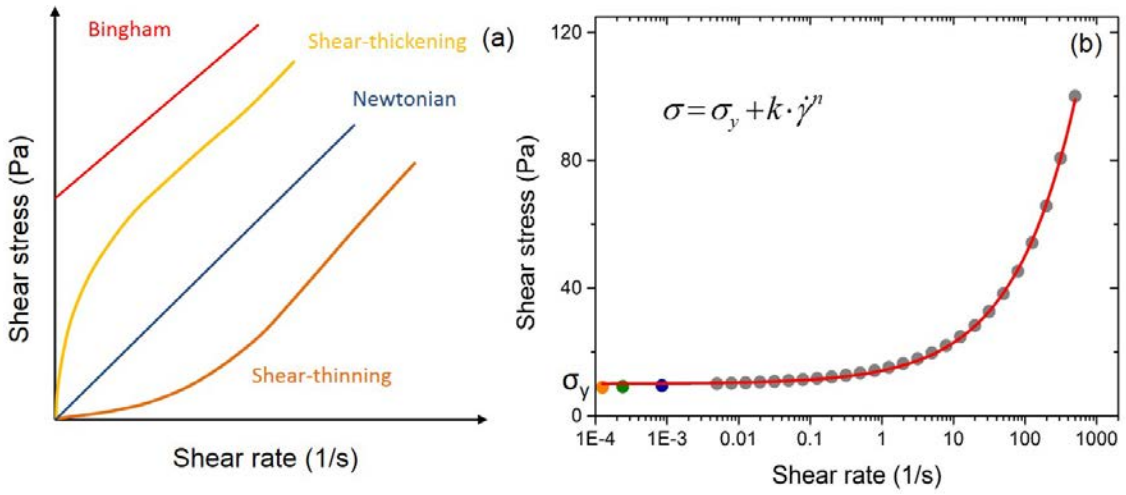

Figure 2.7 – Flow curves for non-Newtonian fluids. (a) The yield stress can be combined with the three other constitutive laws. For example, a Bingham fluid combines a yield stress and a Newtonian behaviour once the yield stress is exceeded. (b) The microgel suspensions have a yield stress above jamming (volume fraction $\phi > 0.64$) and are shear-thinning. This non-Newtonian behaviour is well characterized by the Herschel-Bulkley law, represented here for a microgel suspension with $\phi = 0.7$.

— Shear-thinning or shear-thickening: the viscosity decreases respectively increases with the rate of deformation (orange and yellow).
— The presence of a yield stress: under a minimal stress, the material does not flow. Then the material can have a constant, shear-thinning or shear-thickening behaviour (red).

We mentioned earlier the existence of thixotropic/rheopectic materials: these fluids will present hysteresis if one repeats the measurement of the flow curve. Several models have been written to describe the different fluid behaviours: power law (shear-thinning or shear-thickening), Bingham (yield stress fluid and constant viscosity above the yield stress) models are some of them.

The microgel is subjected to a yield stress, shear-thinning and is a non-thixotropic fluid. Its stress versus shear rate curve is well described by the Herschel-Bulkley (HB) law $\sigma = \sigma_y + k^n$ where σ_y is the yield stress, k the consistency parameter and n the flow index (see figure 2.7 (b)).

Normal stresses

In a pure shear flow, the structures inside a non-Newtonian fluid can sometimes oppose a restoring force to the shear they are submitted to. The objects in the fluid are deformed because of the shear and try to come back to their initial shape. Polymer solutions often exhibit normal forces (figure 2.8 a)). This force is quantified with the diagonal components of the stress tensor through the normal stress differences N_1 and N_2:

$$N_1 = \sigma_{xx} - \sigma_{yy} \tag{2.9}$$

$$N_2 = \sigma_{yy} - \sigma_{zz} \tag{2.10}$$

Some rheometers are equipped with a pressure sensor and are able to measure the normal force required to keep the top part of the rheometer at a constant distance from the bottom part. These stresses are equal to zero for a Newtonian fluid and can be very

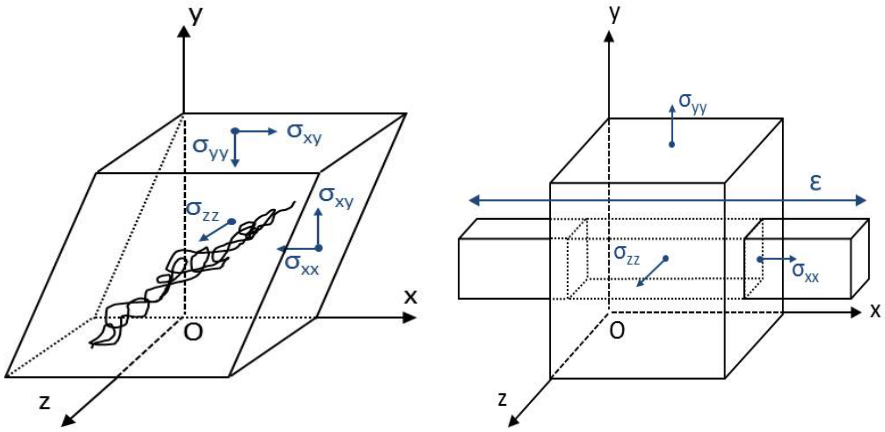

(a) Fluid element under shear

(b) Fluid element in a pure elongational flow

Figure 2.8 – Deformation in non-Newtonian fluids. (a) Viscosity and normal forces are determined in pure shear flow situation. Polymer particles often elongate under shear and exhibit normal forces when they try to recover their original ball shape. (b)Extensional viscosity is determined in extensional flows: the material is elongated along the x axis, by volume conservation it shrinks along the axis y and z the same way.

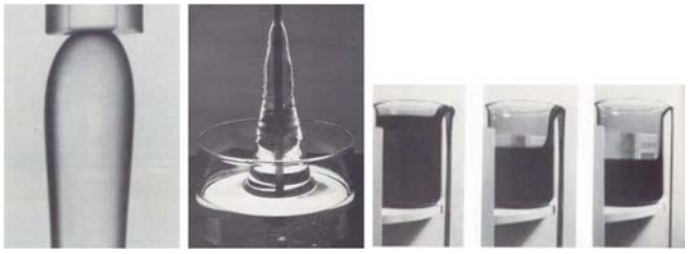

Figure 2.9 – The Weissenberg effect in different experiments from left to right: expansion of the flow at the outlet of a tube, climbing up on a spinning rod and the viscoelastic self-siphoning effect.

high for a non-Newtonian fluid. These forces were discovered by Weissenberg in 1947, they are responsible for impressive flow perturbations (see figure 2.9).

Extensional viscosity

In a pure extensional flow, the fluid particles are stretched without being rotated or sheared, therefore the stress tensor and the rate of deformation tensor are diagonals. In figure 2.8 (b), a fluid element is subjected to an elongation of amplitude ϵ along axis x with a constant elongation rate $\dot{\epsilon}$. By conservation of volume, the fluid element is contracted by $1/\sqrt{\epsilon}$ in y and z directions. By symmetry, $\sigma_{yy} = \sigma_{zz}$, so that the elongational deformation can be characterized by only one normal stress difference: $\sigma_T = \sigma_{xx} - \sigma_{zz}$. As in Newton's law, it is possible to define an elongational viscosity that relates the elongational rate of deformation $\dot{\epsilon}$ to the elongational stress σ_T:

$$\eta_e = \frac{\sigma_T}{\dot{\epsilon}} \tag{2.11}$$

The Trouton's ratio is the ratio of elongational viscosity to shear viscosity. In the case of Newtonian fluids, Trouton's ratio is equal to 3, but in the case of non-Newtonian fluids in

the non-linear regime, this ratio can be much more important and a specific constitutive equation is needed. It is difficult to measure the elongational properties of a fluid because elongation is often combined to shear. The main approaches to try to measure extensional viscosities are to either generate an elongational flow near a stagnation point or to force the liquid through an abrupt or a hyperbolic constriction which generates a flow at high Trouton's ratio. In the first case, elongation of the fluid induces some modifications of the optical properties of the fluid which can be measured by birefringence. In the second case, the pressure loss induced by the sudden geometry change is measured at a constant flow rate. But one has to separate the contribution of shear and elongation to be able to deduce an elongational viscosity. The results of these experiments are still difficult to interpret since, in practice, flows are neither steady nor spatially uniform [148]. Measurements depend on time and on the deformation history of the material. Both kinds of geometries have been implemented in microfluidic devices with promising results concerning low viscosity elastic fluids [59]. They are important for a lot of polymer solutions, or solution that are made of anisotropic objects such as rod-like suspension.

2.3.5 Aging and rejuvenation

Aging is observed in pasty systems. When they are left at rest, they continue to evolve but slower: during aging we can observe the shear stress decreasing with time. It is possible to erase the relaxation of the memory of the system by applying a large stress causing the flow of the system. A main difference between thixotropic and non-thixotropic systems is:

— for non-thixotropic fluid: assuming the stress applied for rejuvenation is large enough so that a stationary flow establishes, the relaxation of the material during aging and the mechanical properties of an aged system only depends on the waiting time after the flow is put at rest. It does not depend on the duration of rejuvenation.

— for thixotropic systems: during rejuvenation, the structure of the sample is modified, so the relaxation of the material during aging and its mechanical properties will be a function of not only the waiting time but also on the deformation amplitude, deformation rate, and rejuvenation duration.

In our case, the mechanical properties of the system evolve during aging but, for example G' and G'' values only depend on the aging time t_w of the system [30].
Since aging can modify the properties of the fluid, we tested the ability of the microgel suspensions to be rejuvenated. Figure 2.10 shows step shear rate experiments performed on a microgel suspension at 3%: the microgel is left at rest during 600 s and then the flow is started at various shear rates (from $0.001\,\mathrm{s}^{-1}$ to $100\,\mathrm{s}^{-1}$). We measure the shear stress as a function of time: the aim is to see how long does the microgel need to reach a stationary flow.

In figure 2.10, we see that for all the shear rates applied, the flow of the microgel 3% becomes stationary upon a minimal deformation around $\gamma = 0.2\%$. The measurement was also performed for a microgel 1.6% and we found that the flow is stationary for $\gamma = 0.1\%$.

These experiments allow us to verify (see later paragraphs 3.2.1 and 3.3) that the flow in our microfluidic channels is stationary.

2.3.6 Yield stress

Yield stress definition

Yield stress means that the material starts to flow above a certain stress. This definition does not presume the flow mechanism: it can be an actual flow or even a rupture. In

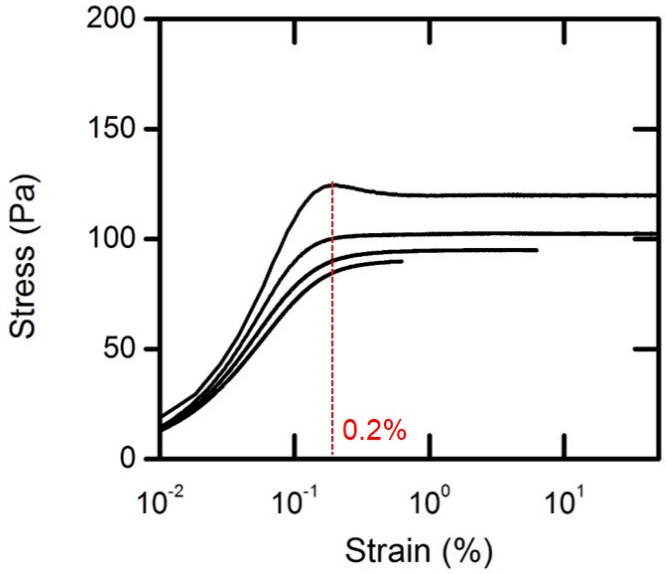

Figure 2.10 – Step shear rate experiments on a microgel suspension at 3% after the same aging duration (600 s). The shear rate imposed is (from top to bottom): $1\,s^{-1}$, $0.1\,s^{-1}$, $0.01\,s^{-1}$ and $0.001\,s^{-1}$. The sample is rejuvenated once a critical deformation is applied: 0.2% in this case.

jammed microgel suspensions, the particles are in contact through flat facets with each other. Under a stress, the particles deform and if the stress applied is sufficient particles change neighbours. Other kind of yield stress are found: in cement paste, yield stress is due to gelation of the paste, for solid material the yield point is when creep occurs.

Measurement of the yield stress

Figure 2.11 (a) represents the flow curve of a microgel suspension at 1.6%. The yield stress σ_y can be read directly from the flow curve: at low shear rate, the flow curve extrapolation crosses the stress axis at a non-zero value.

Creep experiments complete a flow curve measurement. After rejuvenation of the sample a constant stress is applied and the evolution of the shear rate over time is measured. The sample relaxes to reach a stationary state if the stress applied is above the yield stress. An example is shown on figure 2.11 (b) for the case of $\sigma = 9.5$ Pa (blue curve). As the stress applied gets closer to the yield stress, the fluctuations of the shear rate increase because the material is in an out of equilibrium state. An example is shown on figure 2.11 (b) for the case of $\sigma = 9$ Pa (orange curve). Once these regimes are reached, a mean shear rate value can be extracted from the end part of the creep measurements curves. The points extracted from the creep measurements curves (stress applied - mean shear rate value) can be added to the flow curve (the creep measurements of figure 2.11 (b) are added to the flow curve on figure 2.11 (a)). It allows to get a better determination of the yield stress while fitting the curve with a phenomenological model such as the Herschel-Bulkley model (figure 2.11 (a)).

A quick way to obtain a yield stress value is to perform oscillatory measurements such as *strain sweep* measurements. It allows to find the critical deformation above which the material viscous behaviour dominates its elastic behaviour, i.e. above which the material starts to flow. In the elastic domain, the shear stress σ varies linearly with the strain γ. In

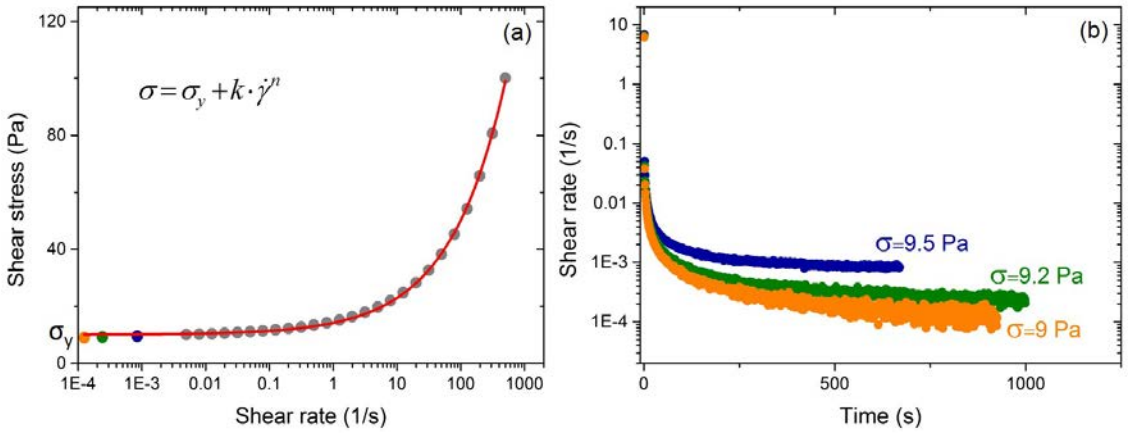

Figure 2.11 – (a) Flow curve of a microgel suspensions at 1.6% (grey dots) with points extracted from creep experiments performed at imposed shear stress of 9.5 Pa (blue), 9.2 Pa (green), 9 Pa (orange). (b) Creep experiments at various imposed shear stress: 9.5 Pa (blue), 9.2 Pa (green), 9 Pa (orange).

the viscous regime, the shear stress varies as a power law with the strain. Each regime is represented on the curve σ as a function of the strain by two straight lines of different slopes. The intersection between the linear asymptotes of each part of the curve gives the yield stress value as shown on figure 2.12 (a). But with this method, the frequency at which the sample is sheared is fixed. So these measurements have to be compared to frequency sweep measurements (figure 2.12 (b)).

Figure 2.12 (b) shows a typical curve of *frequency sweep* measurements. The aim is to probe the material at low strain to stay in the linear regime and at various frequencies. At high frequency, the material responds elastically and at low frequencies a viscous response is obtained. One can measure a yield stress only if the sample is probed at a frequency in its elastic domain, i.e. at a sufficiently high frequency for the material to exhibit elastic behaviour. Indeed, at low frequency, the material will only flow.

On figure 2.12 (a), the strain sweep measurements are performed at a frequency of $1\,\mathrm{rad}\cdot\mathrm{s}^{-1}$. We see on figure 2.12 (b) that at all imposed frequencies, the elastic modulus G' is well above the loss modulus G'' meaning that the fluid behaves as an elastic solid. Therefore the choice of a frequency of $1\,\mathrm{rad}\cdot\mathrm{s}^{-1}$ to perform a strain sweep measurements was appropriate to see a transition from the elastic to the viscous domain of the material.

Another method to measure the yield stress of a material is the *viscosity bifurcation* method [30, 36]. It consists in measuring the viscosity as a function of time for a given applied shear stress. If the stress applied is above the yield stress, the viscosity reaches a stationary state. For a shear stress below the yield stress, the viscosity increases continuously with time. The bifurcation between the two regimes allows to determine the yield stress of the material.

In our case, we used creep mesurements and strain sweep measurements to determine the yield stress. The flow curve of the microgel suspensions in the jamming regime was fitted with the Herschel-Bulkley model to get the constitutive law of the material. Figure 2.11 (a) shows that the suspension have a yield stress and are shear-thinning (see figure 2.11 (a)).

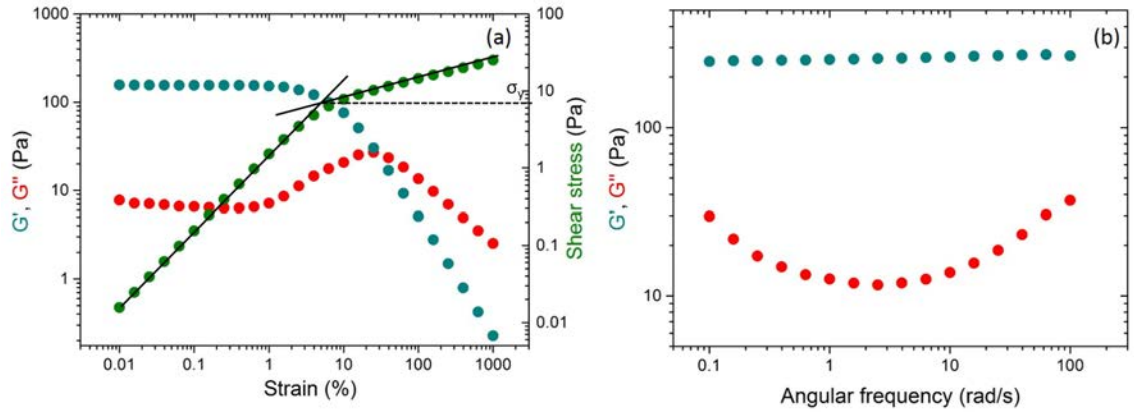

Figure 2.12 – (a) Strain sweep experiment at a frequency of $1\,\mathrm{rad}\cdot\mathrm{s}^{-1}$. Elastic modulus ($G'$, blue) and loss modulus (G'',red) as a function of the deformation amplitude, the shear stress is represented on the right axis. At low deformations, the fluid behaves as an elastic solid, G' dominates. As the deformation amplitude increases, G'' increases and becomes dominant when the material is flowing. The black lines are the asymptotes of the elastic and viscous parts of the curve stress versus strain. Their intersection gives the yield stress value σ_y. (b) Frequency sweep experiment at a strain of 0.5%. At all the frequencies probed, the elastic modulus G' is well above the loss modulus G''. The microgel is in its elastic domain.

Yield stress and visco-elasticity

If a yield stress is present in the flow curve, it means that the fluid exhibits visco-elastic properties. The reverse is not always true. We consider the case of a star polymer presented on figure 2.13. We focus on $C = 109\ \mathrm{mg\,mL^{-1}}$, i.e. the diamond dots. Figure 2.13 (a) shows that the solution of star polymers at $C = 109\ \mathrm{mg\,mL^{-1}}$ has solid elastic properties only above $\omega = 0.6\ \mathrm{rad\,s^{-1}}$. In the flow curve measurement, we are in the domain of long time solicitations corresponding to low frequencies. In this regime, the solution does not exhibit solid-like behaviour. Therefore the flow curve of the star polymer solution at $C = 109\ \mathrm{mg\,mL^{-1}}$ presented on figure 2.13 (b) does not exhibit a yield stress.

2.4 Conclusions on microgel rheology

Microgel suspensions are visco-elasto-plastic yield stress fluids and there are not thixotropic/rheopectic. Microgel suspensions exhibit weak normal forces [164]. We neglect extensional effects in the geometries we will be using. At high deformations the flow curve of microgel suspensions is well characterized by the Herschel-Bulkley law: $\sigma = \sigma_y + k * \dot{\gamma}^n$ with σ_y the yield stress, k the consistency parameter and n the flow index. It is possible to customize the rheology of the suspension by changing its beads volume fraction. Different concentrations of microgel suspensions were used in this study, their rheological properties are summarized in table 2.2.

The suspensions can be seeded with fluorescent tracers that are embedded in the structure of the microgel, so that they are representative of the microgel flow events. We refer to the suspensions by their solid concentration of polymer.

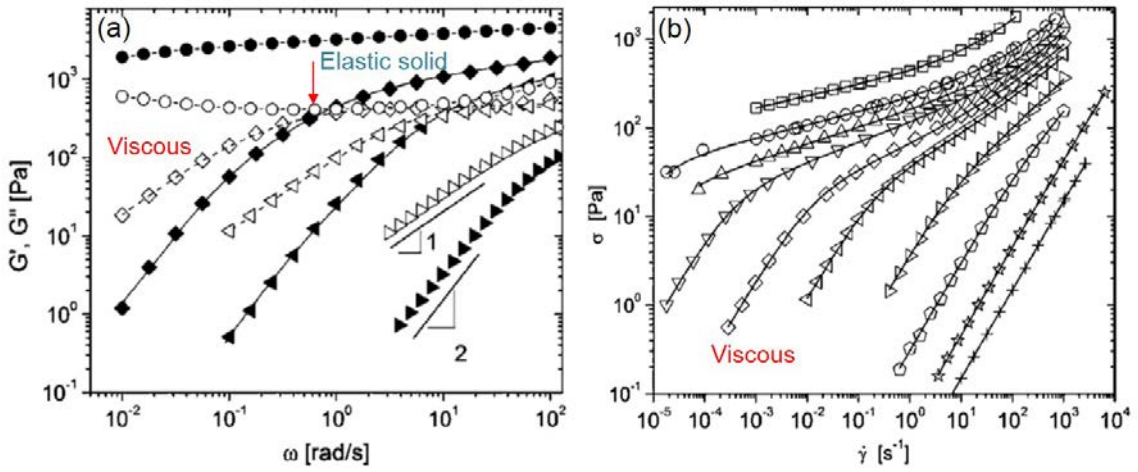

Figure 2.13 – Reproduction from [48]. Storage modulus, loss modulus and flow curve of star solutions at a polymer concentration of $C = 199$ (□), 147 (○), 131 (△),121 (▽), 109 (◇), 98 (◁), 80 (▷), 59 (⬠), 0 (☆) and 0 (+) $\mathrm{mg\,mL^{-1}}$. (a) Storage modulus G' (filled symbols) and loss modulus G'' (open symbols) as a function of frequency at a deformation of $\gamma_0 \leq 1\%$. (b) Shear stress as a function of shear rate for each star solution. The symbols correspond to the same polymer concentration of figure (a).

Table 2.2 – Rheological parameters of the samples of microgel suspensions

Sample	σ_y (Pa)	k ($\mathrm{Pa\,s^{1/2}}$)	n	Concentration ($\mathrm{g\,g^{-1}}$)	Φ [146]
1	11	4.3	0.5	1.6%	$\Phi = 0.7$
2	16.2	5.3	0.5	1.6%	$\Phi = 0.7$
3	15.6	5.1	0.5	1.6%	$\Phi = 0.7$
4	9.4	4.5	0.5	1.6%	$\Phi = 0.7$
5	60.5	10.8	0.5	2.2%	$\Phi = 0.83$
6	16.5	5.6	0.5	1.6%	$\Phi = 0.7$
7	39	9.4	0.5	1.8%	$\Phi = 0.75$
8	86	15.4	0.5	2.2%	$\Phi = 0.83$
9	273	40.9	0.5	3%	$\Phi = 0.98$

Rheology of microgel suspensions

✧ **Microgel suspensions**

- Microgel suspensions are soft glassy materials.
- The microgel suspensions used are above the jamming transition where they exhibit yielding properties.
- The microgel suspensions are non-thixotropic fluids. Under flow they are well described by the Herschel-Bulkley law: $\sigma = \sigma_y + k\dot{\gamma}^n$ with σ_y the yield stress, k the consistency parameter and n the flow index.

Chapter 3

Material and methods

3.1 Fabrication and surface treatments of microfluidic systems

PDMS (PolyDiMethylSiloxane) is the most common material used to fabricate microfluidic systems. In fact, with this technique transparent microfluidic systems can be designed within a day's work at low costs [45]. An alternative material developed in the laboratory is a photopolymerisable glu NOA (Nordland Optical Adhesive). We see what are the advantages of both materials in terms of mechanical and wettability properties. We also show how to modify their surface properties.

3.1.1 Fabrication of silicon masters

Silicon masters are made in the clean room with the lithography technique. Usually a mask with a resolution of 20 µm is used, but this resolution can be better (2 µm) by using chrome mask, when the design demands it. SU8 resin is spincoated on the silicon wafer at a given speed to achieve the desired height for the channels. Different types of SU8 photoresist, having different viscosities, are available to produce heights ranging from 1 µm to 500 µm according to calibration curves (spincoating velocity - height) from the resin supplier. But for liquid resin, the calibration curves to get thicknesses above 100 µm are less robust. It often takes several trials to obtain the right resin height on the silicon wafer. In these cases, the dry film technique gives better performances. It consists in ready-to-use films of SU8 resin, thicknesses from 10 µm to 500 µm are commercially available. The films are set on the silicon wafer by lamination. It is also possible to make multilayers.

The fabrication protocol of SU8 molds with liquid resin and dry films is illustrated on figure 3.1a.

1. Spread the SU8 resin on the mold with spin-coating process for liquid resin and with lamination for the dry films.
2. UV exposure (wavelength 365 nm) through the mask. UV-exposed areas are cross-linked.
3. Post-bake to finalize the cross-linking of the photoresist.
4. Remove the non-exposed resist with developer solvent.
5. Hard-bake to improve adhesion of SU8 on the wafer.

The exposure, post-bake and development times depend on the photoresist thickness and of the type of photoresist used (liquid or dry film photoresist). Depending on the

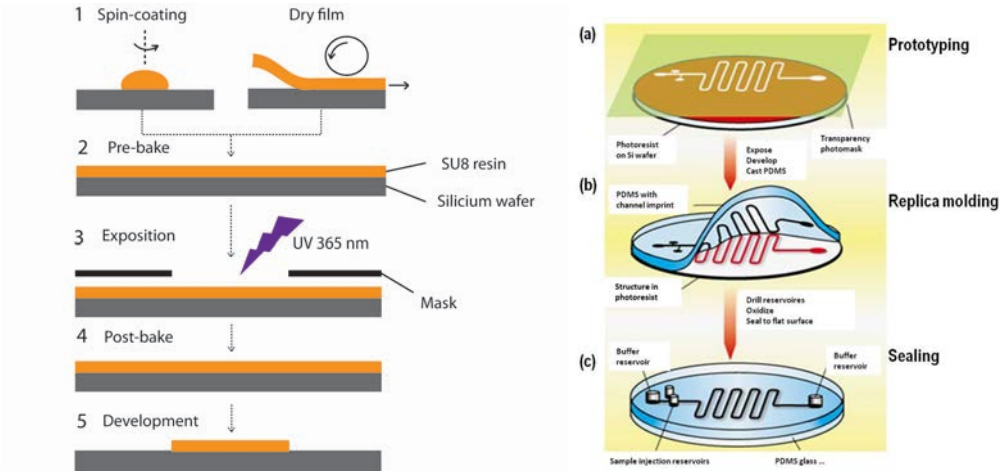

(a) Fabrication of silicon master with a positive mask the channel structure is in relief

(b) Main steps for the fabrication of PDMS systems

Figure 3.1 – Photolithography and PDMS molding. (a) To spread an SU8 film homogeneously on the wafer, two methods are available. With the spin-coating process, the height depends on the rotational speed. In theory, heights from 500 nm to 500 µm can be spin-coated but above 100 µm, the spin-coating speed is difficult to determine precisely and the resin presents heights differences between the center and the border of the wafer. Dry films are SU8 films of predefined heights. They are rolled out on the wafer with a laminator, the rolling step has to be performed with care to avoid the formation of bubbles. This technique is more suited to heights above 100 µm. (b) Once the silicon master is made, it can be used several time to produce PDMS systems. The PDMS mixture is degased, then cured in an oven at 70 °C for at least 1 h.

microsystem fabrication technique used afterwards, it is convenient to print the channels either positively or negatively, that is the channels will respectively appear on relief (PDMS suited) or counter-relief on the wafer (NOA suited).

For the experiments, two kinds of channels were used: shallow straight channels with heights ranging from 7 µm to 100 µm and widths of 1 mm and square channels with heights around 250 µm.

The resolution of photolithography technique is conditioned by the resolution of the mask and by light diffraction occurring at the mask's borders. Diffraction phenomena becomes significant for heights over 100 µm: deep channels start to have a V-shape. To limit this problem, we printed channels of depth larger than 100 µm positively on the wafer. It just involved an extra step of contra-mold fabrication to get the correct stamps for NOA fabrication as we will see below. Dimensions of the silicon master are characterized using a mechanical profilometer (Dektak) or an optical profilometer (Veeco).

3.1.2 Fabrication of PDMS systems (PolyDiMethylSiloxane)

PDMS (PolyDiMethylSiloxane) is an elastomeric material obtained by mixing 10 wt % PDMS crosslinker with PDMS monomer (Sylgard or RTV). The main steps of the fabrication of PDMS systems are represented on figure 3.1b. The mixture is cast onto the silicon master and cured at 70 °C for 1h at least. Then the polymer replica is peeled from the silicon wafer and inlets and outlets are punched carefully with a Harris Uni-Core biopsy sharp punchers (Electron Microscopy Sciences). To close the system, the surface containing

the negative relief of channels is bonded using oxygen plasma [45] to glass surfaces or to another PDMS surface. The surfaces are cleaned with rubber and isopropanol before being brought in the plasma chamber. The plasma chamber is filled with oxygen, then a plasma discharge is applied for 45s. This is enough for the plasma to oxidize the surfaces. When brought together, the surfaces form covalent Si-O-Si bonds.

With a silanization procedure, we can obtain a contra-mold of the PDMS design:

1. Fabrication of a PDMS mold from the original wafer (following the procedure above)
2. Activation of PDMS surface with oxygen plasma
3. Silanization in vapor phase: in a petri dish, place the plasma treated PDMS mold, 5 µL of trichloroperfluorosilane and some grains. Close the Petri dish with parafilm. Wait 40 min.
4. Casting of a PDMS mixture on the silanized mold. Degassing of PDMS and curing at 70 °C for at least 1 h.
5. Peel off the PDMS: the silanization hinders PDMS-PDMS adhesion.

PDMS mold and contra-mold can either be used directly to form microfluidic systems, in this case they are bond to a counter part with oxygen plasma to close the system, or they can be used as a mold for other fabrication procedures such as NOA systems.

3.1.3 Fabrication of NOA systems

NOA (Nordland Optical Adhesive) is a commercial thiolene-based UV photocurable glu. Bartolo *et al.* [11] developed in the laboratory a protocol to use this glu as a material for microfluidic systems to circumvent some drawbacks of PDMS systems. In fact, PDMS swells in most organic solvents. It has a low elastic modulus, therefore that high pressure drops cannot be applied without significant deformations of the channels [62, 70] and surface properties of PDMS are difficult to tune. Flowing yield stress fluids, as a microgel suspension, inside a microfluidic channel requires high pressure drops (up to 5 bar), leading to huge deformations in PDMS channels. This is why most of our systems were built with the NOA glu.

NOA systems are made by soft printing lithography. NOA glu is liquid, and cures into a hard polymer under UV exposure (wavelength 365 nm). A PDMS stamp serves as a mold to pattern the channels in the glu. The printing and capillary methods to fabricate NOA systems are drawn on figure 3.2 and can be decomposed into the following steps:

1. Fabrication of the channel in NOA with the printing or the capillary method
   — Printing method: the stamp is pressed onto a drop deposited on the glass substrate.
   — Capillary method: the stamp is first brought into contact with the substrate, a drop of glu is deposited along the side of the stamp, and thanks to capillary forces the glu fills the gap between the stamp and the substrate.
2. The assembly stamp-NOA-flat is polymerized under UV light (Hammamatsu, maximal power $25\,\mathrm{mW \cdot cm^{-2}}$ for 8 s) at a power of $7.5\,\mathrm{mW \cdot cm^{-2}}$ (30% of maximal power). Since the PDMS is porous, oxygen is present at the interface between the stamp and the glu. Oxygen inhibits the free radical polymerization, which leads to a thin layer of glu that remains uncured.
3. Remove the stamp from the substrate-NOA assembly and close the system with a glass slide preliminary drilled: align glass slide holes with the corresponding fluidic outlets and inlets of the channels.

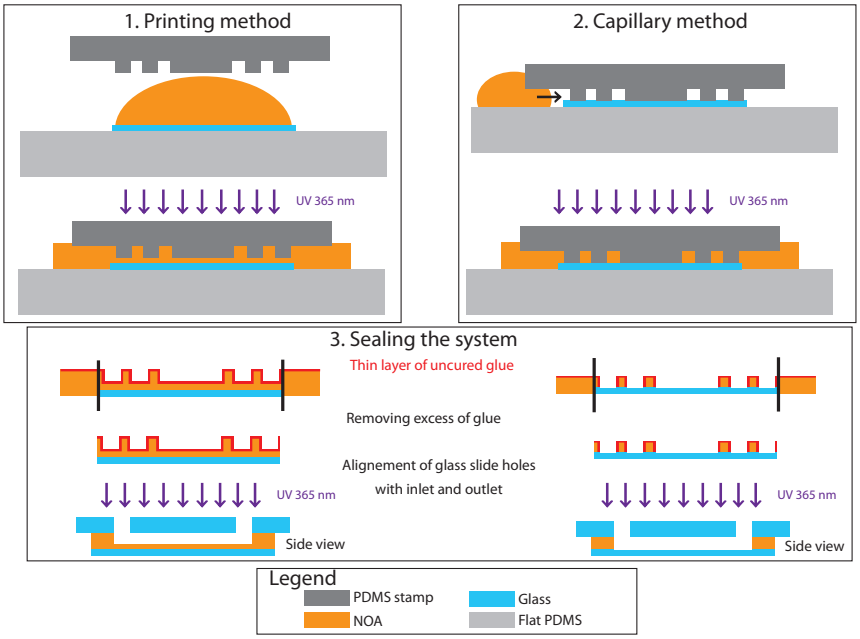

Figure 3.2 – Fabrication of NOA microfluidic systems with the printing method and the capillary method

4. Coverslip is gently pressed with a cotton bud: to create contact between the glu and the glass slide.

5. Exposure of the assembly to UV light for 90 s at 7.5 mW · cm^{-2}.

6. Post-bake the system in an oven at 150 °C for 1 h (necessary for systems reserved for sustaining pressure drops above 2 bar).

7. Glu external connection with epoxy, reticulation in an oven at 70 °C for 20 min.

Assembly between both parts of the system is possible because the presence of dioxygen in the PDMS stamp hinders the polymerization of the glu. A thin layer of uncured glu stays at the surface of the system, this layer spreads on the opposite surface during assembly. For the adhesion to be successful, the assembled surface has to be smooth to favor contacts between itself and the small amount of uncured glu available.

Some practical remarks about the NOA protocol:

— The assembly with the drilled glass slide works because the glass coverslip is sufficiently deformable to ensure that the glu spreads onto the glass slide when pressing it with the cotton bud. Glass slide - glass slide assembly does not work.
— Flat PDMS substrate are practical because the coverslip can stick to it: no air stays between the coverslip and the flat. It avoids the glu to spread on the wrong side of the coverslip (between the coverslip and the flat)
— Figure 3.2 details the different protocols available to obtain systems with 2 or 3 walls of NOA. It is possible to build systems with 4 walls of NOA. In this case, the glass slide has to be covered with NOA using the printing technique or by spincoating.
— In all cases, before starting the fabrication, a degased stamp containing the negative relief of the channel and glass slides with appropriate holes are needed. A sandblaster or the laser printer drills the holes in the glass slide.

3.1.4 Surface treatments

In our experiments we modify the surface properties of our systems. We change the surface roughness and the surface wettability, which are linked to the surface attraction with regards to our microgels. We manage to produce systems with walls of different wettabilities that could sustain high pressure drops.

Techniques to modify the wettability of surfaces

For several microfluidic applications it is necessary to tune surface wettabilities. For example, the production of oil in water or of water in oil droplets require hydrophilic respectively hydrophobic walls. The quality of surface wettability influences greatly droplets stability [43]. In our case, the wettability of surfaces influences the slippage behaviour of our microgel suspensions.

Dry phase treatments such as oxygen plasma [129], UV/ozone ([12, 47, 101]) or a silanization procedure combined to an oxygen plasma treatment are used to control the wettability of PDMS, NOA and glass slides or coverslips [191]. The principle of plasma and UV/ozone treatments is shown on figure 3.3a and 3.3b. The goal is to oxidize the surfaces of the samples to change their chemical compositions: oxygen radical species are present at the surface (figure 3.3c). Indeed, with X-ray photoelectron spectroscopy (XPS) an increase in oxygen content, a decrease in carbon species and the appearance of polar groups at the surface were measured for surfaces treated with high energy sources [109]. The result is an increase in wettability. A silanization procedure performed just after oxidation of the surface, allows to attach groups on the surface with hydrophobic tails.

Wettability of PDMS

PDMS is made of an inorganic siloxane backbone and of pendent methyl groups. The flexibility of PDMS backbone makes the polymer adopt a configuration which presents methyl groups at the surface [140], the Si-O backbone is masked by organic groups. Methyl groups have low surface energy, so PDMS is natively hydrophobic. Surface treatments, such as plasma, UV or UV/ozone exposure, increase PDMS wettability. The chemical composition of oxidized PDMS has been measured by X-ray photoelectron spectroscopy (XPS) to explain the mechanisms for hydrophilization of PDMS. The thin oxidized layer, created by plasma treatment at the surface of the polymer, contains a mixture of original polymer, silicon bounded to 3 or 4 oxygen atoms forming a SiOx rich layer [76], and hydroxyl, carbonyl and carboxyl groups [129, 131]. The silica layer and the polar groups are responsible for PDMS hydrophilization.

However the hydrophilicity given by plasma treatment to PDMS is not a permanent treatment. When stored in air, the surface recovers a hydrophobic behaviour after a few hours [129, 97]. But the morphology [17] and the chemical composition of the recovered surface is different from the original one. Condensation of silanol groups to form siloxane bonds (with water elimination) increases the rigidity of the backbone which hinders the orientation of methyl groups onto the surface [129]. The effect is that the hydrophobic recovery is not total (but in practice, it is very close to the original contact angle). The main mechanism responsible for hydrophobicity recovery is the diffusion of low molecular PDMS chains from the bulk to the surface [181, 109, 141, 76]. Cracks at the treated surface help the diffusion process [141, 56]. Other mechanisms have been identified to

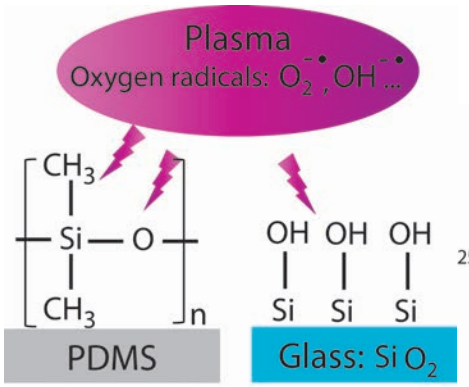

(a) Oxygen plasma

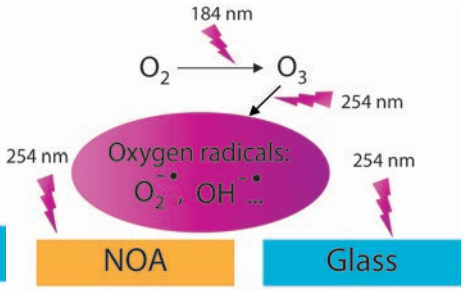

(b) UV/ozone oven

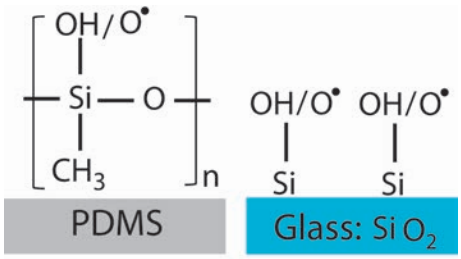

(c) Surface post plasma/UV-ozone treatment

Figure 3.3 – Oxygen plasma and an UV/ozone oven are used for surface treatments: in both cases, highly reactive radical species are created and oxidize the substrate. (a) Oxygen is introduced in the plasma chamber. A high electric discharge applied in the chamber causes the gas to partially ionize, the dioxygen dissociates to form radical species. The mixture of radical species, free charges, dioxygen constitutes the plasma. Radical species are highly reactive. Oxygen radical species in the plasma oxidize the samples in the chamber to form other radical species on their surfaces. (b) UV/ozone oven works with oxygen gas and two wavelengths are emitted: 185 nm and 254 nm. At 185 nm, the dioxygen dissociates, and the single oxygen atoms can recombine with dioxygen to form ozone. At 254 nm, ozone decomposes into dioxygen and oxygen radical species. (c) After a plasma or a UV-ozone treatment, hydroxyl groups are created on glass and PDMS surfaces, giving hydrophilic properties, and radical groups are created which allow covalent assembly between the glass and the PDMS.

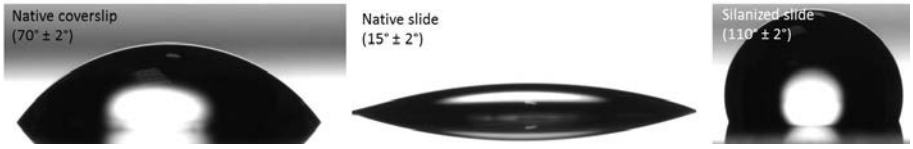

Figure 3.4 – Water in air static contact angle of (from left to right): native glass coverslip, native glass slide, silanized glass slide. The same static contact angle is found for silanized glass coverslip.

contribute to hydrophobic recovery, such as: the diffusion of polar groups, introduced by plasma treatment, into the bulk [129, 131, 141]; reorientation of hydrophilic groups away from the surface [141, 181]; elimination of polar groups by the chemical reaction of silanol condensation [129]. A storage of plasma treated PDMS surface in water prevents hydrophobicity recovery for several days [129, 45].

The gas used for the plasma (air [97], oxygen, azote, argon, NH3 [189]), the type of plasma (MW [76], RF [181, 76], corona discharge [181]) or the treatment duration [83] can be adjusted to enhance PDMS hydrophilicity. The same parameters as well as the storage condition affect the recovery of hydrophobicity [129, 97, 45, 131, 93, 17].

In the laboratory, we use an oxygen, RF plasma. Treatment time is 45 s. Plasma treatment allows the assembly of PDMS to PDMS or glass surfaces [175], because covalent siloxane (Si-O-Si) bonds form between the two oxidized substrates. Treatment time can be adjusted but insufficient oxidation does not produce enough siloxyl groups for covalent bonding and overoxidation leads to the formation of a rough silica layer which is not flat enough to allow adhesion between substrates [27].

Wettability of glass slides and coverslips

Glass slides and coverslips are made of soda lime glass and borosilicate glass respectively. As shown on figure 3.4, they do not have the same wettability: glass slides are natively very hydrophilic (water in air static contact angle 20°) whereas glass coverslip have a water in air static contact angle around 70°. Glass coverslip seem to be more sensitive to impurities contamination than glass slides. After a plasma treatment, both become very hydrophilic: droplet of water spread totally over the surface. With a silanization procedure, glass slides and coverslips become hydrophobic. Quartz slides have the same wettability properties as glass slides.

Wettability of NOA

NOA is a thiol-based glu. The uncured glu is hydrophilic and it is natively weakly hydrophilic when cured, the static contact angle of water in air on a cured NOA surface is around 80°[100, 44]. A. Duboin showed that an oxygen plasma treatment of NOA could decrease the water in air static contact angle to 15°. But after baking the contact angle value comes back to 60°. Post-bake of the system cannot be avoided when one wants to use NOA systems at pressure drops above 2 bar. It is also possible to perform a plasma treatment in a closed system but this procedure is complex and long if the geometry of the channel is tortuous [44].

UV/ozone treatments is another technique to increase wettability of surfaces. Its efficiency on NOA surfaces has been demonstrated in [100]. The treatment holds for weeks. It uses deep UV (wavelengths of 184 nm and 254 nm). While glass absorbs at these

wavelengths, quartz is transparent throughout the UV. By replacing the glass slide in the NOA fabrication protocol by a quartz slide, it is possible to perform a UV/ozone treatment in a closed system. Under deep UV exposure, NOA reticulates completely which causes the following problems:

— for a treatment of the system before assembly: the thin layer of uncured glu reticulates during UV/ozone exposure, so assembly is not anymore possible.
— for a treatment of the system before assembly trough a mask: the thin layer of uncured glu is protected but these systems show less resistivity to high pressure drops [44].
— for a treatment of a closed system without post-baking: unsticking has been observed during the treatment [44].

So it is preferable to fulfill the UV/ozone treatment in closed and post-baked NOA systems to avoid unsticking or adhesion problems during assembly. The treatment time is 1h. The final system is constituted of three walls of NOA and one wall of quartz and is totally hydrophilic.

Mixing 1 wt % APTES with uncured NOA, should give a cured NOA surface hydrophobic according to Wägli *et al.* [185]. But we could not reproduce this result.

Roughness of glass slides

Acting on surface roughness is another way of controlling slippage. The microgel suspension is monodisperse, the beads have a diameter of 500 nm. If a roughness of the order of the beads size is introduced, the first layer of beads will be trapped in the roughness cavities preventing slippage.

Glass slides are atomically smooth. AFM (Atomic Force Microscopy) measurements on silanized glass slides evidence a roughness of the order of 100 nm [102]. This has no impact on the slippage behaviour of the microgel since it is much smaller than the beads size.

It is possible to add a roughness on the glass slide with a sandblaster. Pressurized sand is blown on the glass surface and abrades it. The roughness mean depth is adjusted by changing the pressure at which the sand is blown. We obtain a roughness of the order of 500 nm when the sand is pressurized at 2 bar.

Surface coatings treatment

Métivier *et al.* showed that slippage of carbopol gel can be hindered on PMMA surfaces with a simple PEI (PolyEthyleneimine) surface coating [130]. The treatment is performed in a closed system, PEI adsorbs on PMMA surface. Carbopol gel interact with PEI via attractive interactions so that the first layer of beads stick at the wall preventing the gel from slipping. The treatment is stable over time. Carbopol gels and microgel suspensions are chemically close, so we tried to implement the treatment in our microsystems according to some useful advice from Ilham Mainmouni (Navier laboratory, Marne-la-Vallée). The protocol was:

— Preparation of PEI solution at 1 wt %.
— The solution is left in the system for 6h and is regularly flown.
— Rinsing the system with dionized water.
— Drying the system.

According to Métivier *et al.*, the treatment time does not need to be that long, but some trials with shorter treatment time were not successful.

3.1.5 Compatibility of surface treatments with NOA fabrication protocol

In this paragraph we describe how we could combine the surface treatments listed above with the fabrication protocol of NOA system. The objective is to obtain channels in which the top and bottom surfaces do not have the same surface properties but which sustain high pressure drops.

Adhesion of the glu on surface is due to van der Waals forces. The glu must wet very well the surface so that the molecules of the glu come in very close contact with the substrate allowing van der Waals attraction between the surface and the glu. Therefore, substrate wettability and roughness are essential to a successful bonding.

Figure 3.5 summarizes the main fabrication protocol for each surface treatment used.

Hydrophilic - hydrophilic channels

The two methods used are sketched on figure 3.5 in the frame box "hydrophilic - hydrophilic":

1. Glass slide and coverslip are treated with oxygen plasma before system fabrication. Then we use the capillary method to build the microchannel, both surfaces are hydrophilic, the glu can spread totally on the surfaces, adhesion is very good.
2. We fabricate the channel using the printing method and a quartz slide to close the system. The channel is post-baked at 150 °C for 1 h before UV/ozone treatment for 1 h.

Weakly hydrophilic - hydrophilic channels

Glass slides and coverslip are natively hydrophilic and weakly hydrophilic respectively. We fabricate the microchannel using the capillary method (see figure 3.5 frame box "hydrophilic - weakly hydrophilic"). No surface treatment is required. There is no adhesion problem with these systems.

Rough - smooth hydrophilic channels

We observed that adding a roughness of the surface can decrease adhesion of the glu. When we want to suppress slip using the rough surface technique, the entire channel surface has to be roughened to have a homogeneous flow of the microgel in the channel. Therefore, we roughen a surface slightly larger than the channel area using rubber to protect the other part of the glass slide from sand abrasion. The steps for the fabrication of rough channels are represented on figure 3.5 in the frame box "rough - hydrophilic":

1. Preparation of the glass slide
   — Holes are drilled
   — Place the rubber to protect the glass slide with the help of the mask
   — Roughen the glass side surface
   — Cleaning of the glass slide with ultrasound bath (for 20 min in dionized water)
2. Preparation of the coverslip with the channel mold
   — Plasma treatment of the coverslip
   — Building of the channel geometry using the capillary method
3. Assembly
   — Assemble the glass slide

— UV light exposure for 90 s at a power of 7.5 mW · cm^{-2}.

The NOA channel cannot be built on the roughened side because the asperities will be filled by the glu by capillarity. It is easier to roughen the glass slide than the coverslip. Also since visualization is not optimal through rough surfaces, it is therefore preferable that the surface through which we observe (in our case the coverslip) the sample stays smooth.

Only a thin layer of uncured NOA is available to assemble the glass slide with the NOA channel. Therefore, the roughness at the border of the channel limits the contacts between the surface and the uncured glu, it decreases adhesion. These channels support pressure drops up to 4 bar.

Hydrophobic - hydrophilic channels

NOA adhesion is very good on hydrophilic surfaces and very low on hydrophobic surfaces, because the glu does not spread sufficiently on hydrophobic surfaces. We first attempted to limit the silanized area using rubber to protect locally the coverslip from surface oxidation and silane grafting. The following difficulties raised up:

1. It is important that the entire surface of the channel is silanized, otherwise different flow regimes are observed in the channel. Thus the silanized surface needs to be slightly larger than the channel surface. We used the mask drawing to align the rubber bands protecting the glass.
2. When the glass coverslip is silanized, rubber must be removed for assembly. It is delicate to remove rubber from the coverslip without breaking it.
3. When the rubber is removed, there are no more prints on the coverslip to indicate where the silanized area is. Thus alignment with the glass slide holes is not possible.

To solve these problems, we silanized the glass slide, the holes allow to locate the silanized area after the rubber has been removed. The glass coverslip is treated with oxygen plasma.

Since the border of the channel is hydrophobic, adhesion was not sufficient in these systems to sustain pressure drops higher than 2.5 bar.

We saw in paragraph 3.1.4 the particularity of PDMS wettability: after oxygen plasma PDMS is hydrophilic and it recovers its hydrophobicity a few hours after, when stored in air. We used this property to build systems with asymmetric wettability surfaces that could sustain pressure drops up to 4 bar. The steps of the fabrication are sketched on figure 3.5 in the frame box "hydrophilic - hydrophobic" and are:

1. Preparation of the glass slide (one day before preparation of the system)
   — Holes are drilled.
   — PDMS is spincoated on the glass slide (PDMS height: 50 µm).
   — Spincoated glass slide is baked at 90 °C for one night.
   — Holes are punched to remove the film of PDMS inside them.
2. Preparation of the coverslip
   — Treatment of the coverslip with oxygen plasma.
   — Building of the channel geometry using the capillary method.
   — UV light exposure for 7 s at a power of 7.5 mW · cm^{-2}.
3. Assembly
   — A few minutes before assembly, the glass slide is treated with oxygen plasma, so the PDMS surface becomes hydrophilic.

— Assembly of the glass slide with the coverslip: the glu can spread on the hydrophilic PDMS surface.
— UV light exposure for 90 s at a power of $7.5\,\mathrm{mW \cdot cm^{-2}}$.
— Post-baking of the system for one night at 90 °C: the NOA glu is completely polymerized and the PDMS recovers its hydrophobicity.

These systems could sustain pressure drops up to 4 bar. Good pressure resistivity may be explained by:
— A good spreading of the glu on the hydrophilic PDMS surface that favors creation of van der Waals interactions.
— NOA is a thiol-based glu. After plasma treatment, the PDMS surface is oxidized, so hydrogen bonds may form between oxidized species of the PDMS layer and thiol functions of the glu.

Despite that, adhesion of this system is lower than that of glass slide/coverslip systems. In fact, the PDMS surface is not as smooth as glass slide or coverslip surfaces, it limits the contacts between the glu and the surface leading to a lower adhesion as in the case of rough surfaces.

3.1.6 Conclusions on system fabrication

Materials used to fabricate microfluidic systems are glass, PDMS and NOA. The slippage behaviour of our microgel suspension is very sensitive to surface roughness and wettability. We showed in this section how we can control these parameters and how we can assemble different materials to form microfluidic channels of various surface properties that sustain high pressure drops. In figure 3.5 we wish to summarize the main fabrication protocols used.

3.2 Micro-Particle Image Velocimetry (µPIV)

Particle Image Velocimetry is a quantitative flow visualization method which consists in seeding a fluid with tracer particles to get information on the flow field in the observation plan. In 1998, Santiago *et al.* introduced PIV at the micro-scale using a cross correlation method between recorded images to calculate the two-components velocity field in the measurement plane [161]. Optical access and fluid transparency are needed for the measurements, the sample is observed with a microscope objective and illuminated in volume. But the camera captures only the light emitted by tracers in the focus plan of the objective.

The interval time between two images δt depend on the camera frame rate or on the illumination pulse. The distance δd a single particle has travelled during δt is calculated by image correlation. Details on the advancements of two-dimensional µPIV and developments of three-dimensional µPIV are found in [188].

This method has often been used to characterize slippage phenomena. In the laboratory, P. Joseph developed an original set-up where a Hele-Shaw cell is observed across its height. The optimization of the experiment (a precise determination of the wall position thanks to adsorbed particles at the wall, a small focal plan depth, control of the focalization height with a piezo-controler) allowed to extrapolate from the velocity profiles slip length with a resolution of 100 nm [86, 85]. Recently, the optimization of a nano-PTV method in an evanescent light showed that slip length can be measured with a resolution down to 10 nm on hydrophilic surfaces with sucrose [103].

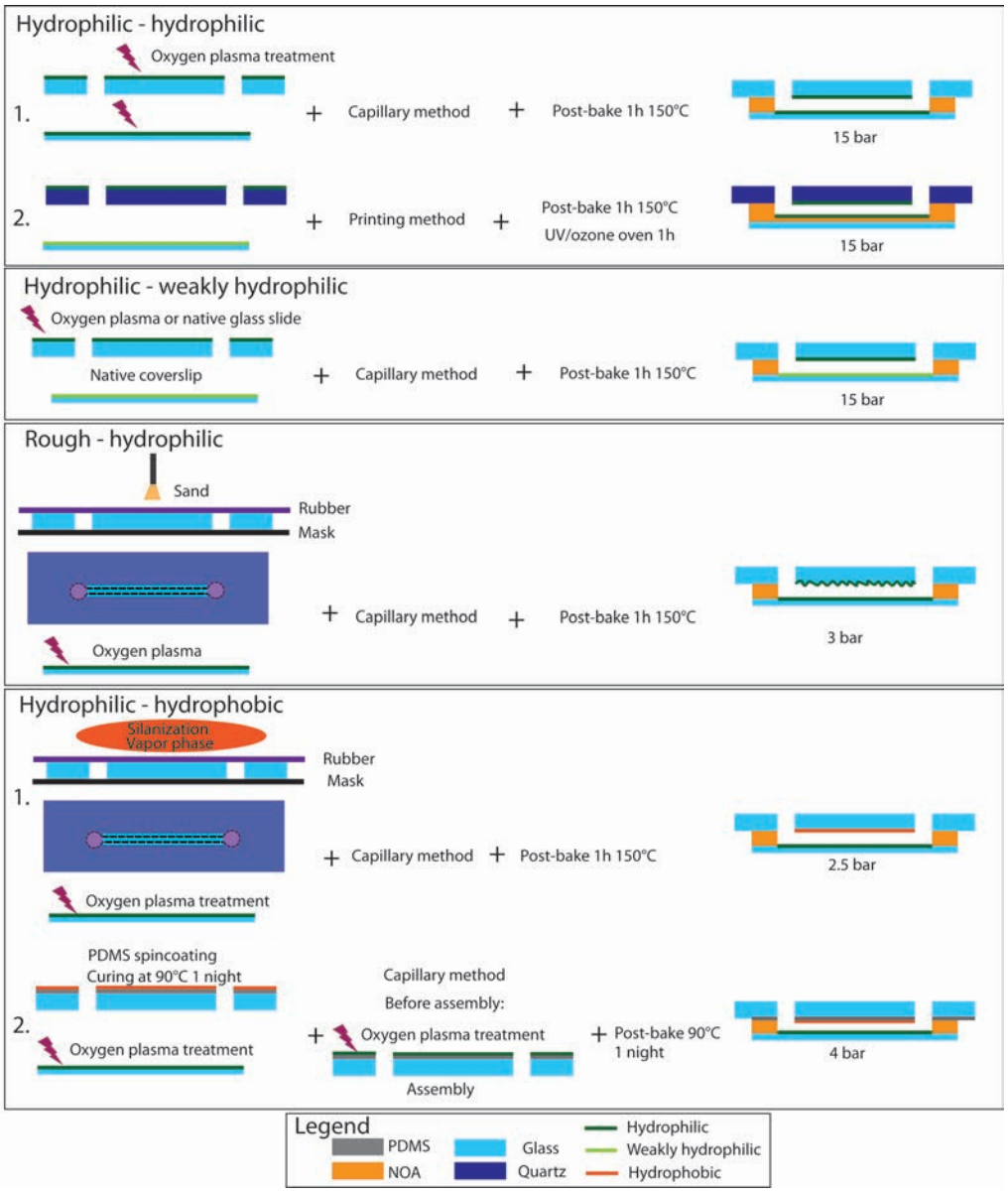

Figure 3.5 – Fabrication of microchannel with different wall wetting properties and roughness that sustain high pressure drops

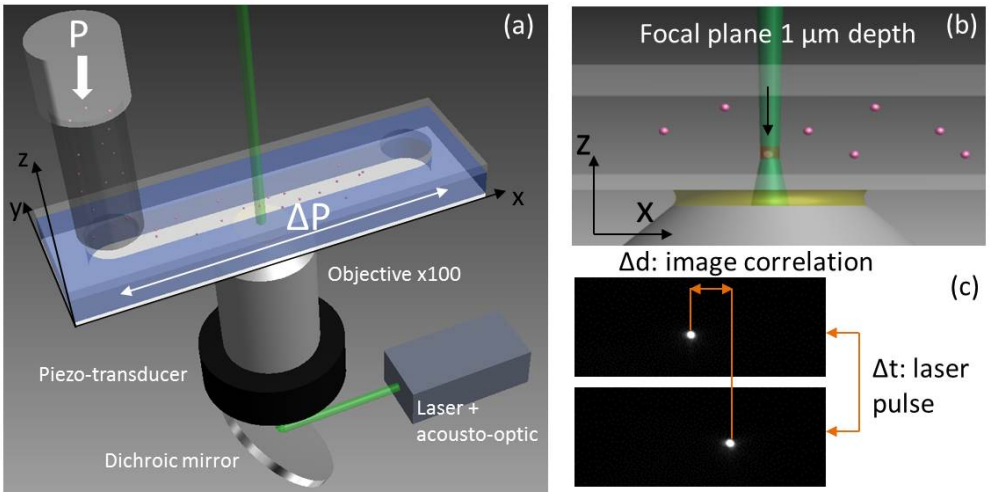

Figure 3.6 – Experimental µPIV set-up. (a) The tracers in the fluid are excited by epifluorescence with a laser beam modulated by an acousto-optic modulator. The emitted signal is transmitted to the camera thanks to the dichroic mirror. (b) The precision of the experiment depends mostly on the focal plan depth which is 1 µm. (c) The displacement of the beads is determined by image correlation, the images are filtered to remove background noise.

A microfluidic environment provides also several advantages for the rheological study of complex fluids. Higher shear rate than standard Couette or cone-plane geometry are accessible. It has been shown that non-linear constitutive laws can be deduced directly from velocity profiles even when slippage occurs in the channel [40]. The use of µPIV with polymer suspension, emulsions, micelles [18], soft [138] or hard [82] colloids suspensions allows to quantify non-Newtonian behaviours such as shear-banding [137], fluid elasticity [157, 139], or flow instabilities [135].

We use the µPIV set-up upgraded by P. Nghe (maximal measurable velocity of $0.1\,\mathrm{m}\cdot\mathrm{s}^{-1}$) to characterize the rheology and slip velocities of model yield stress fluids. Here we describe the experimental set-up (depicted on figure 3.6 (a)) and the image treatment employed to obtain velocity profiles. We explain also how the flow curve is recovered from the velocity profiles.

3.2.1 Flow configuration

Geometry of the microchannels and flow control

The microfluidic channels are Hele-Shaw cells of high rigidity which sustains the high pressures involved in the experiments (30-600 kPa) without appreciable deformation. In most cases, the variation of the channel height was less than the accuracy of the optical detection (1 µm). In only two cases (over eleven which were tested), the channel height was found to vary over about 2-3 µm, which remains negligible compared to its dimension. We also checked that the slide and the coverslip were parallel to one another by measuring the channel heights at different locations along the longitudinal and transverse directions.

In the following, axis Ox represents the direction of the flow along the length L of the channel, Oy is the direction along its width w and Oz along its height h (see figure 3.6 (b)). The velocity field in a Hele-Shaw cell is known to be very simple: $\vec{u} = U(z)\vec{x}$. The general form of the momentum equation for an incompressible fluid is given in equation 2.5. In the Hele-Shaw geometry, the velocity has one component along the x direction which

varies only along the z direction $U(z)$. Equation 2.5 reduces to:

$$\frac{\partial \sigma_{xz}}{\partial z} = \frac{\partial p}{\partial x} = -\frac{\Delta p}{L} \tag{3.1}$$

The suspensions are driven using Fluigent MFCS pressure pumps. To reduce entry effects, we connect the upstream and downstream reservoirs directly onto the chip without any intermediate tubing. Therefore, the pressure drop measured corresponds directly to the pressure drop at the channel borders, the shear stress applied is calculated from equation 3.1.

We checked that the velocity measurements are performed at a stationary state for the microgel suspensions, so that the flow is not affected by aging of the material that stays at rest in the reservoir before being injected. The step shear rate experiments carried out in 2.3.5 showed that a microgel 1.6% reaches a stationary flow for a minimal deformation of $\gamma = 0.1$ %. In our experiments, the wall shear stress applied ranges between 3 to 10 times the yield stress, which corresponds to wall shear rate of $\dot{\gamma_w}$ =30-200 s^{-1}. At these wall shear rates, the material reaches a stationary flow over times of the order of $\gamma/\dot{\gamma_w}$. In our case it corresponds to times between 0.5 and 3 ms. We convert this time to an entry length. The most important velocities measured were of the order of 5 $\mathrm{mm\,s}^{-1}$ which corresponds to entry length between 2.5 and 15 µm. The measurements were always carried out several mm away from the entrance. Therefore the material is probed in a stationary state.

Before each experiment, the suspension is loaded in the upstream reservoir and bubbles are carefully removed by gentle centrifugation.

Fluorescent tracers

The suspensions are seeded at a volume fraction of 10^{-4} with 500 nm in diameter fluorescent sulfonate-functionalized polystyrene tracers from Duke Scientific. The tracers are chosen to have a size comparable to that of the swollen microgels. They are added before swelling to ensure that they are uniformly dispersed in the suspension. Each tracer is in contact with many surrounding microgels so that it experiences the same sequence of dynamical events and moves at the same velocity as its neighbours [164]. The volume fraction of tracers in the suspension is low to not modify the rheology of the microgel suspension. On the observation field (diameter 36 µm) 1 to 5 tracers are in the focal plan (thickness 1 µm) [136].

3.2.2 Optical environment and experimental protocol

The µPIV set-up is depicted in figure 3.6 (a) [136]. All measurements are performed far from the microchannel entrance where the velocity profiles are fully developed. We use an inverse microscope (Leica DM IRB) equipped with an oil immersion objective (x100, NA= 1.3) which has a small focal plane depth (600 nm). The resolution in the observation plane is limited by diffraction. So the resolution of the experiment in the position z is $\approx$ 1 µm (see figure 3.6 (b).

The probe tracers are excited using a laser beam ($\lambda = 532$ nm, 300 mW) modulated at frequency f (up to 30 kHz) with an acousto-optic modulator which transforms the continuous beam into a succession of light pulses. Images are recorded by a CCD camera working in full frame transfer mode (640*480 pixels, Allied Vision Technologies) which allows to collect sequences of pairs of images; two images in a pair are separated by a time interval which depends on the modulation frequency f. In our case, Brownian motion is negligible since the suspensions are highly concentrated. The interval time between images

can be set to maximize the distance crossed by the particle between two light pulses.

The position of the focal plane in the microchannel is controlled by displacing the objective vertically using a piezo-transducer (Physik Instrumente), with minimum steps of 0.25 µm and 10 nm accuracy. The actual z coordinate of the focal plane is obtained after correction of the mechanical position of the actuator by the refractive index of the solution ($n_{sol} = 1.33$) and glass ($n_{glass} = 1.515$):

$$\delta_{fp} = \frac{n_{sol}}{n_{glass}} \tag{3.2}$$

At each depth, we collect up to 40 pairs of images, each containing about 4 fluorescent tracers. The field of observation is a circular area with a diameter of 36 µm. The frequency f, the pulse duration, the delay time between two pairs of images, the steps of the piezo-transducer and the camera are synchronized electronically (EG, R&D Vision). The maximal velocity measurable in this experiment is $0.1\,\mathrm{m} \cdot \mathrm{s}^{-1}$.

3.2.3 Image analysis and profile reconstruction

Image analysis

Once images are obtained, they are processed to obtain the values of the local velocity. The data processing is implemented using a custom Matlab code. A thresholding filter is applied on all images to remove background noise of defocalized particles. Then the program computes the cross correlation between images of the same pair to determine the distance from which the particle has moved (see figure 3.6 (c)). The accuracy of the image correlation is one pixel, i.e. 0.14 µm.

Reconstruction of profile

Velocities were determined at several heights across the whole channel. Each point of a velocity profile corresponds to an average of up to 40 values. Abnormal values (too far from mean value) are eliminated, error bars on the velocity profiles correspond to statistical deviations. Determination of wall position allows to delimitate measurement points belonging to the velocity profile: near the walls abnormal values have to be sorted out. The bottom and top surfaces are located by vertically scanning the channel and determining the positions where tracer particles adsorbed at the wall are observed. If no particles are adsorbed, the wall is set to the height where the first clear fluorescent tracers appear.

Rheological curve

From a velocity profile and the knowledge of the stress applied (according to equation 3.1), one can deduce the constitutive law of the material. The shear rate is calculated from the derivative of the velocity profile. Therefore, the flow curve of the material can be reconstituted. It is possible to adjust the range of shear rate the material is subjected to by changing the height of the microfluidic channel.

Slippage

Slippage is no longer a problem in determining the rheology of the fluid in a µPIV experiment since the velocity profile is only translated in the presence of slippage and

the shear rate values are extracted from its shape. In the case of microgel we measure apparent slippage at the wall. There is a thin lubrication layer between the wall and the first layer of beads which is of the order of 15 nm. The tracers are embedded in the structure of the material so we measure the velocity of the first layer of beads. Considering the resolution of the position along the z-axis (1 µm), it is right to say that the first layer of beads corresponds to the location of the wall.

3.3 Experimental set-up used for the study of fluid displacement

The aim of this experiment is to displace a first yield stress fluid by another fluid which can be non-Newtonian or Newtonian. Before starting the experiment the fluids have to be introduced in the microsystem without bubbles and with a flat interface between them at the beginning of the experiment.

We chose a T-junction geometry represented in figure 3.7 (a). The T-junction allows a good initiation of the microsystem: bubbles can be removed, a flat interface is created between displaced and displacing fluid.

The exit channel used for interface initialization needs to be closed when the experiment starts. Therefore, this outlet is plugged to a Quake valve represented on figure 3.7 (b) [182]: this is a pressure controlled valve. A Quake valve is made of PDMS multilayers: the flow channel is separated from the control channel, which is in the layer above and perpendicular to the flow channel, by a thin membrane. When the control channel is pressurized, the thin membrane deforms and plugs the flow channel so that the flow is stopped [166].

We define **fluid 1** as the **displacing** fluid, and **fluid 2** as the **displaced** fluid. The protocol for system initialization is sketched on figure 3.7 (c):

1. Connect reservoirs of fluid 1 and fluid 2 on entries 1 and 2 respectively, Quake valve open.
2. Start the flow from both entries, the flow exits the system through outlet 3. Continue until no bubbles remain in the channel, the interface should be plane. It is important that no bubbles stay in the tubing linking the system to the Quake valve, otherwise even if the Quake valve is closed, bubble compression will allow the flow to pass through this way during the displacement experiment.
3. Stop the flow, disconnect reservoir of fluid 2 from port 2, close Quake valve.
4. Start the experiment: the flow goes from port 1 to port 2.

The system can be refilled following the same procedure to start a new experiment. A system can be used for several experiments during one day, but not from a day to the other because the microgel starts to dry in the system.

The cross section of the channels are square in most of the cases. To work with acceptable pressure drops in the system, the dimensions of the square channels are 250 µm. The fabrication procedure to get straight walls has been described in paragraph 3.1.1. Typical pressure drops applied range from 30 to 250 kPa.

During the first phase of the experiment, when the interface is still in the channel, we follow it. When it gets out of the channel, we record the evolution of the layer thickness in the channel at several locations. The aim of the experiments is to visualize the layer of the displaced fluid left at the wall, so we use a 10x magnification objective with a focal plane

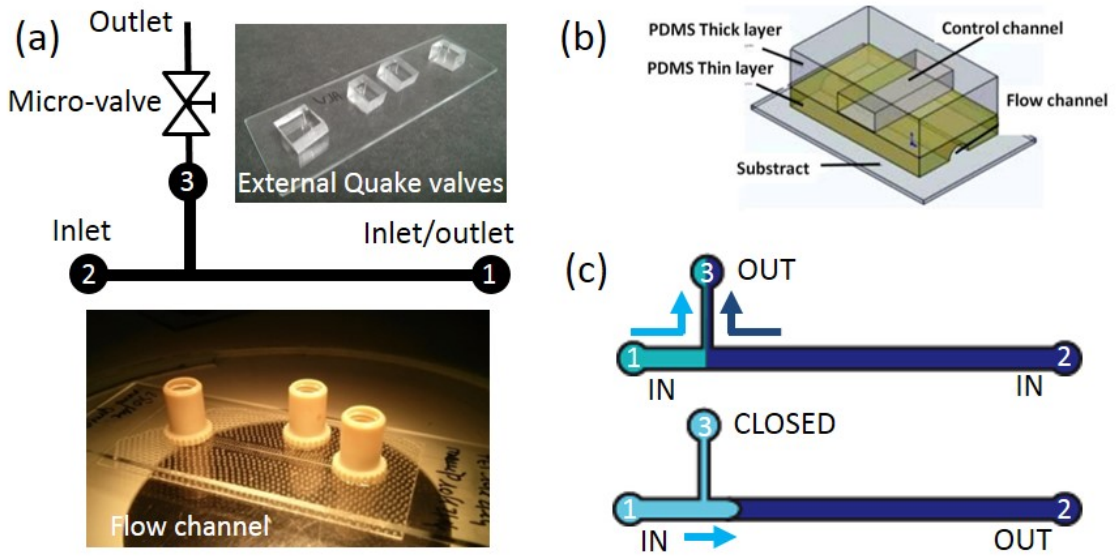

Figure 3.7 – Experimental set-up for the study of fluid displacements. (a) Scheme of the experimental set-up, picture of the glass flow channel made with NOA. (b) In the Quake valve, the control channel is above the flow channel and can seal it when it is being pressurized. Reproduction from [166]. (c) Fluids sequence to initialize the displacement experiment.

depth around 10 µm to be able to see clearly the wall layer. As a consequence, we do not see the whole channel, so that when we move the microscope platform we do not know our position along the x-axis. Therefore a Matlab program was developed to record the microscope platform positions data as a function of time.

As in the µPIV set-up, we checked that the measurements are performed at a stationary state for the microgel suspensions, so that the flow is not affected by aging of the material that stays at rest in the reservoir before being injected. The step shear rate experiments carried out in 2.3.5 showed that a microgel 3% reaches a stationary flow for a minimal deformation of $\gamma = 0.2$ % (In the experiments of displacements, the microgel 3% was the most viscous sample used). In our experiments, the smallest wall shear stress applied was around 1.8 times the yield stress, which corresponds to wall shear rate of $\dot{\gamma}_w = 10\,\mathrm{s}^{-1}$. At these wall shear rates, the material reaches a stationary flow over times of the order of $\gamma/\dot{\gamma}_w$. In our case it corresponds to times around 25 ms. We convert this time to an entry length. The velocities measured were between 30 and 1 mm s^{-1} which corresponds to entry length between 0.6 and 2 µm. Therefore the material reaches its stationary state very soon after the starting of the experiment (the channels for the displacements are 2 to 3 cm long).

Material and methods

✧ **Fabrication and surface treatments of microfluidic systems**
- With the photocurable glu NOA, we build systems that can sustain the high pressure drops (up to 5 bar) encountered in the experiments.
- The attraction between the surfaces of the microchannel and the microgel suspensions are tuned thanks to various surface treatments: silanization, plasma or UV-ozone, coating with PEI. Therefore, the amplitude of the slip of the microgel is customized.
- Slip can be suppressed mechanically by adding a roughness on the wall of the order of the microgel bead size.

✧ **Micro-Particle Image Velocimetry (µPIV)**
- Flow profiles are measured for averaged speeds up to $0.1\,\mathrm{m\,s^{-1}}$, with a micrometric resolution.
- Flow environment: the fluid is seeded with fluorescent particles, it is pressure driven in a rigid Hele-Shaw cell.
- Optical environment: an oil immersion objective with a small focal depth (0.6 µm) is mounted on a piezo-transducer. Therefore the channel is spanned vertically and the velocity profile is acquired step by step.
- Image analysis: images are cross-correlated to measure the displacement of the particles.
- From the velocity profiles measured in the Hele-Shaw cell, it is possible to reconstruct the rheological curve of the material.

✧ **Experimental set-up used for the study of fluid displacement**
- The microfluidic channels are designed to sustain high pressure drops without deformation.
- The set-up includes a T-junction, monitored by externalized microvalves, that control the injection of the fluids.
- The set-up is instrumentalized so that pressures, velocity profiles, interface morphologies, can be accurately determined.

Chapter 4

Dynamical role of slip heterogeneities in confined systems

4.1 Introduction

We start by reviewing succinctly basic definitions of slippage and the different slip mechanisms, in particular in the case of the microgel suspension. We also review briefly current theories and experiments relating to the flows of jammed suspensions and emulsions.

4.1.1 Slippage in general and in the case of microgel suspensions

Slippage in general

Slip is a very general phenomenon giving rise to spectacular applications (see figure 4.1). For smooth surfaces, Newtonian fluids develop a nanometric slippage [179, 134, 22]. For non-Newtonian fluids, the slip length can reach tens of microns such as for wormlike micellar solutions [99, 80], concentrated emulsions [153, 160, 13], foams [88, 41] or colloidal suspensions [122, 82, 8].

The existence of wall slip is of particular interest for many technological processes including extrusions of complex fluids, ink jet applications, and oil migration in porous media. Also for rheologists, wall slip aroused many studies since it has to be taken into account to get a correct determination of fluids rheological properties.

The slip can be characterized by the Navier length b or by the slip velocity at the wall

Figure 4.1 – Reproduction from LiquiGlide company. The left mustard pot does not exhibit slip at the walls whereas the right mustard pot does. The slippery pot is completely cleared out.

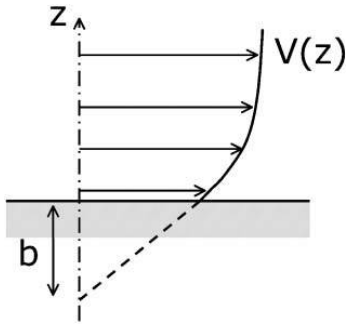

Figure 4.2 – The Navier length b is the length beyond the wall at which the fluid velocity profile is extrapolated to zero.

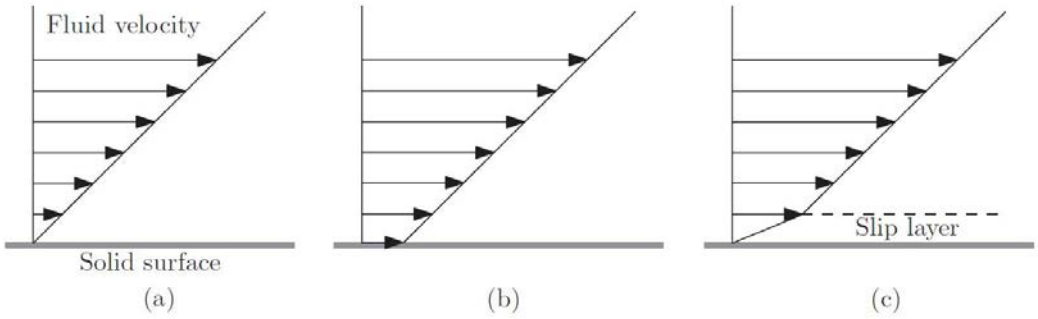

Figure 4.3 – Schematic representation of the difference between (a) no slip, (b) true slip, and (c) apparent slip boundary conditions in a shear flow, reproduction from [168].

V_s which can be related through:

$$V_s = b\frac{\partial V}{\partial z} \tag{4.1}$$

With V_s the slip velocity. The slip length is defined as the effective distance from the surface at which the no slip condition is satisfied.

A distinction has to be made between "true slip" and "apparent slip". In the case of "true slip" there is a discontinuity in the velocity field at the interface between the fluid and the solid boundary. The expression "apparent slip" refers to the case where a thin layer of fluid adjacent to the wall with different rheological properties than the bulk acts as a lubricant for the bulk fluid. Therefore the no-slip boundary condition at the wall is not violated: there is a very large velocity gradient across the thin layer which gives the impression of slip of the bulk phase [168]. In this sense, slip can be viewed as a "wall depletion effect" [10].

Apparent slip is the most common slip mechanism encountered especially with non-Newtonian fluids. In fact, non-Newtonian fluids are multiphase fluids: a dispersed phase of mesoscopic size compared to the flow dimensions, and a continuous phase. In these systems, forces (hydrodynamic, steric...) act on the dispersed phase and displace it away from the solid boundary. The layer of continuous phase left close to the wall has a thickness of $\approx$ 0.01 µm to 10 µm.

Wall slip behaviour is influenced by several parameters. The fluid particles can interact with each other as well as with the solid boundary (through electrostatic interactions or frictional effect). Therefore the physico-chemistry of the surface (wettability, roughness, impurities or gas) and the properties of the fluid (viscosity, elasticity or polarity) are

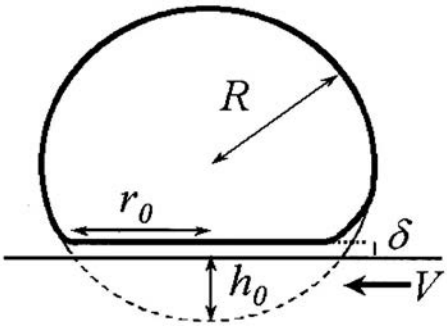

Figure 4.4 – Schematic representation of the microgel particle squeezed against a solid wall and forming a lubricating layer, for which the thickness δ is set by the elastohydrodynamic force between the particle and the wall. Reproduction from [122].

of major importance in slippage phenomena. The flow field itself can influence the slip behaviour: it has been shown in different studies that the slip magnitude varies with the wall shear stress. Also the particles in the fluid can migrate under shear which induces a change of fluid properties near the solid boundary.

The presence of wall slip in a system can induce flow instabilities (for example stick-slip phenomenon) or on the contrary favour flow stability (in polymer extrusion processes). For a detailed review on slip phenomena, we refer to the reviews of Barnes [10] and Sochi [168].

Today, many questions are left open in this area. More generally, understanding the factors that control slippage in non-Newtonian fluids represents an active field of research.

In practice, it is possible to reduce or eliminate slip. Roughening or changing the physicochemical properties of the surface are the two principal techniques used. These treatments are system dependent and can sometimes be ineffective or controversial, as for the case of roughness [87, 6].

Slippage in the case of microgel suspension

The behaviour of soft particles like microgels at surfaces depends on short-range forces between particles and surfaces as described in [162, 163] and of elastohydrodynamic force (EHD) between the particle and the solid boundary [122, 121].

In the case of hydrophobic surfaces, van der Waals attractive forces dominate leading to small or negligible slip velocities. For hydrophilic surfaces, net repulsive interactions between the microgels and the surfaces allow the formation of a lubricating film of water between the wall and the particles resulting in large slip velocities (figure 4.4). Adding a roughness on the surface of the order of the size of the microgel beads suppresses slippage phenomena. This is used during rheological measurements.

4.1.2 A brief review on experiments performed on soft glassy materials flows

Well controlled experiments have been recently carried out on the flows of jammed materials. It renewed our knowledge on the behaviour of soft glassy materials.

Isa *et al.* have driven dense colloidal suspensions in square microchannels (side: 20 particles diameter) and measured the velocity profiles of the suspensions [82]. The walls

of the microchannels were either smooth or rough (roughness ≈ bead size). They found different velocity profiles depending on the boundary condition (rough or smooth walls, see figure 4.5 (a)) and in both cases, the velocity profiles could not be predicted by the bulk rheology. In fact, at all flow rates, the central plug width remained constant, while giving their flow parameters, they should have observed a complete yielding through the channel. Their experimental results were explained quantitatively by using a model where the flow is dominated by interparticle friction and where stress fluctuations in the sample could locally exceed the yield stress. They found that the stress fluctuations were controlled only by what happened at the boundaries. They mention the possible role played by the confinement on the effects observed.

A series of experiments with concentrated emulsions evidenced in details the role played by the confinement on the deviations from the bulk rheology. The flows of concentrated emulsions [65, 67] and of carbopol gels [61] in a confined system with rough walls, gave velocity profiles that were faster and more "rounded" than what was expected from the bulk rheology (see figure 4.5 (b)). Indeed, the material is sheared in the part of the channel where the stress is below the yield stress, there is a fluidization effect. This effect was observed in channels sizes up to 40-diameter beads, above there was no fluidization observed. In both experiments, they observed that the effect of fluidization occurred when the walls of the channel were rough. The velocity profiles were explained theoretically by the non-local fluidity model (phenomenological expression of the KEP model, see 2.1.1). The cooperative length ξ, which represents the size of a zone impacted by a local rearrangement, has been shown to be intrinsic to the material.

A complementary study using molecular dynamics simulations was carried out. In this numerical experiment, the jammed material is sheared and the stress applied is progressively decreased up to the point at which the flow stops. These flow arrest experiments showed that the stress threshold value for the flow to stop depended on the confinement and increased above the yield stress value as the confinement decreases [28]. This observation was explained by the presence of cooperativity in the system.

More recently, concentrated emulsions were driven in channels with various moderate levels of roughness such that slippage is still present [112, 113]. As shown on figure 4.6 (a), they observed that the fluidity at the walls varied non monotonically with the wall roughness. This was presumably due to an ordering of the droplet near the walls. When particles are ordered, it increases the fluidity. They also suggested that ordering depends on the polydispersity of the system.

In the case of attractive laponite suspensions, it has been shown that yielding transition in a wide Couette cell strongly depended on the boundary condition: rough or smooth surfaces [63]. In the case of rough walls, the results were consistent with previous studies. But in the case of smooth walls, the samples were highly heterogeneous: both solid like and fluidized regions were present over long times. The authors identified a length scale representing the size of the solid like zones and they wondered if this length scale could be related to the cooperative length ξ.

Note that other experiments with jammed suspensions in confined channels did not evidence cooperative effects. It has been argued by Mansard *et al.* [113] that it was because no ordering near the surface could take place.

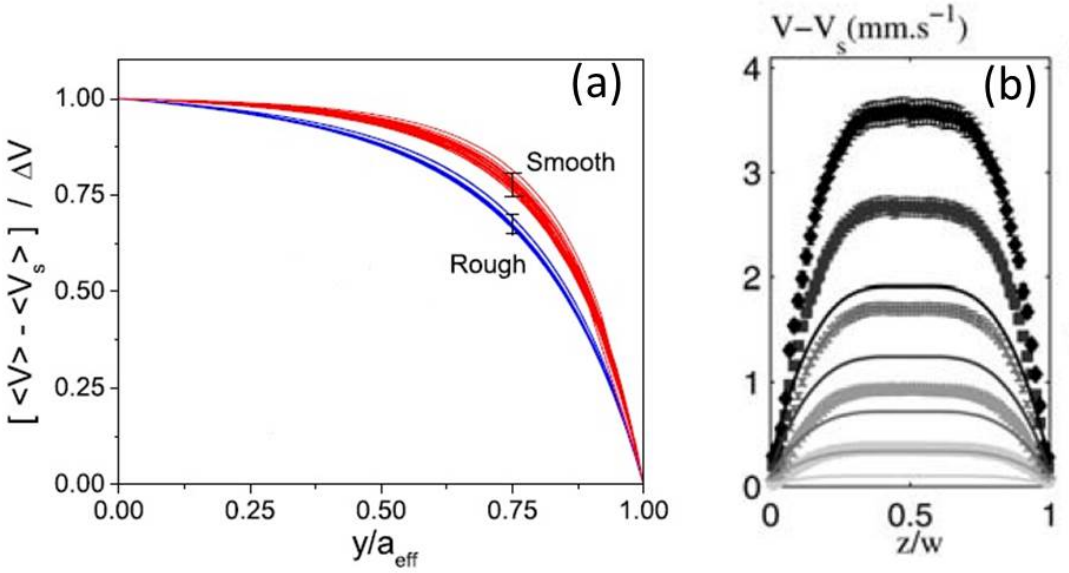

Figure 4.5 – (a) Figure adapted from [82]. Fitting of the velocity profiles V corrected for the slip velocity V_s and normalized by the difference between the central plug velocity V_c and the slip velocity: $\Delta = V_c - V_s$. The curves are plotted versus the effective half width of the channel a_{eff}, which takes into account the roughness of the walls. The data, for all flow rates, collapse onto two master curves for rough (blue) and smooth (red) walls. (b) Figure adapted from [67]. Velocity profiles corrected from the slip velocity for a concentrated emulsion (volume fraction of 0.7) in a w =250 µm thick microchannel with rough surfaces versus the reduced coordinate z/w. The lines represent the Herschel-Bulkley predictions.

Finally, deviations from the expected bulk rheology have been shown in cases where the flow is unconfined and where the surfaces have different chemistries. Seth *et al.* measured the velocity profiles of dense emulsions and of microgel suspensions in rotational shear flows. The top surface was rough to prevent slippage. If the same conditions held for the bottom plate, no deviation from the bulk rheology was observed. The nature of the bottom surface was changed to develop repulsive or attractive interactions with the emulsions or the microgel suspensions. Figure 4.6 (b) shows the case of a microgel suspension flowing between a rough surface on the top and an attractive surface at the bottom. We see that the flow profiles were deformed near the attractive surface, they were curved instead of being linear. The rheology was interpreted as non-local and has been characterized by a length scale much larger than the particle size. But, in contrast with [65], here this length scale was not intrinsic to the material: it depended both on the material properties and on the slip layer mechanism (EHD lubrication).

4.2 Experimental study of Herschel-Bulkley fluids in channels with slip heterogeneities

We carry out a series of µPIV experiments where we measure velocity profiles of microgel suspensions in microchannels. We vary the sizes of the microchannels as well as the wall properties to obtain different structures of the velocity profiles. We are able to tune the surface properties of the channel to change the amplitude of slip of the microgel suspensions. Finally we provide a theoretical interpretation of the observations.

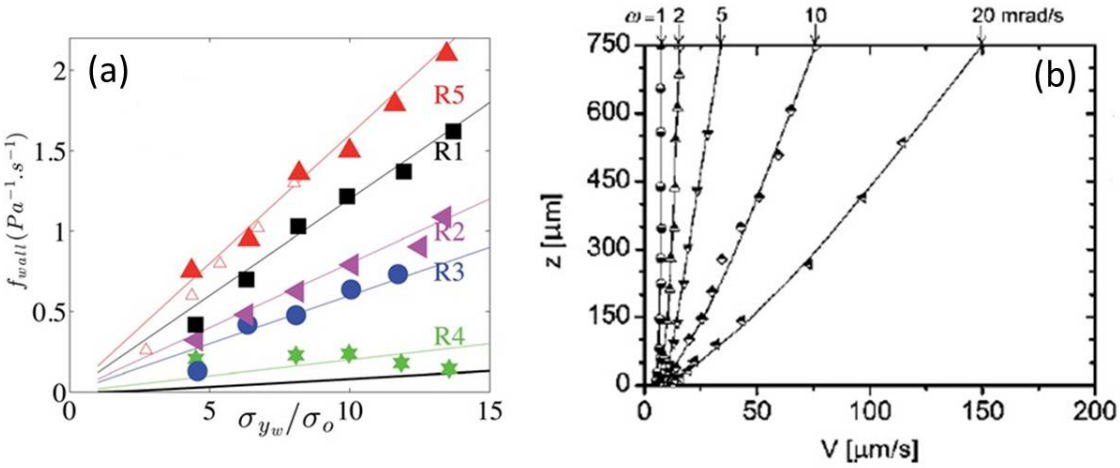

Figure 4.6 – (a) Figure adapted from [113]. Non monotonic variation of the wall fluidity with the roughness of the channels walls versus the reduced stress. The open red triangles and the solid black line at the bottom correspond respectively to the experiments of [67] and to the Herschel-Bulkley bulk fluidity. (b) Figure reproduced from [163]. Velocity profiles of a microgel suspension sheared between a rough surface (top, suppressing slip) and a smooth surface with a cationic silane coating (bottom, attractive surface). The shear rates are different between the two surfaces.

4.2.1 Velocity profiles

We have measured velocity profiles for different channel heights, surface chemistries, and pressure drops. It is convenient to define $V_{s,1}$ and $V_{s,2}$ as the slip velocities at the bottom and top surfaces respectively, and $V_{s,min}$ as the minimum of $V_{s,1}$ and $V_{s,2}$. Figure 4.7 shows the variations of $V - V_{s,min}$ across the channel for each experimental condition.

For $h = 100\,\mu m$ (Fig. 4.7 (a)-(c)), the velocity profiles have the symmetric shape expected for yield stress fluids: a central unyielded plug between two fluidized layers near the walls.

For h =50 µm and 20 µm, similar observations are made when both walls are hydrophilic, figures 4.7 (d) and 4.7 (g), respectively.

However, when the walls are different, the velocity profiles are asymmetric (Figs. 4.7 (f) and (h)). For $h = 20\,\mu m$, a remarkable behaviour appears: the fluidized layer adjacent to the hydrophilic wall starts to disappear in figure 4.7 (h), and finally the unyielded region extends down the wall in figure 4.7 (i).

4.2.2 Slip velocities

The slip velocity corresponds to the velocity of the first layer of beads near the wall. Seth *et al.* [163] showed that above the yield stress, the slip velocity varies linearly with the applied shear stress. In our experiments, two slip velocities are extracted from each velocity profile.

The slip velocities measured in hydrophilic channels are represented in figure 4.8 (a) for symmetric and asymmetric velocity profiles. Globally they increase linearly with the reduced stress.

For channels built with an important wettability contrast between the surfaces (20°-110°), the data are plotted on figure 4.8 (b) for symmetric (100 µm) and asymmetric velocity profiles ($h < 100$ µm). In the case of symmetric profiles (orange circles), the slip velocities seem closer to the hydrophilic data than to the hydrophobic data.

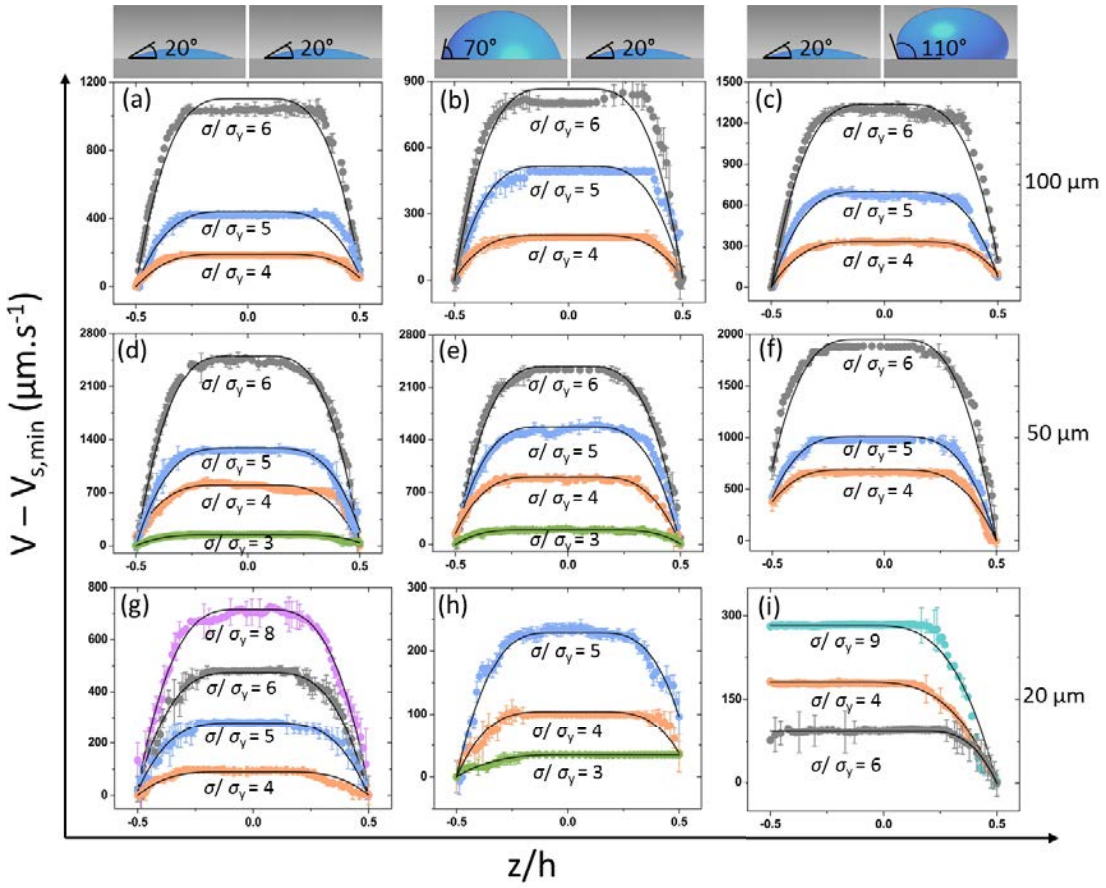

Figure 4.7 – Velocity profiles V corrected from the slip velocity $V_{s,min}$ for various heights, boundary conditions, and reduced stress $\sigma/\sigma_y = 9$ (dark cyan), 8 (purple), 6 (gray), 5 (blue), 4 (red), 3 (green). The solid lines are the best fits to the theoretical expression of the velocity profiles calculated in the asymmetric Herschel-Bulkley flow model 4.2.3.

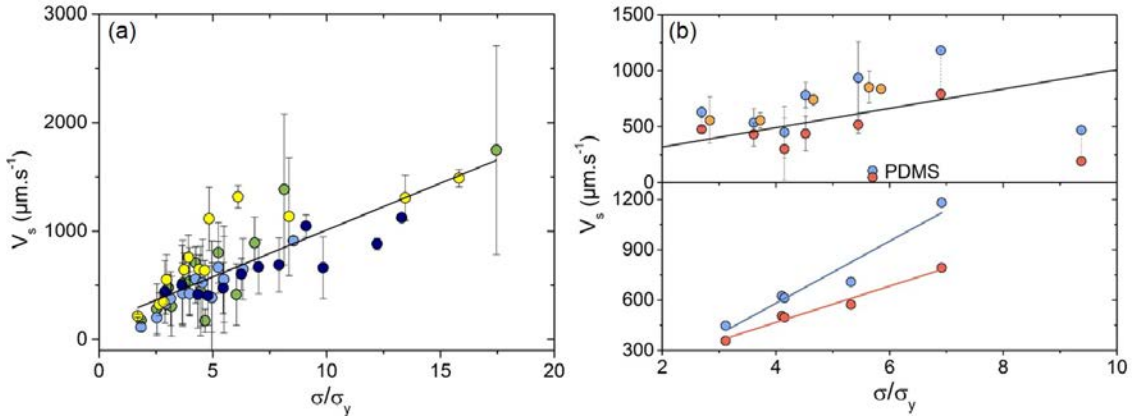

Figure 4.8 – Slip velocities measured in the channels for all the experiments (heights, reduced stress and boundary conditions). (a) Slip velocities extracted from symmetric velocity profiles in symmetric channels 20° - 20° (dark blue), asymmetric velocity profiles in asymmetric channels 20° (light blue) - 70° (green), symmetric velocity profiles in asymmetric channels 20° - 70° (yellow). The black solid line is a linear fit of all the slip velocities on the graph. (b) Top: Slip velocities in asymmetric channels 20° - 110° for which symmetric velocity profiles (orange: same slip velocity on both sides) or asymmetric velocity profiles were obtained (blue: 20° and red: 110°). The black solid line is the linear fit from the data of (a). Bottom: slip velocity for only one channel: slip velocities are larger on the hydrophilic side (blue) than hydrophobic side (red). Solid lines show linear fits.

When we focus on the slip velocities obtained in a single channel, we find that the slip velocities at the hydrophilic surface are larger than those at the hydrophobic surfaces (Figure 4.8 (b) bottom) as it is expected (see 4.1.1).

The glass slides and coverslips are used without surface treatment or are just plasma treated. The hydrophobic treatment is performed by silanization in vapor phase. These treatments allow to tune the magnitude of the slip within a channel, but it is difficult to have a good reproducibility of the slip velocities from one system to the other. Indeed, on figure 4.8 (a) we can see the spreading of the slip velocities over all the systems.

4.2.3 Asymmetric Herschel-Bulkley model

To interpret the results of figure 4.7, we solve the flow equations for a yield stress fluid driven by a pressure gradient G along the x direction, between two infinite surfaces of length L at $z = -h/2$ and $z = h/2$, where the slip velocities are $V_{s,1}$ and $V_{s,2}$ respectively. We place ourselves in the frame of reference translating at the mean slip velocity $(V_{s,1}+V_{s,2})/2$. In this frame of reference, the walls move with opposite velocities $\pm U_s$ where $U_s = (V_{s,1} - V_{s,2})/2$ (Fig. 4.9).

From the momentum equation 2.5, we get the local shear stress $\sigma(z) = \sigma_s - Gz$, where $G = \Delta P/L$ is the pressure gradient and σ_s is a non-zero constant which is due to the fact that the walls are moving at opposite velocities. Here the fluid obeys the Herschel-Bulkley constitutive equation $\sigma = \sigma_y + k\dot{\gamma}^n$ where σ_y is the yield stress, k the consistency parameter and $n = 1/2$. Using this constitutive equation and the expression of $\sigma(z)$ we calculate by solving $\sigma(z) = \sigma(\dot{\gamma})$ over the three different regions: $-h/2 < z < z_1$ where $\dot{\gamma} > 0$, $z_1 < z < z_2$ where $\dot{\gamma} = 0$ and $z_2 < z < h/2$ where $\dot{\gamma} < 0$. z_1 and z_2 denotes the positions of the yield surfaces separating the central plug flow and the fluidized regions At $z = z_1$ and $z = z_2$, we have $\dot{\gamma}(z) = 0$ leading to $z_1 = (\sigma_s - \sigma_y)/G$ and $z_2 = (\sigma_s + \sigma_y)/G$. After integration of the stress equation in each region with the appropriate boundary conditions: $U(z_1) = U(z_2)$, $U(h/2) = -U_s$ and $U(h/2) = U_s$, we obtain (see figure 4.9):

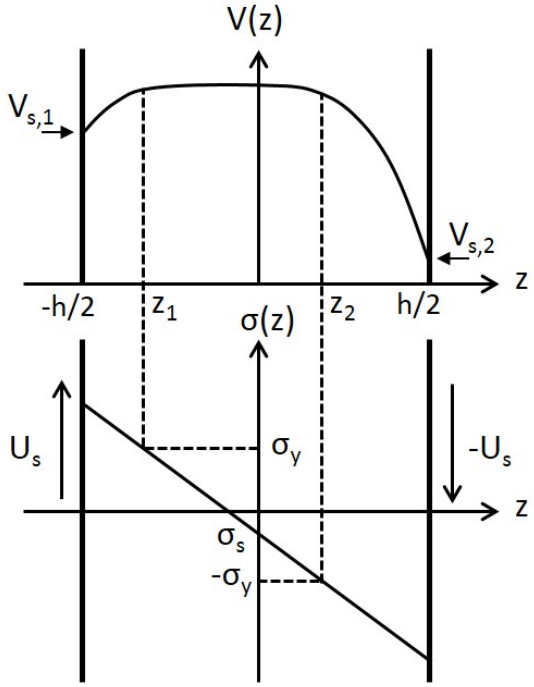

Figure 4.9 – Representation of an asymmetric velocity profile (top) and the corresponding stress variation across the microchannel (bottom).

$$\begin{cases} U(z) = \frac{G^2}{3k^2}\left[-(z_1-z)^3 - \frac{1}{2}\left(z_2-\frac{h}{2}\right)^3 + \frac{1}{2}\left(z_1+\frac{h}{2}\right)^3\right], & -\frac{h}{2} < z < z_1 \\ U(z) = \frac{G^2}{3k^2}\left[-\frac{1}{2}\left(z_2-\frac{h}{2}\right)^3 + \frac{1}{2}\left(z_1+\frac{h}{2}\right)^3\right], & z_1 < z < z_2 \\ U(z) = \frac{G^2}{3k^2}\left[(z_2-z)^3 - \frac{1}{2}\left(z_2-\frac{h}{2}\right)^3 + \frac{1}{2}\left(z_1+\frac{h}{2}\right)^3\right], & z_2 < z < \frac{h}{2} \end{cases} \tag{4.2}$$

z_1 and z_2 are related through the following relations:

$$\begin{cases} U_s = \frac{G^2}{3k^2}\left[-\frac{1}{2}\left(z_2-\frac{h}{2}\right)^3 + \frac{1}{2}\left(z_1+\frac{h}{2}\right)^3\right] \\ z_2 - z_1 = \frac{2\sigma}{Gh} \end{cases} \tag{4.3}$$

These expressions can be made dimensionless by using the scaling variables $\bar{U} = U/\left(G^2h^3/3k^2\right)$, $\xi = z/h$, $\bar{\sigma} = \sigma/Gh$:

$$\begin{cases} \bar{U}(\xi) = -(\xi_1-\xi)^3 - (\xi_2-1/2)^3/2 + (\xi_1+1/2)^3/2, & -1/2 < \xi < \xi_1 \\ \bar{U}(\xi) = (\xi_1+1/2)^3/2 - (\xi_2+1/2)^3/2, & \xi_1 < \xi < \xi_2 \\ \bar{U}(\xi) = (\xi_2-\xi)^3 - (\xi_2-1/2)^3/2 + (\xi_1+1/2)^3/2, & \xi_2 < \xi < 1/2 \end{cases} \tag{4.4}$$

where ξ_1 and ξ_2 are the solutions of:

$$\begin{cases} -(\xi_2-1/2)^3/2 + (\xi_1+1/2)^3/2 = \bar{U}_s \\ \xi_2 - \xi_1 = 2\bar{\sigma_y} \end{cases} \tag{4.5}$$

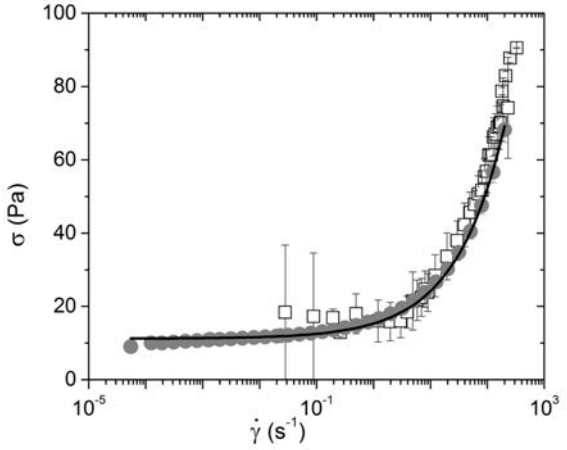

Figure 4.10 – Shear stress versus shear rate for $C = 0.016$ g/g: closed gray circles, macroscopic measurements; open black squares, data extracted from the velocity profiles shown in figures 4.7 (g)-(h); and solid line, best fit to the Herschel-Bulkley equation ($\sigma_y = 11.2$ Pa, $n = 0.5$, and $k = 4.1$ Pa s$^{1/2}$).

The above equations can also be used to describe the velocity profiles composed of a plug region which extends down to the hydrophilic wall (high slip) and a sheared region near the hydrophobic wall (low slip) (see fig. 4.7 (i)). The velocity profiles are given by:

$$\begin{cases} U(z) = \frac{G^2}{3k^2}\left[-\frac{1}{2}\left(z_2 - \frac{h}{2}\right)^3\right], & -\frac{h}{2} < z < z_2 \\ U(z) = \frac{G^2}{3k^2}\left[-(z_2 - z)^3 - \frac{1}{2}\left(z_2 - \frac{h}{2}\right)^3\right], & z_2 < z < \frac{h}{2} \end{cases} \tag{4.6}$$

where z_2 is given by:

$$U_s = \frac{G^2}{3k^2}\left[\frac{1}{2}\left(z_2 - \frac{h}{2}\right)^3\right] \tag{4.7}$$

Or in dimensionless form:

$$\begin{cases} \bar{U}(\xi) = -\bar{U_s}, & -1/2 < \xi < \xi_2 \\ \bar{U}(\xi) = (\xi_2 - \xi) + \bar{U_s}, & \xi_2 < \xi < 1/2 \end{cases} \tag{4.8}$$

where $\bar{U_s} = -1/2\,(\xi_2 - 1/2)^3$.

We have analyzed the experimental velocity profiles shown on figure 4.7 using the predictions of the asymmetric Herschel-Bulkley flow model. In practice, U_s is calculated from $V_{s,1}$ and $V_{s,2}$. k and σ_y are the parameters of the macroscopic HB equation. The predictions from the model are plotted in 4.7 for comparison with experiments. In Figs. 4.7 (a) - (g), the agreement is quantitative within a standard deviation of about 15 % for k. The local flow curves deduced from the velocity profiles and the macroscopic flow curve coincide, which further confirms the validity of the model (figure 4.10).

In figure 4.7 (i) and (h), the theoretical velocity profiles also reproduce the shape of the experimental plots but to get quantitative agreement we allow larger deviations of k. Nevertheless, we can conclude that our generalized model successfully captures the observed phenomena.

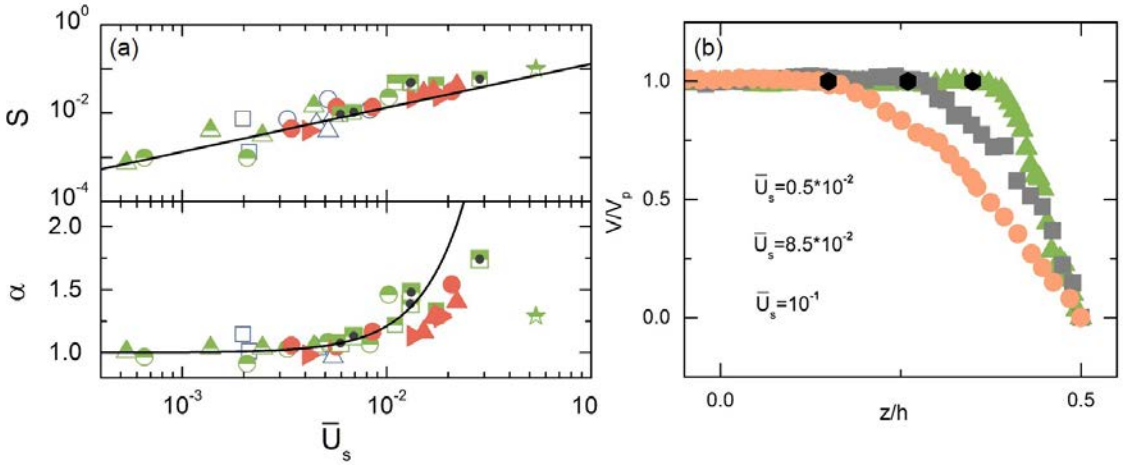

Figure 4.11 – (a) Asymmetry parameter S and velocity ratio α versus slip number $\bar{U}_s$ for different confinements 7 µm, 20 µm, 50 µm, 75 µm, and 100 µm; boundary conditions 20°-20° (blue open symbols), 20°-70° (green half-full symbols), and 20°-110° (red closed symbols); and microgel concentrations 0.016 g/g (symbols without a dot) and 0.022 g/g (dotted symbols). (b) Detail of velocity profiles near the low-slip hydrophobic surface showing slip-induced fluidization. Velocity profiles are scaled by the central plug velocity. The black dots point to the crossover between the central plug and the fluidized layers.

4.3 Discussion

We define a dimensionless number $\bar{U}_s$ from the theoretical description presented in 4.2.3. It is shown that $\bar{U}_s$ which compares slip heterogeneities effects with viscous forces, controls the flow structure. We generalize our results by defining a length scale l^* below which the flow structure is controlled by slip heterogeneities. We also compare our results with the cooperative theory and we discuss the case of the truncated plug flow profiles.

4.3.1 Scaling analysis

The velocity profiles given by equation 4.4 depend on two dimensionless numbers, $\bar{U}_s$ and $\bar{\sigma_y}$. $\bar{\sigma_y}$ is the non dimensional yield stress defined previously. $\bar{U}_s$ is a new dimensionless number, the slip number, which represents the ratio of the velocity associated with slip heterogeneities to the bulk velocity. When $\bar{U}_s$ is small, bulk forces dominate and the velocity profiles are symmetric. When $\bar{U}_s$ is large, the velocity profiles are significantly affected by wall slip heterogeneities and become asymmetric. In the asymptotic limit where $\bar{U}_s \to \infty$, the flow structure is entirely dominated by slip effects and the flow is a pure shear flow.

From our theory, we make two interesting predictions. First, the flow structure is controlled by the slip number $\bar{U}_s$. To test this prediction, we define two new quantities which characterize the alteration of the velocity profiles due to slip heterogeneities. $S = (\xi_1 + \xi_2)/2$ measures the asymmetry in the positions of the yield surfaces; $\alpha = V_p/U_p$ represents the ratio between the plug flow velocity measured experimentally and that computed from the model for a symmetric flow profile. The variations of S and α for the velocity profiles shown in figures 4.7 (a)-(h) are plotted against the slip number $\bar{U}_s$ in figure 4.11 (a).

All the data collapse on master curves showing that both S and α are unique functions

of $\bar{U_s}$. For small $\bar{U_s}$ values, the model predicts that $S{\approx}3\bar{U_s}/4$ and $\alpha{\approx}\bar{U_s}^2$, which agrees well with the experimental results as shown by the full lines on figure 4.7. We consider that the deviations from the symmetrical Herschel-Bulkley model become significant above $\bar{U_s} \sim 10^{-2}$ where S and α have changed by about 10 %.

The second prediction is that the region close to the hydrophobic wall (low slip velocity) tends to fluidize when $\bar{U_s}$ increases. Fluidization is clearly visible in figure 4.11 (b) for the case of the profiles shown in figure 4.7 (i). The sheared region adjacent to the hydrophobic wall becomes thicker and the unsheared plug is reduced. Slip induced fluidization is caused by the important shear rates that develop at the hydrophobic wall as a consequence of the large slip velocities at the hydrophilic wall.

4.3.2 Channel size criterion

In this section, we derive the general expression of a characteristic length scale which sets the size below which slip heterogeneities control the entire bulk flows. The slip number which characterizes the importance of the slip heterogeneities with respect to the driving forces can be written as:

$$\bar{U_s} = (l^*/h)^2 \tag{4.9}$$

In this expression l^* is a mesoscopic length scale which has the expression $l^* = (U_s\mu/G)^{1/2}$ where $\mu = k^2/Gh$ is the characteristic viscosity at the wall. The ratio $(l^*/h)^2$ compares the viscous stress induced by slip heterogeneities to the applied pressure stress. When $h >> l^*$, the driving forces control the flow structure whereas for $h << l^*$, slip heterogeneities dominate. In our experiments, the transition occurs around $l^* \sim h/10$ (see fig. 4.11 (a)). The values for l^* range between 0.5 and 8 µm, which correspond to 1 to 15% of the channel height.

Let us show that the existence of this length scale can be generalized to fluids obeying any other constitutive equation. Above, we have expressed the shear stress as $\sigma(z) = \sigma_s - Gz$. This formula can be rewritten in the form $\sigma(z) = G(-z + \lambda)$ where λ has the dimension of a length. We consider a general constitutive law $\dot{\gamma} = f(\sigma)$ characterizing non-Newtonian fluids without yield stress. The domain of definition of f includes positive and negative values of σ and f is an odd function of σ. For the flow geometry considered in this paper, we have:

$$\dot{\gamma} = \frac{dU}{dz} = f\left[G(-z + \lambda)\right] \tag{4.10}$$

When $\lambda << h$, $-z + \lambda$ can be approximated by $-z$ (except in a region of negligible size) and the solution $U(z)$ gets close to the symmetric solution obtained when the slip velocity difference is $U_s = 0$. When $\lambda >> h$, $\dot{\gamma}$ tends to a constant and the flow is similar to a pure shear flow. The cross over between the two regimes occurs for $\lambda \sim h$. To connect λ to U_s, we carry out a Taylor expansion of $\dot{\gamma}$ at small λ/h assuming that it remains valid on order of magnitude for $\lambda/h \sim 1$:

$$\dot{\gamma} = f(-Gz) + \lambda \left.\frac{\partial f}{\partial \lambda}\right|_{\lambda=0} + \mathcal{O}\left(\lambda^2\right) \tag{4.11}$$

Since f is a function of $(-z + \lambda)$, we have $\frac{\partial f}{\partial \lambda} = \frac{\partial f}{\partial z}$. Integrating 4.11 with respect to z leads to the following expression for $U(z)$, which is valid for small λ:

$$U(z) \approx \hat{f}(-Gz) + \lambda f(-Gz) \tag{4.12}$$

$\hat{f}$ is a primitive function of f. Since $U(\pm h/2) = \pm U_s$ we obtain:

$$\begin{cases} U_s \approx \hat{f}\left[-G\frac{h}{2}\right] + \lambda f\left[-G\frac{h}{2}\right] \\ -U_s \approx \hat{f}\left[G\frac{h}{2}\right] + \lambda f\left[G\frac{h}{2}\right] \end{cases} \tag{4.13}$$

Since f is odd and $\hat{f}$ is even, we obtain from 4.13:

$$U_s \approx \lambda \dot{\gamma}_w \tag{4.14}$$

where $\dot{\gamma} = f\left(-G\frac{h}{2}\right)$ is the wall shear rate when $U_s = 0$.

λ is a new characteristic length scale, equivalent to the Navier length, which is built on the slip velocity difference U_s. To be consistent with our analysis for HB fluids, it has to be of the form: $\lambda = l^{*2}/h$ and the cross over between the two regimes is given by $l^* \sim h$. Interestingly l^* can also be expressed as $l^* = \sqrt{\lambda h}$. This general form can be used to quantify the role of slip heterogeneities on the flow of any materials like concentrated emulsions, Newtonian liquids, polymers and shear banded fluids in confined geometries.

4.3.3 Does cooperativity effects come into play?

This section concerns cooperativity effects which have been found to influence the flow of glassy suspensions in microchannels [65, 61]. We check that adding a cooperative term to our model does not improve the agreement between the predictions and the experimental results.

We hypothesize that the confinement in the microchannels tested up to now is too low to induce measurable cooperative phenomena. Indeed, in previous studies, the maximal confinement at which cooperative effects were observed was 40 layer of particles [66].

Therefore we performed experiments in smaller channels, the height is 7 µm which corresponds to 14 layers of microgels beads. This confinement should be sufficient to observe cooperativity due to inhomogeneity of the shear stress across the height of the channel. The system has a glass surface on one side, and a NOA surface on the other side, the system is treated with UV/ozone to make it totally hydrophilic. The pressure drops applied ranged from 2.5 bar to 5 bar. The same experiment is also carried out with surface heterogeneities: one side was untreated NOA, the other one glass. The velocity profiles obtained are shown in figure 4.12.

Even if the amplitude of the asymmetry is not the same, in both cases, the velocity profiles are asymmetric. Indeed, slip depends highly on the local surface properties. At these scales we cannot guarantee that the surface are homogeneous, and the smallest heterogeneity has immediately a great impact on the velocity profile.

Difficulties arise when we fit the velocity profiles with the cooperative model. The model predicts that the material is fluidized in the central part of the channel where the stress is below the yield stress, which results in a shorter plateau. But we observe on figure 4.12 that the widths of the plateau are closer to the Herschel-Bulkley predictions than to the cooperative model.

To conclude this part, it appears that we have found no indication that cooperative phenomena play a role in our system.

4.3.4 Truncated plug flow profiles

We showed previously (4.2.3) that the case of the truncated plug flow profiles (Figure 4.7 (h) and (i)) could be described by the asymmetric model only qualitatively. We extend

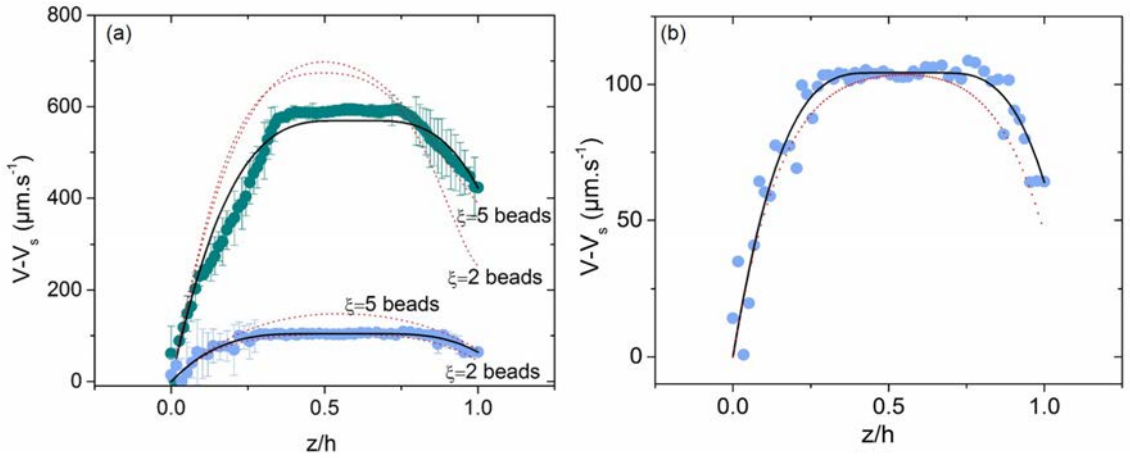

Figure 4.12 – (a) Velocity profiles V corrected from the slip velocity V_s in a channel of 7 µm height. The reduced stress $\sigma/\sigma_y = 9.6$ (dark cyan), 4.5 (blue). The boundary conditions are 20°-70° for the top curve and 20°-20° for the bottom cuve. The black solid lines are the best fits to the theoretical expression of the velocity profiles calculated in the asymmetric Herschel-Bulkley flow model. The dashed red lines are the theoretical expression calculated from the cooperative model, where the bulk fluidity and the boundary condition are equal to the asymmetric Herschel-Bulkley model of the profiles. (b) Closer look to the bottom curve of (a).

the analysis of this particular case here. With the Herschel-Bulkley asymmetric model, we predict theoretically the onset of the truncated plug flow profiles as a function of $\bar{U_s}$ and $\bar{\sigma_y}$ and we compare the results to the experiments.

The model gives the two coordinates ξ_1 and ξ_2 as a function of the dimensionless numbers $\bar{U_s}$ and $\bar{\sigma_y}$:

$$\begin{cases} \bar{U_s} = \frac{1}{2}\left(\xi_2 - \frac{1}{2}\right)^3 + \frac{1}{2}\left(\xi_1 + \frac{1}{2}\right)^3 \\ 2\bar{\sigma_y} = \xi_2 - \xi_1 \end{cases} \tag{4.15}$$

We solve system 4.15 and we look at the limiting cases where $\xi_1 = -1/2$ or $\xi_2 = 1/2$, which correspond to the truncated plug flow configuration.

Figure 4.13 (a) shows that all the points are below the solid line which confirms that the model does not predict the right values for $\bar{U_s}$ and $\bar{\sigma_y}$ to obtain a truncated plug flow shape. Figure 4.13 (b) represents the fact that the truncated plug flow profiles exhibit a wider plateau area than the yield stress value of the microgel. This is consistent with the fact that the model is not in quantitative agreement with the truncated plug flow profiles: in the model, the plateau width is equal to the yield stress of the microgel, which is obviously not the case here.

We generalize this statement with the results obtained in a channel where a rough wall suppresses the slip on the surface (see figure 4.14 (a)). At the opposite wall the microgel slips. Figure 4.14 (b) shows the detail of a truncated plug flow profiles obtained in a channel of height 80 µm. As the pressure gradient is increased, the difference in slip velocities increases, and we observe that the dimensionless number $\bar{U_s}$ stays constant.

It seems that, whatever the pressure gradient applied, the size of the sheared area does not vary. This effect is reminiscent of the flow near a plate that is withdrawn or immersed in a bath filled with a yield stress fluid [21, 108]. Indeed, the authors observe that the thickness of the sheared layer increases very slowly with the velocity of the plate.

We confirm that the shape of the truncated velocity profiles is recovered by the model

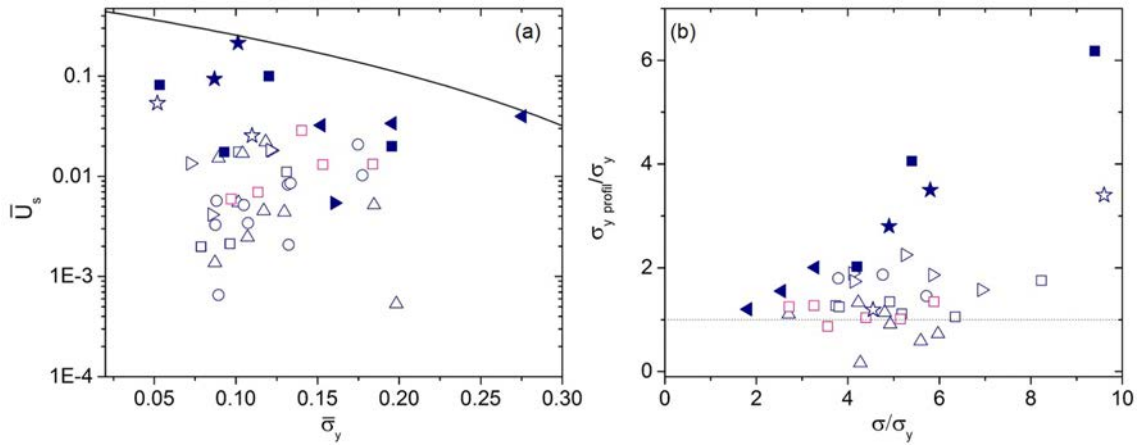

Figure 4.13 – Asymmetric and symmetric velocity profiles (open symbols) and truncated plug flow profiles (filled symbols) for different confinements 7 µm (☆), 20 µm (□), 50 µm (△), 75 µm (▷), and 100 µm (○) and microgel concentrations 0.016 g/g (blue) and 0.022 g/g (pink). Experiments with a rough surface are performed in channel of height 82 µm (◁). (a) The map $\bar{U_s}$ - $\bar{\sigma_y}$. The solid black line represents the theoretical prediction for the onset of the truncated plug flow shape: above the line. (b) Ratio of the yield stress measured on the experimental velocity profiles to the yield stress measured in the rheometer as a function of the reduced stress σ/σ_y.

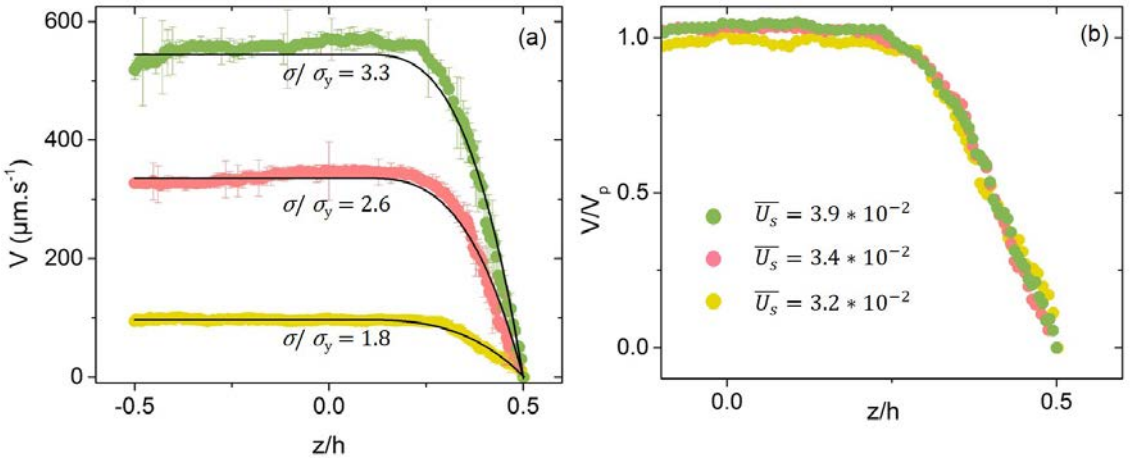

Figure 4.14 – (a) Truncated plug-flow profiles in an asymmetric channel (slip - no slip) at various reduced stress: 1.8 (yellow), 2.6 (pink), 3.3 (green). The solid lines are the best fits to the theoretical asymmetric Herschel-Bulkley profiles. (b) Truncated plug-flow profiles near the rough no slip surface. The velocity profiles are scaled by the central plug velocity.

but it still exists a quantitative discrepancy. We suggest that the origin of the discrepancy is related to the disappearance of the fluidized layer near the wall. Instead a plastic material is in direct contact with the wall and solid friction takes place which is not described by the model.

4.4 Conclusions

We carried out a series of velocity profiles measurements in microchannels for which we tuned the magnitude of the slip velocity at the walls.

We have demonstrated the importance of taking into account slip heterogeneities on the flows of jammed materials in confined systems. We note also that the effect of asymmetry of the velocity profiles is observed in large channels compared to the size of the beads (up to 150 layers of beads) when surface heterogeneities are important. In extreme cases, we observe truncated plug flow profiles where the plug area extends down to the more slippery wall.

We presented an asymmetric Herschel-Bulkley model that describes qualitatively all the velocity profiles observed in system. More interestingly, we could generalize the result obtained by introducing a length scale l^*, valid for all fluids, below which slip heterogeneities dominate the flow.

Throughout this work, there was no indication that cooperative effects may play a role in our systems.

Dynamical role of slip heterogeneities in confined systems

✧ **Results**

- As the system size decreases and as the asymmetry between the surfaces increases, the velocity profiles become more and more asymmetric up to the point where the unyielded region extends down the wall.
- An asymmetric HB model is able to capture the shape of the velocity profiles observed. Quantitative agreement is found except for the case of the truncated plug flow profiles.
- We generalize the result obtained by introducing a length scale l^*, valid for all fluids, below which slip heterogeneities dominate the flow.
- There is no indication of cooperative effects in our system.

Dynamical role of slip heterogeneities in confined flows

Anne-Laure Vayssade,[1] Choongyeop Lee,[1] Emmanuel Terriac,[1] Fabrice Monti,[1] Michel Cloitre,[2] and Patrick Tabeling[1]

[1]*Laboratoire Microfluidique, MEMs et Nanostructures, ESPCI ParisTech, UMR Gulliver 7083, ESPCI, CNRS, 10 Rue Vauquelin, 75005 Paris, France*

[2]*Matière Molle et Chimie, UMR 7167 CNRS - ESPCI ParisTech, ESPCI, 10 Rue Vauquelin, 75005 Paris, France*

(Received 5 December 2013; published 16 May 2014)

We demonstrate that flows in confined systems are controlled by slip heterogeneities below a certain size. To show this we image the motion of soft glassy suspensions in microchannels whose inner walls impose different slip velocities. As the channel height decreases, the flow ceases to have the symmetric shape expected for yield-stress fluids. A theoretical model accounts for the role of slip heterogeneities and captures the velocity profiles. We generalize these results by introducing a length scale, valid for all fluids, below which slip heterogeneities dominate the flow in confined systems. General implications of this notion, concerning the interplay between slip and confinement, are presented.

DOI: 10.1103/PhysRevE.89.052309 PACS number(s): 83.50.Lh, 47.57.Qk, 83.50.Rp, 83.80.Kn

I. INTRODUCTION

Liquids are prone to slip at smooth surfaces [1,2]. The existence of wall slip is of particular interest for many technological processes including die extrusion of complex fluids, ink jet applications, and oil migration in porous media. The importance of slip is often characterized by the slip length, which is defined as the effective distance from the surface at which the no-slip condition is satisfied. Slip lengths of simple liquids lie in the nanometer range [3–5], but they are generally much larger for complex fluids such as wormlike micellar solutions [6,7], concentrated emulsions [8–10], foams [11,12], or colloidal suspensions [13–15]. Today, methods exist to account for the dynamical role of slip irrespective of its origin and control its occurrence in well-characterized laboratory-scale experiments [11,16]. Most of this knowledge applies to ideal situations where the surfaces are spatially uniform, in contrast to what is encountered in real environments where surface roughness and chemistry locally vary so that slip heterogeneities naturally exist. For pressure-driven Stokes flow of simple liquids, the dynamical role of slip heterogeneities has been evaluated in terms of an effective slip length varying with the system size [17]. Crucial questions concern the effect of slip heterogeneities on the global flow fields of a wide range of fluids.

In this article we demonstrate that ignoring spatial slip heterogeneities is acceptable in large systems, but increasingly incorrect as the characteristic flow size decreases. We report pressure-driven flow experiments conducted on well-characterized soft glassy materials flowing in microchannels in the presence of slip heterogeneities. These are created by tuning the short-range interactions between the particles of the fluids and the surfaces using appropriate surface treatments. Remarkably, we find that this albeit simple slip heterogeneity entirely controls the flow structure when the microchannel height decreases below a characteristic length l^*, which depends on the slip velocities and fluid properties. More generally, a similar length scale can be defined for all kinds of fluids moving in microfabricated or natural miniaturized systems, which opens predictive routes to control the structure and rheology of confined flows in the presence of slip heterogeneities.

II. EXPERIMENTS

A. Preparation of microgel suspensions

The working fluids used in this study are concentrated aqueous suspensions of microgel particles. Microgels suspensions can be viewed as the archetypical representatives of a wide class of colloidal fluids consisting of soft and deformable particles such as emulsions, vesicles, micelles, and star polymers [18]. Suspensions are prepared from polyelectrolyte microgels in water. The microgels were synthesized by standard emulsion polymerization at low pH ($\approx$2) from ethyl acrylate (64 wt. %), methacrylic acid (35 wt. %), and a bifunctional monomer as a cross-linker [19]. The polymer latexes obtained at the end of the synthesis were cleaned by ultrafiltration. The solid content of the stock suspension was determined by thermogravimetry. Solutions are prepared by dilution of the stock solution with ultrapure water. At low pH, the microgels are insoluble in water and behave as hard particles. The addition of sodium hydroxide ($1M$) causes the ionization of the methacrylic acid units. The osmotic pressure of the counterions then provokes the swelling of the microgels. In all the experiments reported in this study, the molar ratio of the added base to the available acid groups is around 1, so the totality of the carboxylic functions is neutralized. The particles have a hydrodynamic radius of 220 nm, with a polydispersity of 10%. The experiments reported below are performed at high volume fractions ($C =$ 0.016 and 0.022 g/g) where the suspensions exhibit yielding properties. The effective volume fractions of the microgels in these suspensions, $\varphi \approx 0.72$ and 0.85, were determined using the methodology described in [20,21].

The suspensions are seeded at low concentrations with 500-nm-diam fluorescent sulfonate-functionalized polystyrene tracers from Duke Scientific. The tracers are chosen to have a size comparable to that of the swollen microgels. They are added before swelling to ensure that they are uniformly dispersed in the suspension. Each tracer is in contact with many surrounding microgels so that it experiences the same sequence of dynamical events and moves at the same velocity as its neighbors [20]. After preparation the microgels are kept at rest for at least 24 h. Before each experiment, the suspension is loaded in the upstream reservoir and bubbles are carefully removed by gentle centrifugation.

 ©2014 American Physical Society

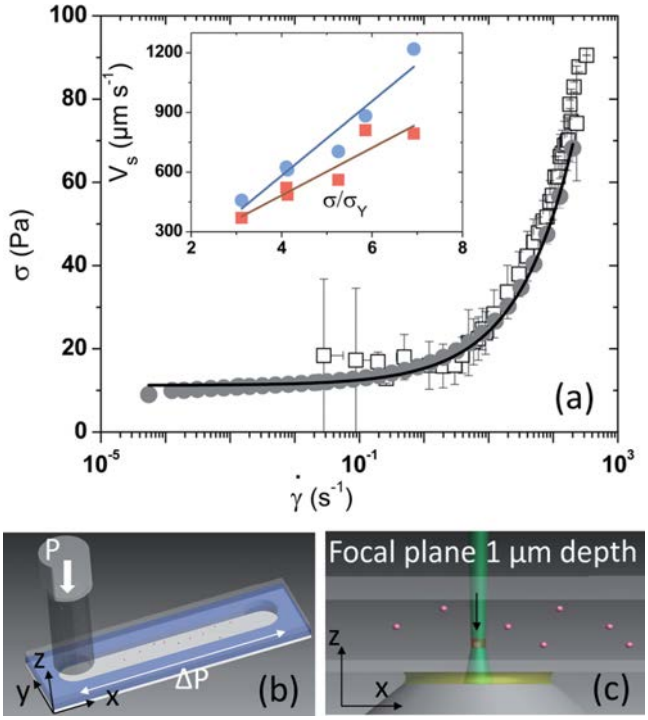

FIG. 1. (Color online) (a) Shear stress versus shear rate for $C = 0.016$ g/g: closed gray circles, macroscopic measurements; open black squares, data extracted from the velocity profiles shown in Figs. 2(g)–2(h); and solid line, best fit to the Herschel-Bulkley equation ($\sigma_y = 11.2$ Pa, $n = 0.50$, and $k = 4.1$ Pa s$^{1/2}$). The inset shows variations of the slip velocity with the reduced stress σ/σ_y at the hydrophilic (closed blue circles) and hydrophobic surfaces (closed red squares) of an asymmetric channel ($h = 75$ μm); solid lines show linear fits. (b) Experimental setup. (c) Sketch of the focal plane in the microchannel.

The bulk flow properties are measured using an Anton Paar MCR 501 rheometer. The shearing surfaces are sandblasted (surface roughness ≈2–4 μm) to suppress slip. The stress versus shear rate curves are well described by the Herschel-Bulkley (HB) equation $\sigma = \sigma_y + k\dot{\gamma}^n$, where σ_y is the yield stress, k is the consistency parameter, and $n = 0.50 \pm 0.02$ [Fig. 1(a)]. The rheological HB parameters obtained for the different samples that were studied are summarized in Table I. For all samples, the parameter n is equal to 0.5.

B. Fabrication of microchannels

The microfluidic device sketched in Fig. 1(b) is a rectangular microchannel, 1.5 mm wide, 7–100 μm high, and 1.3–5.8 cm long. It is made by assembling a glass coverslip and a glass slide, which constitute the bottom (left side of the velocity profiles presented in the following) and top surfaces (right side of the velocity profiles) of the microchannel, respectively. They have a residual roughness lower than 5 nm, which is much smaller than the size of the microgels. The coverslip and the slide were assembled with UV curable optical adhesive NOA81 from Norland, following a technique described elsewhere [22]. This produces high-rigidity devices that sustain the high pressures involved in the experiments (30–600 kPa) without appreciable deformation. In most cases, the variation of the channel height was less than the accuracy of the optical detection (1 μm). In only two cases (over 11 that were tested), the channel height was found to vary over about 2–3 μm, which remains negligible compared to its dimension. We also checked that the slide and the coverslip were parallel to one another by measuring the channel heights at different locations along the longitudinal and transverse directions. Again the standard deviation was smaller than 1 μm. The suspensions are driven using Fluigent MFCS pressure pumps. To reduce entry effects, we connect the upstream and downstream reservoirs directly onto the chip without any intermediate tubing.

TABLE I. Rheological parameters of microgel samples used in this study.

Sample	C (g/g)	σ_y (Pa)	k (Pa s$^{1/2}$)	Fig. 2
1	0.016	11	4.3	(g), (h)
2	0.016	16.2	5.3	(d), (e), (i) gray
3	0.016	15.6	5.1	(f)
4	0.016	9.4	4.5	(a), (b), (c), (i) red, (i) blue
5	0.022	61	10.8	not shown

We create basic slip heterogeneities by tuning independently the affinity of the walls for the microgels. Initially, the glass coverslips are partially hydrophobic with a contact angle against water in the range 70°–80°. Contact angles are measured with the sessile drop method. Similar values of the contact angle are obtained by coating the coverslips with a thin layer of optical resin [22]. Slides and coverslips are made hydrophilic (contact angle ≈20°) by oxygen plasma treatment. Hydrophobic glass slides (contact angle ≈110°) are prepared by silanization with trichloro (1H,1H,2H,2H–perfluorooctyl)silane in vapor phase [Fig. 2(f)]. In some cases, the glass slide was simply coated with a layer of polydimethylsiloxane [Fig. 2(i)].

The behavior of soft particles such as microgels at surfaces depends on short-range forces between particles and surfaces as described in [23,24]. In the case of hydrophobic surfaces, van der Waals attractive forces dominate, leading to small or negligible slip velocities. For hydrophilic surfaces, net repulsive interactions between the microgels and the surfaces allow the formation of a lubricating film of water between the wall and the particles resulting in large slip velocities. In the following, the different contact angles that have been achieved (20°, 70°–80°, and 110°) thus result in different slip velocities at the boundaries.

C. Implementation of particle image velocimetry

The velocity profiles $V(z)$ are measured using the microparticle image velocimetry setup depicted in Fig. 1(c) [25,26]. All measurements are performed far from the microchannel entrance where the velocity profiles are fully developed. We use an inverse microscope (Leica DM IRB) equipped with an oil immersion objective (×100, with a numerical aperture equal to 1.3). The probe tracers are excited using a laser beam ($\lambda = 532$ nm, 300 mW) modulated at frequency f (up to 30 kHz) with an acousto-optic modulator that transforms the continuous beam into a succession of light pulses. Images are

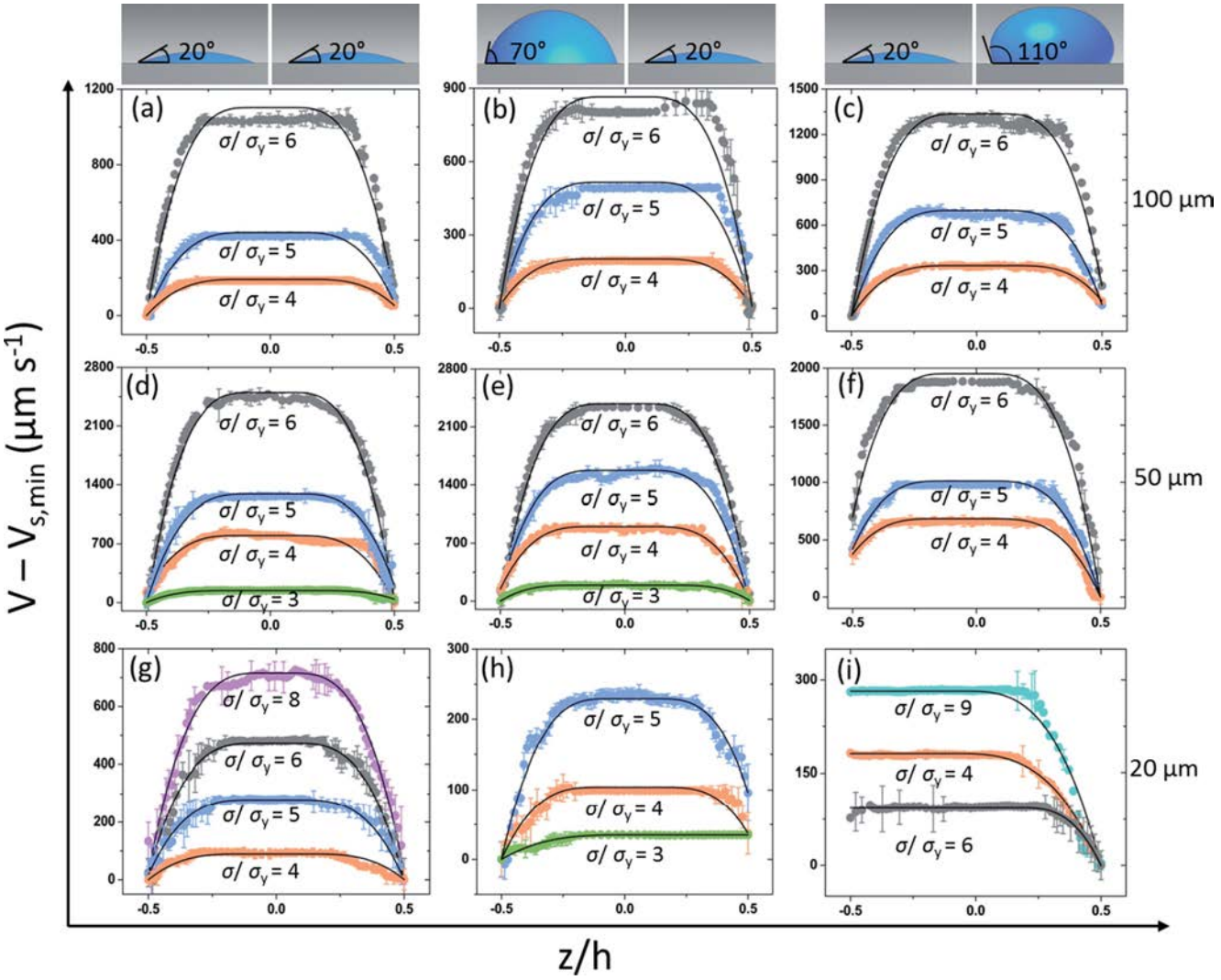

FIG. 2. (Color online) Velocity profiles V corrected from the slip velocity $V_{s,\min}$ for various heights, boundary conditions, and reduced stress $\sigma/\sigma_y = 9$ (dark cyan), 8 (purple), 6 (gray), 5 (blue), 4 (red), and 3 (green). The solid lines are the best fits to the theoretical expression of the velocity profiles calculated in the asymmetric Herschel-Bulkley flow model Eq. (3).

recorded by a CCD camera working in full frame transfer mode (640 × 480 pixels, Allied Vision Technologies), which allows us to collect sequences of pairs of images; two images in a pair are separated by a time interval that depends on the modulation frequency f.

The position of the focal plane in the microchannel is controlled by displacing the objective vertically using a piezotransducer (Physik Instrumente), with minimum steps of 0.25 μm and 10-nm accuracy. The actual z coordinate of the focal plane is obtained after correction of the mechanical position of the actuator by the refractive index of the solution ($n = 1.33$) and glass ($n = 1.51$). At each depth, we collect up to 40 pairs of images, each containing about four fluorescent tracers. The field of observation is a circular area with a diameter of 36 μm. The frequency f, the pulse duration, the delay time between two pairs of images, the steps of the piezotransducer, and the camera are synchronized electronically (EG, R&D Vision). The bottom and top surfaces are located by vertically scanning the channel and determining the positions where tracer particles adsorbed at the wall are observed.

Once images are obtained, they are processed to obtain the values of the local velocity. The data processing is implemented using a custom MATLAB code that applies a filter to the images to adjust the gray level of the fluorescent particles at a value of 150 and computes the cross correlation between images of the same pair. The accuracy of the image correlation is one pixel, i.e., 0.14 μm. Each point of the velocity profile corresponds to an average of up to 40 values. Error bars correspond to statistical deviations.

III. VELOCITY PROFILES

A. Experimental results

We have measured velocity profiles for different channel heights, surface chemistries, and pressure drops. As expected, the slip velocities at the hydrophilic surface are larger than those at the hydrophobic surfaces [Fig. 1(a) inset]. It is convenient to define $V_{s,1}$ and $V_{s,2}$ as the slip velocities at the bottom and top surfaces, respectively, and $V_{s,\min}$ as the

minimum of $V_{s,1}$ and $V_{s,2}$. Figure 2 shows the variations of $V - V_{s,\min}$ across the channel for each experimental condition. For $h = 100$ μm [Figs. 2(a)–2(c)], the velocity profiles have the symmetric shape expected for yield-stress fluids [27,28]: a central unyielded plug between two fluidized layers near the walls. For $h = 50$ and 20 μm, similar observations are made when both walls are hydrophilic [Figs. 2(d) and 2(g), respectively]. However, when the walls are different, the velocity profiles are asymmetric [Figs. 2(f) and 2(h)]. For $h = 20$ μm, a remarkable behavior appears: the fluidized layer adjacent to the hydrophilic wall starts to disappear in Figs. 2(h) and finally the unyielded region extends down the wall [Fig. 2(i)].

B. Asymmetric Herschel-Bulkley flow model

To interpret these results, we solve the flow equations for a yield stress fluid driven by a pressure gradient G in the x direction, between two infinite surfaces of length L at $z = -h/2$ and $h/2$, where the slip velocities are $V_{s,1}$ and $V_{s,2}$, respectively. We place ourselves in the frame of reference translating at the mean slip velocity $(V_{s,1} + V_{s,2})/2$. In this frame of reference, the walls move with opposite velocities $\pm U_s$, where $U_s = (V_{s,1} - V_{s,2})/2$ (Fig. 3). The general form of the momentum equation for an incompressible fluid is

$$\rho \frac{\partial \vec{u}}{\partial t} + \rho(\vec{u} \cdot \vec{\nabla})\vec{u} = \rho \vec{g} - \vec{\nabla} p + \vec{\nabla} \cdot [\sigma], \tag{1}$$

where ρ is the fluid density, $\vec{u}$ the velocity vector, p the pressure, and $[\sigma]$ the deviatoric stress tensor. In our Hele-Shaw geometry, the velocity has one component in the x direction that varies only in the z direction, $U(z)$. Equation (1) then reduces to the very simple form [25]

$$\frac{\partial \sigma_{xz}}{\partial z} = \frac{\partial p}{\partial x} = -\frac{\Delta p}{L}. \tag{2}$$

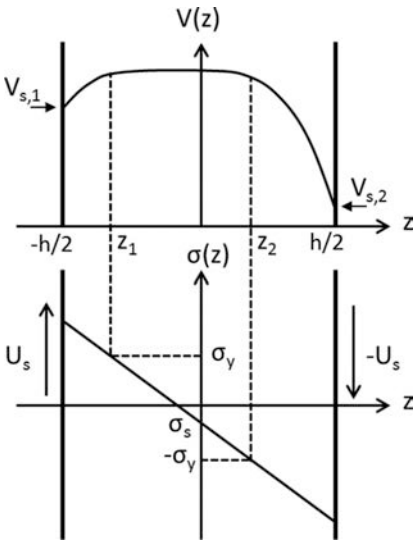

FIG. 3. Representation of an asymmetric velocity profile (top) and the corresponding stress variation across the microchannel (bottom).

From the momentum equation (2), we get the local shear stress $\sigma(z) = \sigma_s - Gz$, where $G = \Delta P/L$ is the pressure gradient and σ_s is a nonzero constant that is due to the fact that the walls are moving at opposite velocities. Here the fluid obeys the Herschel-Bulkley constitutive equation $\sigma = \sigma_y + k\gamma^n$, where σ_y is the yield stress, k is the consistency parameter, and $n = 1/2$. The analysis can be easily extended to the case where $n \neq 1/2$. Using this constitutive equation and the expression of $\sigma(z)$, we calculate $\dot{\gamma}(z)$ by solving $\sigma(z) = \sigma(\dot{\gamma})$ over the three different regions: $-h/2 < z < z_1$ where $\dot{\gamma}(z) > 0$, $z_1 < z < z_2$ where $\dot{\gamma}(z) = 0$, and $z_2 < z < h/2$ where $\dot{\gamma}(z) < 0$. Here z_1 and z_2 denote the positions of the yield surfaces separating the central plug flow and the fluidized regions. At $z = z_1$ and $z = z_2$, we have $\dot{\gamma}(z) = 0$, leading to $z_1 = (\sigma_s - \sigma_y)/G$ and $z_2 = (\sigma_y + \sigma_s)/G$. After integration of the stress equation in each region with the appropriate boundary conditions, i.e., $U(z_1) = U(z_2)$, $U(-h/2) = U_s$, and $U(h/2) = -U_s$, we obtain (Fig. 3)

$$U(z) = \frac{G^2}{3k^2}\left[-(z_1 - z)^3 - \frac{1}{2}\left(z_2 - \frac{h}{2}\right)^3 + \frac{1}{2}\left(z_1 + \frac{h}{2}\right)^3\right] \quad \text{for} \quad -\frac{h}{2} < z < z_1, \tag{3a}$$

$$U(z) = \frac{G^2}{3k^2}\left[-\frac{1}{2}\left(z_2 - \frac{h}{2}\right)^3 + \frac{1}{2}\left(z_1 + \frac{h}{2}\right)^3\right] \quad \text{for} \quad z_1 < z < z_2, \tag{3b}$$

$$U(z) = \frac{G^2}{3k^2}\left[(z_2 - z)^3 - \frac{1}{2}\left(z_2 - \frac{h}{2}\right)^3 + \frac{1}{2}\left(z_1 + \frac{h}{2}\right)^3\right] \quad \text{for} \quad z_2 < z < \frac{h}{2}, \tag{3c}$$

where z_1 and z_2 are related through the relations

$$U_s(z) = -\frac{G^2}{3k^2}\left[\frac{1}{2}\left(z_2 - \frac{h}{2}\right)^3 + \frac{1}{2}\left(z_1 + \frac{h}{2}\right)^3\right], \qquad z_2 - z_1 = \frac{2\sigma_y}{Gh}, \tag{3d}$$

These expressions can be made dimensionless by using the scaling variables $U = U/(G^2h^3/3k^2)$, $\zeta = z/h$, and $\bar{\sigma} = \sigma/Gh$:

$$\bar{U}(\zeta) = -(\zeta_1 - \zeta)^3 - (\zeta_2 - 1/2)^3/2 + (\zeta_1 + 1/2)^3/2 \quad \text{for} \quad -1/2 \leqslant \zeta \leqslant \zeta_1, \tag{4a}$$

$$\bar{U}(\zeta) = (\zeta_1 + 1/2)^3/2 - (\zeta_2 + 1/2)^3/2 \quad \text{for} \quad \zeta_1 \leqslant \zeta \leqslant \zeta_2, \tag{4b}$$

$$\bar{U}(\zeta) = (\zeta_2 - \zeta)^3 - (\zeta_2 - 1/2)^3/2 + (\zeta_1 + 1/2)^3/2 \quad \text{for} \quad \zeta_2 \leqslant \zeta \leqslant 1/2, \tag{4c}$$

where ζ_1 and ζ_2 are the solutions of

$$-(\zeta_2 - 1/2)^3/2 - (\zeta_1 + 1/2)^3/2 = \bar{U}_s, \quad \zeta_2 - \zeta_1 = 2\bar{\sigma}_y. \tag{5}$$

The above equations can also be used to describe the velocity profiles composed of a plug region that extends down to

the hydrophilic wall (high slip) and a sheared region near the hydrophobic wall (low slip) [see Fig. 2(i)]. The velocity profiles are given by

$$U(z) = \frac{G^2}{3k^2}\left[-\frac{1}{2}\left(z_2 - \frac{h}{2}\right)^3\right] \quad \text{for} \quad -\frac{h}{2} < z < z_2, \tag{6a}$$

$$U(z) = \frac{G^2}{3k^2}\left[(z_2 - z)^3 - \frac{1}{2}\left(z_2 - \frac{h}{2}\right)^3\right] \quad \text{for } z_2 < z < \frac{h}{2}, \tag{6b}$$

where z_2 is given by

$$U_s = -\frac{G^2}{3k^2}\left[\frac{1}{2}\left(z_2 - \frac{h}{2}\right)^3\right] \tag{6c}$$

or in dimensionless form

$$\bar{U}(\zeta) = +\bar{U}_s \quad \text{for } -1/2 < \zeta < \zeta_2, \tag{7a}$$

$$\bar{U}(\zeta) = (\zeta_2 - \zeta)^3 + \bar{U}_s \quad \text{for} \quad \zeta_2 < \zeta < 1/2, \tag{7b}$$

where $\bar{U}_s = -1/2(\zeta_2 - 1/2)^3$.

C. Modeling the velocity profiles

We have analyzed the experimental velocity profiles shown in Fig. 2 using the predictions of the asymmetric Herschel-Bulkley flow model. In practice, U_s is calculated from $V_s{}_{,1}$ and $V_s{}_{,2}$; k and σ_y are the parameters of the macroscopic HB equation. The predictions from the model are plotted in Fig. 2 for comparison with experiments. In Figs. 2(a)–2(g), the agreement is quantitative within a standard deviation of about 15% for k. The local flow curves deduced from the velocity profiles and the macroscopic flow curve coincide, which further confirms the validity of the model [Fig. 1(a)]. In Figs. 2(i) and 2(h), the theoretical velocity profiles also reproduce the shape of the experimental plots, but to get quantitative agreement we allow larger deviations of k from its macroscopic value. Nevertheless, we can conclude that our generalized model successfully captures the observed phenomena.

IV. DISCUSSION

A. Scaling analysis

The velocity profiles given by Eq. (4) depend on two dimensionless numbers $\bar{U}_s$ and $\bar{\sigma}_y$, where $\bar{\sigma}_y$ is the nondimensional yield stress defined previously and $\bar{U}_s$ is another dimensionless number, the slip number, which represents the ratio of the velocity associated with slip heterogeneities to the bulk velocity. When $\bar{U}_s$ is small, bulk forces dominate and the velocity profiles are symmetric. When $\bar{U}_s$ is large, the velocity profiles are significantly affected by wall slip heterogeneities and become asymmetric. In the asymptotic limit where $\bar{U}_s \to +\infty$, the flow structure is entirely dominated by slip effects and the flow is a pure shear flow.

From our theory, we make two interesting predictions. First, the flow structure is controlled by the slip number $\bar{U}_s$. To test this prediction, we define two quantities that characterize the alteration of the velocity profiles due to slip heterogeneities: $S = (\zeta_1 + \zeta_2)/2$ measures the asymmetry in the positions

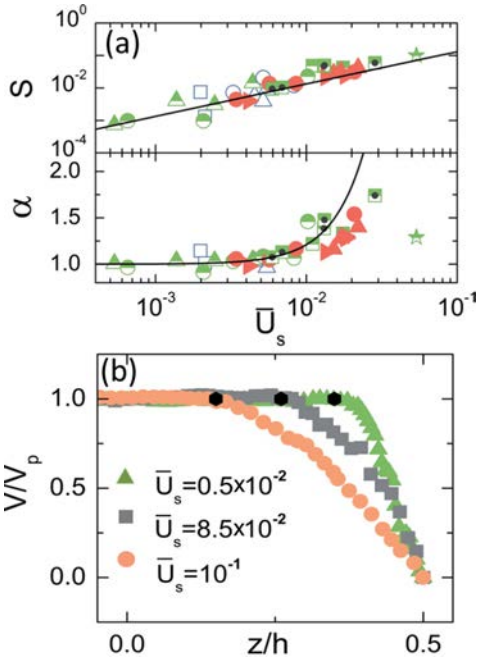

FIG. 4. (Color online) (a) Asymmetry parameter S and velocity ratio α versus slip number $\bar{U}_s$ for different confinements 7 μm (⋆), 20 μm (■), 50 μm (▲), 75 μm (►), and 100 μm (●); boundary conditions 20°-20° (blue open symbols), 20°-70° (green half-full symbols), and 20°-110° (red closed symbols); and microgel concentrations 0.016 g/g (symbols without a dot) and 0.022 g/g (dotted symbols). (b) Detail of velocity profiles near the low-slip hydrophobic surface showing slip-induced fluidization. Velocity profiles are scaled by the central plug velocity. The black dots point to the crossover between the central plug and the fluidized layers.

of the yield surfaces and $\alpha = V_p/U_p$ represents the ratio between the plug flow velocity measured experimentally and that computed from the model for a symmetric flow profile. The variations of S and α for the velocity profiles shown in Figs. 2(a)–2(h) are plotted against the slip number $\bar{U}_s$ in Fig. 4(a). All the data collapse on master curves, showing that both S and α are unique functions of $\bar{U}_s$. For small $\bar{U}_s$ values, the model predicts that $S \approx 3\bar{U}_s/4$ and $\alpha \approx \bar{U}_s^2$, which agree well with the experimental results. We consider that the deviations from the symmetrical Herschel-Bulkley model become significant above $\bar{U}_s \sim 10^{-2}$, where S and α have changed by about 10%. The second prediction is that the region close to the hydrophobic wall (low slip velocity) tends to fluidize when $\bar{U}_s$ increases. Fluidization is clearly visible in Fig. 4(b) for the case of the profiles shown in Fig. 2(i). The sheared region adjacent to the hydrophobic wall becomes thicker and the unsheared semiplateau plug is reduced. Slip-induced fluidization is caused by the important shear rates that develop at the hydrophobic wall as a consequence of the large slip velocities at the hydrophilic wall.

B. Channel-size criterion for the existence of flows controlled by slip heterogeneities

In this section we derive the general expression of a characteristic length scale that sets the size below which slip

heterogeneities control the entire bulk flows. The slip number that characterizes the importance of the slip heterogeneities with respect to the driving forces can be written as $U_s = (l^*/h)^2$. In this expression l^* is a mesoscopic length scale, which has the expression $l^* = (U_s\mu/G)^{1/2}$, where $\mu = k^2/Gh$ is the characteristic viscosity at the wall. The ratio $(l^*/h)^2$ compares the viscous stress induced by slip heterogeneities to the applied pressure stress. When $h \gg l^*$, the driving forces control the flow structure, whereas for $h \ll l^*$, slip heterogeneities dominate. In our experiments, the transition occurs around $l^* \sim h/10$ [Fig. 4(a)].

Let us show that the existence of this length scale can be generalized to fluids obeying any other constitutive equation. Above, we expressed the shear stress as $\sigma(z) = \sigma_s - Gz$. This formula can be rewritten in the form $\sigma(z) = G(-z + \lambda)$, where λ has the dimension of length. We consider a general constitutive law $\dot\gamma = f(\sigma)$ characterizing non-Newtonian fluids without yield stress. The domain of definition of f includes positive and negative values of σ and f is an odd function of σ. For the flow geometry considered in this paper, we have

$$\dot\gamma = \frac{dU}{dz} = f[G(-z + \lambda)]. \tag{8}$$

When $\lambda \ll h$, $-z + \lambda$ can be approximated by $-z$ (except in a region of negligible size) and the solution $U(z)$ gets close to the symmetric solution obtained when the slip velocity difference is $U_s = 0$. When $\lambda \gg h$, $\dot\gamma$ tends to a constant and the flow is similar to a pure shear flow. The crossover between the two regimes occurs for $\lambda \sim h$. To connect λ to U_s, we carry out a Taylor expansion of $\dot\gamma$ at small λ/h, assuming that it remains valid on order of magnitude for $\lambda/h \sim 1$:

$$\dot\gamma = f(-Gz) + \lambda \left.\frac{\partial f}{\partial \lambda}\right|_{\lambda=0} + O(\lambda^2). \tag{9}$$

Since f is a function of $(-z + \lambda)$, we have $\frac{\partial f}{\partial \lambda} = \frac{\partial f}{\partial z}$. Integrating (8) with respect to z leads to the following expression for $U(z)$, which is valid for small λ:

$$U(z) \approx \hat f(-Gz) + \lambda f(-Gz), \tag{10}$$

where $\hat f$ is a primitive function of f. Since $U(\pm h/2) = \pm U_s$ we obtain

$$\begin{aligned} U_s &\approx \hat f\left[-G\frac{h}{2}\right] + \lambda f\left[-G\frac{h}{2}\right], \\ -U_s &\approx \hat f\left[G\frac{h}{2}\right] + \lambda f\left[G\frac{h}{2}\right]. \end{aligned} \tag{11}$$

Since f is odd and $\hat f$ is even, we obtain from (11)

$$U_s \approx \lambda \dot\gamma_w, \tag{12}$$

where $\dot\gamma_w = f(-G\frac{h}{2})$is the wall shear rate when $U_s = 0$.

Here λ is a characteristic length scale, equivalent to the Navier length, which is built on the slip velocity difference U_s. To be consistent with our analysis for HB fluids, it has to be of the form $\lambda = l^{*2}/h$ and the crossover between the two regimes is given by $l^* \sim h$. Interestingly, l^* can also be expressed as $l^* = \sqrt{\lambda h}$. This general form can be used to quantify the role of slip heterogeneities on the flow of any materials such as concentrated emulsions, Newtonian liquids, polymers, and shear banded fluids in confined geometries.

V. CONCLUSION

A final remark concerns cooperativity effects, which have been found to influence the flow of glassy suspensions in microchannels [29–32]. We checked that adding a cooperative term to our model does not improve the agreement between the predictions and the experimental results. We hypothesize that the confinement in the microchannels is too low to induce measurable cooperative phenomena. Whether the existence of slip heterogeneities, as another source of nonlocal rheological effects, may affect cooperativity phenomena is an open question.

ACKNOWLEDGMENTS

The work was supported by Schlumberger, ESPCI, and CNRS. We thank Charlotte Pellet for her help with the rheological bulk measurements and Jens Harting and Lydéric Bocquet for fruitful discussions. M.C. thanks Roger T. Bonnecaze for fruitful discussions on the role of surface chemistries on slip.

[1] R. Buscall, J. Rheol. **54**, 1177 (2010).
[2] H. Barnes, J. Non-Newtonian Fluid Mech. **56**, 221 (1995).
[3] D. C. Tretheway and C. D. Meinhart, Phys. Fluids **14**, L9 (2002).
[4] C. Neto, D. R. Evans, E. Bonaccurso, H.-J. Butt, and V. S. J. Craig, Rep. Prog. Phys. **68**, 2859 (2005).
[5] C. Bouzigues, L. Bocquet, E. Charlaix, C. Cottin-Bizonne, B. Cross, L. Joly, A. Steinberger, C. Ybert, and P. Tabeling, Philos. Trans. R. Soc. London Ser. A **366**, 1455 (2008).
[6] M. P. Lettinga and S. Manneville, Phys. Rev. Lett. **103**, 248302 (2009).
[7] Y. T. Hu, P. Boltenhagen, E. Matthys, and D. J. Pine, J. Rheol. **42**, 1209 (1998).
[8] H. Princen, J. Colloid Interface Sci. **105**, 150 (1985).
[9] J.-B. Salmon, L. Becu, S. Manneville, and A. Colin, Eur. Phys. J. E **10**, 209 (2003).
[10] V. Bertola, F. Bertrand, H. Tabuteau, D. Bonn, and P. Coussot, J. Rheol. **47**, 1211 (2003).
[11] S. Khan, C. Schnepper, and R. Armstrong, J. Rheol. **32**, 69 (1988).
[12] N. D. Denkov, V. Subramanian, D. Gurovich, and A. Lips, Colloid Surf. A **263**, 129 (2005).
[13] S. P. Meeker, R. T. Bonnecaze, and M. Cloitre, Phys. Rev. Lett. **92**, 198302 (2004).
[14] L. Isa, R. Besseling, and W. C. K. Poon, Phys. Rev. Lett. **98**, 198305 (2007).
[15] P. Ballesta, G. Petekidis, L. Isa, W. C. K. Poon, and R. Besseling, J. Rheol. **56**, 1005 (2012).

[16] C. S. Nickerson and J. A. Kornfield, J. Rheol. **49**, 865 (2005).
[17] E. Lauga and H. A. Stone, J. Fluid Mech. **489**, 55 (2003).
[18] R. Bonnecaze and M. Cloitre, Adv. Polym. Sci. **236**, 117 (2010).
[19] M. Cloitre, R. Borrega, F. Monti, and L. Leibler, C. R. Phys. **4**, 221 (2003).
[20] J. R. Seth, L. Mohan, C. Locatelli-Champagne, M. Cloitre, and R. T. Bonnecaze, Nat. Mater. **10**, 838 (2011).
[21] L. Mohan, C. Pellet, M. Cloitre, and R. Bonnecaze, J. Rheol. **57**, 1023 (2013).
[22] B. Levaché, A. Azioune, M. Bourrel, V. Studer, and D. Bartolo, Lab Chip **12**, 3028 (2012).
[23] J. R. Seth, M. Cloitre, and R. T. Bonnecaze, J. Rheol. **52**, 1241 (2008).
[24] J. R. Seth, C. Locatelli-Champagne, F. Monti, R. T. Bonnecaze, and M. Cloitre, Soft Matter **8**, 140 (2012).
[25] G. Degré, P. Joseph, P. Tabeling, S. Lerouge, M. Cloitre, and A. Ajdari, Appl. Phys. Lett. **89**, 024104 (2006).
[26] P. Nghe, G. Degré, P. Tabeling, and A. Ajdari, Appl. Phys. Lett. **93**, 204102 (2008).
[27] K. N. Nordstrom, E. Verneuil, P. E. Arratia, A. Basu, Z. Zhang, A. G. Yodh, J. P. Gollub, and D. J. Durian, Phys. Rev. Lett. **105**, 175701 (2010).
[28] L. Westerberg, T. S. Lundstrom, E. Hoglund, and P. M. Lugt, Tribol. Trans. **53**, 600 (2010).
[29] J. Goyon, A. Colin, and L. Bocquet, Soft Matter **6**, 2668 (2010).
[30] B. Geraud, L. Bocquet, and C. Barentin, Eur. Phys. J. E **36**, 30 (2013).
[31] V. Mansard, Ph.D. thesis, Université Bordeaux I, 2012.
[32] A. Nicolas and J.-L. Barrat, Phys. Rev. Lett. **110**, 138304 (2013).

Chapter 5

Displacement of Herschel-Bulkley fluids in microchannels

5.1 Introduction

The dynamical study of fluid displacements has begun with that of fingering instability using Newtonian and immiscible fluids in Hele-Shaw cells. It was then extended to miscible fluids, radial cells, tubes or square capillaries. Experiments involving non-Newtonian fluids revealed various fingering patterns: fractal growths, fractures, parallel fingers. Here we review succinctly the literature on fingering in Hele Shaw cells and film studies in capillaries, in different cases (Newtonian, complex, miscible, immiscible). The behaviour of yield stress fluids will be described in more detail.

5.1.1 Newtonian immiscible fluids

Hele-Shaw cell

The study of the viscous fingering instability started with an experiment conducted by Hill [75, 77]. He used a Hele-Shaw cell to carry out gravity driven displacements using two fluids: the first fluid is dense and less viscous than the second light fluid. Hill observed a viscous stabilization of the interface between the fluids for a density-unstable configuration. The reverse was also observed: a gravity stabilization of the interface between the fluids for a viscous-unstable configuration.

In 1958, Saffman and Taylor showed that a Hele-Shaw cell [73] could be used to model the flow in a porous media. They carried out displacements of a viscous fluid (glycerin or oil) with an immiscible less viscous fluid (air, water). They observed an unstable interface as shown on figure 5.1 (a) and at a later stage, the formation of a single finger (see figure 5.1 (b)). The relative width of the finger λ results from the competition between viscous forces that tend to narrow the finger and capillary forces that tend to widen it. The control parameter of the system $1/B$ is expressed as a function of the capillary number and of the aspect ratio of the cell: $1/B = Ca * (W/b)^2$. At high velocities, the finger width tends to be equal to the half of the channel. Theoretical and numerical studies led to the comprehension of this limit by taking into account the surface tension [119, 32, 167, 78], which was ignored in the original study. An overview of the Saffman-Taylor instability can be found in [77].

These studies treated the Saffman-Taylor instability as a two-dimensional problem. In reality, the displaced fluid leaves at the bottom and at the top walls a thin wetting film, the drainage film. Park and Homsy [143] found that the drainage film in a Hele-Shaw cell could

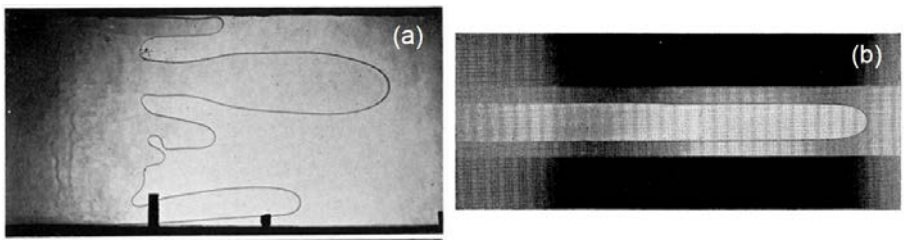

Figure 5.1 – Reproduction from [159]. Top view of the displacement of immiscible fluid in a Hele-Shaw cell. (a) A finger gets ahead of its neighbour. (b) A single finger of water penetrating oil, the width of the finger is equal to the half of the channel width.

be described by Bretherton's law [25]. They also showed that the drainage film implies a modification of the pressure jump at the interface. Tabeling *et al.* [172] measured the film thickness in a Hele-Shaw cell. Figure 5.2 (a) to (c) shows the propagation of a finger in a Hele-Shaw cell viewed from the side (a), the top (b) and the front (c). The drainage film of thickness t is represented on figure 5.2 (a) from the side. Its shape varies with the normal velocity component along the interface as shown on figure 5.2 (c). The maximal thickness of the layer is located in the middle of the finger and follows Bretherton 's law in the range $6 \cdot 10^{-4} < Ca < 3 \cdot 10^{-3}$. They showed, that at high velocities, the film influences the finger width: the relative finger width λ goes below the limit of 0.5 originally observed by Saffman and Taylor as shown on figure 5.2 (d) [172, 173]. In fact, at high velocities, when viscous forces become important compared to capillary forces, the meniscus does not span the gap of the Hele-Shaw cell so that the two-dimensional approximation is not sufficient to describe the phenomena observed.

Further increase of the velocities induces tip-splitting of the finger [173] that was associated to small irregularities or noise in the cell. Recent theoretical and numerical study explains tip-splitting phenomena in radial Hele-Shaw cell by taking into account the wetting film left at the walls in their analysis of the nonlinear regime of the finger instability [4].

Capillaries

A number of displacements studies of immiscible fluids were also carried out in tubes. In tubes, the width of the finger is controlled by the thickness of the film left at the walls during the displacement. The thickness of this film was studied theoretically by Bretherton who showed that the thickness of the film varies with $Ca^{2/3}$ in the limit of low $Ca < 3 \cdot 10^{-3}$ [25]. The theory was confirmed by experimental studies [176, 25, 38].

The displacement of a viscous fluid by a less viscous one in the case of the square capillary showed many similarities with the tube [90]. More recently, Lozar *et al.* performed a systematic study of the Saffman-Taylor instability in various rectangular channel geometries. The aspect ratio of the rectangular channel goes from the Hele-Shaw cell to the square capillary. They defined a new capillary number taking into account the geometry of the cell. The volume fraction of fluid left in the cell m is determined in each geometry and is found to collapse on a master curve above a threshold value of the modified capillary number [39].

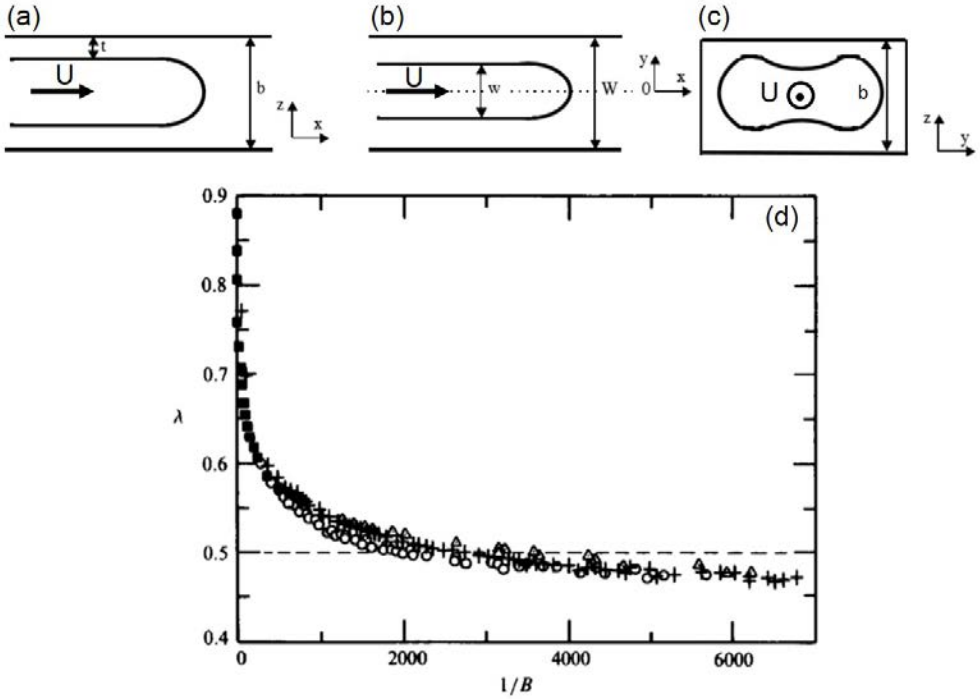

Figure 5.2 – (a) Side view, (b) top view and (c) front view of the propagation of a single finger in a Hele-Shaw cell, reproduction from [104]. t is the thickness of the wetting film left by the finger in the gap direction. (d) Effect of the wetting film: at high velocity, the relative width of the finger λ as a function of the dimensionless number $1/B$. λ goes below the limit 0.5 found by Saffman and Taylor [159]. Reproduction from [173].

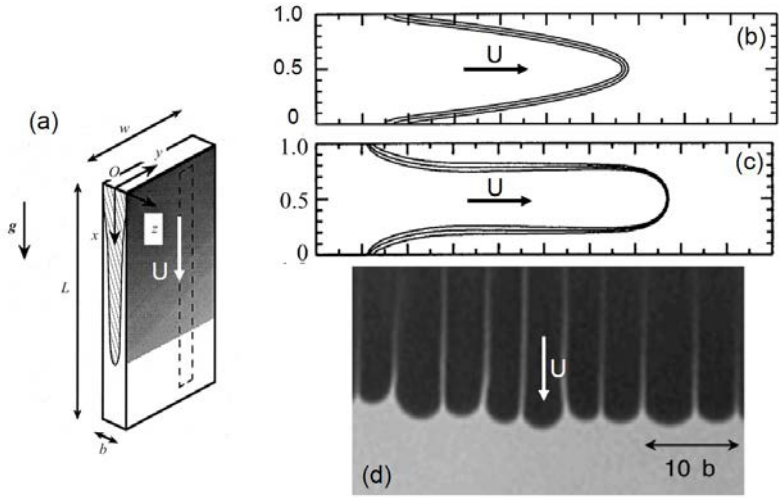

Figure 5.3 – (a) Sketch of the finger across the gap of the Hele-Shaw cell for miscible displacements, reproduction from [95]. (b) Concentration profiles during miscible displacements at high Pe and for viscosity ratio (c)$M = 1$ and (d) $M = 100$, reproduction from [155]. (d) Picture of the 3D instability observed by Lajeunesse *et al.* [94].

5.1.2 Newtonian miscible fluids

Characteristics of the interface between the fluids

In the case of miscible fluids, one has to take into account the diffusion between the two fluids and their mixing. To describe this phenomena we use the Peclet number defined as the ratio of the diffusion time over the convection time: $Pe = UL/D$ with U the characteristic velocity of the flow, L a characteristic length and D the diffusion coefficient.

At low Pe, diffusion between the fluids across the interface is important compared to the advection of the interface. Thus, the interface is fuzzy. At large Pe, a sharp interface between the fluids is formed and persists over times on the order of Pe [147]. In such conditions, attempts have been made to establish boundary conditions that could be analogous to Laplace law. This gave rise to define "effective surface tension" permitting the theoretical treatment of the problem [193]. Here we focus on the large Pe case.

More specifically, Chen *et al.* [29] performed a numerical investigation of miscible displacement in tubes. They showed that the displacements are governed by the Peclet number and by a "viscous" Atwood number, which represents the viscosity difference between the two fluids: $At = \frac{\mu_1 - \mu_2}{\mu_1 + \mu_2}$. They analyzed the concentration profiles of the fluids as a function of these numbers. Lajeunesse *et al.* have provided an experimental support to the numerical study of Chen *et al.*. They showed that the concentration profiles behind the tip of the finger depend on the viscosity ratio between the fluids. If the viscosity ratio between the fluids is close to 1, the concentration profiles spread continuously as sketched on figure 5.3 (b). For important viscosity ratios, the concentration profiles are stationary as sketched on figure 5.3 (c).

Experiments in Hele-Shaw cells

Lajeunesse *et al.* made Newtonian miscible displacement experiments in Hele-Shaw cells at high Pe [94, 95]. They observed a new fingering pattern above a critical viscosity ratio $M = 1.5$ and for a velocity exceeding a threshold value. Figure 5.3 (d) shows this new pattern. It looks like regularly spaced fingers across the width of the channel. Their

wavelength scales with the gap of the Hele-Shaw cell, therefore they were called "3D fingering". The explanation for the occurrence of the 3D fingering could only be obtained by considering the concentration profile of the fluids across the gap of the Hele-Shaw cell.

Recently, Bischofberger *et al.* used the result of Lajeunesse *et al.* to suppress the growth of the fingering instability during the miscible displacements of two fluids in a radial Hele-Shaw cell by increasing the viscosity ratio between the fluids [14].

Experiments in capillaries

Petitjeans *et al.* measured the volume fraction of fluid left at the walls m during the displacements of miscible fluids in a tube as a function of the viscosity ratio of the fluids (a viscous Atwood number). The value of m is found to vary between 0.5 at low Atwood number to 0.6 at high Atwood number. This experimental result is in agreement with the simulation of Chen *et al.* [29]. In her PhD, Céline Gabard also carried out Newtonian miscible displacements in a tube and obtained experimental data in good agreement with these previous results [58].

In the high Pe regime, it is interesting to compare the volume fraction left at the walls m for miscible and immiscible displacements. Petitjeans *et al.* [147] compared their results (obtained with an Atwood number of unity) to the results of Taylor [176] and Cox [38] obtained with immiscible fluids in tubes and found a good agreement. By doing this, they suggested a correspondence between miscible displacements and immiscible displacements in the limit of low surface tension. Kuang *et al.* found similar results at high Pe with miscible displacements of oil in a tube [92].

5.1.3 Non-Newtonian fluids

Immiscible fluids in Hele-Shaw cells

The patterns observed when non-Newtonian fluids are involved in fluid displacements are very rich. Most of the experiments were performed in Hele-Shaw cells with immiscible fluids and focused on the fingering pattern observed across the width of the Hele-Shaw cell rather than across its gap. The influence of several non-Newtonian fluids properties have been studied experimentally and theoretically : shear-thinning behaviour [19, 105, 33, 3, 104, 57, 165, 52, 23, 186], shear-thickening [128], elastic behaviour [105, 60, 81, 156, 111].

The case of yield stress fluids was studied experimentally by [106]. The derivation of a Darcy law for yield stress fluids [34] allowed to quantitatively understand the yield stress regime (low velocity) where several fingers are propagating in parallel in the cell. But the theory did not explain tip-splitting and side-branching observed at higher velocities. This was recently solved in [53].

In viscoelastic and/or yield stress fluids fracturing phenomena were observed resulting in very poor displacement efficiency. Lemaire *et al.* showed a transition from fractal growth to viscoelastic fracturing while displacing a clay smectite suspension [98]. The existence of this transition was also showed for the displacement of associative polymers [190] or more recently for a solution of a viscoelastic micellar fluid in which a cylinder is displaced [64]. Tabuteau *et al.* explained the microscopic mechanisms of the brittleness of viscoelastic fluids [174]. They showed that the brittleness comes from micro cracks within the material. Therefore, the fracture of fluids is observed when the rate of deformation imposed hinders the relaxation of the fluid so that the fluid responds in a solid-manner.

With the concentrated suspensions of microgel we are not concerned by fracturing phenomena since their relaxation times are much shorter than the deformation rate imposed

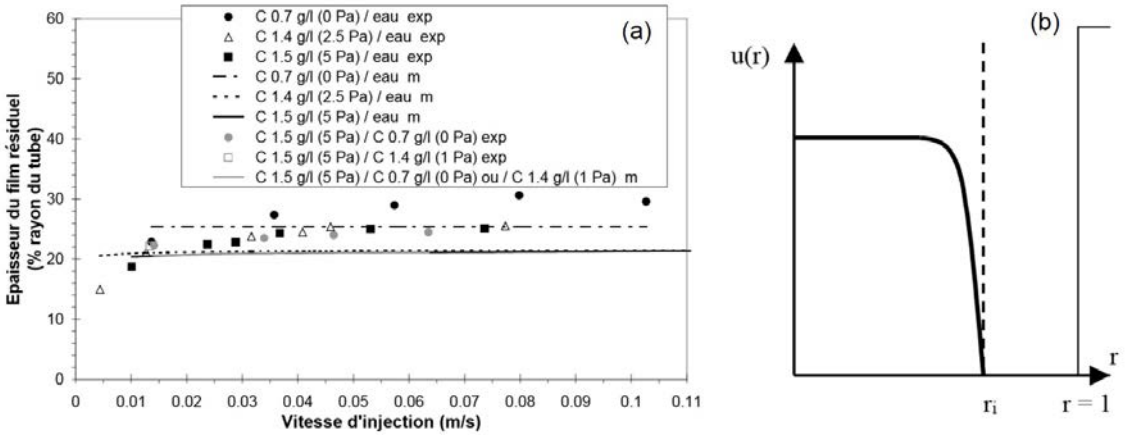

Figure 5.4 – Reproduction from [58]. (a) Thickness of the layer scaled by the tube radius as a function of the injection velocity. (b) Velocity profile of the fluids as a function of the radial component r. r_i is the position of the interface between the fluids. The layer is fully static.

in the experiments.

Setu *et al.* carried out an experimental and a numerical study of the displacement of colloidal suspension at very low interfacial tension [165]. Following the previous work of Tabeling *et al.*, they showed the influence of the gap dimension on the fingering patterns observed at large velocities.

Miscible fluids: characteristics of the interface

The problematic of the interface between miscible non-Newtonian fluids is similar to the Newtonian case. In particular, Truzzolillo *et al.* showed that an effective surface tension can be defined between the fluids. This quantity, which is related to the gradient of composition of the fluids across the interface grows with the size of the particles in the fluid (here the size of microgel beads) [180].

Miscible fluids in capillaries in the case of Herschel-Bulkley fluids

The study we will mostly refer to is the PhD of Céline Gabard [58, 35]. She reported various displacements of non-Newtonian miscible fluids in a tube. In particular she performed displacements of a Carbopol solution (a yield stress fluid) with either water or with another Carbopol solution having a lower yield stress. All the displacements were iso-density. The main experimental results are:

— The thickness of the film increases with the imposed velocity as shown on figure 5.4 (a)
— Above a critical velocity, the thickness of the film tends to a constant value around 26% of the tube radius as shown on figure 5.4 (a).
— At low velocities, the interface between the fluids is irregular and becomes smooth at higher velocities.
— The displacing fluid seems to have a low impact on the film thickness.
— The film formed at the walls of the tube is fully static.

An analysis of the flow in a quasi-parallel approximation could predict the mobility of the residual film at the walls. The analysis looks at the stress profiles across the tube section and at the shape of the velocity profile in the core fluid and in the film. A typical velocity profile is represented on figure 5.4 (b) in the case where a static residual layer is

present at the wall. The result of this analysis gives a maximal thickness for the film to stay static. All the thicknesses of the films measured in the experiments were lower than this value.

For the displacements of yield stress fluids, a model called the *recirculation model* was presented to explain the selection of the layer thickness in the system. The model is based on the minimum of energy dissipation and is detailed in appendix B. The main idea of the model is that, in the frame reference of the advancing finger, the minimum of energy dissipation is obtained at the point where recirculation starts developing in the displaced fluid. The recirculation model appears satisfactory for accounting high velocities regime. We may note that it is remarkable that in such a complex situation, a simple concept explains the phenomena at a quantitative level.

5.1.4 Other aspects of fluid displacements

The annular geometry: direct application to the cementing problem

Displacements in annular geometries have also been considered motivated by applications in the oil industry in cementing processes. The aim of most of these experimental or theoretical [145] studies was to look at the influence of pipe eccentricity on the displacement efficiency.

When the casing is decentered in the wellbore, there is a narrow part in the annulus where the mud is difficult to displace (figure 1.4 (a) shows a picture of an eccentric annulus). In fact, when the cement is pushed, it often bypasses this narrow region. A density difference between the fluids can create secondary azimuthal flows and enhance the bypass of the narrow part of the annulus [177]. Secondary flows can also modify the displacements via dispersion, the secondary flows transport the finger on the wide side of the annulus [110]. It has been shown that moving the casing during the displacement improves the displacement efficiency because it helps to shear the mud on the narrow part of the annulus [120].

Most of the time in the literature, the focus is made on the effect of casing eccentricity on the displacement efficiency, neglecting what's happening over the annular depth. Recently, in an experimental work in an eccentric annular section, the presence of a film on the outer wall was also observed. Even if the Hele-Shaw approximation is able to capture the main characteristic of the displacement [110, 7], it was suggested to include the gap dimension in the model to get a better comparison with the experimental results [110].

Geometries with obstacles

Displacement experiments in a variety of geometries have been investigated over the past 30 years. These experiments have underlined the crucial role of the geometry on the fingering instability. For instance, it has been shown that it is possible to suppress the Saffman Taylor instability between immiscible Newtonian fluids in Hele-Shaw cells of varying depth [1] sketched on figure 5.5 (a) or of conical or spherical shapes [24].

Patterns of wavy fingers and tip-splitting were observed in Hele-Shaw cells in which the cross section is occluded by a step obstacle [142, 71]. The geometry is sketched on figure 5.5 (b). The patterns could be explained theoretically with a depth-averaged model and are presented on figure 5.5 (c) [178].

Mc Cloud *et al.* observed perturbations of the selection of the width of the viscous finger by introducing on one side of the Hele-Shaw cell a rectangular or square lattice pattern [118]. The height of the patterns was varied. Above a threshold the presence of the

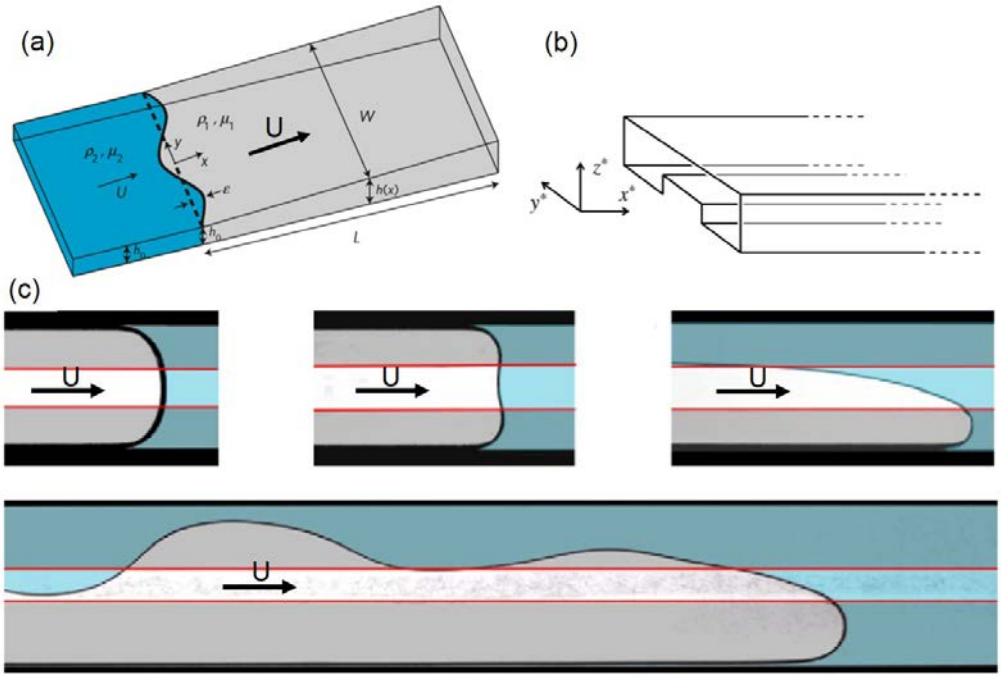

Figure 5.5 – (a) Displacement in a diverging-converging gap Hele-Shaw cell [1]. (b) Schematic view of a Hele-Shaw cell with an obstruction in the gap direction [178]. (c) Examples of the fingering patterns obtained in the obstructed Hele-Shaw cell (b) [178].

lattice induced the selection of wider fingers compared to the unperturbed case [118]. In this case the length of the perturbation is smaller than the capillary length. Other studies, introducing a perturbation larger than the capillary length mainly observed the selection of a narrower width for the finger [79, 192], more references can be found in [118].

5.2 Strategy for the study of the displacement of Herschel-Bulkley fluids

5.2.1 Objectives of the chapter

As pointed out in chapter 1, in centered annular geometries the fronts developed at the interface between the fluids are flat across the azimuthal direction thanks to an appropriate density hierarchy between the fluids. The remaining issue concerns the gap, i.e. whether there exists a film at the walls left by the displaced fluid.

In this work, we use microfluidic tools to collect pertinent information on the subject. Microfluidic devices are much smaller than casings used in oil wells, but, from an hydrodynamical viewpoint, several important dimensionless numbers governing flow behaviours are comparable. This is shown in table 5.1. We can see that microfluidic Reynolds numbers are much smaller than in the oil situation, but both are associated to laminar regimes. Peclet numbers are large in both cases, while other characteristical numbers are comparable. Probably, the main difference is that gravity is negligible in microfluidic devices while it plays an important role in the industrial context. Still, there exist a sufficient number of comparable features to justify the microfluidic studies we have undertaken along the present work. In the meantime, we will take advantage of the microfluidic technology (observation windows, flexibility of changing geometries,...) to provide well controlled data.

Table 5.1 – Comparison of adimensional numbers between the well and the microfluidic experiments.

Numbers	Well	Microfluidic
Re	≈ 500	< 1
Pe (Peclet number, transport property)	$\approx 10^8$	$\approx 10^5$
Wall shear stress/yield stress	1-2	1-15
Surface characteristic	Casing, formation	Physico-chemistry tunable, roughness 0.5 - 30% of channel width
Rheology	$\sigma_y \approx 10$ Pa, $n \approx 0.5$, $k \approx 1 \mathrm{Pa\,s^{-n}}$	$\sigma_y \approx 10$ Pa, $n \approx 0.5$, $k \approx 5 - 25\ \mathrm{Pa\,s^{-n}}$

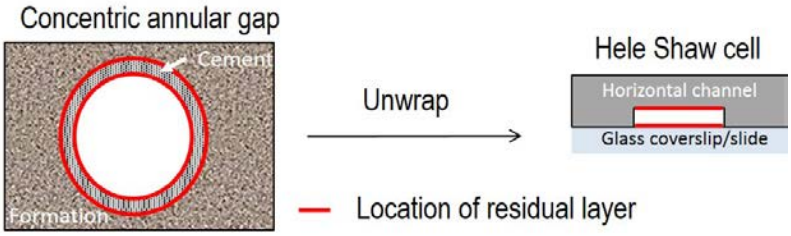

Figure 5.6 – From annular gap to Hele-Shaw cell.

5.2.2 Geometries of the straight channels used in the study

The annular gaps in wells are very thin (1 cm to 5 cm) as compared to its length (1000 m to 6000 m). If we imagine that we unwrap an ideal annular gap (without eccentricity), we end up with a Hele-Shaw cell (figure 5.6). We are interested in the dynamic of the film left by the displaced fluid (see figure 5.6), we would like to observe the plane perpendicular to the streamwise direction.

The fabrication process has limitations, so that compromises have to be made between the following requirements:

1. A direct observation of the film
2. A channel of sufficient height ($\approx 100\,\mu$m) to avoid slip heterogeneities effects
3. A channel with straight walls
4. A channel following the standard protocol of fabrication (described in chapter 2) and in which we can add obstacles where the film is located
5. A channel that sustains high pressure drop, because the fluids used are highly viscous

The geometries considered for the experiments are presented on figure 5.7 with their respective features.

Hele-Shaw cells (left of figure 5.7) are easy to fabricate with standard photolithography process and obstacles can be added on the walls where the film is located. But the major drawback of this geometry is that we have no direct optical access to the film.

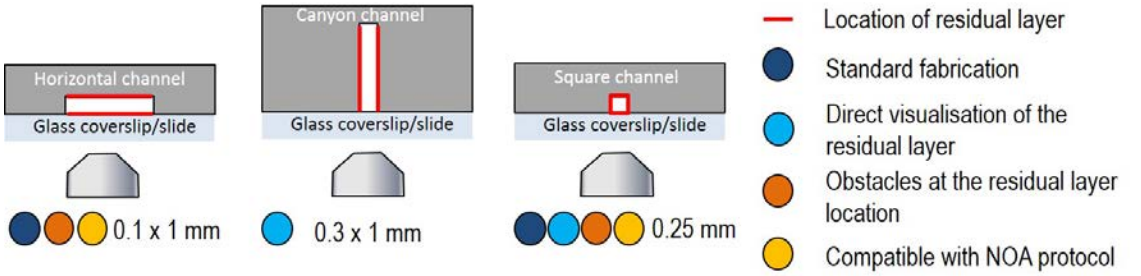

Figure 5.7 – Geometries considered for the displacement experiments and their respective advantages.

In the case of the canyon geometry (see figure 5.7 middle) it is difficult to obtain straight walls with the photolithography process (see chapter 3). Canyons are not adapted to the build-up of obstacles.

A good compromise is the square channel (see figure 5.7 right). A typical dimension of 250 µm allows to fabricate channels with straight walls with the standard photolithography technique. It is possible to add obstacles that can be directly observable. Most of the experiments were carried out with square channels.

5.2.3 Channels with geometry variations in the streamwise direction

Let us recall that inside the annular, several objects such as centralizers, collars or the transition from one casing section to the other induce a restriction across the annular gap (see chapter 1). During cementing, the cement flows from the top of the surface to the bottom of the well, at this point the cement flows in the nose float shoe and has to do a U-turn to enter and to go back up into the annular. The cement and mud that flow in the annular gap are in contact with two different surfaces: on one side the casing and on the other side the rough formation.

Consequently we choose to study three kinds of obstacles:

— A restriction to simulate the presence of collar or section changes.
— Corrugations along the channel walls to simulate the roughness of the formation.
— An angle to simulate a sudden change of direction such as what occurs at the bottom of the well. This part is presented in appendix E.

5.3 The problem of the suppression of the slip in the channels

In chapter 3, our technology led to make channels in which fluids always slip. Here, we want to consider also the important case where slippage is suppressed. For this purpose our microchannels are treated with a PEI solution that hinders the slippage of the microgel suspensions without affecting the optical quality of observation. The treatment changes the repulsive glass surface to an attractive surface with respect to the microgel.

Figure 5.8 represents the velocity profiles obtained in a Hele-Shaw cell (a) and in a square channel (b) that were treated with a PEI solution. The velocity profiles in the square channel are taken at the symmetry plane of the square section ($z = 0$). Since the channels are deep as compared to the working distance of the objective, only half of the velocity profile is measured. All the surfaces being the same, the velocity profiles are assumed to be symmetric with respect to the middle axis of the channel.

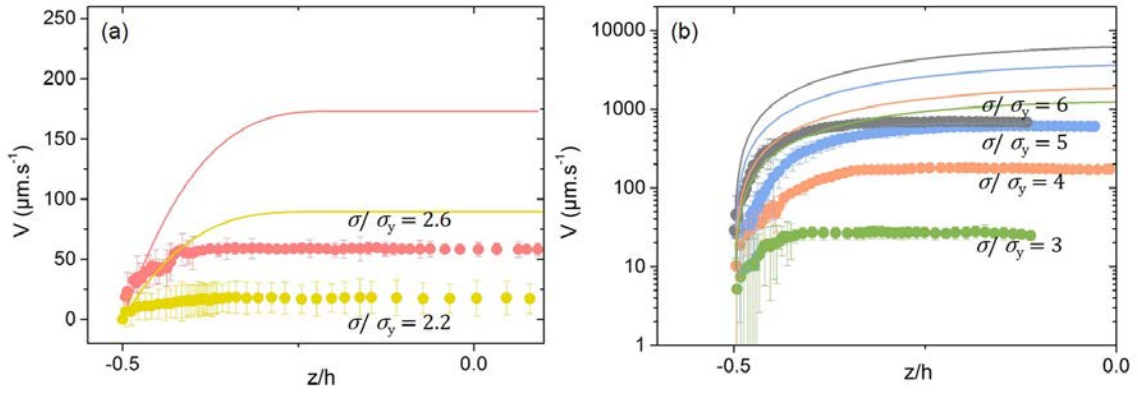

Figure 5.8 – Half velocity profiles V of a microgel 1.6% flowing in (a) a Hele-Shaw cell with $h = 80$ µm and in (b) a square channel with $b = 250$ µm for various reduced stress $\sigma/\sigma_y = 6$ (gray), 5 (blue), 4 (red), 3 (green), 2.6(pink), 2.2 (yellow) with PEI treated walls. There is no slip in the channels. Solid lines are the theoretical Herschel-Bulkley velocity profiles.

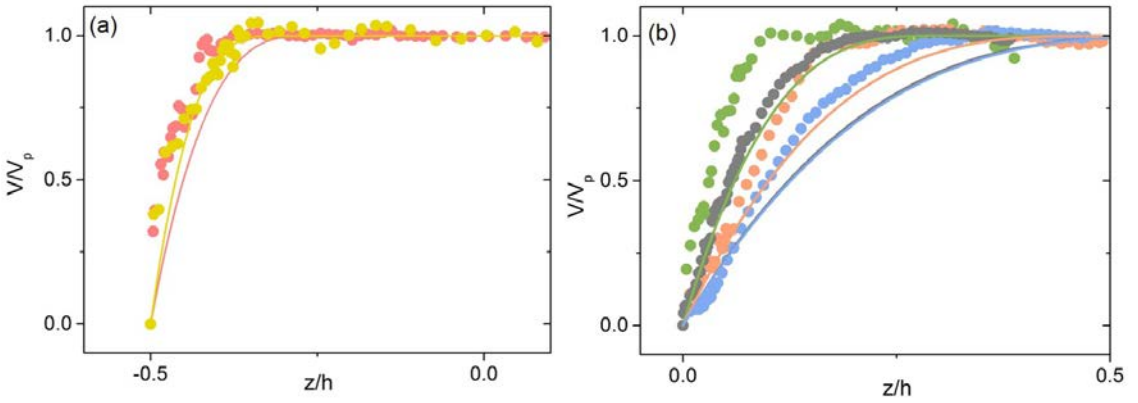

Figure 5.9 – Velocity profiles scaled by the plateau velocity of a microgel concentrations 0.016 g/g flowing in a (a) Hele-Shaw channel of height 80 µm and in a (b) square channel with no slip at various reduced shear stress: $\sigma/\sigma_y = 6$ (gray), 5 (blue), 4 (red), 3 (green), 2.6(pink), 2.2 (yellow). The solid lines are the theoretical shapes of the velocity profiles whose pressure gradients have been adjusted to match the experimental central plug velocities.

Figure 5.8 confirms that the microgel suspension does not slip. Meanwhile, the maximum speed is considerably slowed down (from 3 to 50 times slower) as compared to the expected HB profiles (see solid lines on figure 5.8).

On figure 5.9 we have compared the experimental data with HB profiles for which the plateau speeds have been adjusted to the experimental one. It shows that the behaviour of the microgel near the attractive surface is different from what is expected considering the macroscopic constitutive law of the material. The slope at the wall is larger than expected and the plateau is wider. Consistently with [163], we suggest that the attractive surface induces a non-local rheology.

To summarize, the PEI surface treatment satisfactorily suppresses slippage. However it should not be overlooked that for reasons that are not clearly explained in the literature, this treatment gives rise to non-local rheology that may complicate the interpretation of the results.

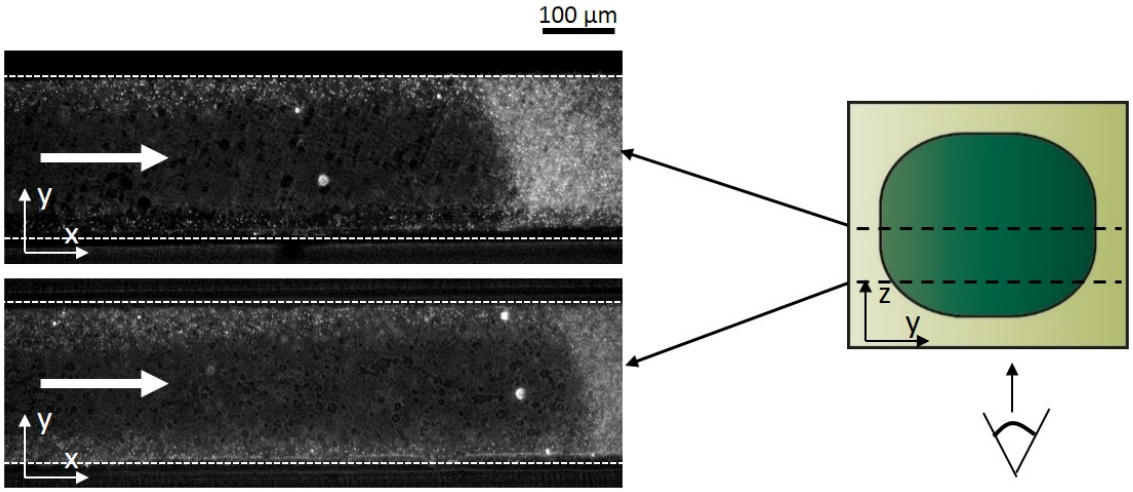

Figure 5.10 – Film left behind the interface for the displacement of a microgel 2.2% by a microgel 1.6% at a pressure drop of 0.5 bar with no slip at the walls. The focus of the microscope objective is made at the symmetry plan (top line) of the channel and denser to the bottom of the channel (bottom). the film thickness varies weakly in the center part of the channel.

5.4 Experimental study of the displacements of HB fluids in square straight channels

5.4.1 Description of the phenomena in square channels

General behaviour of the interface with no slip

In square channels, we carry out displacements of a microgel 2.2% or 3% by a microgel 1.6%, by water, glycerol or oil. The displacements are made at constant pressure drops.

Characteristic 1: the interface leaves a film behind it.

This characteristic is observed on figure 5.10 in the case of a microgel displacing another microgel. The comparison between the top and the bottom line of figure 5.10 shows that the film thickness varies weakly in the central part of the channel up to around 25 µm from the top and bottom surfaces (the depth of field of the objective is around 10 µm which is much smaller than the channel depth).

The observation of the film is confirmed with different displacing fluids as shown on figure 5.11. Figure 5.12 shows that the film thicknesses depend on the nature of the displacing fluid.

In the case of microgel/microgel we shall see that minimum dissipation theory provides an estimate of the film thickness agreeing with the observation.

In the case of oil/microgel (see figure 5.11 (b) and figure 5.12) we suggest that capillarity works at thinning out the film in a way similar to Bretherton's situation. Rough estimates tend to confirm this hypothesis.

The cases of water/microgel and glycerol/microgel is more complex. On figure 5.11 (c) and (d) we observe that the interfaces adopt the shape of a mushroom. Still figure 5.12 shows that a film is present behind the interface. Nonetheless we have not found clues al-

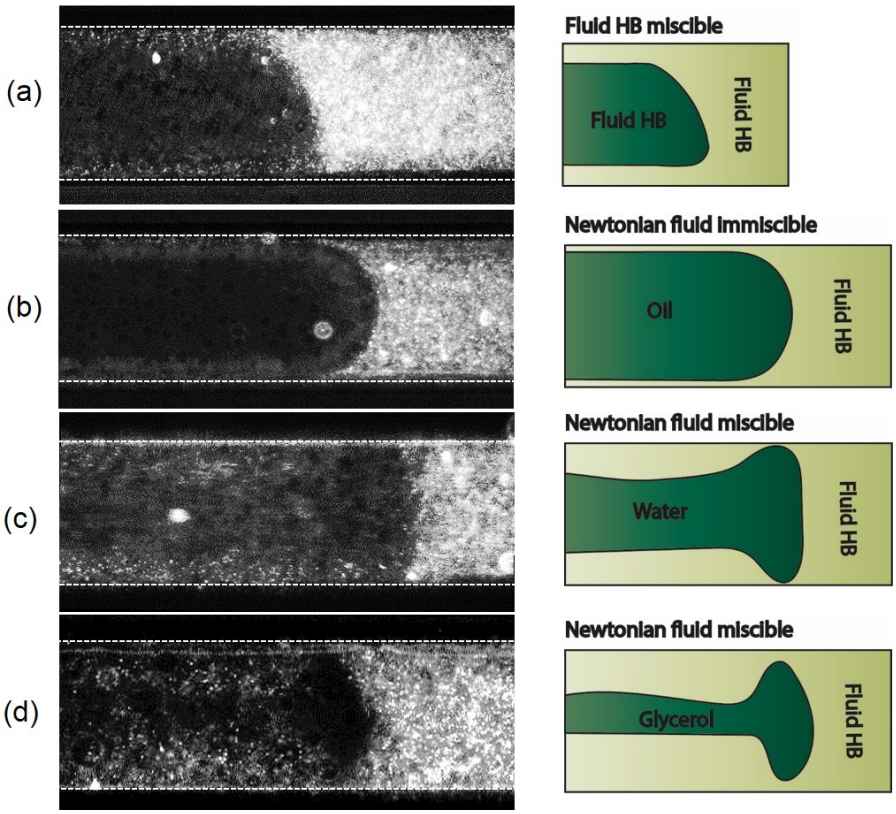

Figure 5.11 – Interface shape between a microgel 2.2% displaced by (from top to bottom): (a) a less viscous microgel 1.6%, (b) immiscible oil $\eta = 25 \cdot 10^{-3}$ Pa s, (c) miscible water $\eta = 10^{-3}$ Pa s and (d) miscible glycerol $\eta = 25 \cdot 10^{-3}$ Pa s.

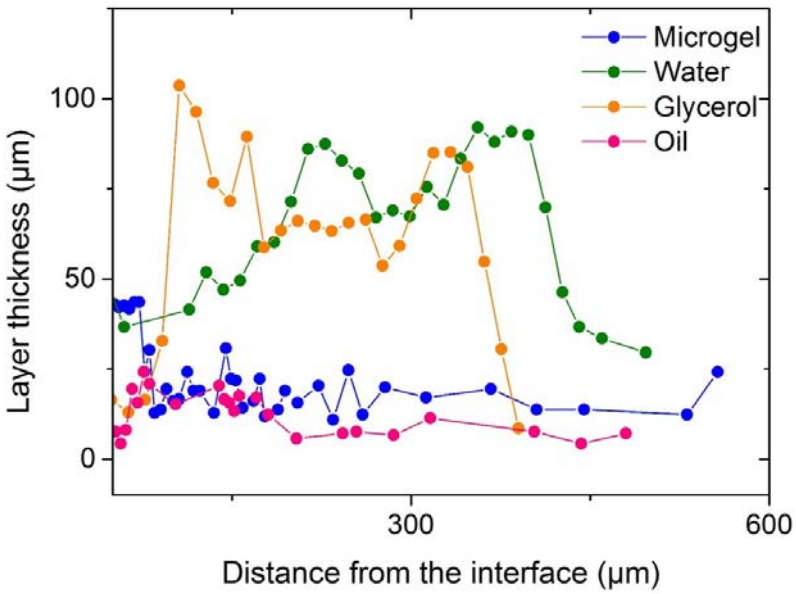

Figure 5.12 – Layer thickness measured behind the interface between a microgel 2.2% displaced by: a microgel 1.6% (blue), water (green), glycerol (orange) and oil (pink).

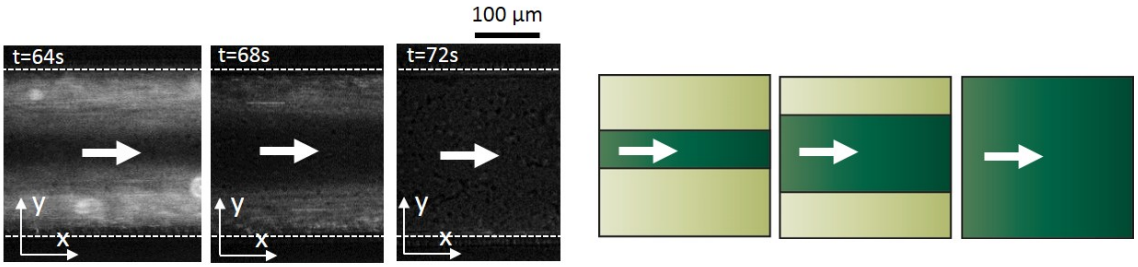

Figure 5.13 – Evolution of the film with time for the displacement experiment in a square channel with a microgel 1.6% displacing a microgel 2.2% at a pressure drop of 0.5 bar with no slip at the walls. From left to right: the film is progressively removed from the channel. The reference for the time scale corresponds to the beginning of the experiment.

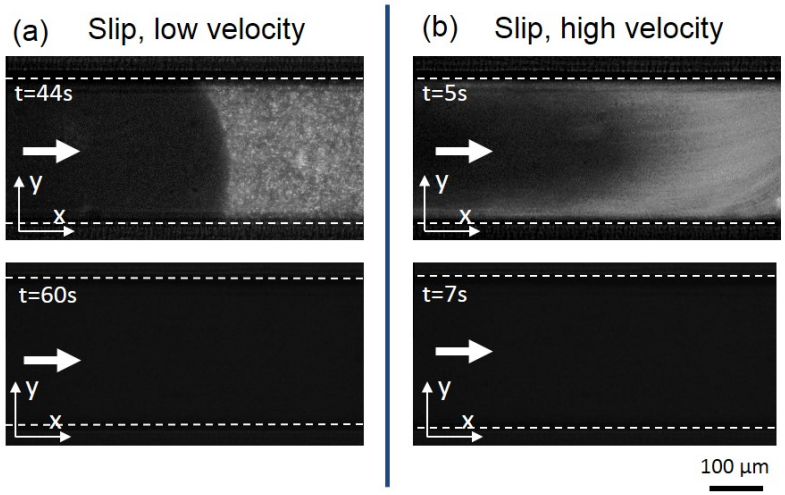

Figure 5.14 – Stages of the displacement in a square channel of a microgel 2.2% by a microgel 1.6% with slip at 0.3 bar (left panel) and at 2.5 bar (right panel) at different times. The reference for the time scale corresponds to the beginning of the experiment.

lowing to understand the film thickness in the case of water/microgel and glycerol/microgel.

Characteristic 2: the film is drained after some time.

Figure 5.13 (from left to right) shows that the layer is drained progressively from the channel after 72 s. This time depends essentially on the pressure drop applied.

Typical behaviour of the interface with slip

The case of slip contrasts with the no slip situation at low speeds. Figure 5.14 (a) shows that there is no measurable film left at the wall within the resolution of the experiment (around 5 µm). In the case of larger speeds (see figure 5.14 (b)), a film is left but it is completely removed after 6 s. As in the no slip case, this time essentially depends on the pressure drop applied.

Evolution of the interface speed in the streamwise direction

Figure 5.15 shows the velocity of the interface as a function of its position in the channel for the displacement of a microgel 2.2% by a microgel 1.6% at various pressure drops. As

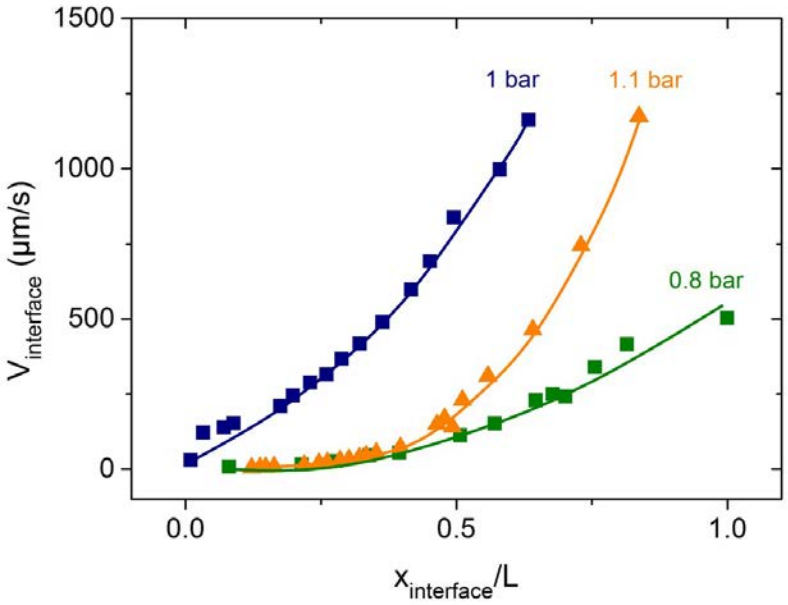

Figure 5.15 – Representation of the velocity of the interface as a function of its position along the x-axis scaled by the channel length L, in the case of the displacement of a microgel 2.2% (square) and a microgel 3% (triangle) at several imposed pressure drop: 0.8 bar (green), 1 bar (dark blue), 1.1 bar (orange). The solid lines are guides for the eyes.

expected, the velocity of the interface increases as it gets closer to the outlet of the channel. This evolution is the consequence of working at constant pressures and not a constant flow rates (which was not practically feasible with Herschel-Bulkley fluids). This absence of invariance along the channel may complicate the interpretation of the phenomena. In practice, we have averaged our measurements along the channel length.

5.4.2 Evolution of the film thickness with the speed

Figure 5.16 represents the film thickness scaled by the half width of the channel as a function of the interface velocity taken at $x = L/2$. These measurements have been obtained in the case of slip and no slip at the walls.

In the no slip case, the film thickness ranges between 20 and 30% of the half side of the channel, independently of the speed. The measurements are in good consistency with C. Gabard work performed with similar fluids in tubular geometry. It indicates that despite the different scales between the experiments, our results provide a comparable quantitative information on the film thickness.

Moreover, the film thickness seems to be understood theoretically since these measurements are consistent with the recirculation model described in appendix B. The recirculation model gives the thickness of the film left at the walls of a tube. We applied this result to our square geometry by taking the hydrodynamical radius of our channels b. We obain the following expression for the relative film thickness:

$$h = b\left(1 - \sqrt{\frac{\bar{U_L}}{U_{L,max}}}\right) \tag{5.1}$$

With b the hydrodynamical radius of our microchannels, $\bar{U_L}$ the mean velocity of the displaced fluid and $U_{L,max}$ the maximale velocity of the displaced fluid.

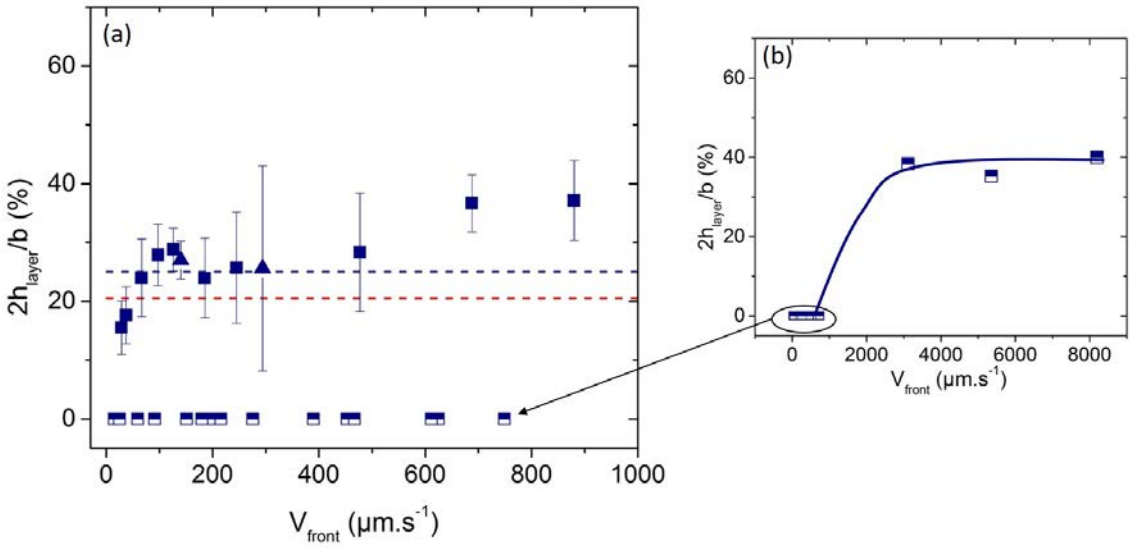

Figure 5.16 – (a) Thickness of the film scaled by the half width of the channel left at the walls as a function of the interface velocity (taken at $x = L/2$) for the displacement of a microgel 2.2 % (square) or 3% (triangle) by a solution of microgel 1.6% in systems without (full symbols) and with (half full symbols) slip. The blue dotted line corresponds to the experimental asymptotic value of the layer thickness for the displacement of a yield stress fluid by another yield stress fluid determined at larger scales in [58]. The red dotted line corresponds to the recirculation model presented in appendix B. (b) Thickness of the film scaled by the half width of the channel left at the walls as a function of the interface velocity (taken at $x = L/2$) for the displacement of a microgel 2.2 % (square) by a solution of microgel 1.6% in systems with slip. The solid line is a guide for the eyes.

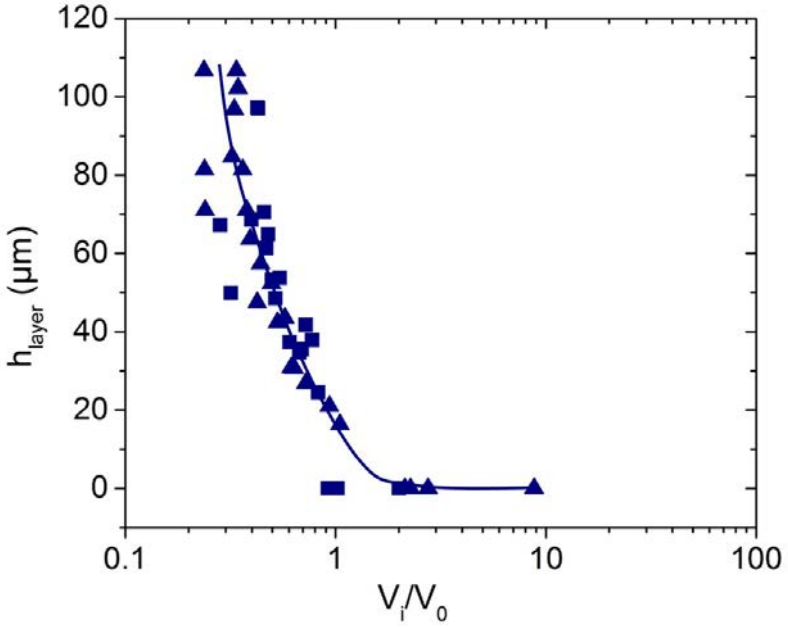

Figure 5.17 – Thickness of the film left at the walls as a function of the number of injected channels volume V_i/V_0 for the displacement of a microgel 2.2% (square) and a microgel 3% (triangle) by a microgel 1.6% at different pressure drops (0.8 to 1.4 bar). The solid line is a guide for the eyes.

The expression of the film thickness (equation 5.1) does not depend on the flow rate which explains the plateau obtained in the experiments at large speeds.

As compared to the literature, the experiments extend the range of validity of the recirculation model down to the micrometric scale. More generally, this suggests that the theory applies in a wide range of system sizes.

In the case of slippage, the picture is different. As shown in section 5.4.1, there is no measurable film at low velocities (see figure 5.16). Above $2\,\mathrm{mm\,s^{-1}}$, a film appears, whose thickness is comparable to the no slip case (see the inset of figure 5.16). We speculate on the origin of the growth of this film by noting that at large pressure drops, the bulk is driven at speeds much larger than the slippage velocity at the wall. The former grows, roughly, by the square of the pressure drop, while the latter grows linearly in the wall stress. In such circumstances, we tend to approach the no-slip case, since slippage tends to become negligible. This may explain why we recover a film with characteristics similar to the no slip case. Nonetheless, a more detailed explanation would be needed to support this hypothesis.

5.4.3 Evolution of the film thickness with time

To analyze the evolution of the film thickness with time, it is convenient to translate time into the fluid volumes injected in the channel: $V_i = Q * t$ in which Q is the flow rate and t the time. V_i is scaled by the channel volume V_0 between the T-junction and the outlet of the channel. This is the number of injected channel volumes. Engineers in the oil industry often use this quantity to evaluate the volume of fluids to be pumped during cementing jobs.

Figure 5.17 collects all the data of the evolution of the film thickness for different fluid rheologies and applied pressure drops. We note that all the data collapse on one curve

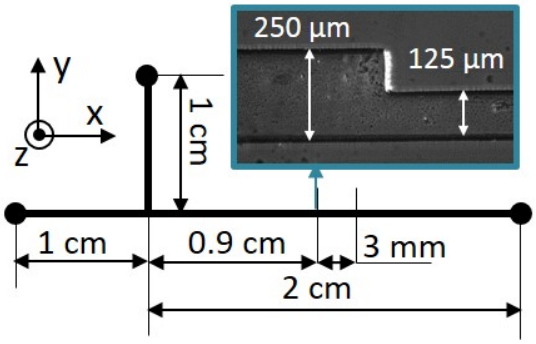

Figure 5.18 – Geometry of the restriction channel.

independently on the fluid rheologies and on the pressure drops. The film is removed completely from the channel within around 1.5 channel volumes injected.

5.4.4 Summary of the results in straight channels

This part has shown that important differences exist between the cases where fluids slip or not. Film thicknesses are much smaller in the former than in the latter case. This may be understood intuitively: flat fronts represent a signature of plug flow profiles observed at small speeds, when slippage is present. Nonetheless more quantitative analysis is certainly needed to reach an acceptable understanding of these phenomena.

5.5 Experimental study of the displacements of HB fluids in channels with restrictions

In this section, we perform displacement experiments in channels with restrictions placed along the streamwise direction (see figure 5.18). Let us recall that this obstacle is a model for objects like centralizers or collar that are currently used to centralize the casing in the borehole (see chapter 1).

5.5.1 Description of the phenomena in the restriction channels

The channel has a square section 250 x 250 µm (see figure 5.18). Before the experiment starts, the channel is filled with the displaced fluid. The restriction width is 125 µm and it extends over a length of 3 mm.

On figure 5.19, the displaced fluid is a microgel 2.2% and the displacing fluid is a microgel 1.6%. The pictures show the channel before and after the restriction with no slip and slip at the walls.

The principal characteristics of the displacement in restriction channels are:

— With no slip (see figure 5.19 left column), the film gets thicker in the restriction and at the outlet of the restriction. It looks counter-intuitive that the film thicknesses before and after the restriction are so different. We have not succeeded to understand the physics of this phenomena.

— With slip at low velocity (see figure 5.19 middle column): the front moves as a plug and leaves no film behind before the restriction. The film thickness increases in the restriction because the velocity increases. It is thin again after the restriction.

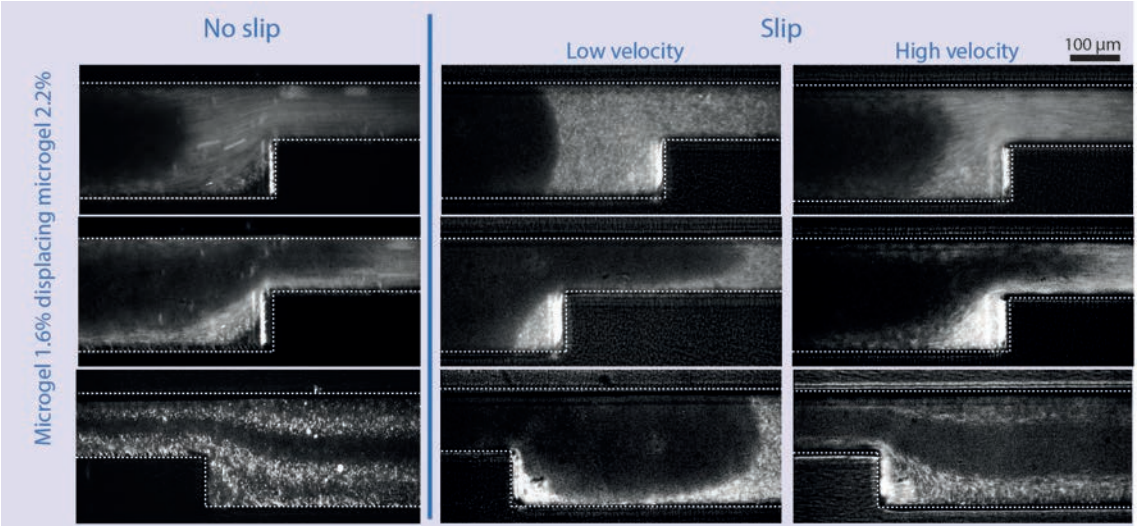

Figure 5.19 – Displacements of a microgel 2.2% by a microgel 1.6% in restriction channels with slip and no slip. With slip, the displacements at low velocities and high velocities exhibit different behaviours, namely a film forms in the latter case.

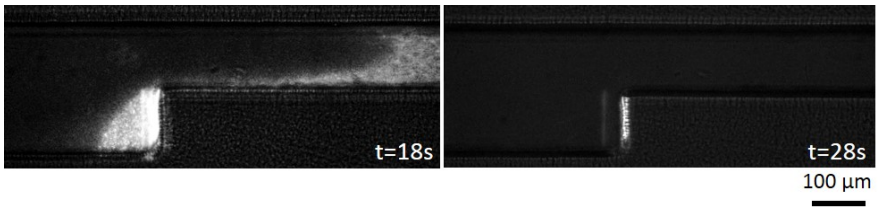

Figure 5.20 – Displacements of a microgel 2.2% by a microgel 1.6% in restriction channels with slip. The restriction retains some of the displaced fluid but only for a short time. The reference for the time scale corresponds to the beginning of the experiment.

— With slip at high velocity (see figure 5.19 right column): a film develops and its thickness increases in the restriction and at the outlet of the restriction. We recover the same characteristics as the no slip case.

The restriction retains some of the displaced fluid. We have not studied this phenomena in details but we have observed that when the interface reaches the outlet, the channel is completely empty as shown on figure 5.20.

5.5.2 Evolution of the film thickness with time

Figure 5.21 shows the evolution of the layer thickness as a function of the number of channel volumes injected for slip and no slip. We observe that in all cases, the film is drained within less than 10 channel volumes injected.

On figure 5.21 two regions can be distinguished: the blue region corresponds to the experiments with slip at the wall and the yellow region corresponds to the experiments with no slip. We can see that it takes about five time less injected channel volumes to remove the film when slippage is present. Figure 5.22 shows the difference between channels with no slip (a) and with slip (b) at the time where the meniscus leaves the channel. We observe that the film is much thicker in the former than in the latter case. This result is intuitive

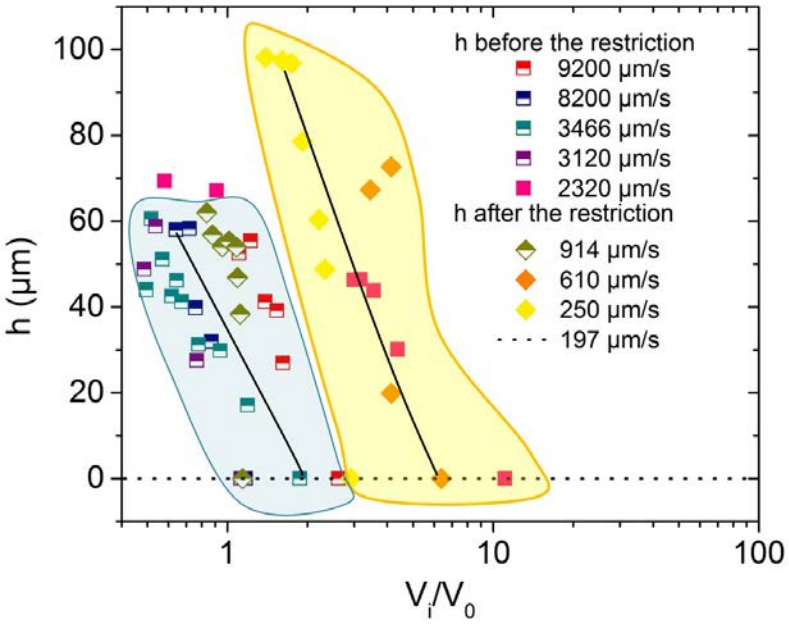

Figure 5.21 – The evolution of the thickness of the layer as a function of the number of injected channels volume V_i/V_0 for slip (half full symbols) and no slip (full symbols) boundary conditions. The solid lines are guides for the eyes.

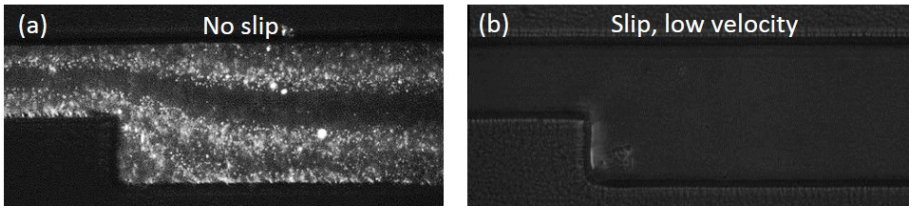

Figure 5.22 – Film thickness at the time the interface leaves the channel for (a) no slip and (b) slip at low velocity for the displacement of a microgel 2.2% by a microgel 1.6%.

for two reasons:

— initially the film is thinner in the slip case
— the film can be more easily mobilized when there is slippage.

Nonetheless, we have not succeeded to provide a quantitative analysis of the film drainage dynamics.

5.5.3 Summary of the results in channels with restrictions

In the no slip case, the film thickness increases in the restriction and at the outlet of the restriction.

In the slip case, the displacement occurs as a plug at moderate velocities. At higher velocities, we observed a behaviour analogous to the no slip case.

In all cases, the layer is drained from the channel within less than 10 channel volumes of fluid injected. The drainage process is faster in the slip case than in the no slip case.

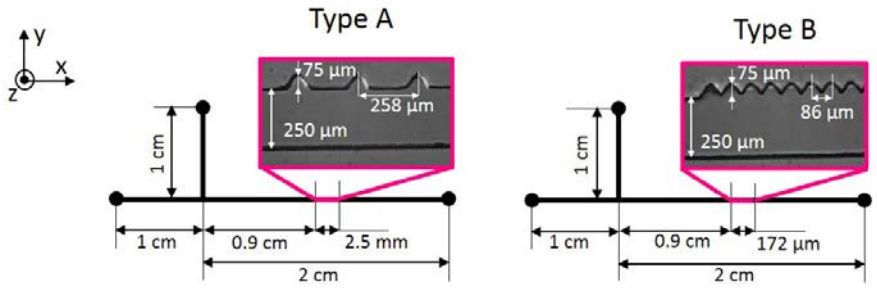

Figure 5.23 – Geometry of the dense and spaced corrugations in the channels, the details of the dimensions of the corrugations are shown on the pictures.

5.6 Experimental study of the displacements of HB fluids in channels with corrugations at the wall

The second type of geometrical feature are channels with corrugations (they represent the roughness of the formation). We analyze the influence of the density of the corrugations, of the pressure gradient and of the slip at the walls.

5.6.1 Description of the experiments in channels wih corrugations at the wall

Figure 5.23 shows the details of the dimensions of the corrugations. Two types of geometries were considered as shown on figure 5.23:

— Type A: the corrugations are spaced.

— Type B: the corrugations are next to each other.

The corrugations are located in the middle of the channel and they extend over a length of 172 µm for the geometry of type B and of 2.5 mm for the geometry of type A. The initialization of the system is the same as the straight and restriction cases.

Figure 5.24 represents pictures of the interface near the corrugations in different cases. The characteristics of the displacement are:

— With no slip a film forms behind the interface as shown on the left column of figure 5.24.

— With slip at low velocity no film forms before the corrugations (as in the paragraph 5.5.2). But figure 5.24 (first lines of (a) and (b)) shows that the presence of the corrugations induces the formation of a film composed of the displaced fluid along them. We observe an asymmetry with respect to the corrugated or non corrugated side. This effect is enhanced when the corrugations are closer to each other. This suggest that the corrugations hinder the slippage and consequently favour the formation of a film.

— With slip at larger speeds the symmetry is restored in both geometries as shown on figure 5.24 (bottom lines of the middle and right columns). Probably we tend to approach the no slip case in both geometries.

5.6.2 Evolution of the drainage of the fluid in the corrugations with time

We measure the area of the displaced fluid present in the corrugations over time in channels with slip or no slip.

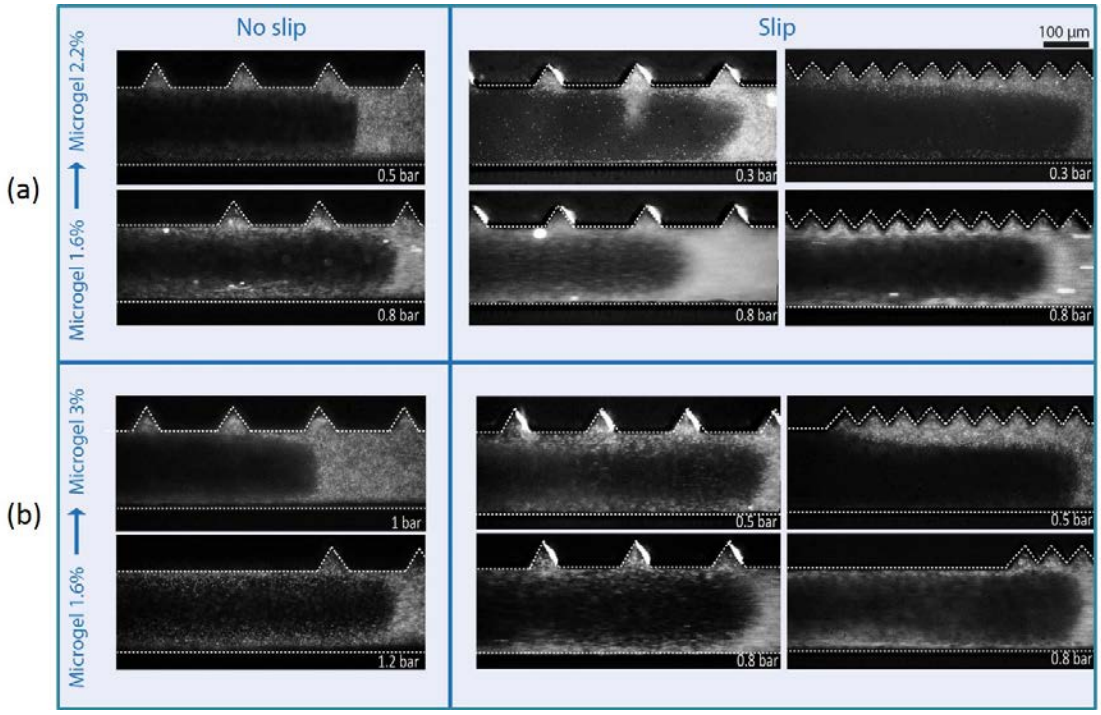

Figure 5.24 – Displacement of a microgel 2.2% (a) and 3% (b) by a microgel 1.6% in the geometry of type A and B with slip and no slip at various constant pressure drops and at a time such that the interface passes along the corrugations. In the slip regime, important differences are observed between the geometries of types A and B during the advancement of the interface along the corrugations.

Figure 5.25 compares the drainage of the fluid in the corrugations with no slip and with slip at large speeds.

Even though the characteristics of the displacement with slip at high velocity is close to the no slip case, we find that, with slip the clearing out of the corrugations is faster. Indeed, figures 5.25 (a) and (b) shows that clearing out is possible with slip while with no slip we still have a significant amount of fluid in the corrugations. Figure 5.26 illustrates the state of the corrugations when 4 channel volumes have been injected.

This point is worth pointed out because it shows a difference between slip and no slip even though some similarities have been observed at large velocities between the two situations (see paragraphs 5.4.2 and 5.5.1).

5.7 Towards a more realistic geometry: the Hele-Shaw cell

5.7.1 Typical behaviour of the interface with no slip

Figure 5.27 shows the propagation of the interface in the channel during the displacement of a microgel 2.2% by a microgel 1.6%. We observe the side of a finger propagating in the channel as shown on the sketch on the right of figure 5.27. By performing the observation in the frame of reference of the interface, we see that a steady film forms behind the interface as the interface advances in the channel (from left to right). This phenomena is similar to the square channel case although, quantitatively, the film thickness is much smaller. For reasons that are unclear, the dissipation theory does not seem to agree with the observation in this case.

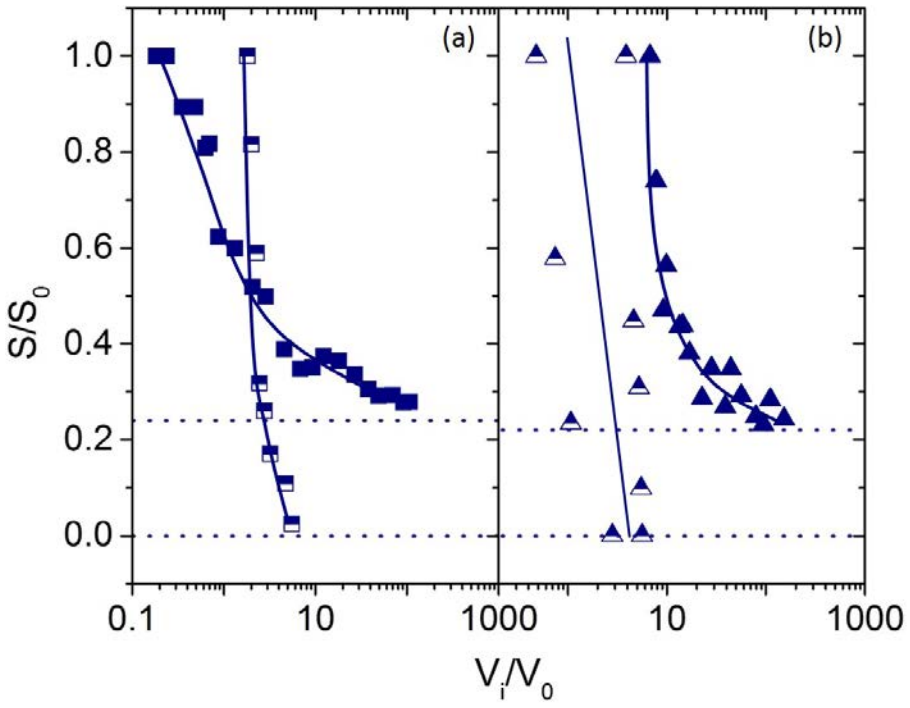

Figure 5.25 – Area of displaced fluid remaining in the corrugation scaled by the area of a corrugation as a function of the number of injected channels volume V_i/V_0 in the geometry A with no slip (full symbols) and with slip in the geometries A and B (half full symbols) for the displacement of (a) a microgel 2.2% (b) a microgel 3% with a microgel 1.6% at the highest velocity (0.8 bar). The solid lines are guides for the eyes.

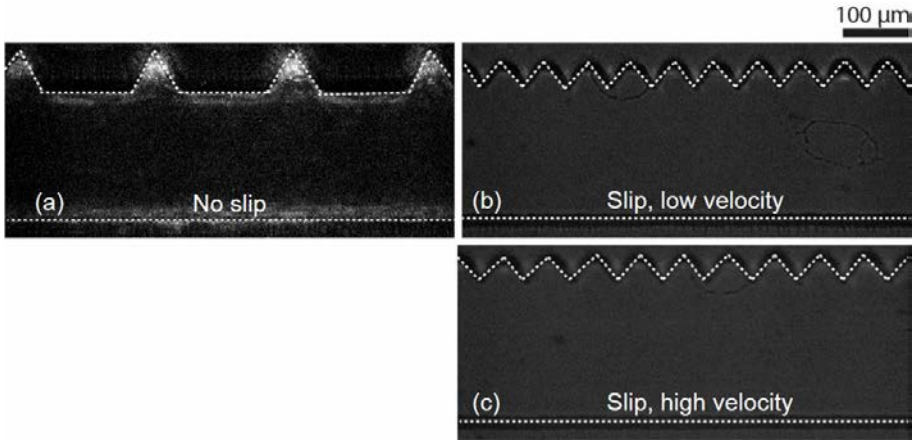

Figure 5.26 – Pictures of the corrugations when 4 channel volumes have been injected for the displacement of a microgel 3% with a microgel 1.6% (a) with no slip at 0.8 bar, (b) with slip at 0.6 bar and (c) with slip at 0.8 bar.

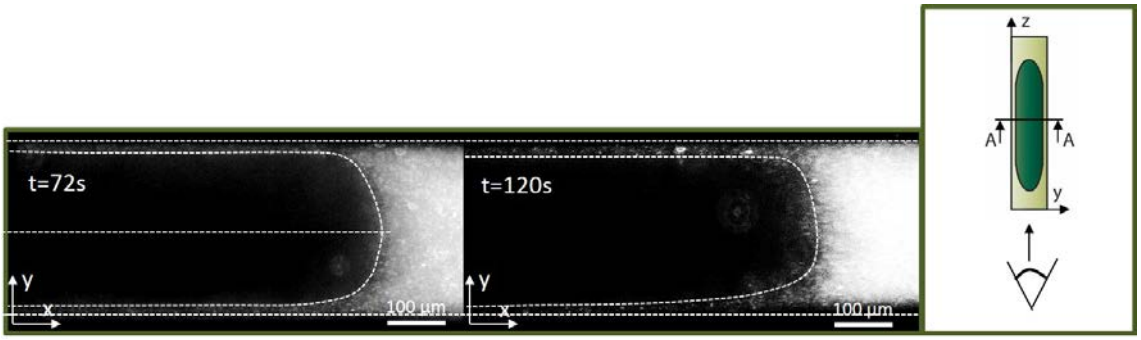

Figure 5.27 – Propagation of the interface in the moving frame of reference of the finger in a canyon channel without slip when a microgel 1.6% is displacing a microgel 2.2% at a constant pressure drop of 0.5 bar. A film is formed behind the interface. The reference for the time scale corresponds to the beginning of the experiment.

Figure 5.28 shows a complex evolution of the film after the interface has exited the channel. First, the film thickness varies considerably and non-monotonically with time (see figure 5.28 (a)). Secondly, an important part of the displaced fluid migrates to the center of a channel, while a thin layer of this fluid stays at the wall (figure 5.28 (b)). Finally, we return to the original situation with the thicker fluid on the side, the thickness of the layer is not constant along the length of the channel (figure 5.28 (c)) and it can be removed at longer times. This complex evolution remains to be understood.

5.7.2 Typical behaviour of the interface with slip

In the case with slip, figure 5.29 shows that no film is left at the walls. This is in agreement with the results obtained in square channels at low speeds.

5.8 Conclusions

All the experiments showed that the presence of slippage at the walls of the channel considerably improves the displacement efficiency in all the geometries considered.

Without slippage, the layer thicknesses measured in straight channels are in quantitative agreement with previous experiments performed at larger scale [58]. The film thickness is well described by a minimum dissipation theory. With slippage a film appears only at large speeds. Without slippage the film decays with time, the decay is faster with slippage.

For some obstacles (corrugations), slippage is the only configuration where the film can be removed from the geometry.

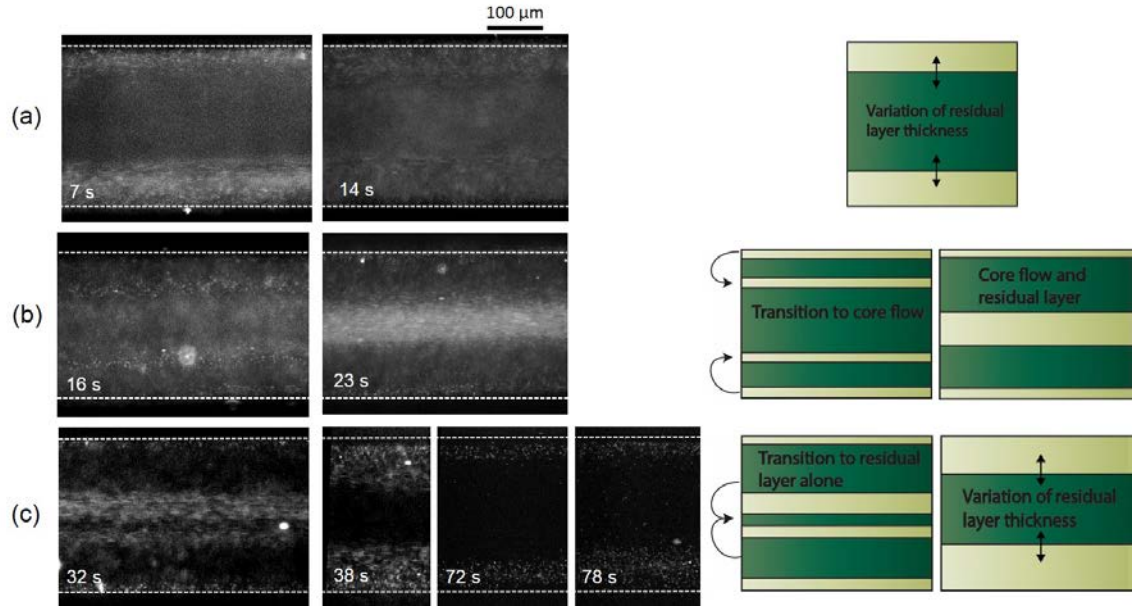

Figure 5.28 – From (a) to (c) Time evolution of the flow of a microgel 2.2% displaced by a microgel 1.6% with no slip at the walls at a constant pressure drop of 0.5 bar after the meniscus has exited the channel: a complex dynamic takes place where the two phases exchange position.

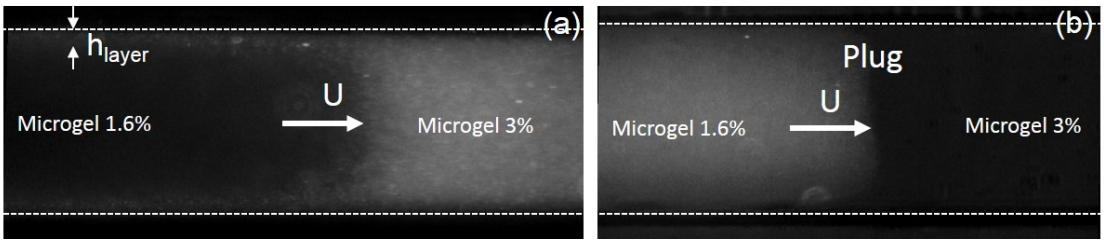

Figure 5.29 – Comparison of the shape of the interface between no slip (a) and slip (b) during the displacement of a microgel 3% by a microgel 1.6% at 0.5 bar. No film is left at the walls in the case of slippage.

Displacement of Herschel-Bulkley fluids in microchannels

- ✧ **Experimental study of the displacements of HB fluids in straight channels**
  - With no slip a film forms. The thickness of the layer measured ranges between 20 and 30% of the channel half width and is comparable to the previous experiments realized at larger scale [58].
  - With slip at low velocity we observe plug-like displacements and no film forms. At high velocities, the interface is stretched which results in the formation of a film.
- ✧ **Experimental study of the displacements of HB fluids in restriction channels**
  - The thickness of the layer increases greatly after the restriction.
  - The drainage of the film is more efficient with slip.
- ✧ **Experimental study of the displacements of HB fluids in corrugation channels**
  - With no slip: a film forms. The corrugations cannot be completely cleared out.
  - With slip at low velocity the displacement shows an asymmetry between the walls with and without corrugations. This effect is enhanced when the corrugations are closer to each other.
  - With slip at high velocity, the displacement is analogous to the no slip case. But the clear out of the corrugations is much more efficient than in the no slip case.

Chapter 6

Simulations with Computational Fluid Dynamics

6.1 Introduction

The equations of fluids mechanics can be summarized as the mass and momentum conservation equations. These equations can only be solved for limited flow configurations. In a lot of other situations, one tries to simplify the equations using approximations and dimensional analysis. An alternative is to consider numerical solutions of the equations. This field is known as Computational Fluid Dynamics (CFD).

The principle of numerical solutions is to obtain an approximate solution of the set of fluid mechanics equations. Therefore, a *discretization method* is used to approximate the equations by a set of algebraic equations, which are then solved on a computer. The results are given at *discrete locations* in space and time. Therefore the domain is divided into smaller domains in space and time (control volume, elements), *the numerical grid or the mesh*, where the approximations are applied. A solver solves the set of non-linear algebraic equations yielded by the discretization process by doing successive linearization of the equation in an iterative scheme (because of the non-linearity of the system). Finally, one needs to decide when the iterative calculation stops, i.e. the *convergence criteria* needs to be determined. Usually two levels of iterations are made: *inner iterations* concern the solving of the linearized system of equations, and *outer iterations* deal with the non-linearity and coupling of the equations. We use the commercially available computational fluid dynamics software Ansys-Fluent [50].

The basic stages followed by Fluent to solve the equations can be summarized as:

1. Division of the domain into discrete control volumes.
2. Integration of the governing equations (mass and momentum) on each control volumes to construct a set of algebraic equations for the variables (velocity, pressure, conserved scalars).
3. Linearization of the discretized equations and solution of the linear equation system, which updates the values of the variables.

Fluent is a CFD tool that accomplishes all the steps described above (discretization, meshing, solving of the equations). Incompressible flows in laminar or turbulent regimes can be calculated amongst other. It is possible to perform steady-state or transient analysis. Also a multiphase flows tool is available. We present briefly the functioning of the Fluent code for the case that interest us: multiphase flows of incompressible fluids in a laminar regime.

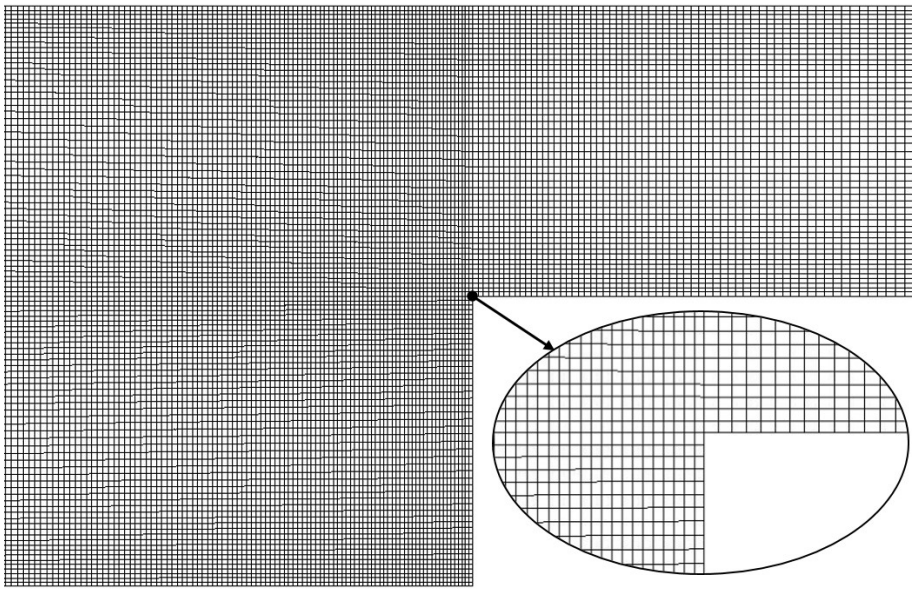

Figure 6.1 – Example of the eulerian mesh used in our simulations.

6.1.1 Mass and momentum equations

Fluent solves the conservation equations for mass and momentum in the eulerian frame of reference. The equation for mass conservation is written as [5]:

$$\frac{\partial \rho}{\partial t} + \nabla \cdot (\rho \vec{u}) = S_m \tag{6.1}$$

Where ρ is the density and $\vec{u}$ the velocity and S_m a source term.

The conservation of momentum is [5]:

$$\rho \frac{\partial \vec{u}}{\partial t} + \rho(\vec{u}.\vec{\nabla})\vec{u} = \rho\vec{g} - \vec{\nabla}p + \vec{\nabla}.\boldsymbol{\sigma} \tag{6.2}$$

ρ is the fluid density, $\vec{u}$ the velocity vector, p the pressure, and $\boldsymbol{\sigma}$ the deviatoric stress tensor. The stress tensor is a function of velocity and fluid viscosity, therefore its form depends on the constitutive law of the fluid (see 2.3.1).

Fluent provides several options to simulate multi-phase flows, including solutions of the mixture equations and solution on a per phase basis.

6.1.2 Mesh

In two-dimensions we use a quadrilateral mesh and in three-dimensions we use a hexahedral mesh. Care is taken to have high resolution near the walls (see figure 6.1).

The size of the mesh results in a compromise between the calculation time (the more cells there are, the longer is the calculation time) and the precision desired. Since the approximation of the set of equation is made over each cell, the smallest the cells are, the better the approximation is.

6.1.3 Discretization method: Finite Volume Method

The Finite Volume method (FV) is one type of discretization method, the two other popular techniques being the Finite Difference method (FD) and the Finite Element method

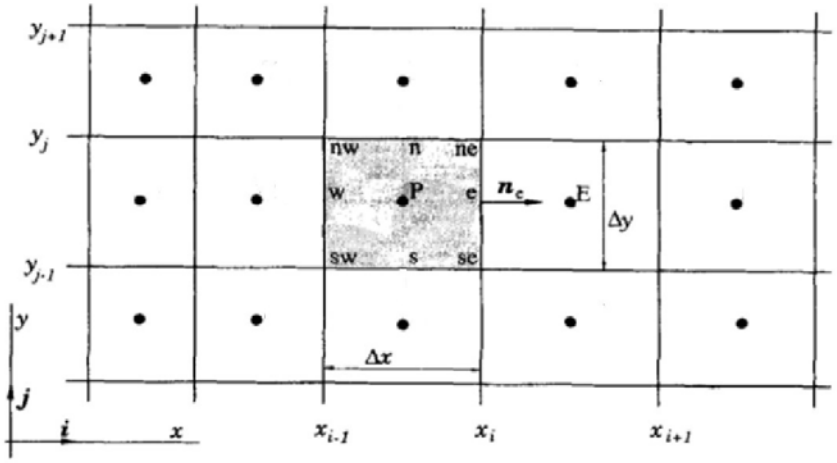

Figure 6.2 – An Eulerian grid with its Control Volume (CV), reproduction from [50].

(FE), they are not described here. The (FV) uses the integral form of the conservation equations on *control volumes (CV)* in the flow domain. A CV is a subdivision of the domain, i.e. a mesh cell. The equation describing the conservation of a scalar variable ϕ over the all domain is:

$$\int_V \frac{\partial \rho\phi}{\partial t} \mathrm{d}V + \oint \rho\phi\vec{u} \cdot \mathrm{d}\vec{A} = \oint \Gamma_\phi \nabla\phi \cdot \mathrm{d}\vec{A} + \int_V S_\phi \mathrm{d}V \tag{6.3}$$

with ρ the density, $\vec{u}$ the velocity vector, $\vec{A}$ the surface area vector, Γ_ϕ a diffusion coefficient for ϕ and S_Φ a source term per unit volume.

The set of equations describing the system needs to be transformed into a discrete (over all the mesh cells) algebraic equation in order to be solved numerically. This is the *discretization process*. At the center of each control volume lies a *computational node* at which the variables are evaluated. The first step of the discretization is to approximate the integrals in terms of the variable values at one or more locations on the cell faces. The approximation of the integrals gives:

$$\frac{\partial \rho\Phi}{\partial t} V + \sum_f^{N_f} \rho_f \vec{u} \Phi_f \cdot \vec{A_f} = \sum_f^{N_f} \Gamma_\Phi \nabla\Phi_f \cdot \vec{A_f} + S_\Phi V \tag{6.4}$$

with N_f the number of faces enclosing the cell, Φ_f the value of Φ convected through face f, $\vec{A_f}$ the area of face f, V the cell volume. Equation 6.4 shows how the surface and volume integrals are approximated in terms of variable values at all the faces surrounding the cell. Indeed, Φ_f is the value of the variable Φ at a face of the CV which is an unknown value. On figure 6.2, Φ is located at point P and Φ_f at the middle of face e.

To transform the initial set of equations into an algebraic system, the surface and volume integrals need to be approximated at each CV using quadrature formulae. Therefore interpolation is used to express the variable value at the center of the cell as a function of the *nodal values* (the center values of the neighbouring CV) and of the surfaces surrounding the CV.

Equation 6.4 contains the unknown scalar variable Φ at the CV center as well as the unknown values in the neighboring CVs. In most of the cases, this equation is non-linear in terms of the other variables. The second step of the discretization is to approximate the

scalar variable Φ_f and its gradient $\nabla\Phi_f$ in terms of the neighbouring nodal values using an interpolation scheme. It results in the linearization of equation 6.4.

Fluent uses an *upwind interpolation* scheme for the approximation of Φ_f in the convective flux term (second term on the left hand side of equation 6.4). It means that the value Φ_f is derived from quantities in the cell upstream relative to the direction of the normal velocity $\vec{u}$. For example, on figure 6.2, if $\vec{u} \cdot \vec{n_e} > 0$, Φ_f on face e is approximated as Φ at point P. Otherwise it would be approximated as Φ at point E. On the right hand side of equation 6.4, $\nabla\Phi_f$ is approximated using *linear interpolation* between the neighbouring and cell center values.

After these two steps, the volume and surface integrals are approximated and linearized in terms of the neighbouring nodal values and it leads to an algebraic system of equations for each control volume for the variable Φ. This procedure is done for all the variables that need to be solved.

6.1.4 Solver methods

The treatment of the momentum equation is complex because there is no independent equation for the pressure, whose gradient contributes to the momentum equation (see equation 6.2). Combining the momentum equation (equation 6.2) and the continuity equation (equation 6.1) allows to determine an equation for the pressure written here for a fluid of constant density and viscosity [50]:

$$\frac{\partial}{\partial x_i}\left(\frac{\partial p}{\partial x_i}\right) = -\frac{\partial}{\partial x_i}\left[\frac{\partial(\rho u_i u_j)}{\partial x_j}\right] \tag{6.5}$$

This way of writing the pressure correction allows the velocity field to satisfy the continuity equation. We see that the governing equations 6.2, 6.1 and 6.5 are coupled to one another. The entire set of governing equations is solved repeatedly until convergence is reached.

We use a pressure-based solver as a numerical method to solve the set of algebraic equations. There are two pressure-based algorithms available in Fluent: a segregated algorithm (SIMPLE algorithm) and a coupled algorithm (COUPLED algorithm).

SIMPLE algorithm

The SIMPLE algorithm solves the governing equations sequentially, it is also called the segregated algorithm. Each variable (velocity components: u, v, w, the pressure p, the volume fraction ρ) has its governing equation which is coupled to the governing equations of the other variables. The SIMPLE algorithm solves these equations one after the other independently from the equations of the other variables (i.e. it solves the equation for u, then for v...). After, the solving the set of variables is updated and convergence is checked.

The advantage is that it is memory-efficient but convergence is slow.

COUPLED algorithm

With the COUPLED algorithm, the system of equation is coupled: the momentum equations (equation 6.2) and the pressure correction (equation 6.5) are solved at the same time. Therefore, the rate of convergence is significantly improved compared to the SIMPLE algorithm, but the memory requirements is twice that of the segregated algorithm.

The main steps of the two algorithms is represented on figure 6.3.

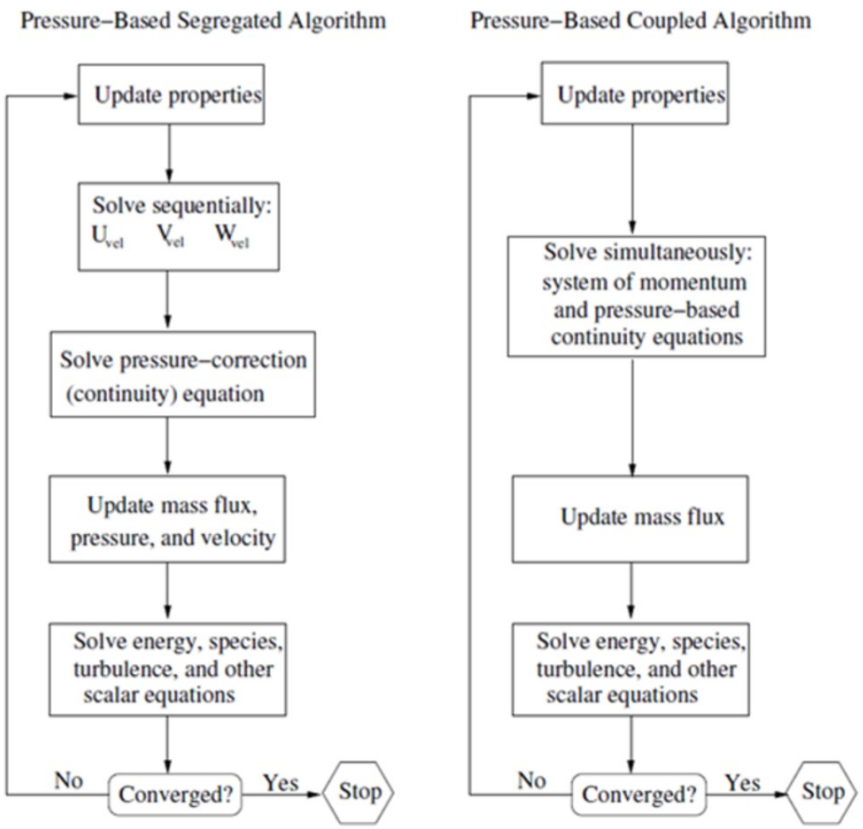

Figure 6.3 – Comparison between the segregated and the coupled algorithms.

6.1.5 Multiphase flows, the Volume Of Fluid method

The Volume Of Fluid (VOF) model is a surface-tracking technique that is designed for multiphase flows where the aim is to find the interface between the fluids. In this model, the fluids share a single momentum equation with density and viscosity depending on the volume fractions of each phase. The velocity field is shared amongst the phases. The volume fraction of each fluid is determined for all the cells of the mesh.

The tracking of the interface between the fluids is made by solving a volume conservation equation for the volume fraction of one of the phases:

$$\frac{\partial c}{\partial t} + \nabla \cdot (c\vec{u}) = 0 \tag{6.6}$$

With c the volume fraction of the fluid.

We do not include surface tension because we consider miscible displacements. Consequently, all stresses are continuous across the interface. Most of the time, and as in our case, the VOF model is used to compute time-dependent solutions.

6.1.6 Courant number

If we take the example of a two phase displacement, the Courant number represents the number of cells over which the interface travels during one time step. It is written as:

$$C = \frac{u\Delta t}{\Delta x} \tag{6.7}$$

With u the imposed velocity, Δt the time step and Δx the cell length. The time step used in the calculation and the size of the mesh are adjusted so that the Courant number is around 1. It means that the interface travels over one cell during one time step. It ensures a good convergence of the calculation and a better precision on the interface position.

6.1.7 Boundary conditions

We need to define the boundary conditions of the system to initiate the calculations. We define the position of the solid boundaries, i.e. the walls of the channel, the area filled with the fluids, the inlet and outlet of the channel and eventually some specific conditions for the walls.

In our calculations, we impose the velocity at the inlet (*velocity inlet* boundary condition) and we impose a constant pressure outlet condition (*pressure outlet*). An alternative set of boundary conditions could be to impose a pressure difference between the inlet and outlet.

In the present study the aim is to study the thicknesses of the films left at the walls and to compare it to experimental data. In the experiments, the films thicknesses are averaged over the channel length. Therefore and for simplicity we choose to carry out the simulations at a fixed velocity rather than at a fixed pressure drop.

This choice simplifies the calculation procedure. It avoids to use variable time step to correct the Courant number over time to keep it around 1. Moreover, there is a high probability that the treatment of the imposed pressure raises numerical difficulties because the pressure is not solved directly (we only have an equation to correct the pressure rather than an independent equation).

In Fluent we impose no slip boundary conditions but a slip boundary condition can be set. It is made by imposing that the walls shear stress equals zero at the wall.

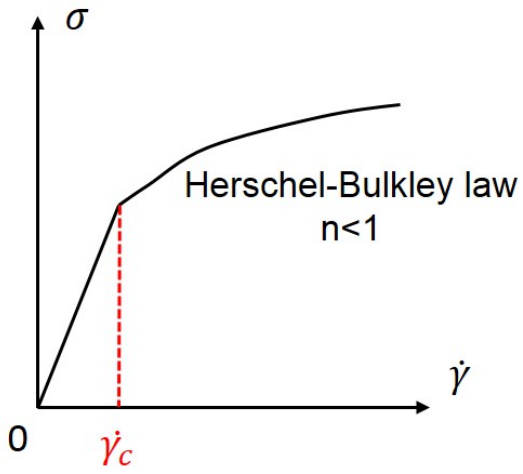

Figure 6.4 – The regularization law used in Fluent for the implementation of the rheological Herschel-Bulkley law.

6.1.8 Yield stress fluids: Regularization law and augmented lagrangian method

The Herschel-Bulkley law, which describes very well the rheology of our fluids, is available in Fluent. The Herschel-Bulkley law has the form: $\sigma = \sigma_y + k\dot{\gamma}^n$ with σ_y the yield stress, k the consistency parameter and n the flow index. The implementation of the Herschel-Bulkley law in Fluent is performed by using a *regularization parameter* in the form of a critical shear rate $\dot{\gamma}_c$. Figure 6.4 shows a graphical representation of the regularization law. The principle of the regularization law is to replace the infinite viscosity at the yield stress by a large but finite viscosity [9]. A review on the use of regularization law is found in [55].

The regularization parameter value sets the precision accessible for the determination of the yield and unyielded surfaces in the flow. We try to set this parameter as low as possible, but too low values can raise convergence problems. Therefore, the choice of the value of the regularization parameter results from a compromise between the precision desired on the determination of the yield/unyielded surfaces and the possibility for Fluent to solve the problem.

Another method has been developed to compute viscoplastic flows which is called the *Augmented Lagrangian (AL) method*. This method uses the variational formulation of the momentum equations and the flow solution is determined via an optimization algorithm [144]. No regularization law is used with this method. It allows a better determination of the yield/unyielded surfaces but it takes much longer time to run and is more complicated to implement than codes using regularization law [9].

6.2 Objectives of the chapter

Numerical simulations are a tool to analyze the physics of complex flows. Oil engineers often use numerical simulations as a help to design new devices for the field and as a complement to experiments. Indeed, it can be useful to get information not directly measurable in the experiment or to vary independently some parameters of the system. An important application of numerical simulations of complex flow in the oil industry is

the design of the drilling or cementing operations of a well. The simulations help engineers to set the fluid rheologies and casing hardware in order to accomplish proper drilling or cementing jobs. The ability of the models to capture the physical phenomena encountered in the well cementing processes is still a challenge. Comparison between field data and the models are constantly carried out to try to improve the modelling. In this chapter, we follow the same approach and the aim is to see if the experimental data obtained in chapter 5 can be recovered by computational fluid dynamics. Fluent is used to perform the flow simulations.

First, we run some test cases extracted from the literature to see if we get some quantitative agreement with Fluent simulations. Most of these studies use another method than regularization law to simulate yield stress fluids (AL method) which is known to be more precise. In this part all the simulations are solved non-dimensionally. We prove that we get a very good agreement with these studies.

Then, we compare numerical results to our experimental results in the case of straight channels, channels with restrictions and channels with corrugations. The fluid properties are modelled by a Herschel-Bulkley law whose parameters are set according to the results of our rheological experiments presented in chapter 2.

6.3 Validation of the Fluent code

The aim of the paragraph is to verify if Fluent is adapted to calculate diverse flow configurations of yield stress fluids. Therefore, comparisons are made with academic papers. Some limitations or special settings in Fluent to insure the success of the calculation are presented.

6.3.1 Single Herschel-Bulkley fluid in two-dimensional plane channels

The simplest case to start with is the stationary flow of a Herschel-Bulkley fluid in two-dimensional plane channels because an analytical solution exists (see equation 3.1). In Fluent we impose the velocity at the entry of the channel, the fluid properties and the geometry of the channel. The generalized Reynolds number can be deduced:

$$Re = \frac{\rho V^{2-n} (2h)^n}{12^{n-1} \left(\frac{2n+1}{3n}\right) k} \tag{6.8}$$

Where ρ is the density of the fluid, V its mean velocity, h is the height of the two-dimensional channel and k and n are the parameters of the Herschel-Bulkley law: $\sigma = \sigma_y + k\dot{\gamma}^n$ with σ_y the yield stress. The Reynolds number is related to the friction factor through:

$$f = \frac{24}{Re} \tag{6.9}$$

When convergence is reached, we extract the pressure gradient dp/dx value calculated and we estimate the friction factor which can also be written as:

$$f = \frac{dp}{dx} \frac{(2h)}{2\rho V^2} \tag{6.10}$$

The two values obtained from equations 6.9 and 6.10 can be compared to verify the calculation obtained with Fluent.

We recall that in the definition of the fluid properties we need to define the critical shear rate $\dot{\gamma_c}$ (see 6.1.8). This parameter sets the precision of the determination of the yield surfaces. For a flow in a channel of width b at a mean velocity V we can define an average shear rate value: $\dot{\gamma_{av}} = V/b$. We define the dimensionless shear rate $\bar{\dot{\gamma}} = \frac{\dot{\gamma_c}}{\dot{\gamma_{av}}}$ to evaluate the precision of the determination of the unyielded surfaces which increases as $\bar{\dot{\gamma}}$ decreases.

We run the two-dimensional calculation for straight channels (100 µmx5 mm) varying the following parameters:

— The dimensionless shear rate value: 1, 0.1, 0.01 and 0.001
— The mesh size: fine (100x4800 cells), medium (52x2400 cells) and coarse (26x1200 cells)
— The number of iterations
— The solver method: SIMPLE or COUPLED algorithm.

Figure 6.5 (a) represents the friction factor f as a function of the generalized Reynolds number Re for the flow of a Herschel-Bulkley fluid in plane channels at various velocities, i.e Reynolds numbers. The points extracted from the calculations are compared to the analytical value (straight line).

Figure 6.5 (a) shows that a good agreement between the calculations and the analytical solution of the flow is obtained for all the mesh sizes and for all values of the critical shear rate tested. We remind that the critical shear rate sets the precision for the determination of the yield surface, the smaller it is the more precise the determination of the position of the unyielded surfaces will be.

Figure 6.5 (b) represents the friction factor as a function of the number of iterations, i.e the convergence rate. It shows how fast the calculation converges to the right value of the friction factor. On figure 6.5 (b), we compare two solvers methods: the COUPLED and the SIMPLE method described in paragraph 6.1.4. We observe that the convergence rate is more efficient when the COUPLED algorithm is used. We precise also that with the SIMPLE algorithm we had to put a very low tolerance criteria to get convergence towards the theoretical solution (down to 10^{-10}).

The value of the dimensionless critical shear rate is problem dependent. We note that with the COUPLED algorithm the value of the critical shear rate cannot be set too low. Indeed we observed some convergence problems when trying to impose too low values of the critical shear rate on a fine mesh.

In practice in the following, we use only the COUPLED method because it is much more efficient than the SIMPLE algorithm. The values of the dimensionless critical shear rate range between 0.1 and 1 for most of the simulations performed in the chapter to ensure a good determination of the unyielded surfaces.

6.3.2 Single Bingham fluid in two-dimensional wavy-channels

Roustaei *et al.* looked at the occurrence of stationary fouling in wavy-walled channels when a Bingham fluid flows slowly inside the channel [158]. They considered the stationary problem rather than the problem of the formation of the fouling layer. They use Stokes flow computation since they assume that stationary flows are non-inertial locally. The geometry is represented on figure 6.6.

Three dimensionless parameters are defined: $\delta = D/L$ represents the aspect ratio

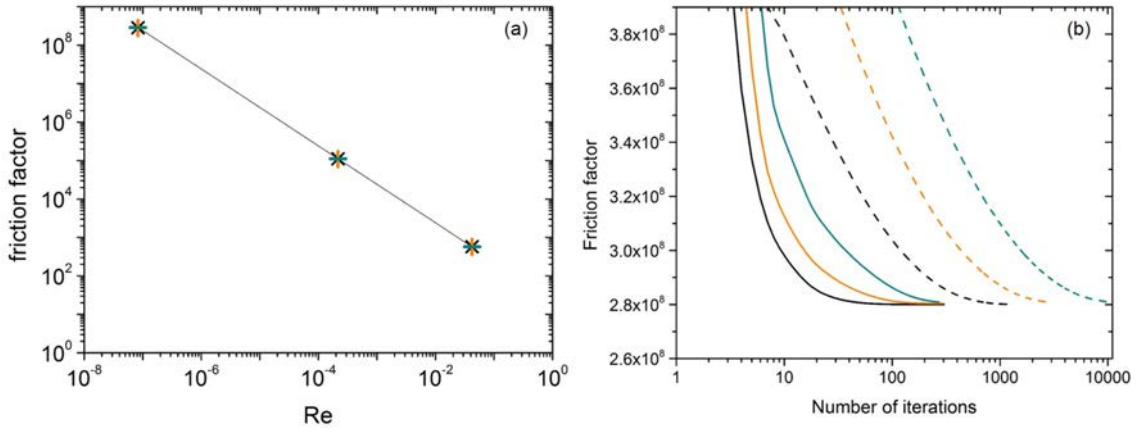

Figure 6.5 – Friction factor calculated for the flow of a Herschel-Bulkley fluid in a plane channel whose rheological properties correspond to a microgel 1.6%. Calculations are performed with a fine (100x4800 cells, dark cyan), a medium (52x2400 cells, orange) and a coarse mesh (26x1200 cells, black). (a) The friction factor as a function of the generalized Reynolds number obtained for different values of the dimensionless critical shear rate: 0.001 (cross), 0.1 (vertical lines) and 1 (horizontal lines). The results are obtained with the COUPLED algorithm. The full line is the theoretical value obtained with equation 6.9. (b) The friction factor as a function of the number of iterations for a Reynolds number of $8 * 10^{-8}$ and a dimensionless critical shear rate of 1 calculated with the SIMPLE algorithm (dotted lines) and with the COUPLED algorithm (full lines).

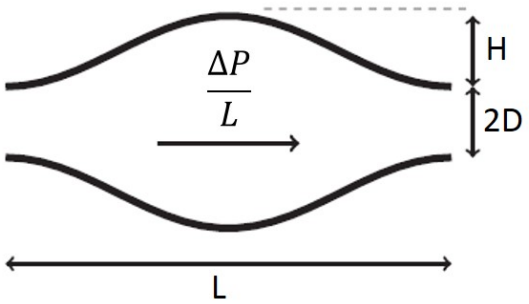

Figure 6.6 – Geometry of the wavy channel studied in [158]. D is the mean channel half-width, H is the depth of the wall perturbation and L the wavelength of the wall perturbation.

between the channel half-width D and the wavelength of the wave L, $h = H/D$ is the maximal depth of the wall perturbation and $B = \sigma_y D/(\mu U_0)$ is the Bingham number with μ the viscosity of the fluid, σ_y its yield stress and U_0 its mean velocity.

Roustaei *et al.* use periodic boundary condition to look at the stationary solution of the flow. We noticed that there is a problem while using the periodic boundary condition in Fluent. Indeed, the pressure field obtained is not coherent with the results of Roustaei *et al.* To circumvent this issue, we used a manual periodic boundary condition by repeating three times the geometry pattern to have a steady flow.

Roustaei *et al.* identified the positions of the unyielded surfaces depending on the geometrical parameters δ and h which set the amplitude of the wave and the channel width. They define the following situations:

— The term *fouling* refers to the cases where an unyielded surface is present near the wavy wall (see figures 6.9 and 6.10). The reverse situation is named *no fouling* (see figure 6.7 and 6.8).

— The term *intact plug flow* refers to the cases where an unyielded surface is present in the center of the channel (see figures 6.8 and 6.10). The term *broken plug flow* means that both yielded and unyielded surfaces are present in the middle of the channel (see figures 6.7 and 6.9).

Four main cases were observed by Roustaei *et al.* which correspond to the combination of fouling/no fouling and broken/intact central plug. The four cases and the corresponding geometrical parameters are listed in the table below:

	Names of the cases	h	δ
Case 1	Broken central plug - no fouling	0.25	0.05
Case 2	Intact central plug - no fouling	0.25	0.25
Case 3	Broken central plug - fouling	4	0.05
Case 4	Intact central plug - fouling	0.5	0.25

In all cases $B = 10$. We reproduce with Fluent the four main cases presented by Roustaei *et al.* [158] and we compare the results. The dimensionless critical shear rate is equal to 0.1.

The results are shown on figure 6.7 for case 1, figure 6.8 for case 2, figure 6.9 for case 3 and figure 6.10 for case 4. The top line of each figure represents the velocity field and the bottom line the pressure field. The unyielded areas are shown in grey on the figure of Roustaei *et al.* and red for our results with Fluent on the pressure field graphs (bottom line of each figure).

Figures 6.7 to 6.10 show that we obtain a good quantitative agreement with Roustaei *et al.* [158]. The only restriction would be that we could not use the periodic boundary condition proposed in Fluent.

6.3.3 Two Bingham fluids in straight channels

Wielage-Burchard and Frigaard looked at the occurrence of a static wall layer in two-dimensional plane channels during the displacement of a Bingham fluid by a Newtonian or a Bingham fluid with a lower yield stress [187]. We remind that Bingham fluids are yield stress fluids with a constant viscosity. It means that once the yield stress is exceeded, the fluid behaves as a Newtonian fluid. Wielage-Burchard and Frigaard compare the layer

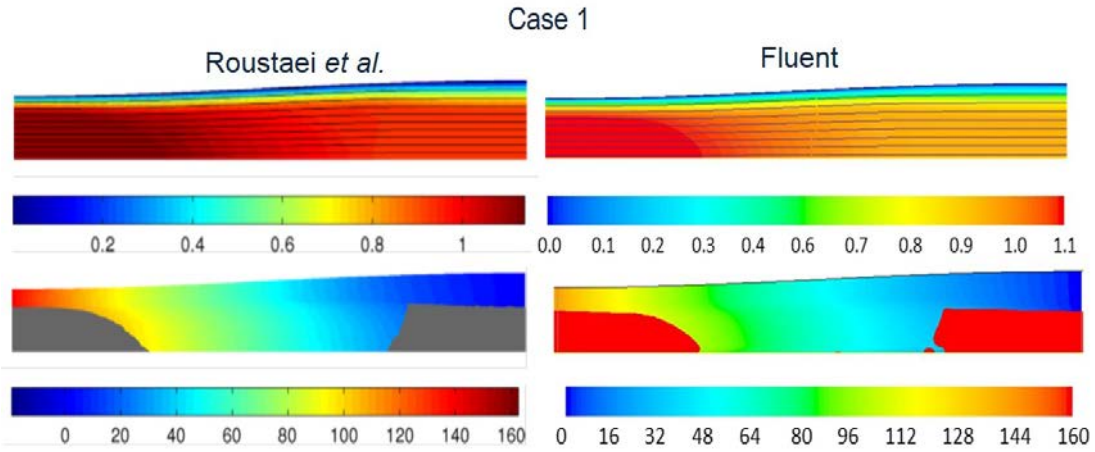

Figure 6.7 – Comparison of case 1: $B = 10$; $h = 0.25$ and $\delta = 0.05$ between the results of Roustaei *et al.* (left panel) and our results with Fluent (right panel). Top: Velocity field (m/s). Bottom: Pressure field (Pa).

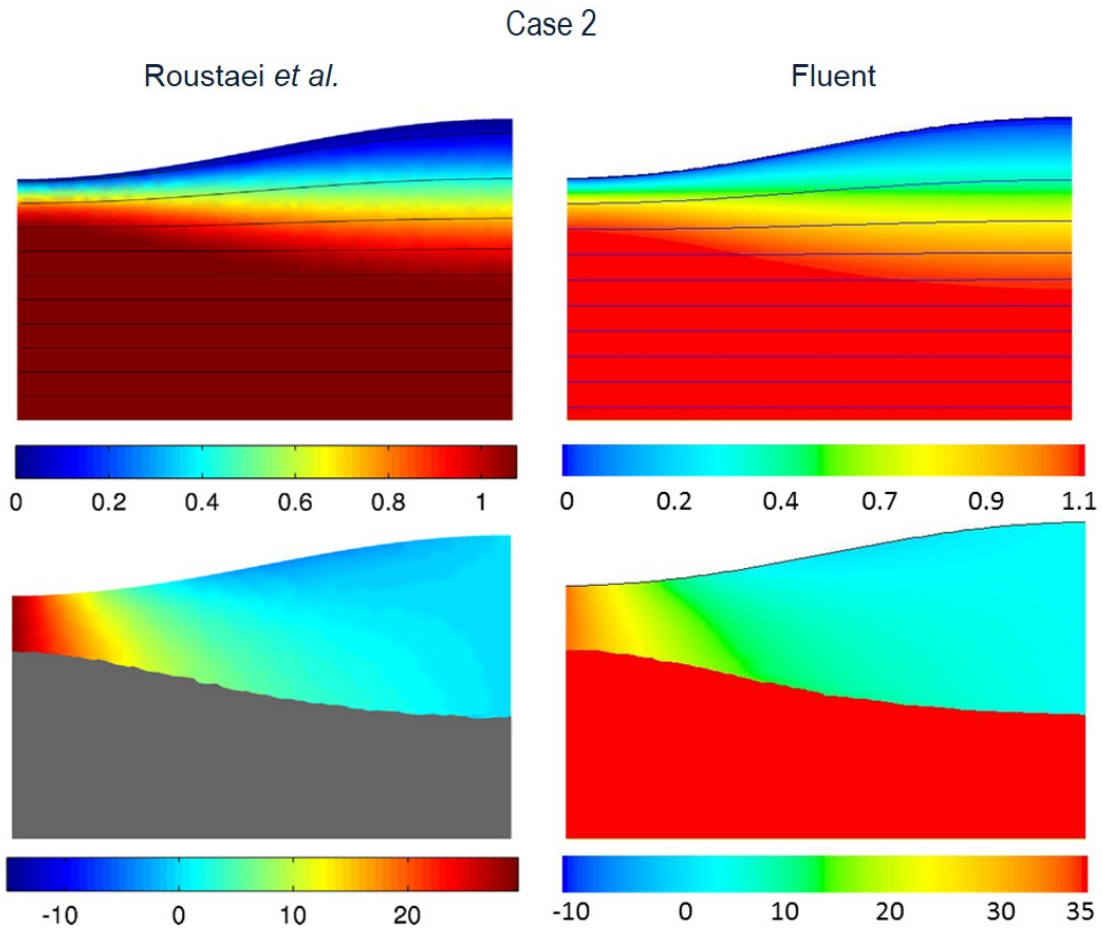

Figure 6.8 – Comparison of case 2: $B = 10$; $h = 0.25$ and $\delta = 0.25$ between the results of Roustaei *et al.* (left panel) and our results with Fluent (right panel). Top: Velocity field (m/s). Bottom: Pressure field (Pa).

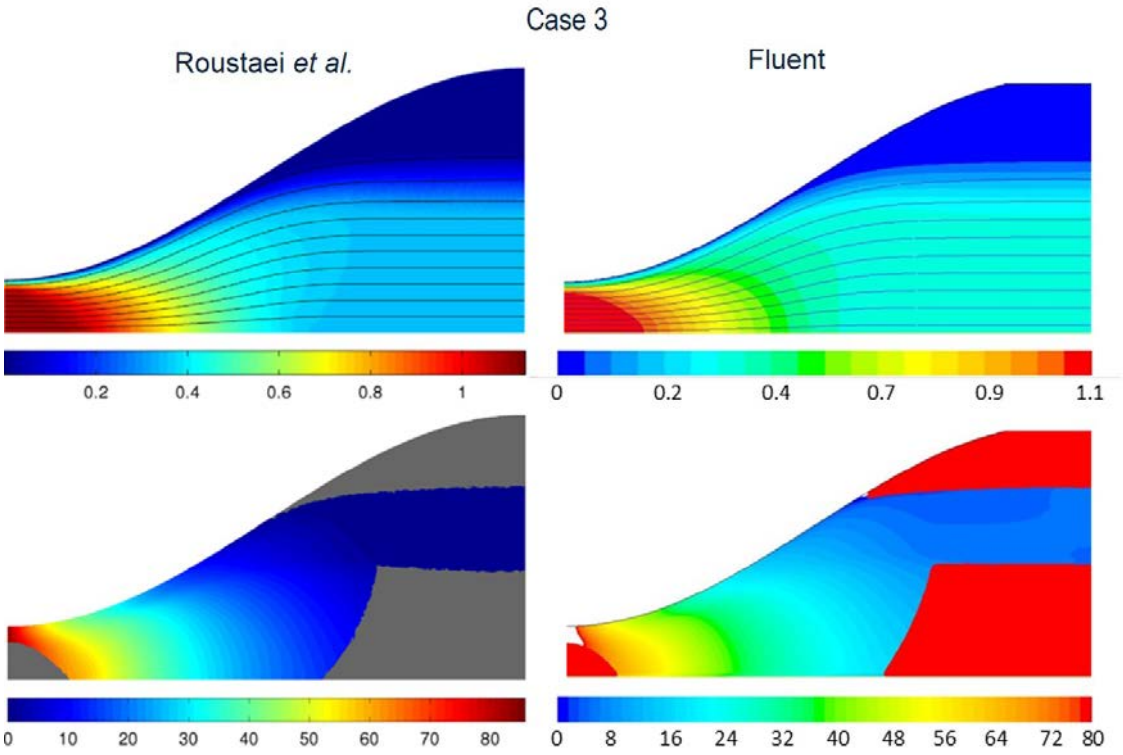

Figure 6.9 – Comparison of case 3: $B = 10$; $h = 4$ and $\delta = 0.05$ between the results of Roustaei *et al.* (left panel) and our results with Fluent (right panel). Top: Velocity field (m/s). Bottom: Pressure field (Pa).

thickness calculated with the work of Allouche *et al.* [2]. The parameters of the study are: the Reynolds number (Re), the Bingham number (B) and the viscosity ratio (M). We reproduce their result in the case of the flow of two Bingham fluids.

The displacement computations are two-dimensional and they use the augmented Lagrangian (AL method) technique to resolve the unyielded regions. Wielage-Burchard and Frigaard aim to improve Allouche *et al.* results by:

— Using the augmented Lagrangian method instead of a viscosity regularization method to better resolve the yield stress behaviour
— To carry longer simulation to see if longer timescale transient behaviour occur and affect the layer thickness.

We focus our comparison on low Reynolds number calculations and on the thickness of the layer left at the walls after the breakthrough of the displacing fluid. The dimensionless critical shear rate is equal to 0.1.

Figure 6.11 represents the displacement of a Bingham fluid by another Bingham fluid that has a lower yield stress in a plane channel. The top line corresponds to the results of Wielage-Burchard and Frigaard and the bottom line corresponds to our results obtained with Fluent. A sharp interface is defined between the displaced and the displacing fluid in both simulations.

Figure 6.12 gathers our results and the results of [187] and [2]. We note that our results are in good quantitative agreement with Wielage-Burchard and Frigaard [187].

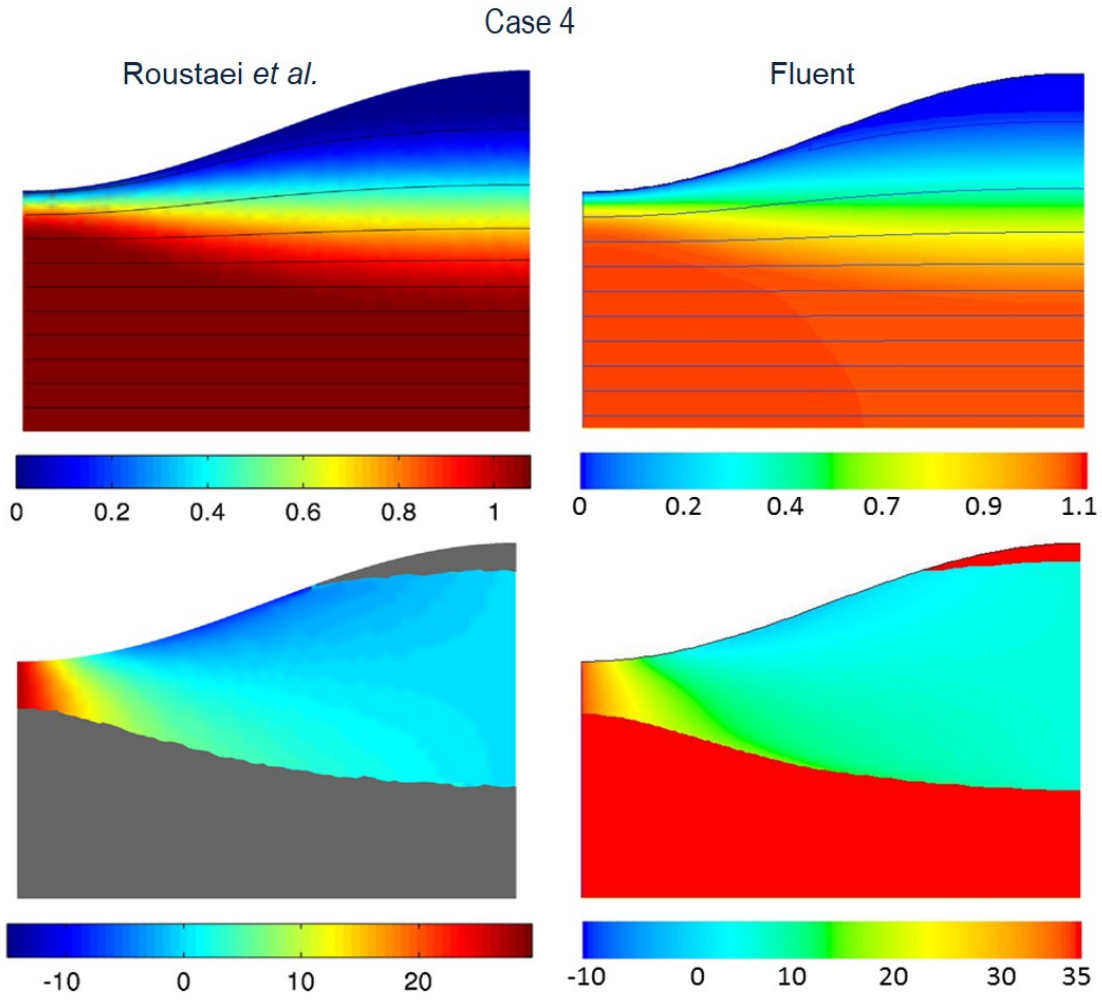

Figure 6.10 – Comparison of case 4: $B = 10$; $h = 0.5$ and $\delta = 0.25$ between the results of Roustaei *et al.* (left panel) and our results with Fluent (right panel). Top: Velocity field (m/s). Bottom: Pressure field (Pa).

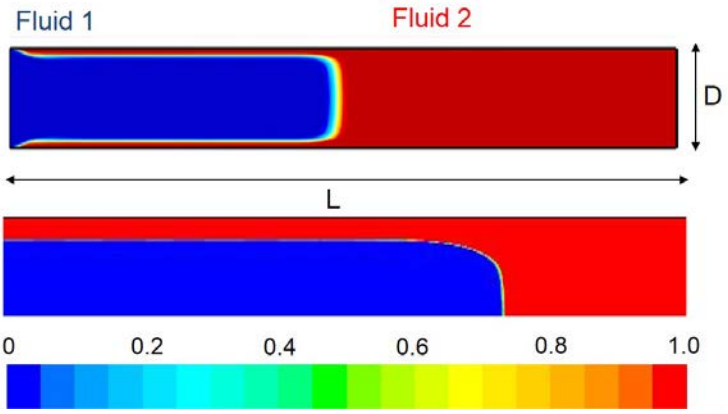

Figure 6.11 – Volume fraction of fluid 2 for the displacement of two Bingham fluids: $Re = 0.1$, $M = 0.1$ and $B = 100$. Top: result extracted from [187], bottom: our result with Fluent. In both cases a sharp interface is defined between the fluids.

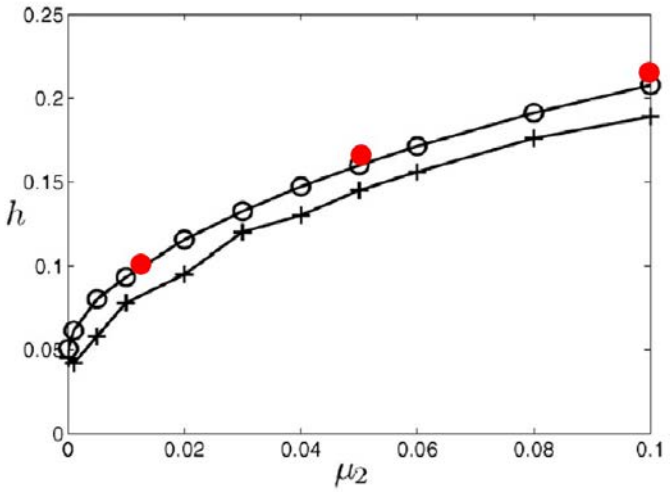

Figure 6.12 – Thickness of the layer left at the walls during the displacement of two Bingham fluids for varying the viscosity of the displaced fluid μ_2 and with $\mu_1 = 0.01$, $\tau_{1,Y} = 0.2$ and $\tau_{2,Y} = 0.5$. (open circle) data from [187], (cross) data from [2], (red full circles) our results with Fluent.

Wielage-Burchard and Frigaard explained the slight offset between their data and the one of Allouche *et al.* by the use of a regularization method by the later [187]. From the results of figure 6.12, we can say that this was probably not the reason for the discrepancy since our results are in very well agreement with the one of Wielage-Burchard and Frigaard and we are using a regularization method for the computation of the rheological law of our Bingham fluid.

6.3.4 Summary of the validation of Fluent

The simulations performed with the Fluent code showed excellent comparison with the results of the literature. The use of a regularization law for the description of the rheology of yield stress fluids does not impact the results obtained.

We found out that a few rules can be defined to get proper calculation results:

— The use of the COUPLED solver: there is no need to put very low convergence tolerance and the convergence is faster than with the SIMPLE solver.

— The adjustment of the regularization parameter: the COUPLED method is very efficient but less robust than the SIMPLE method. A dimensionless critical shear rate between 0.1 and 1 is reasonable to get correct results for the flow studied.

— The use of the periodic boundary condition is not recommended.

6.4 Fluid rheologies

The rheologies of the yield stress fluids considered in the simulations correspond to the rheologies obtained for the microgel 1.6%, 2.2% and 3%. The fluids follow the Herschel-Bulkley law: $\sigma = \sigma_y + k\dot{\gamma}^n$ with σ_y the yield stress, k the consistency parameter and n the flow index. The rheological properties used in the simulations are summarized in table 6.1.

All the displacements are performed using fluid 1 as the displacing fluid.

Table 6.1 – Rheological parameters of the fluid used for the simulations.

	σ_y (Pa)	k Pa s^n	n	Microgel concentration (%)
Fluid 1	19	5	0.5	1.6
Fluid 2	60	10	0.5	2.2
Fluid 3	250	75	0.38	3

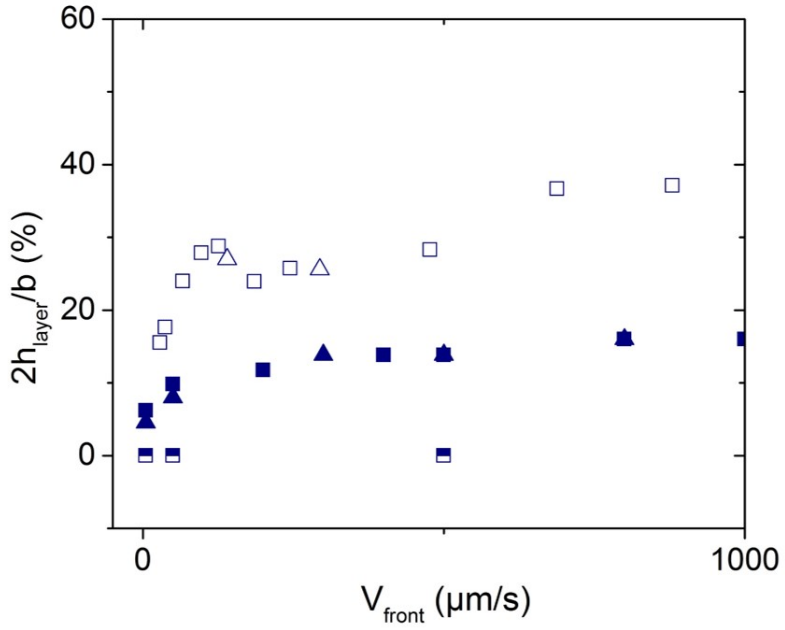

Figure 6.13 – Thickness of the layer scaled by the width of the channel as a function of the front velocity in case of the displacement of a microgel 2.2% (square) and a microgel 3% (triangle) by a microgel 1.6% obtained in the experiments (open symbols) and in the two-dimensional simulations (full symbols).

6.5 Comparison with displacements experiments in straight channels

We recall the main experimental results obtained in straight channels:

— With no slip, the thickness of the layer increases with the velocity of the interface and reaches a plateau at high velocities.

— With slip, the displacement efficiency is greatly improved: at low velocity no layer forms. At high velocities, a film forms and we recover a situation analogous to the no slip case.

— The film could be removed from the channel.

The channels are 250 µm deep and 3 mm long. The dimensionless critical shear rate ranges between 0.005 and 0.5.

6.5.1 Evolution of the film thickness with the speed

Figure 6.13 compares the thickness of the layer obtained in the experiments and in the two-dimensional simulations for different fluid rheologies.

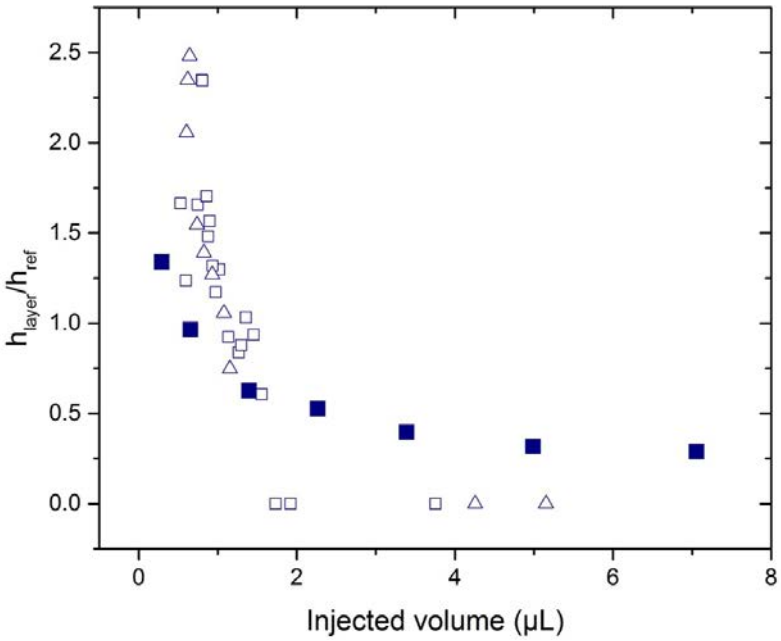

Figure 6.14 – Thickness of the layer after breakthrough of the displacing fluid scaled by its thickness before breakthrough as a function of the injected volume in case of the displacement of a microgel 2.2% (square) and a microgel 3% (triangle) by a microgel 1.6% obtained in the experiments (open symbols) and in the three-dimensional simulations (full symbols) at a velocity of $5\,\mathrm{mm\,s^{-1}}$.

It shows that the layer calculated in the simulations is below the one measured experimentally. But we observe that it follows the same tendency: it increases with the velocity and reaches a plateau at high velocities.

We also observe that with slip no film is left at the walls at low velocity in agreement with experimental results. However, at high velocity, the film is still equal to zero in contradiction with the experimental results.

6.5.2 Evolution of the film thickness with time

As it was the case for the experiments, we translate time into a volume injected. Figure 6.14 represents the evolution of the layer as a function of the injected volume. We use the injected volume instead of the number of injected volumes because the length of our experimental channel is larger than in the simulations so that the number of volumes injected is not the relevant quantity to compare.

The mobility of the layer can be predicted by following the analysis presented in appendix C. The imposed velocity on fluid 1 generates two different pressure gradients in fluid 1 and in fluid 2 which leads to two different wall shear stresses in fluid 1 $\sigma_{w,1}$ and in fluid 2 $\sigma_{w,2}$. The layer of fluid 2 is mobile only if the wall shear stress in fluid 2 is higher than the yield stress of fluid 2: $\sigma_{w,2} > \sigma_{y,2}$. Therefore, it is relevant to look at the evolution of the layer thickness over time only for displacements occurring at a sufficient velocity so that the layer is mobile. The displacement represented on figure 6.14 is made at an imposed velocity of $5\,\mathrm{mm\,s^{-1}}$.

Figure 6.14 shows that the film decreases as more volume of fluid is injected in the channel. Nevertheless, we do not empty the channel over a comparable volume of fluid injected.

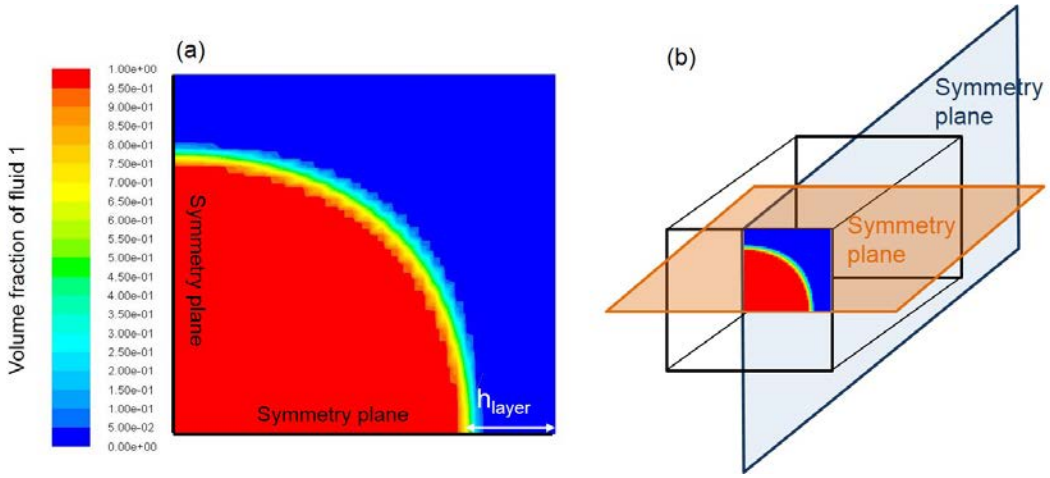

Figure 6.15 – (a) Cross section of a three-dimensional square channel with the measure of the thickness of the layer. (b) Position of the symmetry planes. The simulation is performed only on a quarter of the square channel.

Table 6.2 – Thickness of the layer for the displacement of two Herschel-Bulkley fluids obtained for three-dimensional and two-dimensional simulations

U (m/s)	3D h_{layer} (µm)	2D h_{layer} (µm)
0.005	28.4	29.1
0.0005	18.5	17.3
0.00005	14.3	12.3
0.000005	10.3	7.8

6.5.3 Three-dimensional and two-dimensional modelling of straight channels

We compare two-dimensional and three-dimensional calculations to see if the additional overhead of getting closer to the experimental square geometry was useful.

Figure 6.15 (a) shows a front view of the cross section of a three-dimensional displacement calculation performed in a square channel which is sketched on figure 6.15 (b). We indicate that we measure the thickness of the layer in the square channel at the symmetry plane.

The results obtained for the thickness of the layer in a three-dimensional and two-dimensional channels are summarized in table 6.2.

Table 6.2 shows that the layer thicknesses between the two-dimensional and three-dimensional simulations are comparable.

6.5.4 Summary of the displacements simulations in straight channels

With no slip, the thicknesses obtained in the simulations are lower than the one obtained in the experiments. However, the right tendency for the evolution of the layer thickness as a function of the imposed velocity is recovered. Three-dimensional simulations did not allow to obtain a better comparison with the experiments.

With slip at high velocities no film is obtained which is in contradiction with the experimental results.

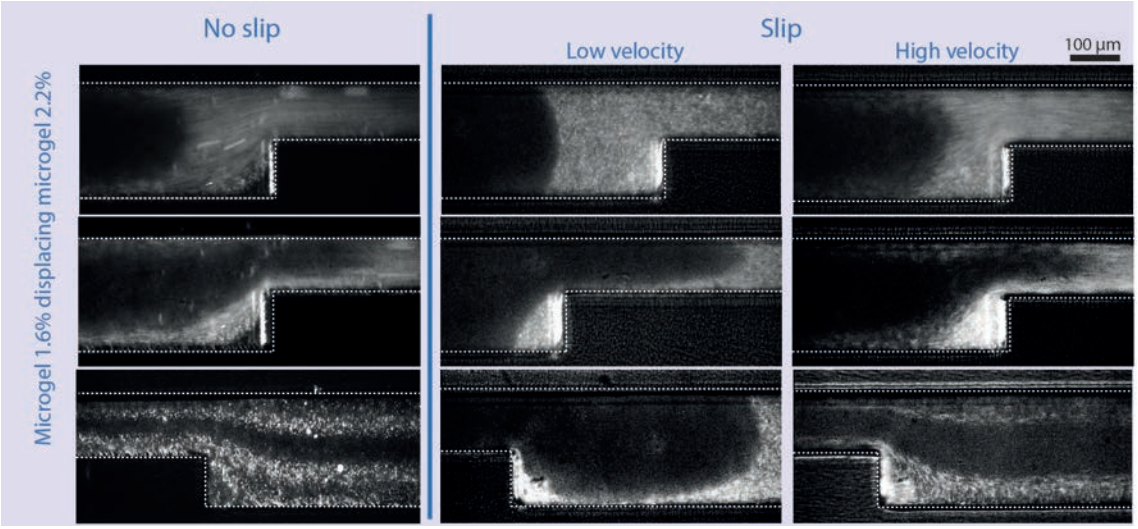

Figure 6.16 – Displacement of a microgel 2.2% by a microgel 1.6% in a channel with a restriction with slip and no slip boundary conditions. With slip boundary conditions, the displacements at low velocity and high velocity exhibit different behaviours, namely a film forms in the latter case.

With slip at low velocities, the displacements in the simulation is plug-like and no film is left at the walls in agreement with the experimental results.

6.6 Comparison with displacements experiments in channels with restrictions

We recall that the main experimental results obtained in channels with restrictions are:
— With no slip, the thickness of the layer is much thicker after the restriction than before the restriction.
— With slip, the displacement efficiency is greatly improved: at low velocity no film forms. At high velocity a film is present. But in this case, the channel is still completely cleared out.
— The drainage of the film is faster with slip than with no slip.

Figure 6.16 reminds the main results of the experimental displacements in channels with restrictions. The objective is to look for these principal effects in the simulations.

6.6.1 Evolution of the film thickness with the speed

Simulations at different velocities were performed in two-dimensional channels with slip and no slip at the walls at velocities ranging from $50\,\mu m\,s^{-1}$ to $5\,mm\,s^{-1}$ for the displacement of a microgel 2.2% by a microgel 1.6%.

In the no slip case, figure 6.17 shows on the left panel the evolution of the interface as a function of its position in the channel and as a function of the imposed velocity. We observe that for both velocities presented the interface expands and fills the channel as soon as it gets out of the restriction. We do not observe the transient regime seen in the experiments where the film becomes thicker at the outlet of the restriction.

We note that at the highest velocity ($5\,mm\,s^{-1}$), the calculation in channels with restrictions raised numerical difficulties. Indeed, it was not possible to obtain convergence without increasing the dimensionless shear rate up to 5. In all the other cases the critical shear rate ranged between 0.05 and 0.25. This impacted the results since we can see on

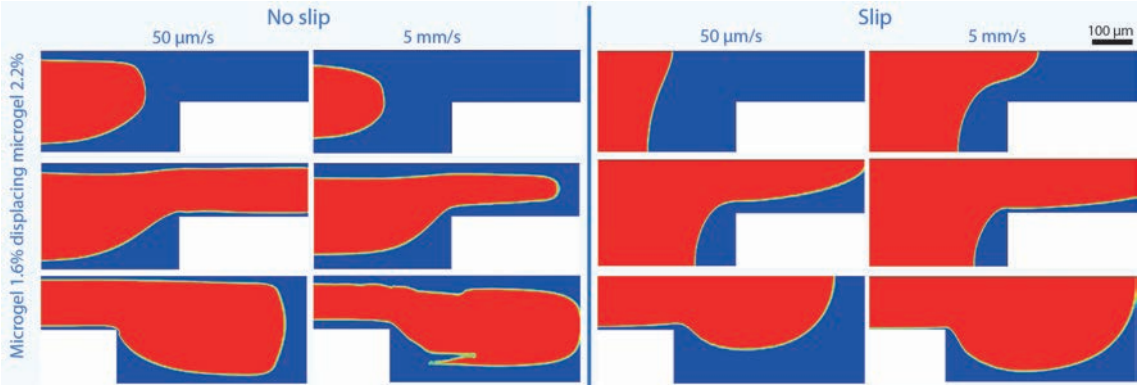

Figure 6.17 – Shape of the interface for a displacement of a microgel 2.2% by a microgel 1.6% with no slip (left panel) and slip (right panel) at the walls from before (top line) to after the restriction (bottom line) and as a function of the imposed velocity: $50\,\mu m\,s^{-1}$ and $5\,mm\,s^{-1}$ (from left to right).

Table 6.3 – Thickness of the layer for the displacement of two Herschel-Bulkley fluids obtained for three-dimensional and two-dimensional simulations in a channel with a restriction at a velocity of $5\,mm\,s^{-1}$

Position	3D (µm)	2D (µm)	3D (%)	2D (%)
Before the restriction	17.5	20.1	14	16
Inside the restriction	9.5	13.7	15	22
After the restriction	29	36	23	29

figure 6.17 (left panel bottom line) that the interface at $5\,mm\,s^{-1}$ presents irregularities after the restriction.

In the slip case, figure 6.17 shows the evolution of the interface as a function of its position in the channel and of the imposed velocity. There is no film observed in the channel. Even at the highest velocity, the displacement is plug-like up to the restriction. As soon as the interface gets out of the restriction, it expands. A similar behaviour was also observed in the experiments with slip at low velocity (see figure 6.16).

6.6.2 Three-dimensional and two-dimensional modelling of channels with restrictions

We checked if three-dimensional simulations could improve the comparison with the experimental data. We average the thickness of the layer over the x-axis (along the channel length) before, inside and after the restriction. The results are given in table 6.3.

Table 6.3 shows that the thickness of the layer between the two-dimensional and three-dimensional simulations are comparable. Also we observe that the layer thickness increases gradually as it goes through the restriction.

Nonetheless, it did not provide a better quantitative comparison with the experiments.

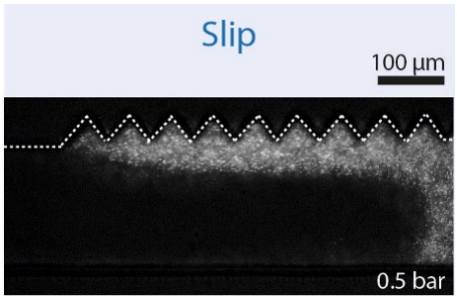

Figure 6.18 – Shape of the interface for the experimental displacement of a microgel 3% by a microgel 1.6% with slip at the walls in a channel of type B at a pressure drop of 0.5 bar.

6.6.3 Summary of the displacements simulations in channels with restrictions

With no slip, we did not see the increase of the film thickness after the restriction observed in the experiments neither with three-dimensional nor two-dimensional simulations.

With slip, we obtained a qualitative agreement with the experiments at low velocities. At high velocities, the interface keeps its flat shape whereas, in the experiments, it is deformed and a film forms. In this case, we hypothesize that this is due the way slippage is modelled in Fluent. Indeed, the shear stress equals zero at the walls, consequently no deformation can ever occur in the fluid.

6.7 Comparison with displacements experiments in channels with corrugations at the wall

In the experiments, we measure the clearing out of the corrugations with time. We vary the boundary conditions (no slip and slip) and the geometry of the channels. Two different packing densities for the corrugations on the side of the channel (types A and B) were investigated. The dimensionless critical shear rate ranges between 0.0005 and 0.5.

We recall that the main experimental results obtained in channels with corrugations are:

— With no slip, 20% of the corrugation can never be cleared out at.
— With slip, all the corrugations can be cleared out.
— With slip, there is an influence of the density of the corrugations: the interface avoids the corrugations when they are close to each other as recalled on figure 6.18.

The channels are 250 µm deep and 3 mm long, the corrugations have the same dimensions as in the experiments.

6.7.1 Evolution of the drainage of the fluid in the corrugations with time

Figure 6.19 shows the shape of the interface near the corrugations for the displacements of a microgel 2.2% by a microgel 1.6% in the geometries of types A and B with slip and no slip at velocities of $50\,\mu m\,s^{-1}$ and $50\,mm\,s^{-1}$.

The main observations are:

— The interface becomes thinner as the velocity increases as shown on figure figure 6.19. The same behaviour is observed in the experiments.
— With slip, figure 6.19 shows that no layer forms in the geometry A.

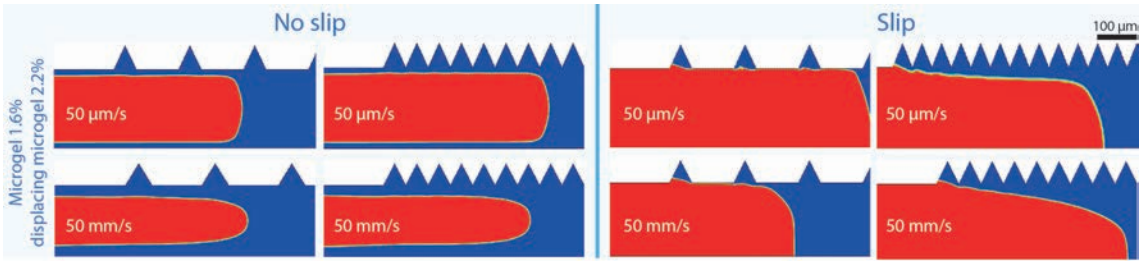

Figure 6.19 – Shape of the interface near the corrugations obtained for the simulations of the displacements of a microgel 2.2% by a microgel 1.6% in the geometries A and B with no slip (left panel) and slip (right panel) at velocities of $50\,\mu m\,s^{-1}$ (top line) and $50\,mm\,s^{-1}$ (bottom line).

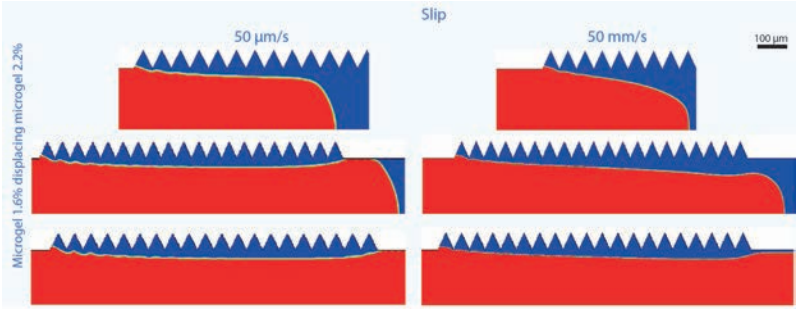

Figure 6.20 – Shape of the interface near the corrugations obtained for the simulations of the displacements of a microgel 2.2% by a microgel 1.6% in the geometry B with slip at $50\,\mu m\,s^{-1}$ (left) and $50\,mm\,s^{-1}$ (right). The displacement is shown at increasing time steps from top to bottom.

— With slip, in the geometry B, we observe that the interface avoids the corrugations as in the experiments. Figure 6.20 shows the details of the evolution of the interface near the corrugations as a function of time. The behaviour is close to the experimental one (see figures 6.18 and 5.24).

We never observe a clearing out of the corrugations. Figure 6.21 shows the velocity field in the channel and in the corrugations. Indeed, we observe that no recirculation occurs in the corrugations neither with slip nor with no slip and even at very high imposed velocities ($50\,mm\,s^{-1}$) as compared to the velocities encountered in the experiments (up to $10\,mm\,s^{-1}$).

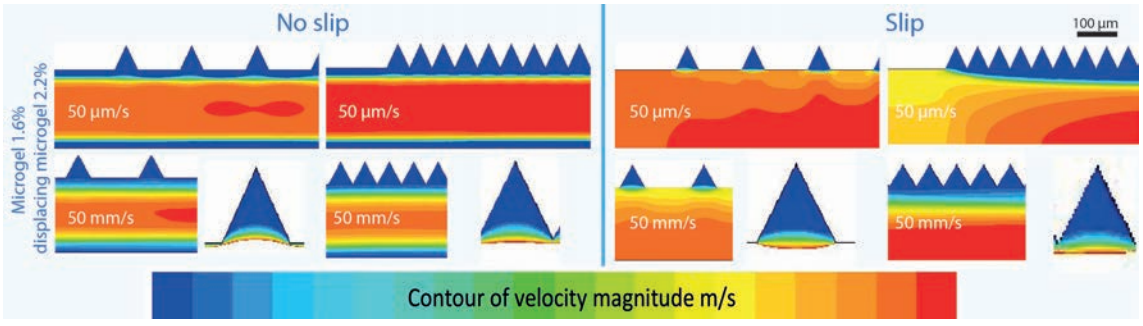

Figure 6.21 – Velocity field near the corrugations obtained for the simulations of the displacements of a microgel 2.2% by a microgel 1.6% in the geometries A and B with no slip (left panel) and slip (right panel) at velocities of $50\,\mu m\,s^{-1}$ (top line) and $50\,mm\,s^{-1}$ (bottom line). The velocity field is taken at the time the interface leaves the channel.

6.7.2 Summary of the displacements simulations in channels with corrugations at the wall

In all cases tested, we never observe a clearing out of the corrugations, the analysis of the velocity field shows that no flow occurs in the corrugations in contradiction with what is seen in the experiments.

With no slip the shape of the interface is in agreement with the experiments.

With slip, we observe the influence of the density of the corrugations. Indeed, the interface avoids the corrugations when they are close to each other in agreement with the experimental observations.

6.8 Conclusions

In this chapter, we have first shown that Fluent gives results that are in very good agreement with calculations extracted from the literature that use another method for modelling yield stress fluids. It proves that calculations using regularization law for the yield stress fluid can be very efficient.

With no slip, the comparison between the experiments and the numerical results is difficult.

The results provided by Fluent suggest that numerical simulations capture the experimental observations at low velocities in the cases where slippage is present in the system.

Simulations with Computational Fluid Dynamics

✧ **Computational Fluid Dynamics (CFD)**
- CFD is a useful tool to explore complex flows.
- The principle is to approximate the mass and momentum equations by a set of algebraic equations which are then solved numerically.

✧ **Validation of the Fluent code**
- We validated the Fluent code against referenced cases of the literature. We obtained good quantitative agreement.
- The periodic boundary conditions provided by Fluent do not work well.

✧ **Comparison with experiments**
- With no slip, the comparison with the experimental data is difficult.
- With slip, qualitative agreement is obtained at low velocities.

Conclusion

The work we have performed includes two parts:

- ✧ **A fundamental study of the effect of slippage heterogeneities on Herschel-Bulkley flows in microchannels.** This work showed that, as the confinement increases, slippage heterogenities play an increasing role. In the smallest microchannels we investigated, slippage heterogeneities fully control the flow structure. From this study, we inferred a new length scale that allows to estimate the influence of slippage heterogeneities on the internal structure of channel flows, in laminar regimes. The definition of this length scale applies for all rheologies.

- ✧ **An investigation of the effect of slippage on the film left behind interfaces separating two miscible Herschel-Bulkley fluids driven through microchannels.** These microchannels can be straight, or include a restriction or corrugations at one wall. We observed that the phenomena are complex, sometimes unexpected. For instance:
  - Consistently with a recent observation, a local rheology appears close to walls treated chemically to suppress slippage (see 5.3). An intuitive reasoning would suggest that the chemical treatment affects the internal structure of the dispersion at a microscopic scale right at the wall and not in the bulk.
  - Complexes flow patterns appear in the case where two Herschel-Bulkley fluids are driven in Hele Shaw cells in the no slip case (inversion of phases,...).
  - Films are much thicker behind a restriction than before, while intuitively we would expect that the thicknesses should be the same.

Owing to this complexity, proposing a quantitative theoretical interpretation of these phenomena seems challenging. Still, we have succeeded to single out strong features that were not known before our work and that may be valuable to take into consideration in the oil industry context.

- ✧ Slippage is a crucial parameter. It controls the film thickness left behind the interfaces along with its dynamics. Without slippage, the displaced fluid always leaves a thick film behind it (30% of the channel height) while with slippage, a film only appears at large speeds. Without slippage, the film thickness decays slowly with time, while, when slippage is present this decay is much faster.
- ✧ In the case of no slip conditions, the film thickness is well described by a minimum dissipation theory. It is remarkable that, in such a complex environment, a simple concept seems to be operational.
- ✧ In the case of slip conditions, there is a characteristic speed above which a film appears behind the interface. This critical speed is a few millimeters per seconds in our case. We propose a physical interpretation of this quantity.
- ✧ The conclusions are mostly confirmed by the numerical study of chapter 6.

Our work thus enlighten the physics of the film appearing (or not) when one Herschel-Bulkley fluid displaces another one in microchannels, with and without obstacles or wall corrugations. Wherever comparisons can be made, our results agree well with Gabard *et al.*'s work, conducted in tubular geometries of centimeter sizes. This remark supports the pertinence of our microfluidic approach.

Based on this, on extrapolating our results to channels of centimeter sizes, we estimate that the cementing process always stands well above the characteristic speed mentioned before. This implies that, whatever the slip conditions can be at the walls, a significant mud film always forms in the annulus. We may speculate whether this film is removed by washing procedures undertaken in the oil industry. Nonetheless, in all cases, our works suggests that it is advantageous to favour slippage in order to accelerate, or permit (in the case of obstacles) the complete removal of this film.

Appendix A

Fabrication of the microgel suspension

The suspensions used in this study are prepared from polyelectrolyte microgels in water. The microgels were synthesized by standard emulsion polymerization at low pH ($\approx$ 2) from ethyl acrylate (64 wt.%), methacrylic acid (35 wt.%), and a bifunctional monomer as a crosslinker [31]. The polymer latexes obtained at the end of the synthesis were cleaned by ultrafiltration. The solid content of the stock suspension was determined by thermogravimetry. Stock suspensions at solid content of $ES = 27.2wt.\%$ and $ES = 24.5wt.\%$ were used. Samples are prepared by dilution of the stock solution with ultrapure water. We define the microgel suspension by the massic concentration C of dry polymer present in the final solution:

$$C = \frac{m_{sp}}{m_t} \tag{A.1}$$

with m_{sp} the mass of solid polymer present in the final microgel suspension, m_t the total mass of microgel suspension prepared. The mass of stock solution m_p taken is:

$$m_p = m_{sp}/ES = m_t * C/ES \tag{A.2}$$

With ES the solid content of the stock solution. In our case we used stock suspensions of $ES = 0.272$ g g^{-1} and $ES = 0.245$ g g^{-1}.

At low pH, the microgels are insoluble in water, and behave as hard particles. The addition of sodium hydroxide ($C_{NaOH} = 1M$) causes the ionisation of the methacrylic acid units. The osmotic pressure of the counterions then provokes the swelling of the microgels. In all the experiments reported in this study, the molar ratio of the added base to the available acid groups is around 1, so that the totality of the carboxylic functions are neutralized. Therefore, the number of sodium hydroxide mole needed is equal to the number of mole of methacrylic acid (MAA) and is:

$$n_{NaOH} = n_{MAA} = \frac{m_t * C * C_{MAA}}{M_{MAA}} \tag{A.3}$$

With $C_{MAA} = 0.35$ g g^{-1} the massic concentration of methacrylic acid in the solid content of the stock solution, $M_{MAA} = 86.09$ g the molar mass of methacrylic acid. The volume of hydroxide sodium needed is:

$$V_{NaOH} = n_{NaOH}/M_{NaOH} \tag{A.4}$$

with M_{NaOH} the molar mass of hydroxide sodium. And the mass of hydroxide sodium is:

$$m_{hs} = V_{NaOH}/\rho_{NaOH} \tag{A.5}$$

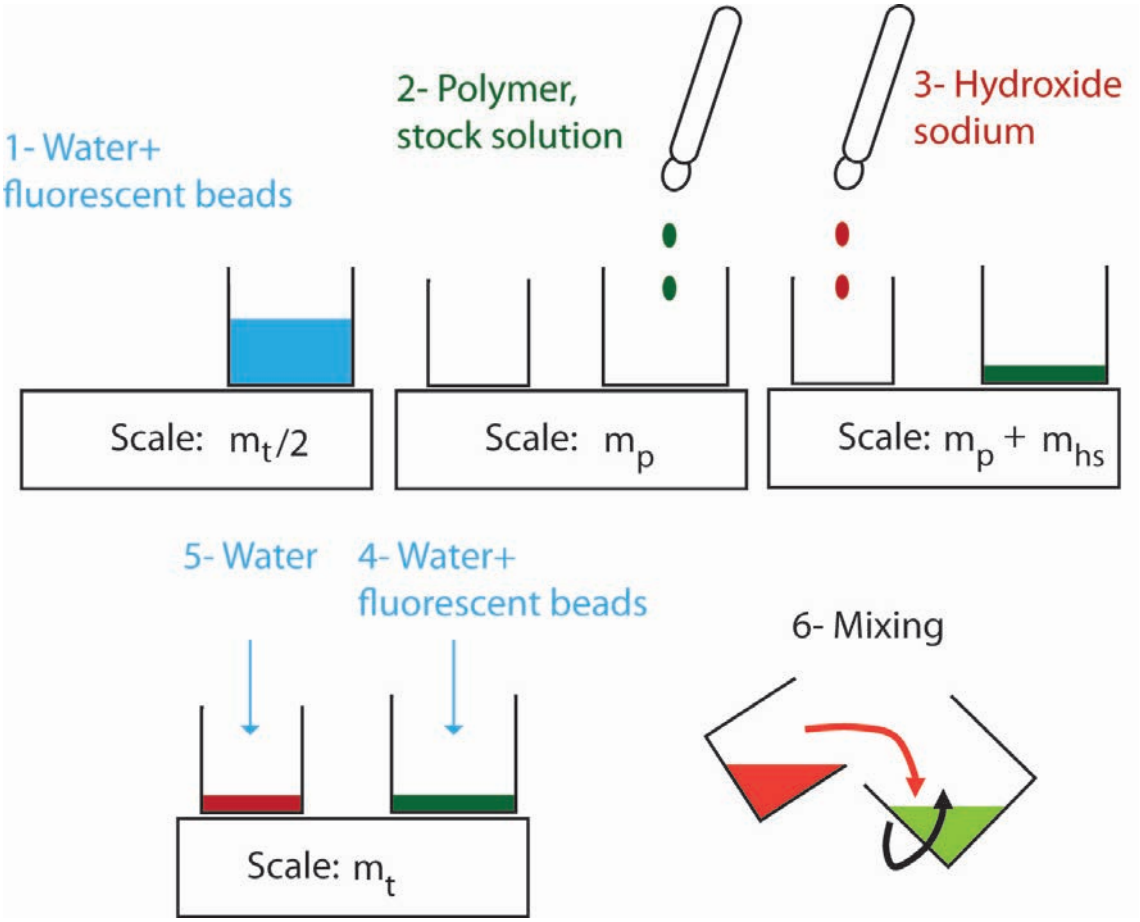

Figure A.1 – Experimental protocol for the fabrication of the microgel suspension.

With $\rho_{NaOH} = 1.04\ \mathrm{g\,cm^{-3}}$ the density of a solution of sodium hydroxide at 1M at 20 °C. The mass of water is simply $m_w = m_t - m_p - m_{hs}$.

Figure A.1 represents the experimental protocol for the fabrication of a microgel suspension. The mass of water is separated into two parts: one is used to dilute the polymer solution with the fluorescent beads, the other part is used to dilute the hydroxide sodium. The last step of the preparation consists in adding slowly the diluted solution of hydroxide sodium to the polymer solution. While hydroxide sodium is added the operator should rotate slowly the tank containing the polymer solution.

In the document we refer to the microgel suspensions by their mass concentrations of solid polymer. We used microgel suspensions at concentrations of 1.6%, 1.8%, 2.2% and 3%.

Appendix B

The recirculation model

In her PhD, Céline Gabard presented a model called the *recirculation model*. This model applies to displacement of a yield stress fluid by another yield stress fluid in a tube, when a static layer is present at the wall. We are always in the case where the yield stress of the displaced fluid is larger than the yield stress of the displacing fluid, which is a necessary condition to get a static wall layer.

This model is able to predict the thickness of the static wall layer. The theory is based on the minimum of energy dissipation: the thickness of the layer is choosen by the system in a way that it minimizes the global dissipative energy. More precisely, it is hypothesized that the dissipative function is minimale at the onset of a recirculation in the displaced fluid in front of the finger.

B.1 Maximale thickness of the layer: h_{max}

The condition that the layer is static gives an upper limit for the layer thickness h_{max}. The stress profile in a tube is given as $\sigma(r) = Gr/2$ with G the pressure gradient and r the radial coordinate. The layer is static if the stress at the interface position is below the yield stress of the displaced fluid (fluid 2), therefore:

$$h_{max} = 1 - r_{min} = 1 - \frac{2\sigma_{Y,2}}{G} \tag{B.1}$$

B.2 Onset of the recirculation: h_{circ}

The finger is represented on figure B.1 (a) in the fixed reference frame of the laboratory. The velocity profiles of the fluids are represented by $U_{-L}(r)$ upstream of the finger front and by $U_L(r)$ downstream of the finger front. The plastic zones of each velocity profile are represented by $R_{1,Y}$ in fluid 1 and by $R_{2,Y}$ in fluid 2. In the layer the velocity is equal to zero since the layer is static.

We place ourselves in the reference frame of the finger front which moves at the velocity $-S$, the mean velocity of the finger. The quantity $-S$ is substracted to the velocity profiles, as shown on figure B.1 (b). This implies the existence of a recirculation zone in the finger (the dotted line on figure B.1 (b) resulting from the opposite direction between the components of the velocity profile: blue and red arrows).

The existence of a recirculation zone in front of the finger depends if the subtraction of the mean velocity of the finger $-S$ to the velocity profile in the front zone of the finger leads to opposite velocity components or not. If $U_{L,max}$ is the maximale velocity of fluid 2,

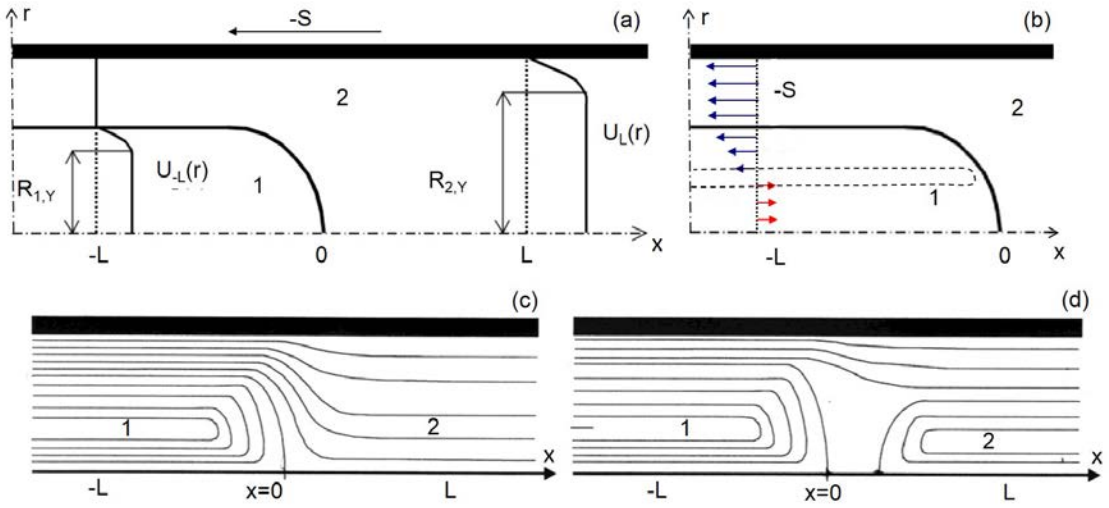

Figure B.1 – Reproduction from [58]. (a) Representation of the front of the finger in the reference frame of the laboratory. The velocity profiles of the fluids upstream and downstream of the finger are represented by $U_{-L}(r)$ and $U_L(r)$ respectively. The values $R_{1,Y}$ and $R_{2,Y}$ represent the plastic zones of the velocity profiles, where the stress is below the yield stress of the fluid. The layer is static, its velocity is equal to zero. (b) The reference frame is now moving at the finger velocity $-S$. The new velocity profile in the finger is represented by the arrows: the velocity $-S$ was subtracted to the velocity profile in the fluid, which leads to negative (blue arrows) and positive (red arrows) velocity components in the reference frame of the finger front. The opposite signs of the velocity components leads to a recirculation of the fluid in the finger (dotted line). (c) Streamlines showing a recirculation in fluid 1 in the finger. (d) Streamlines showing a recirculation in fluid 1 and in fluid 2 upstream of the finger.

there is no recirulation in front of the finger if $U_{L,max} - S \leqslant 0$ for all r. We aim to find the width of the finger r_{circ}, i.e. the interface position, for which the recirculation in fluid 2 starts: $U_{L,max} - S = 0$. If $\bar{U_L}$ is the mean velocity of fluid 2 and r the position of the interface, the mass conservation leads to:

$$\bar{U_L} * R^2 = S * r^2 \tag{B.2}$$

Therefore, the condition for no recirculation in fluid 2 becomes:

$$U_{L,max} - \bar{U_L} * \left(\frac{R}{r_{circ}}\right)^2 \leqslant 0 \tag{B.3}$$

which leads to

$$r_{circ} = R * \sqrt{\frac{\bar{U_L}}{U_{L,max}}} \tag{B.4}$$

To conclude, if $r \leqslant r_{circ}$ there is no recirculation zone in fluid 2 (figure (c)), and for $r \geqslant r_{circ}$ a recirculation zone develops in fluid 2 at the front of the finger.

The quantities $U_{L,max}$ and $\bar{U_L}$ can be determined analytically as a function of the rheological parameters of fluid 2.

B.3 Why does the minimum dissipation occurs at the onset of the recirculation?

The main hypothesis of the model is that the minimum of the dissipative function is achieved at the onset of a recirculation of fluid 2 upstream of the finger. The dissipative function is written as [58]:

$$D\left(U\right) = \sum_{i=1,2} \left[K_i \cdot \dot{\gamma}\left(U\right)^2 + \sigma_{i,y} \cdot \dot{\gamma}\left(U\right)\right] d\Omega \tag{B.5}$$

We briefly recall the physical arguments presented in [58] to justify the hypothesis of the model.

If there is no recirculation in fluid 2 in front of the finger, we have $h_{max} \geq h > h_{circ}$ and only fluid 1 recirculates in the finger. If the thickness of the layer decreases, i.e. the width of the finger increases, the contribution of the fluids to the dissipative function can be summurized as follows:

- The layer is static, its contribution is equal to zero
- The increase of the width of the finger does not change a lot the streamlines in fluid 2, therefore the contribution of fluid 2 stays roughly constant: $\Delta D_{Fluid2} \approx constant$
- The width of the finger increases, therefore its dissipative contribution decreases: $\Delta D_{Fluid1} < 0$

As a whole, the global viscous dissipation decreases (see figure B.2).

If h reaches the critical value of h_{circ} and continues to decrease, a recirculation starts to take place in fluid 2 at the front of the finger and the width of the finger continues to increase:

- The layer is static, its contribution is equal to zero
- The width of the finger increases, therefore its dissipative contribution decreases: $\Delta D_{Fluid1} < 0$
- The onset of the recirculation increases a lot the dissipative contribution of fluid 2: $\Delta D_{Fluid2} > 0$

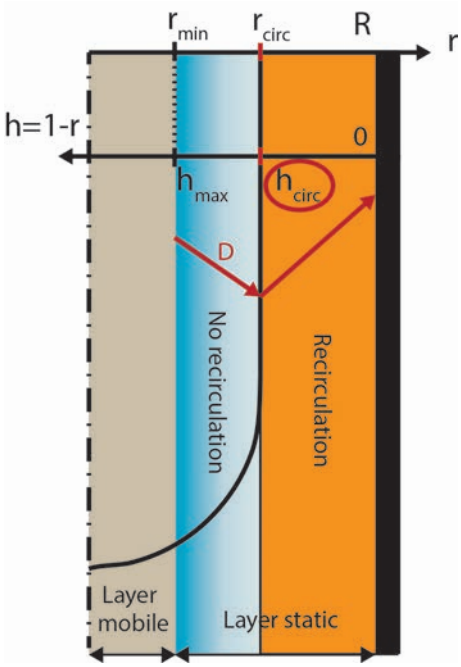

Figure B.2 – Schematic representation of the front of the finger and of the limits for the layer thickness: h_{max} is the maximal thickness the layer can reach while staying static, h_{circ} sets the onset of the recirculation in fluid 2 at the front of the finger.

— Fluid 2 is more viscous than fluid 1, therefore: $|\Delta D_{Fluid2}| > |\Delta D_{Fluid1}|$

As a whole, the global viscous dissipation increases and its minimum is found at $h = h_{circ}$ (see figure B.2).

Appendix C

Flow of a Herschel-Bulkley fluid in a channel of various cross sections

The Rabinowitsch-Mooney equation was originally developed to calculate the wall shear rate in a tube or a plane channel for non-Newtonian fluids [154, 127]. This formulation was extended to obtain a general expression for the average velocity in ducts of arbitrary cross sections [91]:

$$\left(\frac{8U}{D_h}\right) = \frac{1}{c_1}{\sigma_w}^{-c_2/c_1}\int_0^{\sigma_w}\sigma^{c_2/c_1-1}f\left(\sigma\right)\mathrm{d}\sigma \tag{C.1}$$

with U the mean velocity, D_h the hydraulic diameter, σ_w the wall shear stress, $f\left(\sigma\right)=\dot{\gamma}$ is the constitutive law of the fluid relating the shear stress σ to the shear rate $\dot{\gamma}$, c_1 and c_2 the constants which depend on the duct shape and aspect ratio [132].

In the case of a Herschel-Bulkley fluid, the constitutive law of the material writes as:

$$\begin{cases}\sigma < \sigma_y & \dot{\gamma} = f\left(\sigma\right) = 0\\ \sigma > \sigma_y & \dot{\gamma} = f\left(\sigma\right) = \left(\frac{\sigma-\sigma_y}{k}\right)^{1/n}\end{cases} \tag{C.2}$$

The resolution of the equations C.1 and C.2 gives the relation between the mean velocity of the fluid and the wall shear stress in ducts of arbitrary cross sections. For simplicity we took $n = 0.5$ which corresponds to the rheology of our microgel and we obtain:

$$\frac{8U}{D_h} = \frac{1}{k^2}\frac{1}{c_2}\left[\left(\sigma_w-\sigma_w\right)^2 - \frac{2\sigma_w^2 c_1}{c_2+2c_1} + \frac{2\sigma_w\sigma_y c_1}{c_1+c_2} - 2{\sigma_w}^{-\frac{c_2}{c_1}}{\sigma_y}^{\frac{c_2}{c_1}+2}\left(\frac{c_1}{c_2+c_1}-\frac{c_1}{c_2+2c_1}\right)\right] \tag{C.3}$$

The geometrical coefficients for the shapes that interest us are summarized in table C.1.

Table C.1 – Geometrical coefficient c_1 and c_2 for tubes, square channels and rectangular channels with aspect ratio of $\epsilon = 0.5$. The values are extracted from [132].

	c_1	c_2
Tube	1/4	3/4
Square	0.21233	0.67091
Rectangle $\epsilon = 0.5$	0.24394	0.72580

Therefore, it is possible to estimate the mean velocity of a Herschel-Bulkley fluid flowing in a square, a tube or a rectangular channel for a given pressure drop. Indeed the walls shear stress is related to the pressure drop through:

$$\begin{cases} \sigma_w = \frac{\Delta P}{L}\frac{b}{4} \text{for a tube of diameter } b \text{ or a square channel of side } b \\ \sigma_w = \frac{\Delta P}{L}\frac{ab}{2(a+b)} \text{for a rectangular channel of width } b \text{ and height } a \end{cases} \tag{C.4}$$

With $\frac{\Delta P}{L}$ the pressure gradient.

Appendix D

Estimation of the velocity of the interface

One of the objective of the displacement experiments is to look at the evolution of the thickness of the layer as a function of the number of injected volume, i.e. the injected volume scaled by the volume to displace. The number of injected volume is a parameter often use in the oil industry. It can be calculated from:

$$V_{injected} = v_1 * S_{flow} * \Delta t_{flow} \tag{D.1}$$

where the displacing fluid (fluid 1) flows through the section S_{flow} during the time Δt_{flow} at the mean velocity v_1.

The displacement experiments are performed under a constant applied pressure drop. Three main phases characterize the displacement:

1. Phase 1: the interface is in the channel, its velocity increases up to the breakthrough time when the interface gets out of the channel.
2. Phase 2: the interface is out of the channel, we have a core-flow: fluid 1 flows in the center. Fluid 2 forms a layer at the wall which is static if $\sigma_w < \sigma_y$ and mobile if $\sigma_w > \sigma_y$.
3. Phase 3: the channel is filled with fluid 1.

These information allow us to complete the experimental data. We are not able to follow the interface and measure the interface velocity during a whole displacement experiment. Indeed, in some experiments the aim was to observe what was happening in the middle of the channel. Moreover during phase 2 we have no means of measuring the velocity of fluid 1. We describe below how we estimate v_1 during these phases.

The hypothesis that we make for the estimation of the velocity of fluid 1 are:

— At a given time t, the thickness of the layer measured at one location of the channel is considered as an averaged measure over the whole channel length.

— We neglect the velocity of the residual layer for the estimation of the injected volume.

D.1 Phase 1: Before breakthrough time

The objective is to estimate the evolution of the velocity of the interface during the displacement of one fluid by another one at a constant given pressure drop. We model the flow by two serial resistances which values vary as a function of the position of the interface as sketched on figure D.1.

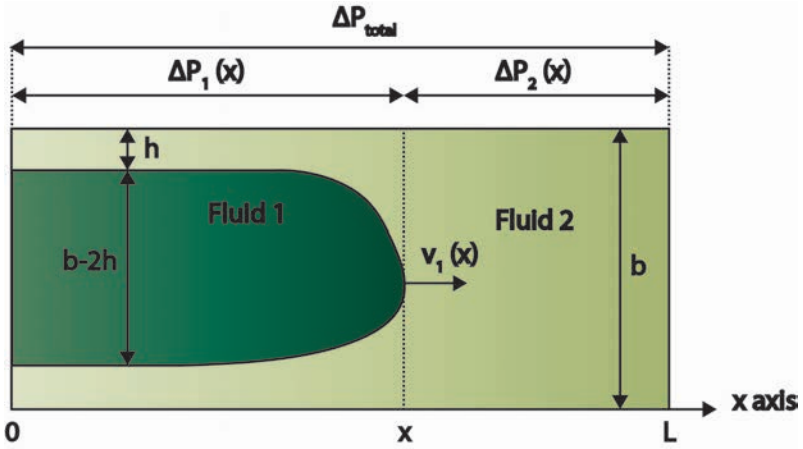

Figure D.1 – As the interface advances in the channel under a constant pressure drop applied ΔP_{total}, the pressure drop over fluid 1 $\Delta P_1(x)$ increases and the pressure drop over fluid 2 $\Delta P_2(L-x)$ decreases and the velocity of the interface v_1 increases.

Under a constant applied pressure drop ΔP_{total} and as the interface gets closer to the outlet of the channel:

— the velocity of the interface v_1 increases.
— the pressure drop over phase 1 $\Delta P_1(x)$ increases.
— the pressure drop over phase 2 $\Delta P_2(L-x)$ decreases.

We can write:

$$\Delta P_{total} = \Delta P_1(x) + \Delta P_2(x) \tag{D.2}$$

During the displacement we consider that:

— Fluid 1 flows in a tube of diameter $b-2h$.
— Fluid 2 flows in a square channel of section b.

Therefore, the velocities in fluid 1 and fluid 2 are related through the mass conservation:

$$Q = v_1(x)\frac{\pi(b-2h)^2}{4} = v_2(x)\,b^2 \tag{D.3}$$

with Q the flow rate. To solve the problem we need to express the pressure $\Delta P_1(x)$ and $\Delta P_2(x)$ as a function of the velocities of:

— fluid 1 in a tube if $h \neq 0$.
— fluid 1 in a square channel if $h = 0$.
— fluid 2 in a square channel.

The cases with and without slip are slightly different and are detailed below.

No slip boundary conditions

With no slip boundary condition, a residual layer is formed at the walls. We consider that fluid 1 flows in a tube of diameter $b-2h$ with $h \neq 0$. In the previous appendix (C) we have obtained the expression of the velocity as a complex function of the pressure drop for channels of any cross sections. But here, to solve the problem we need to express the pressure $\Delta P_1(x)$ and $\Delta P_2(x)$ as a function of the velocities of fluid 1 and 2 in a tube and in a square channel respectively.

In the case of a tube, Swamee *et al.* derived an explicit expression of the Darcy friction

factor as a function of the velocity for Herschel-Bulkley fluids [171]:

$$f = \frac{64}{Re} + \frac{64}{Re}\left[\frac{He}{\left[36 + \left(\frac{1.5}{n}\right)^{2.64}\right]^{0.5} Re}\right]^{\frac{0.958n}{2-n}} \tag{D.4}$$

with Re the generalized Reynolds number and He the Hedstrom number defined by:

$$Re = \frac{8D^n v^{2-n}\rho}{k}\left(\frac{0.5n}{1+3n}\right)^n \tag{D.5}$$

and

$$He = \frac{D^2\rho}{k}\left(\frac{\sigma_y}{k}\right)^{(2-n)/n} \tag{D.6}$$

with D the tube diameter, v the mean velocity of the fluid, ρ the density of the fluid and the parameters of the Herschel-Bulkley law: $\sigma = \sigma_y + k\dot{\gamma}^n$.

The Darcy friction factor is related to the pressure drop through:

$$f = \frac{2D\Delta P}{\rho L v^2} = \frac{8\sigma_w}{\rho v^2} \tag{D.7}$$

with L the length of the tube, σ_w the wall shear stress.

These equations solve partially the problem, we still need to have a relation between the pressure drop and the velocity in the square part of the channel. We try to see, if the relation between the pressure drop and the velocity for a square or a rectangular cross section could be obtained from the relation in a tube with the same hydraulic diameter. Thanks to the results obtained in C, we compare on figure D.2 the wall shear stress obtained at a given velocity in a square or rectangular channel with the wall shear stress obtained in a tube that has the same hydraulic diameter.

Figure D.2 gives a corrective coefficient $\alpha = \frac{\sigma_{w,rect}}{\sigma_{w,tube}}$ to get the value of the wall shear stress in a rectangular channel at a given velocity from a calculation made in a tube of equivalent hydraulic diameter.

We are now able to plot a family of curves in the plan v_1 - ΔP_{total} for different values of the position of the interface x and for a given layer thickness and fluid rheologies (figure D.3).

Slip boundary conditions

In the case of slip, we have seen in the experiments that:
— at low pressure drops, no residual layer is formed in the channel
— at high pressure drops, the interface is deformed. The residual layer that forms is quickly removed.

To simplify, we considered that the displacing fluid is always flowing in the square section. In the case of slip boundary condition during phase 1, two regimes can be distinguished:

1. the flow is dominated by slip: the velocity of the interface varies linearly with its position along the x-axis
2. the flow is dominated by the viscous forces: the velocity of the interface follows the evolution described in the previous paragraph (D.1)

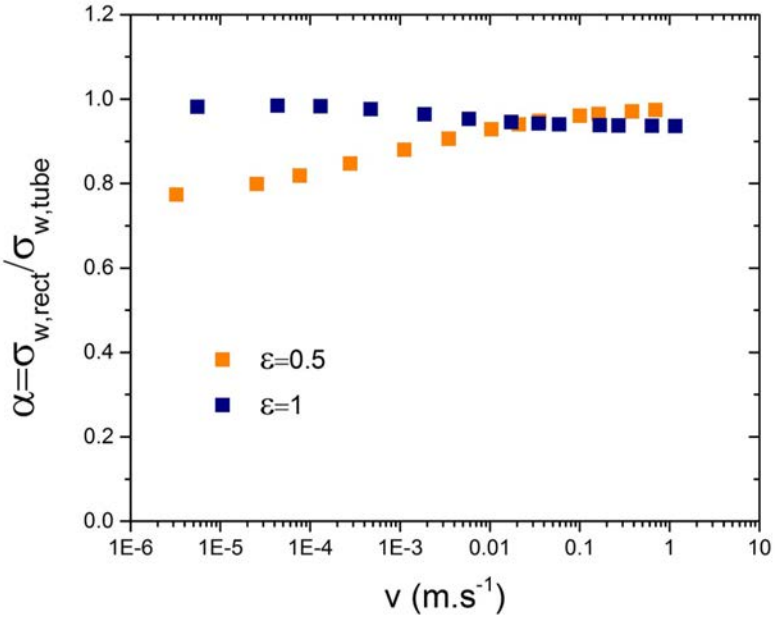

Figure D.2 – Ratio of the wall shear stress obtained in a rectangular channel to the wall shear stress in a tube of equivelent hydraulic diameter as a function of the mean velocity of a Herschel-Bulkley fluid. The aspect ratio of the rectangular channels are $\epsilon = 1$ (blue) (it is a square channel) and $\epsilon = 0.5$ (orange) which corresponds to the restriction geometry of chapter 5.

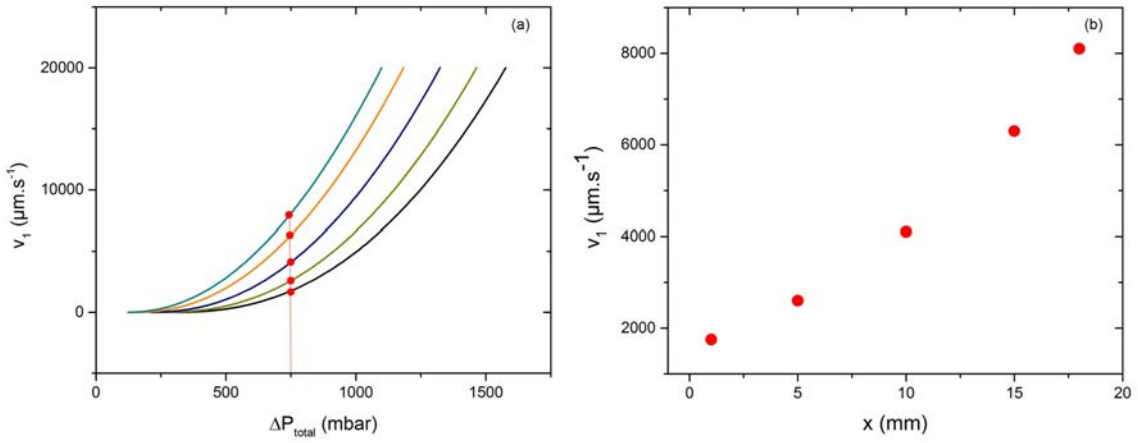

Figure D.3 – (a) Familiy of curves representing the velocity of the interface v_1 as a function of the total pressure drop applied for various x-position of the interface: $x = 1$ mm (black), $x = 5$ mm (dark yellow), $x = 10$ mm (blue), $x = 15$ mm (orange), $x = 18$ mm (dark cyan) for the displacement of a microgel 2.2% by a microgel 1.6% leaving at the wall a residual layer of thickness 20 µm. (b) Evolution of the velocity of the interface as a function of the position of the interface for a constant applied pressure drop of $\Delta P = 750$ mbar for the displacement of a microgel 2.2% by a microgel 1.6% leaving at the wall a residual layer of thickness 20 µm.

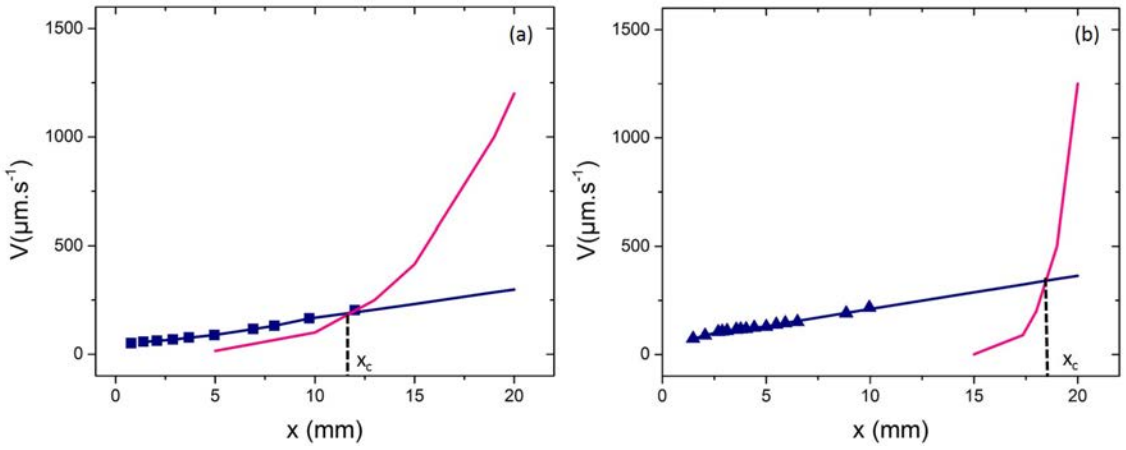

Figure D.4 – Evolution of the velocity of the interface as a function of its x-position for the displacement of (a) a microgel 2.2% and of (b) a microgel 3% by a microgel 1.6% at a pressure drop of 0.3 bar. The symbols are the experimental measurements. The blue lines corresponds to the linear fit of the slip regime observed at the beginning of the experiment. The pink line corresponds to the calcul of the velocity of the interface with no slip boundary conditions.

The transition from one regime to the other occurs at a critical position x_c which depends on the rheology of the fluids and of the total pressure drop applied. As shown on figure D.4, the more viscous is the displaced fluid, the later the transition occurs.

The measurements of the velocity of the interface at the beginning of the displacement gives the slope of the linear slip regime. We also estimate the velocity of the interface in the case of no slip. To estimate the velocity of the interface we plot both curves (slip and no slip). We first follow the slip regime and at the cross-over we use the calcul for no slip boundary conditions.

Restriction

In the case of a restriction the principle to calculate the injected volume is the same except that more serial resistances have to be considered: before, inside and after the restriction and fluid 1 and fluid 2 (six serial resistances).

D.2 Phase 2: After breakthrough time

The interface is out of the channel and there is a residual layer of thickness h near the walls. We consider that the displacing fluid is flowing in a tube of diameter $b - 2h$. The velocity is estimated by following the method described in C.

D.3 Phase 3: the displacing fluid is alone in the channel

There is no residual layer left at the wall and the displacing fluid is flowing in a square channel of side b. The velocity is estimated by following the method described in C.

Appendix E

Experiments in channels with angles

At the bottom of the well during a cementing stage, the cement flows through the guide shoe and is submitted to a U-turn before going back up in the annular. We perform displacement experiments in a channel with an angle to see the influence of a change of direction of the interface. The experiments are carried out with slip and no slip boundary condition. We look at how much and how fast can the angle be cleared out. The geometry of the channel is presented on figure E.1.

Figure E.2 shows the difference of the efficiency of the clear out between the slip and no slip cases. With slip boundary conditions, the angle can be much more cleared out and with a smaller amount of injected volume.

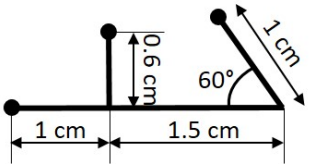

Figure E.1 – Geometry of the channel with an angle.

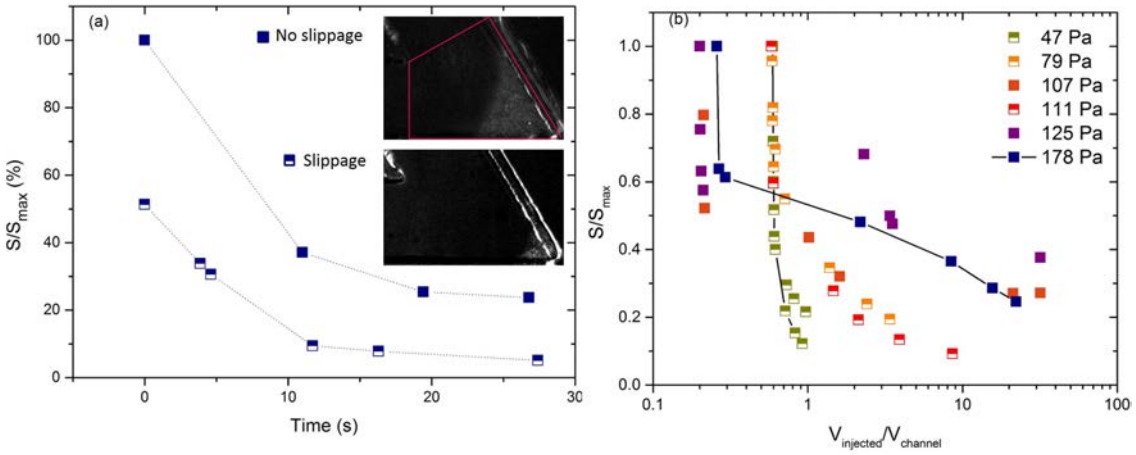

Figure E.2 – (a) Clear out of the corner in the case of slip (half full symbols) at a pressure drop of 0.7 bar and no slip (full symbols) at a pressure drop of 1 bar as a function of time. The front velocity is the same between slip and no slip case. The area delimited with the pink lines corresponds to the surface of the corner S_{max}. (b) Clear out of the corner in the case of slip (half full symbols) and no slip (full symbols) boundary conditions during the displacement of a microgel 2.2% by a microgel 1.6% at various wall shear stress calculated when the displacing fluid is alone in the channel. The solid black lines are just guides for the eyes.

Résumé de la thèse en français

1 Introduction

La construction d'un puit de pétrole se décompose en plusieurs étapes. Tout d'abord, le forage permet de creuser un trou dans le sol. Un tube en acier, le casing, est inséré dans ce trou et est cimenté. Le but de la cimentation est de créer l'étanchéité entre le casing et la formation environnante. Il faut remplir de ciment l'espace annulaire situé entre le casing et la formation rocheuse. Un puit atteint des profondeurs de plusieurs milliers de mètres. Afin d'éviter son effondrement, le puit est construit par sections : les étapes de forage, casing et de cimentation sont répétées à la suite jusqu'à atteindre la profondeur désirée. Lorsque le puit est au niveau du réservoir d'huile, une étape de perforation où l'on tire avec une arme spéciale à travers le casing et la couche annulaire de ciment permet de laisser l'huile entrer dans le puit.

Dans la thèse, nous nous intéresserons plus particulièrement à l'étape de cimentation. Pour remplir de ciment l'espace entre le casing et la paroi rocheuse, le ciment est pompé depuis la surface par le casing vers le fond du puit. Au fond, le ciment remonte dans l'espace annulaire. Sur son chemin, le ciment déplace la boue de forage. Les boues de forage sont circulées dans le puit pendant le forage pour nettoyer le puit des débris rocheux créés par le forage. Après le forage, les boues sont présentes dans le casing ainsi que dans l'annulaire. Si les boues de forage ne sont pas complètement déplacées par le ciment, leurs résidus peuvent empêcher le ciment de prendre correctement et la qualité de l'étanchéité du puit est réduite.

De plus, des outils de cimentation (centraliseurs, colliers...) sont présents dans l'espace annulaire. Ces outils sont conçus pour aider le déplacement de la boue par le ciment. Souvent, les fluides déplacés par le ciment sont plus visqueux que celui-ci. L'interface entre les fluides est donc instable et des digitations visqueuses peuvent se produire dans la direction azimutale. Celles-ci réduisent considérablement l'efficacité de déplacement. Cependant, les densités des fluides sont ajustées de manière à supprimer cette instabilité. Toutefois, ces mesures ne présagent pas du comportement de l'interface dans l'épaisseur de l'espace annulaire. En effet, le fluide déplacé peut laisser un film le long de l'annulaire sur le casing et sur la formation. Ce film réduit la qualité de prise du ciment et des fuites dans la couche de ciment peuvent apparaitre.

L'étape de cimentation est capitale pour l'exploitation d'un puit de pétrole. Elle conditionne sa rentabilité ainsi que sa longévité. Les conséquences d'une mauvaise cimentation sont économiquement et environnementalement catastrophiques. La productivité du puit est réduite (fuites) et les zones géologiques environnantes peuvent être contaminées par

l'huile. L'accident du puit Macondo dans le Golfe du Mexique est un exemple probant de catastrophe écologique due à une mauvaise cimentation.

Dans la thèse, nous utilisons la microfluidique afin d'étudier la question du film de boue laissé dans l'espace annulaire pendant l'étape de cimentation. Le ciment et la boue sont modélisés par des suspensions de microgel qui ont des propriétés rhéologiques similaires (fluides de Herschel-Bulkley). Les échelles microfluidiques (10 µm) sont plus petites que la taille réelle de l'espace annulaire ($\approx 2-5$ cm). Néanmoins, certains nombres sans dimension pertinents sont comparables et ainsi, des informations utiles peuvent être extraites de l'étude microfluidique. L'environnement microfluidique permet de travailler avec différents fluides, géométries, conditions de surface et permet une observation expérimentale directe du film de bonne qualité.

Nous avons également mis en évidence un nouvel effet associé à une échelle caractéristique lors de l'écoulement de fluides de Herschel-Bulkley en systèmes confinés. Cette étude fondamentale montre la richesse de la dynamique des fluides de Herschel-Bulkley.

La thèse est organisée en six chapitres :

- ✧ Le **chapitre 1** introduit la problématique pétrolière. Nous décrivons la fabrication d'un puit de pétrole, les pratiques en vigueur et les problèmes rencontrés lors de la cimentation d'un puit.

- ✧ Le **chapitre 2** décrit la synthèse et la caractérisation rhéologique des suspensions de microgel utilisées dans les expériences.

- ✧ Le **chapitre 3** présente les techniques de fabrication utilisées pour construire des micro-canaux capables de supporter des pertes de charges importantes sans déformations. Des traitements de surfaces permettent de modifier indépendamment les différentes parois des canaux. Les deux expériences (set-up de µPIV et set-up de déplacements de fluides) sont décrites.

- ✧ Le **chapitre 4** est consacré à l'étude de l'écoulement d'une suspension de microgel dans un canal microfluidique en présence de glissement. L'écoulement est caractérisé par des mesures de profils de vitesse avec le set-up de µPIV. Ces mesures sont comparées à celles obtenues en rhéométrie classique au chapitre 2. Nous montrons que les hétérogénéités de glissement contrôlent la structure de l'écoulement lorsque la taille du système décroit.

- ✧ Le **chapitre 5** présente les résultats des expériences de déplacements de fluides de Herschel-Bulkley. Les expériences sont réalisées dans différentes géométries (canaux droits, canaux droits avec restrictions ou cavités). Nous insistons sur l'influence du glissement sur la dynamique du film laissé derrière le fluide déplacé.

- ✧ Le **chapitre 6** présente les résultats numériques obtenus avec le logiciel commercial de dynamique des fluides Fluent. Le code est d'abord testé avec différents cas d'écoulements issus de la littérature, puis nous comparons les simulations aux résultats expérimentaux.

Dans ce résumé, nous rappelons brièvement les résultats des chapitres 2 à 6.

Table E.1 – Paramètres rhéologiques des différentes suspensions de microgel utilisées.

Echantillon	σ_y (Pa)	k (Pa s$^{1/2}$)	n	Concentration (g g^{-1})	Φ [146]
1	11	4.3	0.5	1.6%	$\Phi = 0.7$
2	16.2	5.3	0.5	1.6%	$\Phi = 0.7$
3	15.6	5.1	0.5	1.6%	$\Phi = 0.7$
4	9.4	4.5	0.5	1.6%	$\Phi = 0.7$
5	60.5	10.8	0.5	2.2%	$\Phi = 0.83$
6	16.5	5.6	0.5	1.6%	$\Phi = 0.7$
7	39	9.4	0.5	1.8%	$\Phi = 0.75$
8	86	15.4	0.5	2.2%	$\Phi = 0.83$
9	273	40.9	0.5	3%	$\Phi = 0.98$

2 Caractérisation des suspensions de microgel

Les suspensions de microgel sont des particules colloïdales constituées d'un réseau de polymère gonflé par un solvant (500 nm). Les suspensions utilisées dans la thèse sont en régime de jamming (pour des concentrations massiques de particules supérieures à $C = 0.016$ g g^{-1}, ce qui correspond à $\Phi = 0.72$.) dans lequel elles possèdent un seuil de contrainte.

Les suspensions de microgel sont des fluides non-Newtoniens. Leurs propriétés rhéologiques sont caractérisées à l'aide d'un rhéomètre rotationnel cône-plan. Les suspensions de microgel sont des fluides viscoélastique, ils sont non thixotropes et possèdent de faibles forces normales. Leur courbe d'écoulement est bien décrite par la loi de Herschel-Bulkley : $\sigma = \sigma_y + k * \dot{\gamma}^n$ avec σ_y le seuil d'écoulement, k le paramètre de consistance et n l'indice d'écoulement. En changeant la concentration en polymère de la suspension, il est possible d'en modifier les propriétés rhéologiques. Des particules fluorescentes ont été ajoutées aux suspensions, elles sont imbriquées dans la structure du microgel afin d'être représentatives de son écoulement. Des suspensions de concentrations différentes ont été fabriquées, leurs propriétés rhéologiques sont rassemblées dans le tableau E.1.

3 Matériel et méthodes

3.1 Fabrication et traitements de surface des systèmes microfluidiques

Les systèmes microfluidiques utilisés dans la thèse sont fabriqués à l'aide de la colle photoréticulable NOA. Cette technologie, développée au laboratoire, permet de fabriquer des systèmes en verre qui supportent des pertes de charge importantes (jusque 10 bar) sans déformation.

Différents traitements de surface (silanisation, plasma ou UV-ozone) permettent de modifier indépendamment l'attraction des surfaces supérieures et inférieures d'un canal avec les suspensions de microgel. Ainsi, l'amplitude de la vitesse de glissement dans les micro-canaux a pu être ajustée.

Le glissement dans le système peut être supprimé mécaniquement en ajoutant une rugosité de l'ordre de grandeur de la taille des particules (≈500 nm) sur les parois du système.

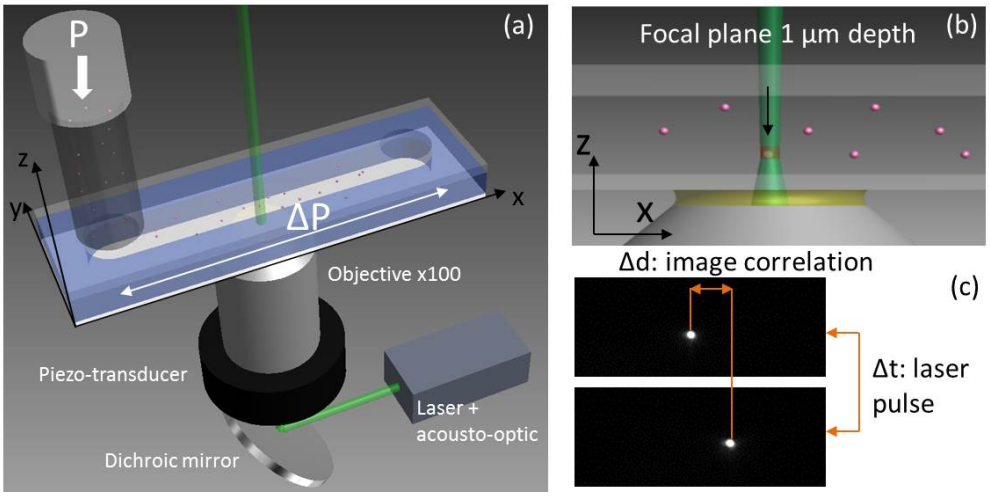

FIGURE E.3 – Experimental µPIV set-up. (a) Les traceurs fluorescents dans le fluide sont excités par épifluorescence avec un faisceau laser modulé par un dispositif acousto-optique. Le signal émis est transmis à la caméra à travers un miroir dichroïque. (b) La précision des expériences dépend principalement de la profondeur du plan focal qui est de 1 µm dans notre expérience. (c) Le déplacement des billes est déterminé par corrélation d'images, les images sont filtrées pour enlever le bruit de fond.

3.2 Vélocimétrie par images de particules (µPIV)

La vélocimétrie par images de particules est une méthode quantitative d'analyse d'écoulements. Le fluide contient des particules fluorescentes qui sont imagées par un système de microscopie afin de récupérer les informations du champ de vitesse comme indiqué sur la figure E.3 (a). La caméra récupère les images des particules dans le plan focal de l'objectif (figure E.3 (b)). L'intervalle de temps entre deux images δt dépend du pulse d'illumination ou de la fréquence de trame de la caméra. La distance entre deux positions d'une même particule δd est calculée par corrélation d'images (figure E.3 (c)). La vitesse de la particule est donc $V = \delta d/\delta d$.

Nos expériences de mesures de profils de vitesses sont faites dans des cellules de Hele-Shaw qui permettent de simplifier l'analyse quantitative de l'écoulement (approximation de plaques parallèles). Une expression analytique du profil de vitesse le long de l'axe z peut être calculée.

3.3 Système expérimental pour l'étude des déplacements de fluides

L'objectif de cette expérience est de déplacer un premier fluide à seuil avec un second fluide non-Newtonien ou Newtonien. Avant de démarrer l'expérience, les fluides doivent être introduits dans le microsystème sans bulle et il faut former une interface plane entre les fluides.

Nous avons donc choisi une jonction T pour initialiser l'expérience. Le système est représenté sur la figure E.4 (a). Le canal de sortie est bouché pendant le déplacement à l'aide d'une vanne Quake représentée sur la figure E.4 (b). Le protocole de l'expérience est schématisé sur la figure E.4 (c) et se compose des étapes suivantes :

1. Connecter les réservoirs des fluides déplaçant et déplacé sur les entrées 1 et 2 respectivement.
2. Pressuriser les réservoirs afin de créer un écoulement de chaque fluide vers la sortie 3.

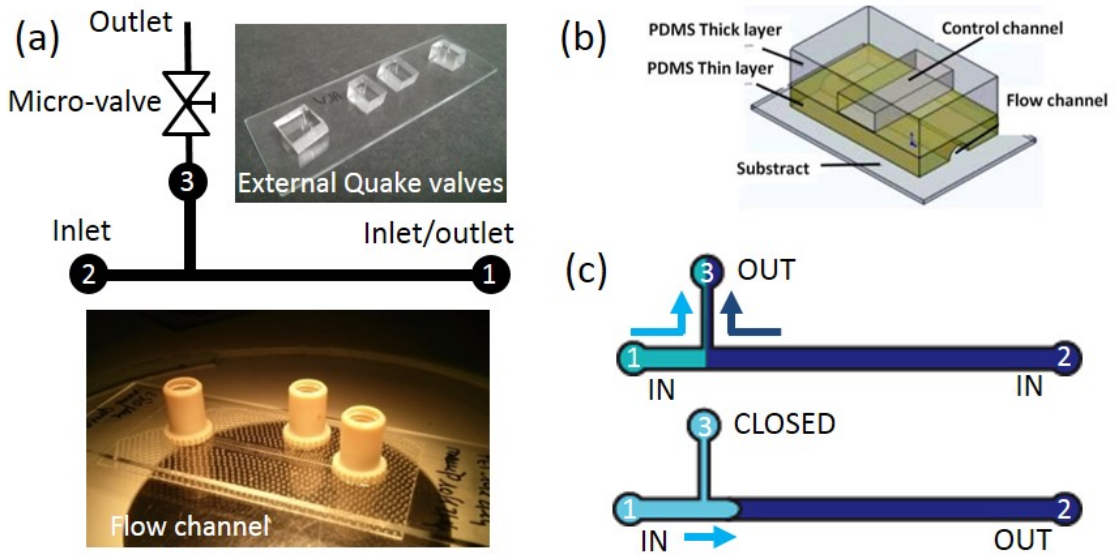

Figure E.4 – Dispositif expérimental pour l'étude de déplacements de fluides. (a) Schéma de l'expérience, image du canal en verre fabriqué avec la colle NOA. (b) Dans la vanne Quake, le canal de contrôle de la vanne se situe au-dessus du canal d'écoulement et peut boucher ce dernier quand il est pressurisé. Reproduction de [166]. (c) Séquence des fluides pour l'initialisation de l'expérience de déplacement.

Maintenir l'écoulement jusqu'à ce que toutes les bulles soient retirées. Une interface plane se forme entre les fluides au niveau de la jonction T.

3. Arrêter l'écoulement, déconnecter le réservoir du fluide à déplacer, fermer la vanne Quake.
4. Démarrer l'expérience en pressurisant le réservoir du fluide déplaçant. L'écoulement se fait de 1 vers 2.

4 Rôle des hétérogénéités de surfaces en systèmes confinés

4.1 Profils de vitesse

Nous avons mesuré les profils de vitesse de suspensions de microgels dans des canaux de différentes hauteurs, à différents gradients de pression et avec plusieurs types de surfaces. On définit $V_{s,1}$ et $V_{s,2}$ comme les vitesses de glissement du microgel sur les surfaces inférieures et supérieures du canal, et $V_{s,min}$ est le minimum de $V_{s,1}$ et $V_{s,2}$. La figure E.5 montre les variations de $V - V_{s,min}$ dans le canal pour les différentes conditions expérimentales.

Pour $h = 100\,\mu m$ (figure E.5 (a)-(c)), les profils de vitesse ont une forme symmétrique attendue pour un écoulement de fluide à seuil : la zone centrale est un plug, et les zones adjacentes au plug et aux parois sont cisaillées.

Pour h =50 µm and 20 µm, nous observons un comportement similaire lorsque les deux parois sont hydrophiles. Ces profils sont représentés sur les figures E.5 (d) et E.5 (g) respectivement.

Cependant, lorsque les parois sont différentes les profils de vitesse sont asymétriques (Figs. E.5 (f) and (h)). Pour $h = 20\,\mu m$, un comportement étonnant apparait : la couche fluidisée près de la paroi hydrophile disparait sur la figure E.5 (h) et finalement, la région non cisaillée s'étend jusqu'à la paroi sur la figure E.5 (i).

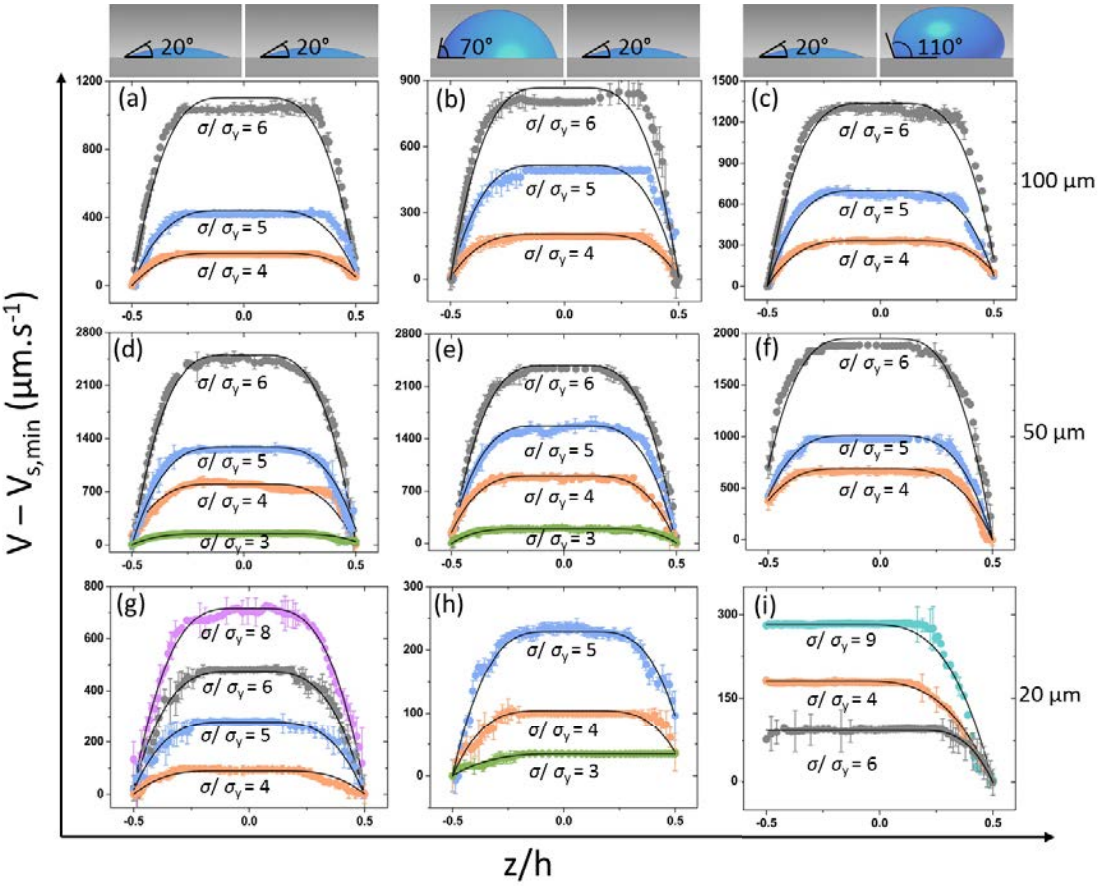

FIGURE E.5 – Profiles de vitesse V auquel est soustraite la vitesse de glissement $V_{s,min}$ pour les différentes hauteurs, conditions de surfaces et contraintes appliquées $\sigma/\sigma_y = 9$ (cyan foncé), 8 (pourpre), 6 (gris), 5 (bleu), 4 (rouge), 3 (vert). Les lignes continues sont les fits de l'expression théorique des profils de vitesse calculées avec le modèle de Herschel-Bulkley asymétrique présenté au paragraphe 4.2.

4.2 Modèle de Herschel-Bulkley asymétrique

Afin d'interpréter les résultats de la figure E.5, nous résolvons les équations de l'écoulement d'un fluide à seuil mis en mouvement par un gradient de pression constant $G = \Delta P/L$ le long de la direction x entre deux plans infinis de longueur L positionnés à des hauteurs $z = -h/2$ et $z = h/2$ où les vitesses de glissement sont $V_{s,1}$ et $V_{s,2}$ respectivement. Nous nous plaçons dans le référentiel en mouvement à une vitesse moyenne $(V_{s,1} + V_{s,2})/2$. Dans ce référentiel, les parois se déplacent à des vitesses opposées $\pm U_s$ où $U_s = (V_{s,1} - V_{s,2})/2$. La contrainte s'écrit $\sigma(z) = \sigma_s - Gz$ avec σ_s une constante non nulle qui traduit le fait que les parois se déplacent à des vitesses opposées. Le calcul donne les expressions suivantes pour les profils de vitesse :

$$\begin{cases} U(z) = \frac{G^2}{3k^2}\left[-(z_1 - z)^3 - \frac{1}{2}\left(z_2 - \frac{h}{2}\right)^3 + \frac{1}{2}\left(z_1 + \frac{h}{2}\right)^3\right], & -\frac{h}{2} < z < z_1 \\ U(z) = \frac{G^2}{3k^2}\left[-\frac{1}{2}\left(z_2 - \frac{h}{2}\right)^3 + \frac{1}{2}\left(z_1 + \frac{h}{2}\right)^3\right], & z_1 < z < z_2 \\ U(z) = \frac{G^2}{3k^2}\left[(z_2 - z)^3 - \frac{1}{2}\left(z_2 - \frac{h}{2}\right)^3 + \frac{1}{2}\left(z_1 + \frac{h}{2}\right)^3\right], & z_2 < z < \frac{h}{2} \end{cases} \tag{E.1}$$

Les expressions de l'équation E.1 peuvent être mises sous forme adimensionnelle à l'aide des variables suivantes : $\bar{U} = U/\left(G^2h^3/3k^2\right)$, $\xi = z/h$, $\bar{\sigma} = \sigma/Gh$ et elles peuvent être étendues au cas des profils composés d'une région non cisaillée qui s'étend jusqu'à une des parois.

Les profils de vitesse expérimentaux sont analysés à l'aide de ce modèle Herschel-Bulkley asymétrique. La valeur de U_s est calculée à partir des mesures expérimentales de $V_{s,1}$ et $V_{s,2}$. k et σ_y sont les paramètres rhéologiques de la loi de Herschel-Bulkley. k est le seul paramètre libre des fits. Les prédictions du modèle sont représentées par les lignes continues sur la figure E.5. Sur les figures E.5 (a) - (g), l'accord est quantitatif avec un écart-type pour k d'environ 15%. Sur les figures E.5 (i) et (h), le profil de vitesse théorique reproduit la forme des profils expérimentaux mais nous avons toléré de plus grandes déviations du paramètre k afin d'obtenir une superposition avec les courbes expérimentales. Néanmoins, nous pouvons conclure que notre modèle de Herschel-Bulkley généralisé reproduit tous les phénomènes observés.

4.3 Discussion

Le modèle théorique permet de définir un nombre adimensionnel $\bar{U_s}$. Nous montrons que $\bar{U_s}$, qui compare les effets des hétérogénéités de glissement aux forces visqueuses, contrôle la structure de l'écoulement. Nous généralisons nos résultats en définissant une longueur l^* définit par $\bar{U_s} = (l^*/h)^2$ en-dessous de laquelle la structure de l'écoulement est contrôlée par les hétérogénéités de surface.

Ce résultat peut être généralisé à tous les fluides en définissant une longueur λ tel que $U_s \approx \lambda\dot{\gamma_w}$ où U_s est la différence de glissement entre les deux parois du système et $\dot{\gamma_w} = f\left(-G\frac{h}{2}\right)$ est le cisaillement à la paroi dans le cas où $U_s = 0$. f est une loi constitutive générale : $\dot{\gamma} = f(\sigma)$. Dans notre cas, nous avons $\lambda = l^{*2}/h$. La transition entre le régime où les hétérogénéités de surface dominent et celui où les forces visqueuses dominent est donnée par $l^* \sim h$.

4.4 Conclusions

Nous avons montré l'importance de prendre en compte les hétérogénéités de glissement lors de l'écoulement de suspensions concentrées dans des systèmes confinés. Dans des cas extrêmes, nous avons observé des profils tronqués : la zone non cisaillée s'étend jusqu'à la paroi.

Nous avons présenté un modèle de Herschel-Bulkley asymétrique qui décrit qualitativement tous les profils de vitesse observés. Nos résultats peuvent être généralisés à tous les fluides en introduisant une longueur l^* en-dessous de laquelle l'écoulement est dominé par les hétérogénéités de glissement.

5 Déplacements de fluides à seuil dans des micro-canaux

5.1 Stratégie pour l'étude des déplacements de fluides de Herschel-Bulkley

Nous déplaçons un fluide de HB avec un autre fluide de HB miscible et nous nous intéressons à l'épaisseur du film laissé aux parois derrière le fluide déplacé. Différentes géométries sont testées, dans ce résumé nous présentons les déplacements en canaux de sections carrées avec obstacles (restrictions pour représenter la présence de colliers ou de changements de sections dans les puits et les cavités pour représenter la rugosité de la paroi rocheuse) ou sans obstacles.

Les suspensions de microgel présentent d'importantes vitesses de glissement dans nos systèmes en verre. Un traitement de surface qui crée une attraction forte entre les particules de microgel et les parois permet de supprimer le glissement. Cependant, ce traitement de surface induit un changement dans l'écoulement : les vitesses d'écoulements sont réduites par rapport à ce qui est attendu théoriquement et la forme du profil près des parois est modifiée. Nous n'expliquons pas ce phénomène déjà observé dans la littérature [163].

5.2 Etude expérimentale du déplacement de fluides de Herschel-Bulkley dans des canaux droits à sections carrées

La figure E.6 représente l'évolution de l'épaisseur du film adimensionnée par la demi-largeur du canal en fonction de la vitesse de l'interface prise à $x = L/2$. Ces mesures ont été obtenues dans des systèmes avec et sans glissement.

Dans le cas sans glissement, l'épaisseur du film est comprise entre 20 et 30% de la demi-largeur du canal indépendamment de la vitesse de l'interface. Nous observons un bon accord quantitatif avec les mesures de C. Gabard obtenues en tubes avec des fluides similaires [58].

L'épaisseur du film semble être comprise théoriquement : les mesures sont en bon accord avec le modèle de recirculation présenté aussi dans [58]. Ce modèle théorique donne une expression de l'épaisseur de film qui ne dépend pas du débit ce qui explique le plateau observé à hautes vitesses dans les expériences sur la figure E.6.

Dans les cas avec glissement, il n'y a pas de films à basses vitesses. Pour des vitesses supérieures à $2\,\mathrm{mm\,s^{-1}}$, un film apparait et son épaisseur est comparable au cas sans glissement. En effet, à des gradients de pression élevés, la vitesse du bulk est beaucoup plus importante que la vitesse de glissement. Ainsi, à hautes vitesse, on tend vers le cas sans glissement.

Le film observé dans les expériences est mobile, il peut être enlevé du canal en maintenant l'écoulement dans le canal.

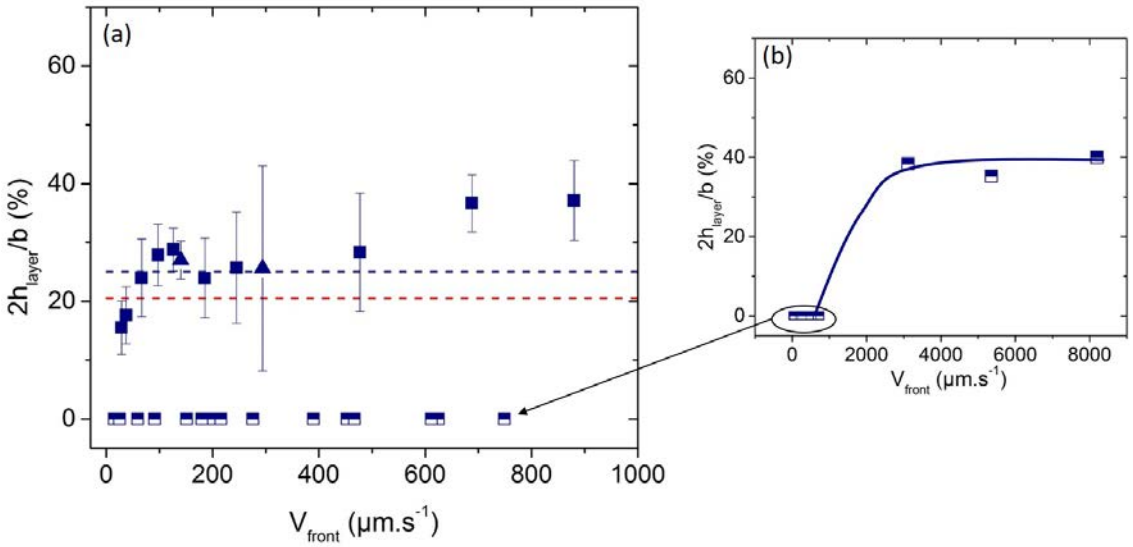

Figure E.6 – (a) Epaisseur du film adimensionnée par la demi-largeur du canal qui est laissé aux parois du canal en fonction de la vitesse de l'interface (prise à $x = L/2$) lors du déplacement d'un microgel 2.2 % (carrés) ou 3% (triangles) par une solution de microgel 1.6% dans des systèmes sans (symboles pleins) et avec (symboles mi-pleins) glissement. La ligne en pointillés bleus correspond à la valeur expérimentale asymptotique de l'épaisseur du film lors du déplacement d'un fluide à seuil par un autre déterminée à plus grande échelle dans [58]. La ligne en pointillés rouges correspond au modèle de recirculation présenté dans [58]. (b) Epaisseur du film adimensionnée par la demi-largeur du canal qui est laissé aux parois du canal en fonction de la vitesse de l'interface (prise à $x = L/2$) lors du déplacement d'un microgel 2.2 % (carrés) par une solution de microgel 1.6% dans des systèmes avec glissement. Les lignes continues sont des guides pour les yeux.

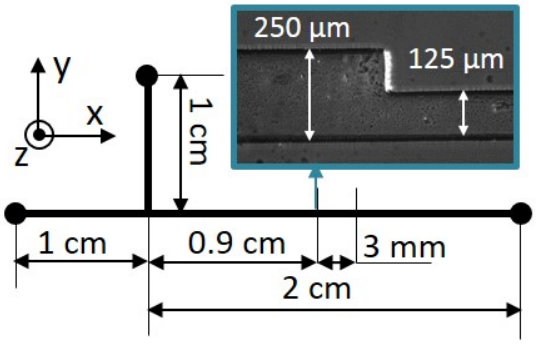

FIGURE E.7 – Géométrie des canaux avec une restriction selon l'axe x.

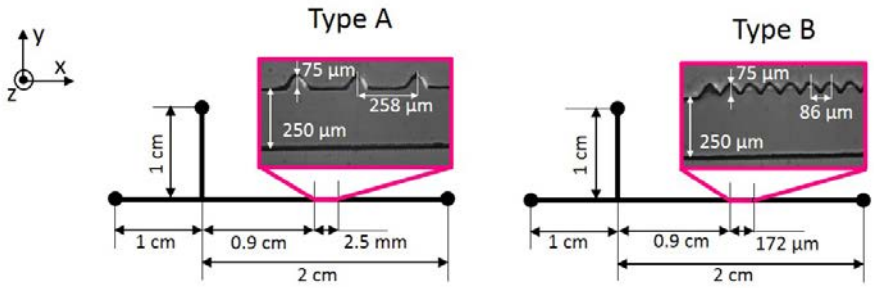

FIGURE E.8 – Géométries des cavités denses et espacées présentes dans les canaux, les détails des dimensions des cavités sont montrés sur les photos.

5.3 Etude expérimentale du déplacement de fluides de Herschel-Bulkley dans des canaux avec des restrictions

Des expériences de déplacements d'un fluide de Herschel-Bulkley par un autre fluide de Herschel-Bulkley sont réalisées dans des canaux avec une restriction dans l'axe de l'écoulement. La géométrie est présentée sur la figure E.7. Des systèmes avec et sans glissement ont été utilisés.

Dans les cas sans glissement, l'épaisseur du film augmente dans la restriction et à la sortie de la restriction.

Dans les cas avec glissement, le déplacement est bouchon à faibles vitesses. À hautes vitesses, nous observons un comportement analogue aux cas sans glissement.

Dans tous les cas, le film est éliminé du canal avec moins de 10 volumes de fluide injectés. Le processus de drainage du film est plus rapide dans les cas avec glissement que sans glissement.

5.4 Etude expérimentale du déplacement de fluides de Herschel-Bulkley dans des canaux avec des cavités

Des expériences de déplacements d'un fluide de Herschel-Bulkley par un autre fluide de Herschel-Bulkley sont réalisées dans des canaux avec des cavités le long du canal dans l'axe de l'écoulement. La géométrie est présentée sur la figure E.8. Des systèmes avec et sans glissement ont été utilisés.

Dans les cas sans glissement, un film se forme le long du canal comme dans les cas étudiés précédemment.

Dans les cas avec glissement, à faibles vitesses le déplacement est bouchon avant les

cavités. Cependant, au niveau des cavités, un film se forme. Nous observons une asymétrie entre le côté du canal avec les cavités (où un film se forme) et le côté opposé sans les cavités (où aucun film ne se forme). Cela suggère que les cavités empêchent localement le glissement. Á hautes vitesses, la symétrie est restaurée et un film se forme des deux côtés. Nous tendons de nouveau vers les comportements observés dans les cas sans glissement.

Nous avons mesuré la quantité de fluide restant dans les cavités et leur évolution en fonction du nombre de volumes de fluide injectés dans le système. Même si les caractéristiques des déplacements à hautes vitesses dans le cas du glissement sont similaires à celles observées dans les cas sans glissement, nous observons que la vidange des cavités est plus rapide dans le cas avec glissement. En effet, dans les cas sans glissement, nous avons toujours un volume significatif du fluide à déplacer qui reste dans les cavités.

5.5 Conclusions

Toutes les expériences réalisées ont montré que la présence de glissement dans le système améliore considérablement l'efficacité du déplacement dans toutes les géométries considérées.

Sans glissement, l'épaisseur du film mesurée est en accord quantitatif avec des mesures réalisées préalablement à plus grande échelle [58] et cette épaisseur est bien décrite par un modèle de minimum de dissipation. Avec glissement, un film se forme seulement à hautes vitesses. L'épaisseur du film décroit avec le temps, cette décroissance est plus rapide en présence de glissement dans le système.

Dans le cas des cavités, la présence de glissement est la seule configuration pour laquelle il est possible d'éliminer complètement le film du système.

6 Analyse numérique de dynamique des fluides

6.1 Comparaison avec la littérature

Nous testons le code commercial de dynamique des fluides Fluent en reproduisant des cas étudiés dans la littérature. Le but est de vérifier que Fluent est adapté au calcul d'écoulements de fluides à seuil dans différents types de géométries. Les cas testés sont les suivants :

- Ecoulement d'un fluide de Herschel-Bulkley dans une cellule de Hele-Shaw. Le profil de vitesse théorique peut être calculé en utilisant une approximation de plans parallèles infinis. Les profils calculés sont comparés aux résultats donnés par Fluent.
- Ecoulement d'un fluide de Bingham dans un canal ondulé. Les résultats sont comparés à [158]. Les cartes de pressions et de vitesses obtenues sont en accord quantitatif avec les résultats de [158].
- Déplacements d'un fluide de Bingham par un autre dans un canal à deux-dimensions. Nous comparons les épaisseurs de films laissées aux parois avec les résultats de [187] et nous obtenons un bon accord quantitatif.

Tous les cas testés montrent un bon accord quantitatif avec les publications ou avec les calculs théoriques.

6.2 Comparaison avec les expériences

Nous souhaitons à présent reproduire les résultats expérimentaux avec la simulation numérique. Nous choisissons des rhéologies de fluides comparables aux suspensions de microgels utilisées dans les expériences. Tous les fluides suivent la loi de Herschel-Bulkley.

Les cas expérimentaux reproduits sont les suivants :
— Déplacements de microgels 2.2% et 3% par un microgel 1.6% dans des canaux droits avec et sans glissement.
— Déplacements de microgels 2.2% par un microgel 1.6% dans des canaux droits avec des restrictions dans la direction de l'écoulement avec et sans glissement.
— Déplacements de microgels 2.2% par un microgel 1.6% dans des canaux droits avec des cavités le long du canal avec et sans glissement.

Canaux droits

Sans glissement, l'épaisseur de film calculée est significativement inférieure aux résultats expérimentaux. Dans le cas avec glissement il n'y a jamais de film déposé même à très hautes vitesses.

Canaux droits avec restrictions

Sans glissement, nous n'avons pas observé l'augmentation de l'épaisseur du film dans les restrictions et à leurs sorties. Avec glissement, comme dans le cas des canaux droits sans obstacle, le déplacement se fait toujours en bouchon même à hautes vitesses.

Canaux droits avec cavités

Dans tous les cas testés, nous n'observons jamais une vidange des cavités contrairement aux expériences. Une analyse du champ de vitesse montre qu'aucun n'écoulement n'a lieu dans les cavités. Avec glissement, nous observons que l'interface évite la zone des cavités : un film se forme près des cavités seulement. Cette observation est en accord avec l'expérience.

6.3 Conclusions

Nous montrons que Fluent donne des résultats qui sont en bon accord quantitatif avec des cas sélectionnés dans la littérature qui utilisent une autre méthode pour la modélisation des fluides à seuil.

La comparaison avec les expériences est difficile dans les cas sans glissement. Les résultats suggèrent que les simulations numériques reproduisent les résultats expérimentaux obtenus à faibles vitesses dans les cas avec glissement.

7 Conclusions

La thèse comprend deux parties principales :

✧ **Une étude fondamentale des effets des hétérogénéités de glissement sur les écoulements de fluides de Herschel-Bulkley dans des micro-canaux.** Le travail a montré que lorsque le confinement augmente, les hétérogénéités de glissement jouent un rôle croissant. Nous définissons une nouvelle longueur qui permet d'estimer l'influence des hétérogénéités de glissement sur la structure des écoulements.

✧ **Une investigation des effets du glissement sur le film laissé derrière une interface séparant deux fluides miscibles de Herschel-Bulkley s'écoulant dans un micro-canal.** Différentes géométries ont été testées : canaux droits, avec restrictions et avec cavités. Nous montrons que le glissement est un paramètre crucial de l'expérience. En présence de glissement, il existe une vitesse critique au-delà

de laquelle un film apparait derrière l'interface. En-dessous de cette vitesse, les déplacements sont bouchons. Une partie des résultats expérimentaux est reproduite par les simulations numériques.

Les processus de cimentation se produisent à des vitesses supérieures à la vitesse critique mentionnée précédemment. Ainsi, un film de boue sera laissé aux parois quelque soient les conditions de glissement aux parois. Néanmoins, notre travail suggère que dans tous les cas, la présence de glissement favorise les déplacements de fluides : elle permet (dans le cas des obstacles) ou accélère l'élimination du film.

Bibliography

[1] Talal T. Al-Housseiny, Peichun A. Tsai, and Howard A. Stone. Control of interfacial instabilities using flow geometry. *Nature Physics*, 8(10):747–750, October 2012.

[2] M. Allouche, I. A. Frigaard, and G. Sona. Static wall layers in the displacement of two visco-plastic fluids in a plane channel. *Journal of Fluid Mechanics*, 424(1):243–277, 2000.

[3] Martine Ben Amar and Eugenia Corvera Poiré. Pushing a non-Newtonian fluid in a Hele-Shaw cell: From fingers to needles. *Physics of Fluids (1994-present)*, 11(7):1757–1767, July 1999.

[4] Pedro H. A. Anjos and José A. Miranda. Radial viscous fingering: Wetting film effects on pattern-forming mechanisms. *Physical Review E*, 88(5):053003, November 2013.

[5] ANSYS. ANSYS Fluent Theory Guide, 2013.

[6] Birnur K. Aral and Dilhan M. Kalyon. Effects of temperature and surface roughness on time-dependent development of wall slip in steady torsional flow of concentrated suspensions. *Journal of Rheology (1978-present)*, 38(4):957–972, July 1994.

[7] Pedro Aranha, Cristiane Miranda, Walter Cardoso, Gilson Campos, Andre Martins, Frederico Gomes, Simone de Araujo, and Marcio Carvalho. A Comprehensive Theoretical and Experimental Study on Fluid Displacement for Oilwell-Cementing Operations. *SPE Drilling & Completion*, 27(4), December 2012.

[8] P. Ballesta, G. Petekidis, L. Isa, W. C. K. Poon, and R. Besseling. Wall slip and flow of concentrated hard-sphere colloidal suspensions. *Journal of Rheology*, 56(5):1005, 2012.

[9] Neil J. Balmforth, Ian A. Frigaard, and Guillaume Ovarlez. Yielding to Stress: Recent Developments in Viscoplastic Fluid Mechanics. *Annual Review of Fluid Mechanics*, 46(1):121–146, January 2014.

[10] Ha Barnes. A Review of the Slip (wall Depletion) of Polymer-Solutions, Emulsions and Particle Suspensions in Viscometers - Its Cause, Character, and Cure. *Journal of Non-Newtonian Fluid Mechanics*, 56(3):221–251, March 1995. WOS:A1995QQ22200001.

[11] Denis Bartolo, Guillaume Degré, Philippe Nghe, and Vincent Studer. Microfluidic stickers. *Lab on a Chip*, 8(2):274, 2008.

[12] Yevgeny Berdichevsky, Julia Khandurina, András Guttman, and Y. H. Lo. UV/ozone modification of poly(dimethylsiloxane) microfluidic channels. *Sensors and Actuators B: Chemical*, 97(2–3):402–408, February 2004.

[13] V. Bertola, F. Bertrand, H. Tabuteau, D. Bonn, and P. Coussot. Wall slip and yielding in pasty materials. *Journal of Rheology*, 47(5):1211, 2003.

[14] Irmgard Bischofberger, Radha Ramachandran, and Sidney R. Nagel. Fingering versus stability in the limit of zero interfacial tension. *Nature Communications*, 5, October 2014.

[15] S. H. Bittleston, J. Ferguson, and I. A. Frigaard. Mud removal and cement placement during primary cementing of an oil well – Laminar non-Newtonian displacements in an eccentric annular Hele-Shaw cell. *Journal of Engineering Mathematics*, 43(2-4):229–253, August 2002.

[16] Lydéric Bocquet, Annie Colin, and Armand Ajdari. Kinetic Theory of Plastic Flow in Soft Glassy Materials. *Physical Review Letters*, 103(3):036001, July 2009.

[17] Dhananjay Bodas and Chantal Khan-Malek. Hydrophilization and hydrophobic recovery of PDMS by oxygen plasma and chemical treatment—An SEM investigation. *Sensors and Actuators B: Chemical*, 123(1):368–373, April 2007.

[18] E. S. Boek, J. T. Padding, V. J. Anderson, W. J. Briels, and J. P. Crawshaw. Flow of entangled wormlike micellar fluids: Mesoscopic simulations, rheology and μ-PIV experiments. *Journal of Non-Newtonian Fluid Mechanics*, 146(1–3):11–21, October 2007.

[19] D. Bonn, H. Kellay, M. Bräunlich, M. Ben Amar, and J. Meunier. Viscous fingering in complex fluids. *Physica A: Statistical Mechanics and its Applications*, 220(1–2):60–73, October 1995.

[20] J.-P. Bouchaud. Weak ergodicity breaking and aging in disordered systems. *Journal de Physique I*, 2:265, 1992.

[21] Jalila Boujlel, M. Maillard, A. Lindner, Guillaume Ovarlez, Xavier Chateau, and Philippe Coussot. Boundary layer in pastes—Displacement of a long object through a yield stress fluid. *Journal of Rheology*, 56:1083, 2012.

[22] C.I Bouzigues, L Bocquet, E Charlaix, C Cottin-Bizonne, B Cross, L Joly, A Steinberger, C Ybert, and P Tabeling. Using surface force apparatus, diffusion and velocimetry to measure slip lengths. *Philosophical Transactions of the Royal Society A: Mathematical, Physical and Engineering Sciences*, 366(1869):1455–1468, April 2008.

[23] Rodolfo Brandão, João V. Fontana, and José A. Miranda. Interfacial pattern formation in confined power-law fluids. *Physical Review E*, 90(1):013013, July 2014.

[24] Rodolfo Brandão, João V. Fontana, and José A. Miranda. Suppression of viscous fingering in nonflat Hele-Shaw cells. *Physical Review E*, 90(5):053003, November 2014.

[25] F. P. Bretherton. The motion of long bubbles in tubes. *Journal of Fluid Mechanics*, 10(02):166–188, March 1961.

[26] M. Carrasco-Teja and I. A. Frigaard. Non-Newtonian fluid displacements in horizontal narrow eccentric annuli: effects of slow motion of the inner cylinder. *Journal of Fluid Mechanics*, 653:137–173, June 2010.

[27] Kenny Chau, Brent Millare, Adam Lin, Srigokul Upadhyayula, Vicente Nuñez, Hong Xu, and Valentine I. Vullev. Dependence of the quality of adhesion between poly(dimethylsiloxane) and glass surfaces on the composition of the oxidizing plasma. *Microfluidics and Nanofluidics*, 10(4):907–917, November 2010.

[28] Pinaki Chaudhuri, Vincent Mansard, Annie Colin, and Lyderic Bocquet. Dynamical Flow Arrest in Confined Gravity Driven Flows of Soft Jammed Particles. *Physical Review Letters*, 109(3):036001, July 2012.

[29] Ching-Yao Chen and Eckart Meiburg. Miscible displacements in capillary tubes. Part 2. Numerical simulations. *Journal of Fluid Mechanics*, 326:57–90, 1996.

[30] Michel Cloitre, Régis Borrega, and Ludwik Leibler. Rheological Aging and Rejuvenation in Microgel Pastes. *Physical Review Letters*, 85(22):4819–4822, November 2000.

[31] Michel Cloitre, Régis Borrega, Fabrice Monti, and Ludwik Leibler. Structure and flow of polyelectrolyte microgels: from suspensions to glasses. *Comptes Rendus Physique*, 4(2):221–230, March 2003.

[32] Roland Combescot, Thierry Dombre, Vincent Hakim, Yves Pomeau, and Alain Pumir. Shape Selection of Saffman-Taylor Fingers. *Physical Review Letters*, 56(19):2036–2039, May 1986.

[33] Eugenia Corvera Poiré and Martine Ben Amar. Finger Behavior of a Shear Thinning Fluid in a Hele-Shaw Cell. *Physical Review Letters*, 81(10):2048–2051, September 1998.

[34] Philippe Coussot. Saffman–Taylor instability in yield-stress fluids. *Journal of Fluid Mechanics*, 380:363–376, 1999.

[35] Philippe Coussot and Julie Goyon. Rapport d'étude Navier, Schlumberger internal report, 2012.

[36] Philippe Coussot, Q. D. Nguyen, H. T. Huynh, and Daniel Bonn. Avalanche Behavior in Yield Stress Fluids. *Physical Review Letters*, 88(17):175501, April 2002.

[37] Philippe Coussot and Jean-Michel Piau. A large-scale field coaxial cylinder rheometer for the study of the rheology of natural coarse suspensions. *Journal of Rheology (1978-present)*, 39(1):105–124, January 1995.

[38] B. G. Cox. On driving a viscous fluid out of a tube. *Journal of Fluid Mechanics*, 14(01):81–96, September 1962.

[39] A. de Lózar, A. L. Hazel, and A. Juel. Scaling Properties of Coating Flows in Rectangular Channels. *Physical Review Letters*, 99(23):234501, December 2007.

[40] Guillaume Degré, Pierre Joseph, Patrick Tabeling, Sandra Lerouge, Michel Cloitre, and Armand Ajdari. Rheology of complex fluids by particle image velocimetry in microchannels. *Applied Physics Letters*, 89(2):024104, 2006.

[41] Nikolai D. Denkov, Vivek Subramanian, Daniel Gurovich, and Alex Lips. Wall slip and viscous dissipation in sheared foams: Effect of surface mobility. *Colloids and Surfaces A: Physicochemical and Engineering Aspects*, 263(1-3):129–145, August 2005.

[42] C. Derec, A. Ajdari, and F. Lequeux. Rheology and aging: A simple approach. *The European Physical Journal E*, 4(3):355–361, March 2001.

[43] Remi Dreyfus, Patrick Tabeling, and Herve Willaime. Ordered and Disordered Patterns in Two-Phase Flows in Microchannels. *Physical Review Letters*, 90(14), April 2003.

[44] Aurélien Duboin. *Écoulements de fluides complexes en présence d'interfaces dans des systèmes microfluidiques*. PhD thesis, Université Pierre et Marie Curie-Paris VI, 2013.

[45] David C. Duffy, J. Cooper McDonald, Olivier J. A. Schueller, and George M. Whitesides. Rapid Prototyping of Microfluidic Systems in Poly(dimethylsiloxane). *Analytical Chemistry*, 70(23):4974–4984, December 1998.

[46] D. J. Durian. Bubble-scale model of foam mechanics:mMelting, nonlinear behavior, and avalanches. *Physical Review E*, 55(2):1739–1751, February 1997.

[47] Kirill Efimenko, William E. Wallace, and Jan Genzer. Surface Modification of Sylgard-184 Poly(dimethyl siloxane) Networks by Ultraviolet and Ultraviolet/Ozone Treatment. *Journal of Colloid and Interface Science*, 254(2):306–315, October 2002.

[48] Brian M. Erwin, Michel Cloitre, Mario Gauthier, and Dimitris Vlassopoulos. Dynamics and rheology of colloidal star polymers. *Soft Matter*, 6(12):2825, 2010.

[49] M. L. Falk and J. S. Langer. Dynamics of viscoplastic deformation in amorphous solids. *Physical Review E*, 57(6):7192, 1998.

[50] Joel H Ferziger and M Peric. *Computational methods for fluid dynamics*. Springer, Berlin; New York, 2002.

[51] S. M. Fielding, M. E. Cates, and P. Sollich. Shear banding, aging and noise dynamics in soft glassy materials. *Soft Matter*, 5(12):2378–2382, 2009.

[52] João V. Fontana, Eduardo O. Dias, and José A. Miranda. Controlling and minimizing fingering instabilities in non-Newtonian fluids. *Physical Review E*, 89(1):013016, January 2014.

[53] João V. Fontana, Sérgio A. Lira, and José A. Miranda. Radial viscous fingering in yield stress fluids: Onset of pattern formation. *Physical Review E*, 87(1):013016, January 2013.

[54] Fred H. Bartlit. Macondo the gulf oil disaster, 2011.

[55] I. A. Frigaard and C. Nouar. On the usage of viscosity regularisation methods for visco-plastic fluid flow computation. *Journal of Non-Newtonian Fluid Mechanics*, 127(1):1–26, April 2005.

[56] Jennifer L. Fritz and Michael J. Owen. Hydrophobic Recovery of Plasma-Treated Polydimethylsiloxane. *The Journal of Adhesion*, 54(1-4):33–45, November 1995.

[57] C. Gabard and J.-P. Hulin. Miscible displacement of non-Newtonian fluids in a vertical tube. *The European Physical Journal E - Soft Matter*, 11(3):231–241, July 2003.

[58] Céline Gabard. *Déplacements de fluides miscibles non-newtoniens en conduite cylindrique verticale*. Thèse de doctorat, France, 2001.

[59] F. J. Galindo-Rosales, M. A. Alves, and M. S. N. Oliveira. Microdevices for extensional rheometry of low viscosity elastic liquids: a review. *Microfluidics and Nanofluidics*, 14(1-2):1–19, July 2012.

[60] Vishal Gauri and Kurt W. Koelling. The motion of long bubbles through viscoelastic fluids in capillary tubes. *Rheologica Acta*, 38(5):458–470, November 1999.

[61] Baudouin Geraud, Lyderic Bocquet, and Catherine Barentin. Confined flows of a polymer microgel. *The European Physical Journal E*, 36(3), March 2013.

[62] Thomas Gervais, Jamil El-Ali, Axel Günther, and Klavs F. Jensen. Flow-induced deformation of shallow microfluidic channels. *Lab on a Chip*, 6(4):500, 2006.

[63] Thomas Gibaud, Catherine Barentin, and Sébastien Manneville. Influence of Boundary Conditions on Yielding in a Soft Glassy Material. *Physical Review Letters*, 101(25):258302, December 2008.

[64] Joseph R. Gladden and Andrew Belmonte. Motion of a Viscoelastic Micellar Fluid around a Cylinder: Flow and Fracture. *Physical Review Letters*, 98(22):224501, May 2007.

[65] J. Goyon, A. Colin, G. Ovarlez, A. Ajdari, and L. Bocquet. Spatial cooperativity in soft glassy flows. *Nature*, 454(7200):84–87, July 2008.

[66] Julie Goyon. *Matériaux amorphes: des solides qui coulent de façon collective*. Thèse de doctorat, École doctorale des Sciences chimiques, Talence ; Gironde, France, 2008.

[67] Julie Goyon, Annie Colin, and Lydéric Bocquet. How does a soft glassy material flow: finite size effects, non local rheology, and flow cooperativity. *Soft Matter*, 6(12):2668–2678, June 2010.

[68] Wolfgang Götze. Recent tests of the mode-coupling theory for glassy dynamics. *Journal of Physics: Condensed Matter*, 11(10A):A1, March 1999.

[69] Etienne Guyon, Jean-Pierre Hulin, and Luc Petit. *Hydrodynamique physique*. EDP sciences Les Ulis, France, 2012.

[70] Brian S. Hardy, Kawika Uechi, Janet Zhen, and H. Pirouz Kavehpour. The deformation of flexible PDMS microchannels under a pressure driven flow. *Lab on a Chip*, 9(7):935, 2009.

[71] A. L. Hazel, M. Pailha, S. J. Cox, and A. Juel. Multiple states of finger propagation in partially occluded tubes. *Physics of Fluids (1994-present)*, 25(6):062106, June 2013.

[72] Pascal Hébraud and François Lequeux. Mode-coupling theory for the pasty rheology of soft glassy materials. *Physical review letters*, 81(14):2934, 1998.

[73] H. S. Hele-Shaw. Flow of Water. *Nature*, 58:520, September 1898.

[74] David L. Henann and Ken Kamrin. A predictive, size-dependent continuum model for dense granular flows. *Proceedings of the National Academy of Sciences*, 110(17):6730–6735, April 2013.

[75] S. Hill and F. Inst. P. Channeling in packed columns. *Chemical Engineering Science*, 1(6):247–253, 1952.

[76] H. Hillborg, J. F. Ankner, U. W. Gedde, G. D. Smith, H. K. Yasuda, and K. Wikström. Crosslinked polydimethylsiloxane exposed to oxygen plasma studied by neutron reflectometry and other surface specific techniques. *Polymer*, 41(18):6851–6863, August 2000.

[77] G M Homsy. Viscous Fingering in Porous Media. *Annual Review of Fluid Mechanics*, 19(1):271–311, 1987.

[78] D. C. Hong and J. S. Langer. Analytic Theory of the Selection Mechanism in the Saffman-Taylor Problem. *Physical Review Letters*, 56(19):2032–2035, May 1986.

[79] Viktor Horváth, Tamás Vicsek, and János Kertész. Viscous fingering with imposed uniaxial anisotropy. *Physical Review A*, 35(5):2353–2356, March 1987.

[80] Y. T. Hu, P. Boltenhagen, E. Matthys, and D. J. Pine. Shear thickening in low-concentration solutions of wormlike micelles. II. Slip, fracture, and stability of the shear-induced phase. *Journal of Rheology*, 42(5):1209–1226, October 1998. WOS:000075748600011.

[81] P. C Huzyak and K. W Koelling. The penetration of a long bubble through a viscoelastic fluid in a tube. *Journal of Non-Newtonian Fluid Mechanics*, 71(1–2):73–88, July 1997.

[82] Lucio Isa, Rut Besseling, and Wilson C K Poon. Shear Zones and Wall Slip in the Capillary Flow of Concentrated Colloidal Suspensions. *Physical Review Letters*, 98(19), May 2007.

[83] Ville Jokinen, Pia Suvanto, and Sami Franssila. Oxygen and nitrogen plasma hydrophilization and hydrophobic recovery of polymers. *Biomicrofluidics*, 6(1):016501, March 2012.

[84] Pierre Jop, Vincent Mansard, Pinaki Chaudhuri, Lydéric Bocquet, and Annie Colin. Microscale Rheology of a Soft Glassy Material Close to Yielding. *Physical Review Letters*, 108(14):148301, April 2012.

[85] Pierre Joseph. *Etude expérimentale du glissement sur surfaces lisses et texturées*. PhD thesis, Paris 6, 2005.

[86] Pierre Joseph and Patrick Tabeling. Direct measurement of the apparent slip length. *Physical Review E*, 71(3), March 2005.

[87] Dilhan M. Kalyon. Letter to the editor: Comments on the use of rheometers with rough surfaces or surfaces with protrusions. *Journal of Rheology (1978-present)*, 49(5):1153–1155, September 2005.

[88] Sa Khan, Ca Schnepper, and Rc Armstrong. Foam Rheology .3. Measurement of Shear-Flow Properties. *Journal of Rheology*, 32(1):69–92, January 1988. WOS:A1988L834700005.

[89] K. Kimura, K. Takase, J. E. Griffith, R. A. Gibson, D. S. Porter, and T. E. Becker. Custom-blending foamed cement for multiple challenges. pages 353–362, 1999.

[90] W. Blake Kolb and Ramon L. Cerro. Coating the inside of a capillary of square cross section. *Chemical Engineering Science*, 46(9):2181–2195, 1991.

[91] W. Kozicki, C. H. Chou, and C. Tiu. Non-Newtonian flow in ducts of arbitrary cross-sectional shape. *Chemical Engineering Science*, 21(8):665–679, August 1966.

[92] Jun Kuang, Tony Maxworthy, and Philippe Petitjeans. Miscible displacements between silicone oils in capillary tubes. *European Journal of Mechanics - B/Fluids*, 22(3):271–277, May 2003.

[93] J.Y. Lai, Y.Y. Lin, Y.L. Denq, S.S. Shyu, and J.K. Chen. Surface modification of silicone rubber by gas plasma treatment. *Journal of Adhesion Science and Technology*, 10(3):231–242, January 1996.

[94] E. Lajeunesse, J. Martin, N. Rakotomalala, and D. Salin. 3d Instability of Miscible Displacements in a Hele-Shaw Cell. *Physical Review Letters*, 79(26):5254–5257, December 1997.

[95] E. Lajeunesse, J. Martin, N. Rakotomalala, D. Salin, and Y. C. Yortsos. Miscible displacement in a Hele-Shaw cell at high rates. *Journal of Fluid Mechanics*, 398:299–319, 1999.

[96] R. G. Larson. Constitutive equations for thixotropic fluids. *Journal of Rheology (1978-present)*, 59(3):595–611, May 2015.

[97] Renée A. Lawton, Colin R. Price, Anne F. Runge, Walter J. Doherty III, and S. Scott Saavedra. Air plasma treatment of submicron thick PDMS polymer films: effect of oxidation time and storage conditions. *Colloids and Surfaces A: Physicochemical and Engineering Aspects*, 253(1–3):213–215, February 2005.

[98] E. Lemaire, P. Levitz, G. Daccord, and H. Van Damme. From viscous fingering to viscoelastic fracturing in colloidal fluids. *Physical Review Letters*, 67(15):2009–2012, October 1991.

[99] M. Paul Lettinga and Sébastien Manneville. Competition between Shear Banding and Wall Slip in Wormlike Micelles. *Physical Review Letters*, 103(24):248302, December 2009.

[100] Bertrand Levaché, Ammar Azioune, Maurice Bourrel, Vincent Studer, and Denis Bartolo. Engineering the surface properties of microfluidic stickers. *Lab on a Chip*, 12(17):3028, 2012.

[101] Yunchao Li, Zhen Wang, Lily M. L. Ou, and Hua-Zhong Yu. DNA Detection on Plastic : Surface Activation Protocol To Convert Polycarbonate Substrates to Biochip Platforms. *Analytical Chemistry*, 79(2):426–433, 2006.

[102] Zhenzhen Li. *Microfluidics at micrometric and sub-micrometric scale : NanoPTV, droplets formation, and sub-micrometric model.* phdthesis, Université Pierre et Marie Curie - Paris VI, July 2014.

[103] Zhenzhen Li, Loïc D'eramo, Choongyeop Lee, Fabrice Monti, Marc Yonger, Benjamin Chollet, Bruno Bresson, Yvette Tran, and Patrick Tabeling. Near-wall nanovelocimetry based on Total Internal Reflection Fluorescence with continuous tracking. *arXiv:1405.1372 [physics]*, May 2014. arXiv: 1405.1372.

[104] Anke Lindner. *L'instabilité de Saffman-Taylor dans les fluides complexes: relation entre les propriétés rhéologiques et la formation de motifs.* Thèse de doctorat, France, 2000.

[105] Anke Lindner, Daniel Bonn, Eugenia Corvera Poiré, Martine Ben Amar, and Jacques Meunier. Viscous fingering in non-Newtonian fluids. *Journal of Fluid Mechanics*, 469:237–256, October 2002.

[106] Anke Lindner, Philippe Coussot, and Daniel Bonn. Viscous Fingering in a Yield Stress Fluid. *Physical Review Letters*, 85(2):314–317, July 2000.

[107] Christopher W. Macosko. *Rheology: principles, measurements and applications.* Wiley-VCH, 1994.

[108] M. Maillard, J. Boujlel, and P. Coussot. Flow characteristics around a plate withdrawn from a bath of yield stress fluid. *Journal of Non-Newtonian Fluid Mechanics*, 220:33–43, June 2015.

[109] Honest Makamba, Jin Ho Kim, Kwanseop Lim, Nokyoung Park, and Jong Hoon Hahn. Surface modification of poly(dimethylsiloxane) microchannels. *ELECTROPHORESIS*, 24(21):3607–3619, 2003.

[110] S. Malekmohammadi, M. Carrasco-Teja, S. Storey, I. A. Frigaard, and D. M. Martinez. An experimental study of laminar displacement flows in narrow vertical eccentric annuli. *Journal of Fluid Mechanics*, 649:371–398, 2010.

[111] Sahil Malhotra and Mukul M. Sharma. Impact of fluid elasticity on miscible viscous fingering. *Chemical Engineering Science*, 117:125–135, September 2014.

[112] Vincent Mansard. *Non-local rheology of soft glassy materials.* Thèse de doctorat, Laboratoire du Futur, Bordeaux, France, 2012.

[113] Vincent Mansard, Lydéric Bocquet, and Annie Colin. Boundary conditions for soft glassy flows: slippage and surface fluidization. *Soft Matter*, 10(36):6984–6989, April 2014.

[114] Vincent Mansard and Annie Colin. Local and non local rheology of concentrated particles. *Soft Matter*, 8(15):4025, 2012.

[115] Vincent Mansard, Annie Colin, Pinaki Chaudhuri, and Lydéric Bocquet. A molecular dynamics study of non-local effects in the flow of soft jammed particles. *Soft Matter*, 9(31):7489, 2013.

[116] Vincent Mansard, Annie Colin, Pinaki Chauduri, and Lyderic Bocquet. A kinetic elasto-plastic model exhibiting viscosity bifurcation in soft glassy materials. *Soft Matter*, 7(12):5524, 2011.

[117] J. Clerk Maxwell. On the Dynamical Theory of Gases. *Philosophical Transactions of the Royal Society of London*, 157:49–88, January 1867.

[118] K. V. McCloud and J. V. Maher. Pattern selection in an anisotropic Hele-Shaw cell. *Physical Review E*, 51(2):1184–1190, February 1995.

[119] J. W. McLean and P. G. Saffman. The effect of surface tension on the shape of fingers in a Hele Shaw cell. *Journal of Fluid Mechanics*, 102:455–469, 1981.

[120] R.H. Mclean, C.W. Manry, and W.W. Whitaker. Displacement Mechanics in Primary Cementing. *Journal of Petroleum Technology*, 19(2), February 1967.

[121] Steven Meeker, Roger Bonnecaze, and Michel Cloitre. Slip and Flow in Soft Particle Pastes. *Physical Review Letters*, 92(19), May 2004.

[122] Steven P. Meeker, Roger T. Bonnecaze, and Michel Cloitre. Slip and flow in pastes of soft particles: Direct observation and rheology. *Journal of Rheology*, 48(6):1295, 2004.

[123] Lavanya Mohan, Roger T. Bonnecaze, and Michel Cloitre. Microscopic Origin of Internal Stresses in Jammed Soft Particle Suspensions. *Physical Review Letters*, 111(26):268301, December 2013.

[124] Lavanya Mohan, Charlotte Pellet, Michel Cloitre, and Roger Bonnecaze. Local mobility and microstructure in periodically sheared soft particle glasses and their connection to macroscopic rheology. *Journal of Rheology*, 57(3):1023–1046, May 2013. WOS:000318252400013.

[125] Cécile Monthus and Jean-Philippe Bouchaud. Models of traps and glass phenomenology. *Journal of Physics A: Mathematical and General*, 29(14):3847, July 1996.

[126] Fabrice Monti. *Microrhéologie de suspensions colloïdales non ergodiques: Relaxations locales, dynamiques lentes et vieillissement*. Thèse de doctorat, France, 2010.

[127] Melvin Mooney. Explicit Formulas for Slip and Fluidity. *Journal of Rheology*, 2(2):210, 1931.

[128] S. Mora and M. Manna. Saffman-Taylor instability for generalized Newtonian fluids. *Physical Review E*, 80(1):016308, July 2009.

[129] M Morra, E Occhiello, R Marola, F Garbassi, P Humphrey, and D Johnson. On the aging of oxygen plasma-treated polydimethylsiloxane surfaces. *Journal of Colloid and Interface Science*, 137(1):11–24, June 1990.

[130] Christel Métivier, Yahya Rharbi, Albert Magnin, and Antoine Bou Abboud. Stick-slip control of the Carbopol microgels on polymethyl methacrylate transparent smooth walls. *Soft Matter*, 8(28):7365, 2012.

[131] Tatsunosuke Murakami, Shin-ichi Kuroda, and Zenjiro Osawa. Dynamics of Polymeric Solid Surfaces Treated with Oxygen Plasma: Effect of Aging Media after Plasma Treatment. *Journal of Colloid and Interface Science*, 202(1):37–44, June 1998.

[132] Y. S. Muzychka and J. Edge. Laminar Non-Newtonian Fluid Flow in Noncircular Ducts and Microchannels. *Journal of Fluids Engineering*, 130(11):111201, 2008.

[133] Erik B. Nelson and Dominique Guillot. *Well cementing*. Schlumberger, 2006.

[134] Chiara Neto, Drew R Evans, Elmar Bonaccurso, Hans-Jürgen Butt, and Vincent S J Craig. Boundary slip in Newtonian liquids: a review of experimental studies. *Reports on Progress in Physics*, 68(12):2859–2897, December 2005.

[135] P. Nghe, S. M. Fielding, P. Tabeling, and A. Ajdari. Interfacially Driven Instability in the Microchannel Flow of a Shear-Banding Fluid. *Physical Review Letters*, 104(24), June 2010.

[136] Philippe Nghe. *Ecoulements de fluides complexes en géométries microfluidiques*. phdthesis, Université Pierre et Marie Curie - Paris VI, November 2009.

[137] Philippe Nghe, Guillaume Degré, Patrick Tabeling, and Armand Ajdari. High shear rheology of shear banding fluids in microchannels. *Applied Physics Letters*, 93(20):204102, 2008.

[138] K. N. Nordstrom, E. Verneuil, P. E. Arratia, A. Basu, Z. Zhang, A. G. Yodh, J. P. Gollub, and D. J. Durian. Microfluidic Rheology of Soft Colloids above and below Jamming. *Physical Review Letters*, 105(17), October 2010.

[139] Thomas J. Ober, Simon J. Haward, Christopher J. Pipe, Johannes Soulages, and Gareth H. McKinley. Microfluidic extensional rheometry using a hyperbolic contraction geometry. *Rheologica Acta*, 52(6):529–546, May 2013.

[140] Michael J. Owen. The Surface Activity of Silicones: A Short Review. *Industrial & Engineering Chemistry Product Research and Development*, 19(1):97–103, 1980.

[141] Michael J. Owen and Patrick J. Smith. Plasma treatment of polydimethylsiloxane. *Journal of Adhesion Science and Technology*, 8(10):1063–1075, January 1994.

[142] M. Pailha, A. L. Hazel, P. A. Glendinning, and A. Juel. Oscillatory bubbles induced by geometrical constraint. *Physics of Fluids (1994-present)*, 24(2):021702, February 2012.

[143] C.-W. Park and G. M. Homsy. Two-phase displacement in Hele Shaw cells: theory. *Journal of Fluid Mechanics*, 139:291–308, 1984.

[144] S. Pelipenko and I. A. Frigaard. Two-dimensional computational simulation of eccentric annular cementing displacements. *IMA Journal of Applied Mathematics*, 69(6):557–583, December 2004.

[145] S. Pelipenko and I. A. Frigaard. Visco-plastic fluid displacements in near-vertical narrow eccentric annuli: prediction of travelling-wave solutions and interfacial instability. *Journal of Fluid Mechanics*, 520:343–377, 2004.

[146] Charlotte Pellet. Suspensions concentrées de microgels ioniques: verres colloïdaux et verres encombrés, 2012.

[147] P. Petitjeans and T. Maxworthy. Miscible displacements in capillary tubes. Part 1. Experiments. *Journal of Fluid Mechanics*, 326:37–56, 1996.

[148] Christopher J.S. Petrie. Extensional viscosity: A critical discussion. *Journal of Non-Newtonian Fluid Mechanics*, 137(1-3):15–23, August 2006.

[149] G. Picard, A. Ajdari, F. Lequeux, and L. Bocquet. Elastic consequences of a single plastic event: A step towards the microscopic modeling of the flow of yield stress fluids. *The European Physical Journal E*, 15(4):371–381, November 2004.

[150] Guillemette Picard, Armand Ajdari, Lydéric Bocquet, and François Lequeux. Simple model for heterogeneous flows of yield stress fluids. *Physical Review E*, 66(5):051501, November 2002.

[151] Guillemette Picard, Armand Ajdari, François Lequeux, and Lydéric Bocquet. Slow flows of yield stress fluids: Complex spatiotemporal behavior within a simple elastoplastic model. *Physical Review E*, 71(1):010501, January 2005.

[152] Olivier Pouliquen and Yoel Forterre. A non-local rheology for dense granular flows. *Philosophical Transactions of the Royal Society of London A: Mathematical, Physical and Engineering Sciences*, 367(1909):5091–5107, December 2009.

[153] H.M Princen. Rheology of foams and highly concentrated emulsions. II. experimental study of the yield stress and wall effects for concentrated oil-in-water emulsions. *Journal of Colloid and Interface Science*, 105(1):150–171, May 1985.

[154] B. Rabinowitsch. Über die viskosität und elastizität von solen. *Z. Phys. Chem. A*, 145:1–26, 1929.

[155] N. Rakotomalala, D. Salin, and P. Watzky. Miscible displacement between two parallel plates: BGK lattice gas simulations. *Journal of Fluid Mechanics*, 338:277–297, May 1997.

[156] J. S Ro and G. M Homsy. Viscoelastic free surface flows: thin film hydrodynamics of Hele-Shaw and dip coating flows. *Journal of Non-Newtonian Fluid Mechanics*, 57(2–3):203–225, May 1995.

[157] L.E. Rodd, J.J. Cooper-White, D.V. Boger, and G.H. McKinley. Role of the elasticity number in the entry flow of dilute polymer solutions in micro-fabricated contraction geometries. *Journal of Non-Newtonian Fluid Mechanics*, 143(2-3):170–191, May 2007.

[158] A. Roustaei and I.A. Frigaard. The occurrence of fouling layers in the flow of a yield stress fluid along a wavy-walled channel. *Journal of Non-Newtonian Fluid Mechanics*, 198:109–124, August 2013.

[159] P. G. Saffman and Geoffrey Taylor. The Penetration of a Fluid into a Porous Medium or Hele-Shaw Cell Containing a More Viscous Liquid. *Proceedings of the Royal Society of London. Series A. Mathematical and Physical Sciences*, 245(1242):312–329, June 1958.

[160] J.-B. Salmon, L. Bécu, S. Manneville, and A. Colin. Towards local rheology of emulsions under Couette flow using Dynamic Light Scattering. *The European Physical Journal E - Soft Matter*, 10(3):209–221, March 2003.

[161] J. G. Santiago, S. T. Wereley, C. D. Meinhart, D. J. Beebe, and R. J. Adrian. A particle image velocimetry system for microfluidics. *Experiments in Fluids*, 25(4):316–319, September 1998.

[162] Jyoti R. Seth, Michel Cloitre, and Roger T. Bonnecaze. Influence of short-range forces on wall-slip in microgel pastes. *Journal of Rheology*, 52(5):1241, 2008.

[163] Jyoti R. Seth, Clémentine Locatelli-Champagne, Fabrice Monti, Roger T. Bonnecaze, and Michel Cloitre. How do soft particle glasses yield and flow near solid surfaces? *Soft Matter*, 8(1):140, 2012.

[164] Jyoti R. Seth, Lavanya Mohan, Clémentine Locatelli-Champagne, Michel Cloitre, and Roger T. Bonnecaze. A micromechanical model to predict the flow of soft particle glasses. *Nature Materials*, 10(11):838–843, November 2011.

[165] Siti Aminah Setu, Ioannis Zacharoudiou, Gareth J. Davies, Denis Bartolo, Sébastien Moulinet, Ard A. Louis, Julia M. Yeomans, and Dirk G. A. L. Aarts. Viscous fingering at ultralow interfacial tension. *Soft Matter*, 9(44):10599, 2013.

[166] Bingqing Shen. *Transport and self-assembly of droplets in microfluidic devices*. PhD thesis, Paris 6, 2014.

[167] Boris I. Shraiman. Velocity Selection and the Saffman-Taylor Problem. *Physical Review Letters*, 56(19):2028–2031, May 1986.

[168] Taha Sochi. Slip at Fluid-Solid Interface. *Polymer Reviews*, 51(4):309–340, October 2011.

[169] Peter Sollich. Rheological constitutive equation for a model of soft glassy materials. *Physical Review E*, 58(1):738–759, July 1998.

[170] Peter Sollich, François Lequeux, Pascal Hébraud, and Michael E. Cates. Rheology of Soft Glassy Materials. *Physical Review Letters*, 78(10):2020–2023, March 1997.

[171] Prabhata K. Swamee and Nitin Aggarwal. Explicit equations for laminar flow of herschel-bulkley fluids. *The Canadian Journal of Chemical Engineering*, 89(6):1426–1433, December 2011.

[172] P. Tabeling and A. Libchaber. Film draining and the Saffman-Taylor problem. *Physical Review A*, 33(1):794–796, January 1986.

[173] P. Tabeling, G. Zocchi, and A. Libchaber. An experimental study of the Saffman-Taylor instability. *Journal of Fluid Mechanics*, 177:67–82, 1987.

[174] H. Tabuteau, S. Mora, G. Porte, M. Abkarian, and C. Ligoure. Microscopic Mechanisms of the Brittleness of Viscoelastic Fluids. *Physical Review Letters*, 102(15):155501, April 2009.

[175] K. C. Tang, E. Liao, W. L. Ong, J. D. S. Wong, A. Agarwal, R. Nagarajan, and L. Yobas. Evaluation of bonding between oxygen plasma treated polydimethyl siloxane and passivated silicon. *Journal of Physics: Conference Series*, 34(1):155, April 2006.

[176] G. I. Taylor. Deposition of a viscous fluid on the wall of a tube. *Journal of Fluid Mechanics*, 10(02):161–165, March 1961.

[177] M. A. Tehrani, S. H. Bittleston, and P. J. G. Long. Flow instabilities during annular displacement of one non-Newtonian fluid by another. *Experiments in Fluids*, 14(4):246–256, February 1993.

[178] Alice B. Thompson, Anne Juel, and Andrew L. Hazel. Multiple finger propagation modes in Hele-Shaw channels of variable depth. *Journal of Fluid Mechanics*, 746:123–164, May 2014.

[179] Derek C. Tretheway and Carl D. Meinhart. Apparent fluid slip at hydrophobic microchannel walls. *Physics of Fluids*, 14(3):L9, 2002.

[180] Domenico Truzzolillo, Serge Mora, Christelle Dupas, and Luca Cipelletti. Off-Equilibrium Surface Tension in Colloidal Suspensions. *Physical Review Letters*, 112(12):128303, March 2014.

[181] András Tóth, Imre Bertóti, Marianne Blazsó, György Bánhegyi, Alajos Bognar, and Pál Szaplonczay. Oxidative damage and recovery of silicone rubber surfaces. I. X-ray photoelectron spectroscopic study. *Journal of Applied Polymer Science*, 52(9):1293–1307, 1994.

[182] Marc A. Unger, Hou-Pu Chou, Todd Thorsen, Axel Scherer, and Stephen R. Quake. Monolithic Microfabricated Valves and Pumps by Multilayer Soft Lithography. *Science*, 288(5463):113–116, April 2000.

[183] F. Varnik, L. Bocquet, J.-L. Barrat, and L. Berthier. Shear Localization in a Model Glass. *Physical Review Letters*, 90(9), March 2003.

[184] Dimitris Vlassopoulos and Michel Cloitre. Tunable rheology of dense soft deformable colloids. *Current Opinion in Colloid & Interface Science*, 19(6):561–574, December 2014.

[185] Ph. Wägli, A. Homsy, and N.F. de Rooij. Norland optical adhesive (NOA81) microchannels with adjustable wetting behavior and high chemical resistance against

a range of mid-infrared-transparent organic solvents. *Sensors and Actuators B: Chemical*, 156(2):994–1001, August 2011.

[186] Andrew R. White and Thomas Ward. Constant pressure gas-driven displacement of a shear-thinning liquid in a partially filled radial Hele-Shaw cell: Thin films, bursting and instability. *Journal of Non-Newtonian Fluid Mechanics*, 206:18–28, April 2014.

[187] K. Wielage-Burchard and I.A. Frigaard. Static wall layers in plane channel displacement flows. *Journal of Non-Newtonian Fluid Mechanics*, 166(5–6):245–261, March 2011.

[188] Stuart J. Williams, Choongbae Park, and Steven T. Wereley. Advances and applications on microfluidic velocimetry techniques. *Microfluidics and Nanofluidics*, 8(6):709–726, June 2010.

[189] D. J. Wilson, R. C. Pond, and R. L. Williams. Wettability of Chemically Modified Polymers: Experiment and Theory. *Interface Science*, 8(4):389–399, October 2000.

[190] H. Zhao and J. V. Maher. Associating-polymer effects in a Hele-Shaw experiment. *Physical Review E*, 47(6):4278–4283, June 1993.

[191] Jinwen Zhou, Amanda Vera Ellis, and Nicolas Hans Voelcker. Recent developments in PDMS surface modification for microfluidic devices. *ELECTROPHORESIS*, 31(1):2–16, 2010.

[192] Giovanni Zocchi, Bruce E. Shaw, Albert Libchaber, and Leo P. Kadanoff. Finger narrowing under local perturbations in the Saffman-Taylor problem. *Physical Review A*, 36(4):1894–1900, August 1987.

[193] Giovanni Zocchi, Patrick Tabeling, and Martine Ben Amar. Saffman-Taylor plumes. *Physical Review Letters*, 69(4):601–604, July 1992.